Strong coupling regime of cavity quantum electrodynamics and its consequences on molecules and materials

Thibault Chervy

UNIVERSITÉ DE STRASBOURG

ÉCOLE DOCTORALE ED222

UMR 7006

THÈSE présentée par :

Thibault CHERVY

soutenue le : **15 Septembre 2017**

pour obtenir le grade de : **Docteur de l'université de Strasbourg**

Discipline/ Spécialité : Physique

Strong coupling regime of cavity quantum electrodynamics and its consequences on molecules and materials

Régime de couplage fort de l'électrodynamique quantique en cavité et conséquences pour les molécules et les matériaux

THÈSE dirigée par :

M. EBBESEN W. Thomas	Prof. Dr., ISIS, Université de Strasbourg

RAPPORTEURS :

M. RUBIO Angel	Prof. Dr., Max Planck institute for structure and dynamics of matter
M. GOMEZ RIVAS Jaime	Prof. Dr., Dutch institute for fundamental energy research

---

AUTRES MEMBRES DU JURY :

M. GENET Cyriaque	Dr., ISIS, CNRS - Université de Strasbourg
M. PUPILLO Guido	Prof. Dr., IPCMS, Université de Strasbourg
M. IMAMOGLU Ataç	Prof. Dr., Institut für Quantenelektronik

CONTENTS

LIST OF PUBLICATIONS

JOURNAL PUBLICATIONS

Work covered in this thesis

- T. Chervy, A. Thomas, E. Akiki, R. M. A. Vergauwe, A. Shalabney, J. George, E. Devaux, J. A. Hutchison, C. Genet and T. W. Ebbesen
  Vibro-polaritonic IR emission in the strong coupling regime,
  Submitted for publication

- T. Chervy*, S. Azzini*, E. Lorchat, S. Wang, Y. Gorodetski, J. A. Hutchison, S. Berciaud, T. W. Ebbesen and C. Genet,
  Spin-momentum locked polariton transport in the chiral strong coupling regime,
  Submitted for publication

- X. Zhong, T. Chervy, L. Zhang, A. Thomas, J. George, C. Genet, J. A. Hutchison and T.W. Ebbesen,
  Energy transfer between spatially separated entangled molecules,
  Angew. Chem. Int. Ed. (2017)

- J. George*, T. Chervy*, A. Shalabney, E. Devaux, H. Hiura, C. Genet and T. W. Ebbesen,
  Multiple Rabi splittings under ultra-strong vibrational coupling,
  Phys. Rev. Lett., 117, 153601 (2016).

- T. Chervy, J. Xu, Y. Duan, C. Wang, L. Mager, M. Frerejean, J. A. W. Münninghoff, P. Tinnemans, J. A. Hutchison, C. Genet, A. E. Rowan, T. Rasing and T. W. Ebbesen,

High efficiency second-harmonic generation from hybrid light-matter states,
Nano Lett., *16*, *7352-7356 (2016)*

- S. Wang*, S. Li*, T. Chervy*, A. Shalabney, S. Azzini, E. Orgiu, J. A. Hutchison, C. Genet, P. Samorì and T. W. Ebbesen,
Coherent coupling of WS_2 monolayers with metallic photonic nanostructures at room temperature,
Nano Lett., *16*, *4368-4374 (2016)*

- X. Zhong, T. Chervy, S. Wang, J. George, A. Thomas, J. A. Hutchison, E. Devaux, C. Genet and T. W. Ebbesen,
Non-radiative energy transfer mediated by hybrid light-matter states,
Angew. Chem. Int. Ed., *55*, *6202-6206 (2016)*

- J. George, S. Wang, T. Chervy, A. Canaguier-Durand, G. Schaeffer, J.-M. Lehn, J. A. Hutchison, C. Genet and T. W. Ebbesen,
Ultra-strong coupling of molecular materials: spectroscopy and dynamics
Farad. Discuss., *178*, *281-294 (2015)*

- S. Wang, T. Chervy, J. George, J. A. Hutchison, C. Genet and T. W. Ebbesen
Quantum yield of polariton emission from hybrid light-matter states
J. Phys. Chem. Lett., *5*, *1433-1439 (2014)*

Other publications

- A. Thomas, J. George, A. Shalabney, M. Dryzhakov, S. J. Varma, J. Moran, T. Chervy, X. Zhong, E. Devaux, C. Genet, J. A. Hutchison and T. W. Ebbesen,
Ground-state chemical reactivity under vibrational coupling to the vacuum electromagnetic field,
Angew. Chem. Int. Ed., *128*, *11634 (2016)*.

- R. M. A. Vergauwe, J. George, T. Chervy, J. A. Hutchison, A. Shalabney, V. Torbeev and T. W. Ebbesen,
  Quantum strong coupling with protein vibrational modes,
  J. Phys. Chem. Lett., 7, 4159-4164 (2016).

- Y. Gorodetski, T. Chervy, S. Wang, J. A. Hutchison, A. Drezet, C. Genet and T. W. Ebbesen,
  Tracking surface plasmon pulses using ultrafast leakage imaging,
  Optica, 3, 48-53, (2016)

CONFERENCE PRESENTATIONS

- *ACS on Campus*, Strasbourg November 25, 2016 (Talk)
  Hybrid light-matter states: a molecular and material science perspective
  T. Chervy

- *NIE scientific day*, Strasbourg June 14, 2016 (Poster)
  Multiple Rabi splitttings under vibrational ultra-strong coupling
  J. George*, T. Chervy*, A. Shalabney, E. Devaux, H. Hiura, C. Genet and T. W. Ebbesen

- *GDR Ondes on Nonlinear and Quantum Plasmonics*, Marseille June 2, 2016 (Talk)
  Efficient second harmonic generation from hybrid light-matter states
  T. Chervy, J. Xu, Y. Duan, C. Wang, L. Mager, M. Frerejean, J. A. W. Münninghoff, P. Tinnemans, J. A. Hutchison, C. Genet, A. E. Rowan, T. Rasing and T. W. Ebbesen

- *ICSCE8 on Hybrid Polaritonics*, Edinburgh April 25-29, 2016 (Poster)
  Multiple Rabi splitttings under vibrational ultra-strong coupling
  J. George*, T. Chervy*, A. Shalabney, E. Devaux, H. Hiura, C. Genet and T. W. Ebbesen

- *International School of Physics 'Enrico Fermi' on Complex photonics*, Varenna July 18, 2015 (Talk)
  Molecules in the strong coupling regime
  J. George, S. Wang, T. Chervy, A. Canaguier-Durand, G. Schaeffer, J.-M. Lehn, J. A. Hutchison, C. Genet and T. W. Ebbesen

- *Faraday discussion on Nanoplasmonics*, London February 16-18, 2015 (Poster)
  Ultra-strong coupling of molecular materials: spectroscopy and dynamics
  J. George, S. Wang, T. Chervy, A. Canaguier-Durand, G. Schaeffer, J.-M. Lehn, J. A. Hutchison, C. Genet and T. W. Ebbesen

- *ISIS Young Scientist Seminar*, Strasbourg July 3, 2014 (Talk)
  The strong coupling of your light with my matters
  T. Chervy

SYNOPSIS

Since its early developments in cold atoms physics in the 1980*s* [1], the vacuum strong coupling regime of cavity quantum electrodynamics (cQED) has emerged as a new frontier of science by providing unprecedented control of matter by light and of light by matter [2]. Recent achievements in Bose-Einstein condensation [3–6], superfluidity [7–9], entanglement swapping [10], topological operations [11], synthetic gauge design [12, 13] and modified chemical reactions [14, 15] among many others, hold great promises for future technological applications of strongly coupled systems [16], and open new avenues of fundamental research [17].

This regime has been realized on a rich variety of platforms, embracing semiconductor quantum wells [18], superconducting q-bits [19], nuclear X-ray transitions [20], as well as electronic [21] and vibrational [22] transitions of organic materials. Quite remarkably, such different realizations of light-matter strong coupling, ranging from the gigahertz to the hard X-ray energies, can all be understood on the basis of a very simple coupled oscillators Hamiltonian [23]. When the light-matter coupling strength becomes sufficiently high, this model predicts the appearance of new eigen-states, termed polaritonic states, sharing properties of both light and matter. The hybrid nature of such states provides a unique opportunity to intertwine the non-local and propagating behavior of light with the localized, interacting, and potentially nonlinear behavior of matter. Thus, despite their formal equivalence, the specificities of each platforms in terms of their coupling to an 'environment' and their intrinsic non-linearities give rise to a wealth of different research directions.

In this thesis, we have investigated different aspects of light-matter strong coupling involving macroscopic ensembles

of molecules collectively coupled to a common cavity mode. The new chemical and material properties offered by those polaritonic states pave ways to the currently emerging field of Rabi chemistry. Our contribution to this work has been organized in four chapters.

- The first chapter aims at giving a broad overview of the vacuum strong coupling regime of cQED, starting with a brief historical perspective, and introducing some of the key concepts of strong light-molecules interaction. Several state of the art developments are exposed, giving a general context to this work.

- In the second chapter, we investigate the population dynamics and energy pathways in strongly coupled molecular systems. This chapter compiles different experimental approaches both in the static and transient regimes, and gives a glimpse at the broad range of possibilities offered by light-matter strong coupling in complex molecular landscapes.

- The third chapter is concerned with the strong coupling of optical resonances with molecular vibrations in the IR domain. This regime of vibrational strong coupling opens new horizons in the context of modified chemical reactions under light-matter interaction, and non-linear polariton dynamics.

- In chapter 4, we investigate the rich interplay between light-matter strong coupling and chirality. This is done by coupling chiral spin-orbit plasmonic modes at a metal surface with the valley contrasted excitons of a 2D transition metal dichalcogenide monolayer. In this regime, we observe surprisingly robust material coherences, revealing the ability of polaritonic states to protect specific degrees of freedom from decoherence, a phenomenon underlying several other results presented in this thesis.

1

LIGHT-MATTER STRONG COUPLING FOR NOVEL MATERIAL AND CHEMICAL PROPERTIES

Light-matter interaction is a key process in modern technologies, constituting a fast interface between propagating optical modes mediating information over long distances, and localized material states with potentially large nonlinearities. This interplay between weakly and strongly interacting systems allows for efficient switching, routing and computing, which are currently driving the research effort in a broad field ranging from material sciences to cold atoms and from telecom optics to nanophotonics. In quest of integrability, tailoring light-matter interaction at the (sub-)wavelength scales is thus leading to an emerging class of devices with unprecedented properties, where an effective photon-photon interaction is obtained from the nonlinearity of the material medium [24–28].

Light-matter interaction can however also be considered from a opposite perspective, where an effective nonlocality arises in the material due to its interaction with extended photonic modes. This approach is rooted in the pioneering work of Purcell on the modification of the relaxation rate of a spin in a RLC resonator in 1946 [29] and its later extension to the visible frequency domain by Drexhage in 1974 [30]. In those celebrated experiments, the light matter coupling frequency remained lower than the relaxation frequency of each systems toward the environment, such that only the spontaneous decay rate and the Lamb shift of the transition could be affected. This regime, later termed ‘weak coupling regime’, constitutes

nevertheless the first demonstration of the modification of material properties by tailoring the surrounding electromagnetic vacuum. In other words, properties that were thought to be intrinsic to matter turned out to be properties of the matter dressed by its electromagnetic environment. The possibility of dressing material resonances to control and modify specific molecular properties is at the heart of this thesis work.

1.1 A BRIEF AND PARTIAL HISTORICAL PERSPECTIVE

Even though remarkable effects of the surrounding electromagnetic environment on the radiative properties of atoms and molecules could be observed by placing them near a metallic reflector, the most dramatic modifications of their properties were expected to happen when the light-matter coupling strength would overcome any of the possible relaxation rates. To our knowledge, the first experimental demonstration of this strong coupling regime was reported in 1975 by Yakovlev, Nazin and Zhizhin [31], following the theoretical work of Agranovich and Malshukov [32]. In 1983, the first cold atoms experiment to reach this regime was reported by Kaluzny and coworkers, using a cloud of sodium Rydberg atoms in a superconducting Fabry-Pérot resonator [1].

In such cavity QED experiments, the spectral density $J(\omega)$, quantifying the interaction strength between the atoms and their surrounding electromagnetic vacuum states is dramatically modified by the field boundary conditions imposed by the cavity. The redistribution of this spectral density over sharp frequency ranges, *i.e.* cavity modes, can lead to situations where $J(\omega)$ is non-constant over an energy range of the order of $J(\omega)/\hbar$, resulting in a light-matter coupling frequency higher than the memory time of the cavity mode [2, 33]. In this ringing regime of cQED, favored by coupling large ensembles of absorbers to high finesse cavities, the dynamical evolution of the absorber-field system is strikingly different from that observed under weak coupling. In particular, the irreversible

spontaneous emission is replaced by a reversible exchange of energy between the field and the atoms, giving rise to periodic Rabi oscillations. Accordingly, the energy levels of the atoms and the field hybridize into two new polaritonic eigen-states which are coherent superpositions of light and matter, separated in energy by the inverse of the Rabi period T_R, the Rabi splitting Ω_R [23].

With Rabi splittings potentially reaching significant fractions of the energy of the coupled transitions, light-matter strong coupling must lead to a complete redefinition of the potential energy surfaces of the system, with profound implications on its chemical and material properties. Moreover, provided that the N absorbers present in the cavity remain indistinguishable with respect to their coupling to the mode, they would participate collectively in the formation of the hybrid light-matter states [34]. This collective eigen-states splitting is one of the hallmarks of the light-matter strong coupling regime. It shows how an incoherent ensemble of distant absorbers can spontaneously cooperate in shared and delocalized hybrid states. We have here the two levers that will be used throughout this work: modified energetics and collectivity.

The observation of temporal Rabi oscillations and energy levels splitting triggered a huge interest from a broad community of researchers, while the fundamental aspect of this phenomenon allowed different platforms to be explored, in particular using quantum wells in semiconductor microcavities [18]. While major efforts were devoted to reach the single atom strong coupling regime, with the aim of realizing highly nonlinear systems where, for instance, the state of a single atom could switch the transitivity of the whole system [35], the pioneering groups of semiconductor strong coupling [36] focused on the possibilities offered by polariton-polariton interactions inherent to many-body strong coupling.

After 25 years of active research, the field of semiconductor strong coupling continues to progress with the demonstration of polariton Bose-Einstein condensation [3–6], superfluid-

ity [7–9], entanglement swapping [16], topological operations [11], or synthetic gauge design [12, 13] among many others.

Unlike those very dynamical developments in inorganic semiconductors, the early demonstration of molecular strong coupling passed almost unnoticed, likely due to the typically small exciton radii in such systems (hence the weak polariton-polariton interactions) and the comparatively high material disorder. Room temperature exciton-surface plasmon strong coupling was indeed already reported in 1982 by Pockrand and coworkers [21] using Langmuir-Blodgett films of molecular self-assemblies. Fifteen years (and 14 citations) later, a theoretical proposal by Agranovich [37] and two experimental papers by Fujita *et al.* [38] and Lidzey *et al.* [39] renewed the interest in this field. With their small dielectric constants and high oscillator strengths organic semiconductors were shown to provide the large and robust Rabi splittings required for room temperature strong coupling, while their hybridization with Wannier-Mott inorganic excitons could offer new ways to engineer relaxation mechanisms. With the technical progresses in thin film deposition and cavity mirror coatings, it thus became apparent that organic strong coupling could play a key role as a low cost, easy to make, room temperature stable candidate to realize the fascinating phenomena observed with quantum well polaritons. This perspective has driven a considerable research effort over the last decade, eventually leading to the demonstration of room temperature polariton lasing [40–44] and superfluidity [45] in organic materials.

But beside their robust excitonic nature and relative ease of processability, strongly coupled molecular materials had something fundamentally new to offer: their chemical complexity and direct link to material sciences. This aspect of molecular strong coupling, completely overlooked at this time, is what motivated Ebbesen and coworkers to undertake research on this subject in 2003 [46], laying the ground for a new field at the interface of cQED and molecular and material sciences.

1.2 LIGHT-MOLECULES STRONG COUPLING

Rather than directly giving an Hamiltonian description of a generic strongly coupled system [47–49], we will here follow a more heuristic approach, and try to introduce some of the key concepts of molecular polariton physics as they reveal themselves through experiments. The celebrated Jaynes-Cummings model of polariton physics [23] will then naturally arise as an extreme simplification of those systems. Recent extensions of this model toward an accurate description of strong coupling in complex molecular systems will be briefly reviewed.

1.2.1 *Molecules for cQED?*

Molecules, often displaying hundreds of ro-vibrational modes, flexible backbones, inherent disorder and notoriously interacting with their environment, are clearly not the first systems that come in mind when thinking about QED experiments. Despite this fact, several studies have shown that they can display a rich variety of quantum phenomena, directly related to the survival of electronic or vibrational coherences over picoseconds time scales. For instance, oscillatory dynamics in the transient absorption spectra of photosynthetic complexes was already reported in 1995 [50], raising fascinating questions on the role of quantum coherences in the function and reactivity of chemical and biological systems. The wealth of experiments that followed [51] opened the blossoming field of quantum biology, where coherences, entanglement and disorder participate in the efficiency of energy transport in pigment-protein complexes [52, 53].

Another striking example where quantum effects emerge in molecular systems is found in supramolecular aggregates [54, 55]. In such systems, individual chromophores can self-assemble into supramolecular entities with excited states spanning extended domains of coherently coupled monomeric units. As the molecular excitons are then delocalized over tens of

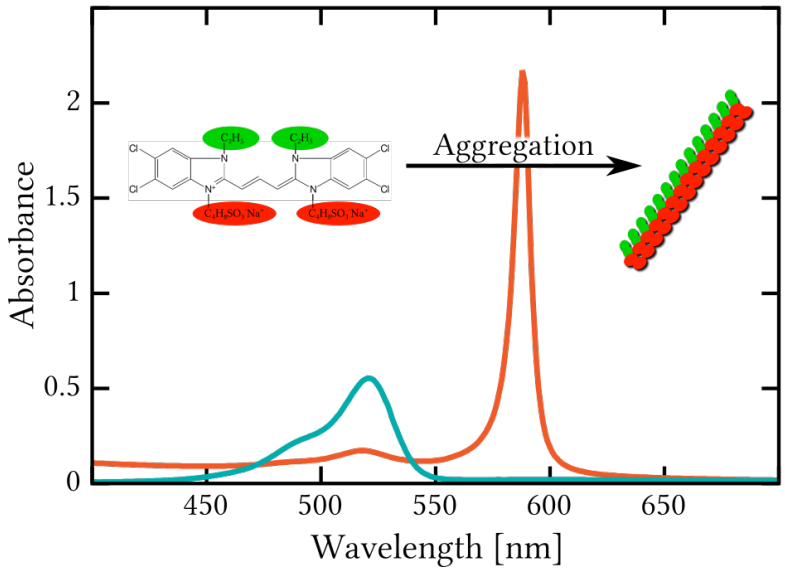

Figure 1.1 – Absorbance spectrum of a dilute monomeric solution of the amphiphilic cyanine dye TDBC in ethanol (cyan curve), and of its J-aggregated form obtained by the addition of a strong base (NaOH, orange curve).

monomers, their absorption and emission spectra dramatically change from a broad vibronic progression to a sharp and very intense line with essentially no vibrational substructure (see *e.g.* Fig. 1.1). Such a disappearance of vibrational substructure, reminiscent of motional narrowing for solvated molecules, is here a direct manifestation of quantum delocalization where the exciton wavepacket sees an effective disorder averaged over its localization volume [56–58].

Besides the perspectives they offer in exploiting room temperature quantum coherences, molecular systems naturally lend themselves as good candidates for cQED experiments due to their potentially very large transition dipole moments (extinction coefficients up to $10^6\,\mathrm{M}^{-1}\mathrm{cm}^{-1}$), favoring their coupling to electromagnetic modes. As we will discuss in the next sections, this coupling can in some cases compare favorably to any other relaxation rates of the molecular excitons, setting the stage for light-molecule strong coupling.

A typical visible absorption spectrum of a solution of molecules at room temperature is shown in Fig. 1.2(a). It results from a complex variety of electronic transitions from molecular

ground states to different vibrationally hot excited states. Just after the rapid electronic transition, the new charge distribution is usually out of equilibrium with the surrounding medium and the molecular backbone, leading to an energy relaxation toward a new equilibrium configuration (Fig. 1.2(b)). From this relaxed configuration, the molecule can decay back to the electronic ground state manifold via many different processes such as the emission of a photon, internal vibrational relaxation or inter-system crossing to a manifold of different spin multiplicity followed by phosphorescence.

The linewidth of absorption of a single molecule at $T = 0K$, assuming the absence of intramolecular vibrations, consists of a sharp and intense line corresponding to a purely electronic transition (PEL), as sketched in Fig. 1.2(c), top-left. The linewidth $\Gamma(0)$ of such a transition is only determined by the electronic state lifetime, and usually lies in the range of $10^{-4} - 10^{-3}cm^{-1}$ for allowed optical transitions [59]. In condensed phase, this PEL is accompanied by a broad continuum corresponding to the coupling of the electronic excited state to the spectrum of acoustic phonons of the embedding matrix or solvent. As the temperature is raised, the thermal population of those phonons modes can (quasi-)elastically scatter off the excited electron, causing random phase jumps in its wavefunction. This purely dephasing mechanism thus effectively shortens the lifetime of the quantum coherent state, while leaving its population unchanged, and hence corresponds to a broadening of the PEL linewidth Γ with temperature:

$$\Gamma(T) = \frac{1}{\pi c T_2(T)} = \frac{1}{\pi c}\left(\frac{1}{2T_1(T)} + \frac{1}{T_2^*(T)}\right), \tag{1.1}$$

where T_2 is the overall coherence time of the excited electronic state, T_1 is the population lifetime, including radiative and non-radiative decays, and T_2^* is the phase relaxation time. In addition to PEL broadening, increasing the temperature also transfers absorption strength from the PEL to its phonon side-bands, resulting in the absence of such purely electronic sharp line

in the measured room temperature spectra, even for individual molecules, as sketched in Fig. 1.2(c), top row. Moreover, owing to their backbone structure, molecules also have intramolecular vibrational modes, giving rise to vibronic zero-phonon lines where the electronic transition is accompanied by the excitation of a molecular vibration, without populating the phonon modes of the environment. These vibronic zero-phonon lines are also accompanied by their own phonon side-bands, as depicted in the middle row of Fig. 1.2(c), and their oscillator strength are determined by Franck-Condon factors, optical selection rules, and the symmetry and populations of the states involved. Finally, when measuring molecular ensembles, as in Fig. 1.2(a), the dynamic local energetic disorder associated with the solvation of molecules shuffles these spectral features over a broad span of *c.a.* $100 - 1000\text{cm}^{-1}$. At room temperature, this inhomogeneous broadening usually dominates the spectral response of disordered molecular ensembles, as shown in the last row of Fig. 1.2(c).

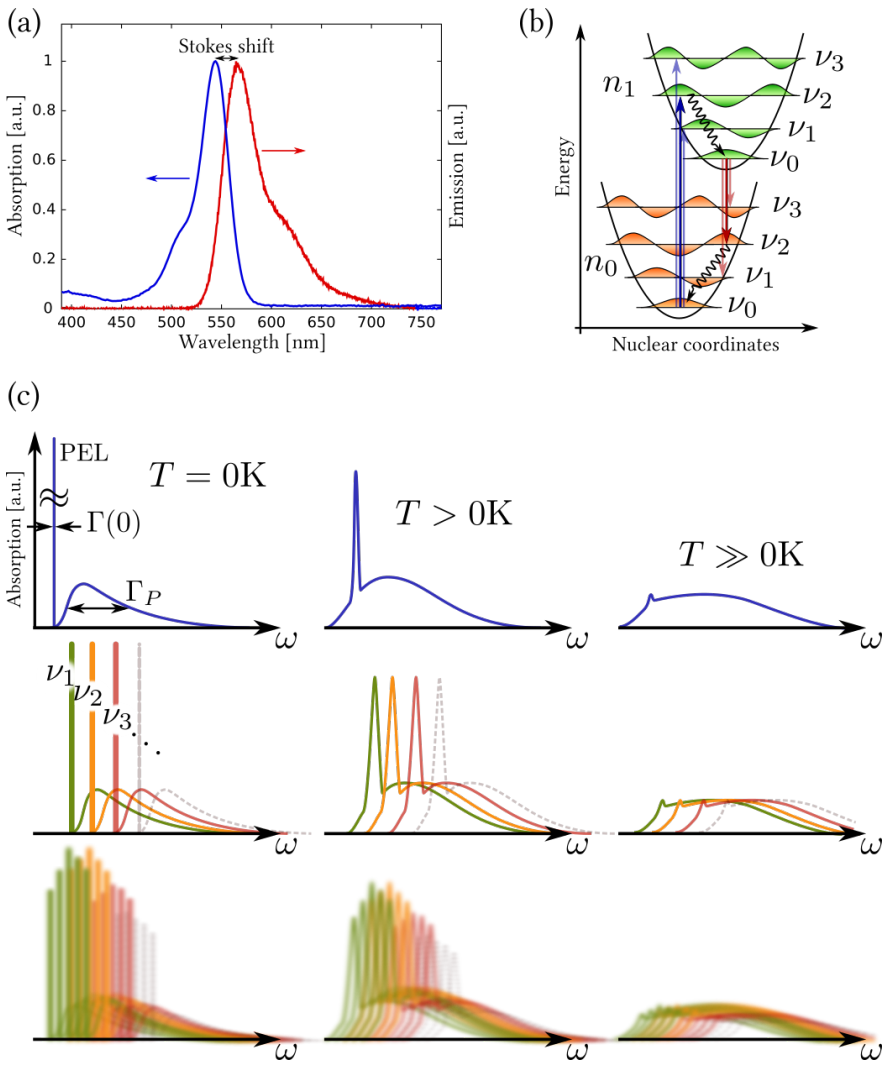

Figure 1.2 – (a) Normalized absorption and emission spectra of Rhodamine B in an ethanol solution. The energy shift in fluorescence emission (Stokes shift) indicates the relaxation dynamics of the electronic wave-function in the excited and ground state manifolds following the optical transitions. (b) Schematic energy levels diagram of the optical cycle between the ground (n_0) and excited (n_1) electronic state manifolds. The strength of the different vibronic optical transitions are dictated by the Franck-Condon overlaps, optical selection rules, the symmetry of the molecular orbitals and the occupancy of the states. (c) First row: schematic absorption spectrum of a solvated two-levels molecule. With increasing temperatures, the PEL linewidth Γ broadens and looses strength while the phonon side-band broadens and increases in intensity. Second row: schematic including additional vibronic transitions ν_i and their phonon side-bands. Third row: ensemble averaging of the spectra in presence of (Gaussian) energetic disorder. The schematic illustrations are adapted from [59].

Overall, these different factors result in broad, inhomogeneous and complex line shapes for the room temperature molecular chromophores ensembles that we will study. This inhomogeneity, combined with the tremendous variety of possible excited and ground states dynamics, exploring multi-dimensional intertwined potential energy surfaces, confers to molecular strong coupling a potential that remains to be fully understood. In the next section, we will elaborate on different theoretical approaches, aiming at a first understanding of the light-molecules strong coupling regime.

1.2.2 *The molecular strong coupling regime*

Following the path of typical cQED experiments, we would like to investigate the new eigen-states that the system might develop when immersed in a structured electromagnetic vacuum. To simplify the discussion, we will focus on the case of molecules embedded in a Fabry-Pérot (FP) cavity, however the main results derived here will remain valid for any kind of electromagnetic resonator, provided that the light-matter coupling strength and the resonator losses remain in the same ratio. In particular, the strong coupling to plasmonic resonators will reveal as a versatile tool as we will see in the last chapter of this thesis. We will start by describing the optical response of the resonator when filled with molecular absorbers using classical linear response theory before introducing a quantum mechanical description of the coupled systems dynamics. The abstraction of the system to two coupled levels will give us insights in the nature of the new light-matter eigen-states, while its extension to more complex situations will provide a more realistic guideline to understand experimental results.

Despite its completely classical character, linear response theory remains a very accurate tool at describing the modal structure of many quantum systems. This fact should not be too surprising given that one can always cast a linear response function that will effectively describe the (quantum mechan-

ical) microscopic response of the system to a weak external probe. This weak perturbation response is precisely what one is looking for when investigating the modal structure of a system either quantum or classical. The linear response function will obviously not be an accurate tool to describe the dynamics of the system when non-linearities emerge or when quantum statistics become important.

The mode structure of a FP cavity is ruled by the interference between multiple scattering of light on the cavity mirrors. The condition for constructive interference thus defines the resonant cavity modes where the electromagnetic field builds up, while the field amplitude is strongly reduced elsewhere:

$$\phi = 2L\omega n/c + 2\phi_r = 2m\pi \quad (m \in \mathbb{N}), \tag{1.2}$$

where ϕ is the round trip phase accumulation in the cavity of length L, n is the real part of the refractive index of the intra-cavity medium, ω is the vacuum frequency of light, ϕ_r is the reflection phase from the cavity mirrors, and m labels the order of the cavity modes. We show in Fig. 1.3(a) the calculated round-trip phase accumulation for a 140 nm thick FP cavity with 35 nm thick Ag mirrors, together with its simulated transmission spectrum using transfer matrix methods (TMM). As can be seen, a Lorentzian resonance develops at the energy where the round-trip phase accumulation corresponds to an integer times 2π, with a quality factor $Q \simeq 20$ as set by the Ag mirrors.

When such a cavity is filled with a highly absorbing molecular layer, the refractive index of the intra-cavity medium becomes strongly dispersive close to the peak of absorption owing to Kramers-Kronig relations [60]. This dispersive line shape contributes directly to the round-trip phase accumulation, allowing multiple solutions to the resonance condition (1.2) for a given cavity mode order. As shown in Fig. 1.3(b), for a sufficiently strong absorbing medium, *i.e.* a sufficiently dispersive refractive index, three distinct solutions to the resonance condition develop, with the concomitant emergence of a split

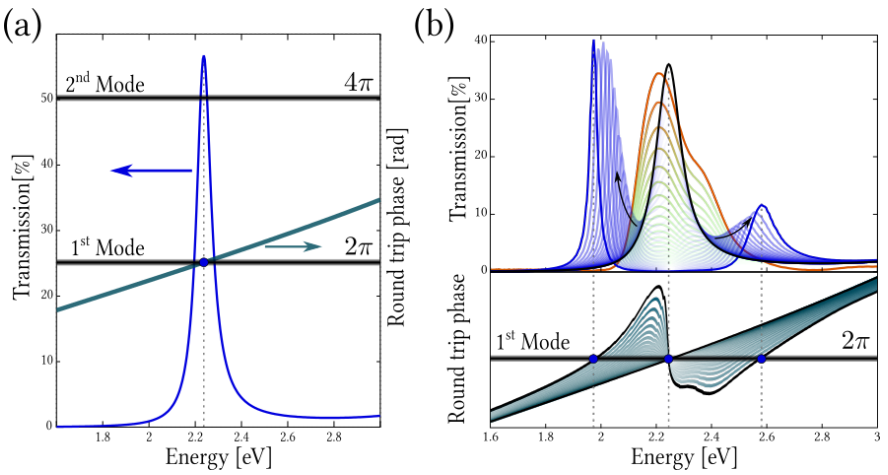

Figure 1.3 – (a) Transfer matrix simulation of the transmission spectrum of a 140 nm thick FP cavity with 35 nm thick Ag mirrors. A resonant mode appears every times the round-trip phase accumulation (cyan curve) matches an integer times 2π (horizontal black lines). (b) Cavity transmission spectra (blue curves) for an increasingly strong embedded absorber (green to red curves). The corresponding round-trip phase accumulation functions (bottom panel) show multiple crossings with a given mode order for sufficiently strong absorption.

doublet in the cavity transmission spectrum. The absence of the central solution from the cavity transmission spectrum is due to the strong dissipation occurring at this energy, preventing the mode to build up.

From this modal approach, it is then straightforward to derive the temporal response of the system, subjected to a pulsed probe field. For a femto-second (fs) incident probe field having a Fourier limited frequency content large enough to cover the two transmission peaks of the spectrum of Fig. 1.3(b), the time dependent transmitted intensity displays damped oscillations, as shown in Fig. 1.4(b), with a period τ given by

$$\tau = 2\pi/\Omega_R, \tag{1.3}$$

where Ω_R is the frequency splitting between the cavity modes, and an attenuation constant that depends on the finesse of the bare resonator and on the absorption losses at the new peaks positions.

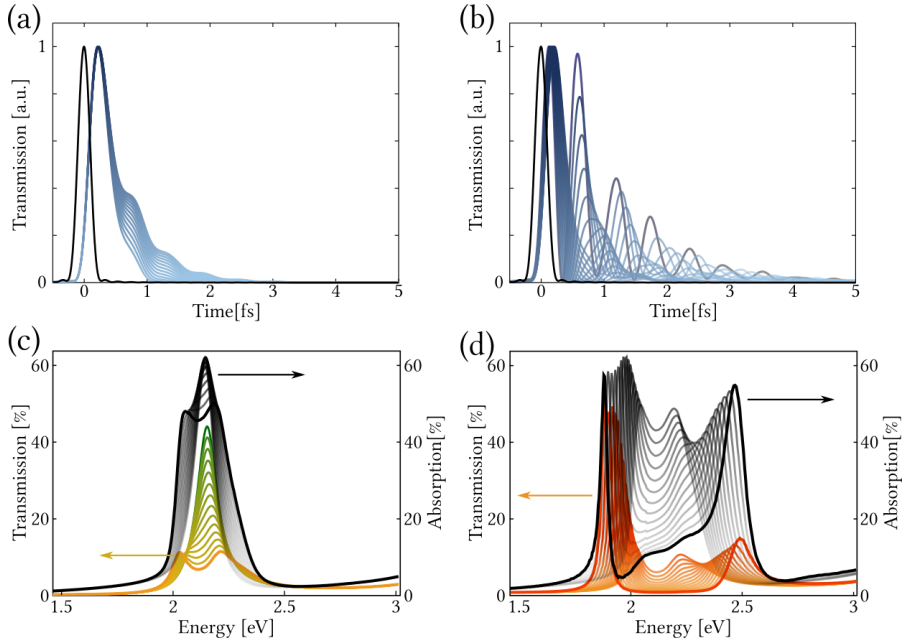

Figure 1.4 – (a,b) Simulation of the time dependent transmission of the cavity of Fig. 1.3(b) for an increasingly strong absorber. The incident fs pulse is shown in black. For clarity, the panel (a) shows absorbance ranging from 0.01 to 0.13, and panel (b) from 0.15 to 1. The corresponding transmission (green to orange curves) and absorption spectra (black curves) are shown in (c) and (d).

Thus, we naturally recover from the linear response theory the two hallmarks of the strong light-matter coupling regime: eigen-states splitting and ringing temporal dynamics. The strong light-matter coupling condition stated in section 1.1 can thus be recast in the linear dispersion theory as follow: the dispersive line-shape of the refractive index must give solutions to the FP equation (1.2) that are separated by more than the full width at half maximum (FWHM) of the absorption line shape (avoiding strong absorption losses) and more than the cavity FWHM (sustaining at least one ringing oscillation) [61].

Remarkably, at the onset of strong coupling (between panels (a) and (b) of Fig. 1.4), their exist a regime where even though the transmission spectrum shows a clear splitting (*e.g.* orange curve of panel (a)), the corresponding splitting in the absorption spectrum is not well resolved, while in the time domain the dynamical behavior of the system displays over-damped oscillations. This intermediate coupling regime corresponds to a non-perturbative, non-ringing regime that has been discussed in both atomic [62] and semiconductor physics [63, 64]. It results that the actual strong coupling (ringing) regime requires the observation of a resolved splitting in absorption, not only in transmission or in reflection as it will be quantitatively discussed below.

An interesting consequence of this linear dispersion model is that the total polariton relaxation rate depends both on the photon escape rate γ and on the damping at the frequency of the polariton modes $\rho(\omega_0 \pm \Omega_R)$ due to the tails of absorption of the active layer, a quantity that can significantly vary depending on the material under study. This polariton drag could potentially be suppressed by selectively bleaching an inhomogeneously broadened active layer at the polariton frequencies, hence leading to an increased coherence time in the system as proposed by Krimer and coworkers [65].

In order to see how ringing dynamics can emerge at a microscopic level, we now turn to a quantum mechanical description of the light-molecules coupled system. We will start with a very basic Hamiltonian approach to the problem,

idealizing the molecular medium to an assembly of N two-level systems (*e.g.* purely electronic transitions), and modeling the cavity by a single quantized mode. We will then discuss some recent developments that significantly improve this model to describe more realistic light-molecule strongly coupled systems.

1.2.3 *A two-level systems approach: the Jaynes-Cummings model*

Let us start by considering the following Hamiltonian describing the dipolar coupling of a charge q to the electric field of an optical mode [2]:

$$\mathcal{H}^{\text{dip}} = -q\mathcal{R}\cdot\mathcal{E}(0), \tag{1.4}$$

with $\mathcal{R}$ the position operator of the coupled charge and $\mathcal{E}(0)$ is the electric field operator taken at the position of the charge. In the second quantization formalism, the electric field operator at a point $\vec{r}$ of the considered optical mode $(\omega_c, \vec{k}_c, \vec{\epsilon_c})$ is mapped onto a quantized harmonic operator:

$$\mathcal{E}(\vec{r}) = i\,\zeta_0\left[\vec{\epsilon_c} f(\vec{r}) a e^{i\vec{k}_c\cdot\vec{r}} - \vec{\epsilon_c}^{\,*} f^*(\vec{r}) a^\dagger e^{-i\vec{k}_c\cdot\vec{r}}\right], \tag{1.5}$$

where ζ_0 is a normalization factor, f is a dimensionless scalar function describing the spatial structure of the cavity mode of polarization $\vec{\epsilon_c}$ and wave-vector $\vec{k}_c$, and $a^\dagger(a)$ is the usual bosonic ladder operator populating (depleting) the photonic field. The relationship between the mode frequency ω_c and its wave-vector $\vec{k}_c$ is fixed by a dispersion relation $\omega(\vec{k}_c)$ that we will derive below for the specific case of a FP cavity. Setting the electromagnetic field energy of a state with n photons to be equal to $\omega_c(n+1/2)$, we obtain the following normalization condition:

$$\langle n|\int \epsilon_0|\mathcal{E}(\vec{r})|^2 d^3r\,|n\rangle = \omega_c\,(n+1/2)\,, \tag{1.6}$$

where the zero-photon energy $\omega_c/2$ corresponds to the zero-point motion of the field operator. From this constrain we can express the factor ζ_0 as:

$$\zeta_0 = \sqrt{\frac{\omega_c}{2\epsilon_0 \mathcal{V}}}, \tag{1.7}$$

with the effective mode volume $\mathcal{V}$ defined as:

$$\mathcal{V} = \int |f(r)|^2 d^3r. \tag{1.8}$$

It should be noted that, while this definition of the mode volume is formally correct, it diverges for realistic cavity designs. In particular, it has been generalized to treat lossy cavities in the quasi-mode formalism [66]. For planar FP cavities, the lateral mode extension is set by the photon in-plan diffusion length, a quantity in turn related to the cavity mirrors losses.

We now express the dipole moment operator $\mathcal{D} = q\mathcal{R}$ in terms of spin-flip operators $\sigma_{+,-}$. A $1/2-$spin immersed into a fictive magnetic field will be our toy model for matter, considered as a two level system at this stage. Assuming that the fictive magnetic field is aligned with a chosen spin quantization axis, the two eigenstates of this system are the usual up $|0\rangle$ and down $|1\rangle$ states with respective eigenenergies $+1$ and -1. In this framework, the transition between two different energy states $|g\rangle$ and $|e\rangle$ of the absorber corresponds to the spin-flip $|1\rangle \rightarrow |0\rangle$. In the Fock state representation, $\mathcal{D}$ is purely non-diagonal as it corresponds to transitions between the available energetic states. Expanding $\mathcal{D}$ along the spin-flip matrices we obtain:

$$\mathcal{D} = d\,(\vec{\epsilon_a}\sigma_- + \vec{\epsilon_a}^*\sigma_+)\,, \tag{1.9}$$

where $\vec{\epsilon_a}$ is the polarization of the transition and d is the corresponding dipole matrix element:

$$d\vec{\epsilon_a} = q\,\langle g|\mathcal{R}|e\rangle\,. \tag{1.10}$$

The dipolar coupling Hamiltonian now reads:

$$\mathcal{H}^{\text{dip}} = -d\,[\vec{\epsilon_a}\sigma_- + \vec{\epsilon_a}^*\sigma_+]\cdot i\,\zeta_0\left[\vec{\epsilon_c}f(0)a - \vec{\epsilon_c}^* f^*(0)a^\dagger\right]. \quad (1.11)$$

Setting $f(0) = 1$ at the position of the absorber, we can expend the scalar product and obtain:

$$\mathcal{H}^{\text{dip}} = -i\,\frac{\Omega_0}{2}\left[a\sigma_+ - a^\dagger\sigma_-\right] - i\,d\zeta_0\left[\vec{\epsilon_a}\cdot\vec{\epsilon_c}\,a\sigma_- - \vec{\epsilon_a}^*\cdot\vec{\epsilon_c}^*\,a^\dagger\sigma_+\right], \quad (1.12)$$

where the coupling constant $\Omega_0/2$ is defined as:

$$\Omega_0/2 = d\zeta_0\vec{\epsilon_a}\cdot\vec{\epsilon_c}^* = d\sqrt{\frac{\omega_c}{2\epsilon_0\mathcal{V}}}\vec{\epsilon_a}\cdot\vec{\epsilon_c}^*. \quad (1.13)$$

Ω_0 is termed the vacuum Rabi frequency. The first part of the coupling Hamiltonian (1.12) describes the emission/absorption of light by a two level system. The second part accounts for processes in which, either the absorber emits and one photon is absorbed, or the absorber gets excited while one photon is emitted. For near resonant light-matter interaction, those latter terms beat at high frequencies in the rotating frame and can thus be neglected as long as Ω_0 remains a small fraction of ω_c [2]. However, if Ω_0 approaches ω_c, these counter-rotating terms become important, leading to a qualitatively new regime, termed the ultra-strong coupling regime, where phenomena such as ground-state squeezing, band-gap opening, and dynamical Casimir effect appear [67–71]. We will explore some aspects of this regime in the context of strong coupling of light with molecular vibrations in chapter 3.

The total light-matter Hamiltonian in the rotating-wave approximation (RWA) is known as the Jaynes-Cummings model [23]:

$$\mathcal{H}_{\text{JC}} = \omega_{eg}\,(\sigma_+\sigma_- - \mathbb{I}/2) + \omega_c\left(a^\dagger a + \mathbb{I}/2\right) - i\,\frac{\Omega_0}{2}\left[a\sigma_+ - a^\dagger\sigma_-\right], \quad (1.14)$$

with ω_{eg} the energy of the optical transition of the absorber. This model has been extended by Tavis and Cummings to N independent absorbers immersed in the same cavity mode, showing that its main features remained qualitatively unchanged upon replacing the absorber operator by collective bosonic excitation (Dicke) operators [34] and replacing the individual coupling frequency Ω_0 by a collective Rabi frequency:

$$\Omega_R = \Omega_0 \sqrt{N}. \tag{1.15}$$

This extension thus results in the appearance of collectivity in the ensemble of absorbers, and the concomittant enhancement of the light-matter coupling strength by a factor that depends on the number of absorbers in the optical mode volume, *i.e.* the concentration of the active medium.

The Jaynes-Cummings Hamiltonian (1.14) can be directly diagonalized in the single excitation manifold via the Hopfield-Bogoliubov procedure [72], yielding eigen-states that are linear combinations of optical and material excitations: the polaritonic states

$$\begin{cases} |P^+\rangle = \cos(\theta/2)\,|e,0\rangle + i\sin(\theta/2)\,|g,1\rangle & (1.16) \\ |P^-\rangle = \sin(\theta/2)\,|e,0\rangle - i\cos(\theta/2)\,|g,1\rangle\,, & (1.17) \end{cases}$$

where the mixing angle θ is defined as $\tan(\theta) = \Omega_R/\Delta$, with $\Delta = \omega_{eg} - \omega_c$ the detuning parameter. This very fundamental model of an absorber immersed in the vacuum fluctuations of an optical mode thus directly gives rise to maximally entangled excited states, separated by the Rabi frequency Ω_0 (or Ω_R in the N absorbers case).

Another key feature of hybrid light-matter states that triggered a huge interest stems from their peculiar dispersion relation. In the specific case of a planar FP cavity, translational invariance allows us to label the different polaritonic states

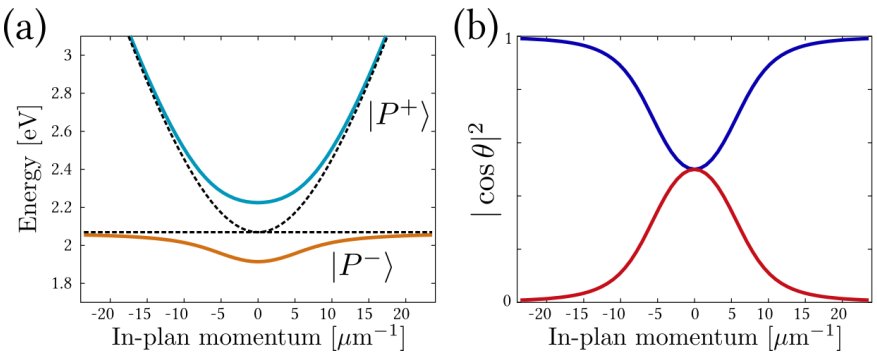

Figure 1.5 – (a) Energy dispersion of the polaritonic states as obtained from (1.14). The uncoupled absorber and photonic modes are shown in black dashed lines, yielding resonant coupling at $k_{//} = 0$. (b) Photonic Hopfield coefficient of the lower (red) and upper (blue) polaritonic states. At resonance, the two polaritonic states have equal optical and material character.

according to the conserved in-plan momentum of their photonic component $k_{//}$. The energy dispersion of the FP cavity mode:

$$\omega_c(k_{//}) = \frac{c}{n_c}\|\vec{k}\| = \frac{c}{n_c}\sqrt{\left(\frac{m\pi}{L}\right)^2 + k_{//}^2}, \tag{1.18}$$

with c the celerity of light, n_c the background refractive index, m the cavity mode order and L the cavity thickness, here translates into a $k_{//}$-dependent detuning. The polaritonic dispersion, obtained by diagonalizing (1.14) at different $k_{//}$, shows an energy minimum at $k_{//} = 0$, and a parabolic behavior in its vicinity (see *e.g.* Fig. 1.5). This polariton trap in momentum space, associated with the low transverse mass of the light-matter eigenstates:

$$m^*_{//} = \left(\frac{d^2}{dk_{//}^2}\omega_c(k_{//})\right)^{-1}, \tag{1.19}$$

down to $\sim 10^{-4}$ times the effective mass of an exciton in a solid, is at the heart of the studies on polariton BEC.

In the time domain, the dynamical evolution of an opened system subjected to the Hamiltonian (1.14) and to Markovian material and optical losses can be described using a quantum trajectories algorithm. As shown in Fig. 1.6 (a, blue histogram),

the relaxation dynamics of an initial photon population toward the optical reservoir of states (photon escaping the cavity) shows an exponential decay when the light-matter coupling strength is smaller that the relaxation rates. In this weak coupling regime, the relaxation is already modified with respect to that of an empty cavity (dashed curve) as some of the initial photon population ends up in the absorber reservoir (green histogram). This effect is reminiscent of donor-acceptor energy transfer dynamics, as we will discuss further in chapter 2. When the light-matter coupling strength overcomes the losses, Fig. 1.6(b), the system enters the strong coupling regime with a typical damped Rabi oscillatory behavior similar to that of Fig. 1.4(b). The clear quadrature between the photon and the absorber reservoirs directly reveals the periodic energy exchange between the two coupled systems. This transition from weak to strong coupling can be quantified by looking at the eigen-solutions of (1.14) when the uncoupled modes frequencies are complex. In this case, the diagonalization yield complex polariton energies whose real parts are separated by a frequency splitting:

$$\Delta\omega = \sqrt{|\Omega_R|^2 - \left(\frac{\kappa}{2} - \frac{\gamma}{2}\right)^2} \tag{1.20}$$

Thus the ringing regime of strong coupling, *i.e* $\Delta\omega$ being real, results from the condition $|\Omega_R|^2 > (\frac{\kappa}{2} - \frac{\gamma}{2})^2$. However, as discussed in the previous section from a spectroscopic view point, the distinguishability of the two new polaritonic eigenstates as a criterion of strong coupling implies the more restrictive condition [63]: $|\Omega_R|^2 > \frac{\kappa^2+\gamma^2}{2}$. In other words, the polariton splitting (twice the interaction frequency) must be larger than the average FWHM of the uncoupled modes. Despite those technical considerations, it can be seen from the decay dynamics in the non-pertubative no-ringing regime that profound modifications of the light-matter system can already occur at moderated coupling strength.

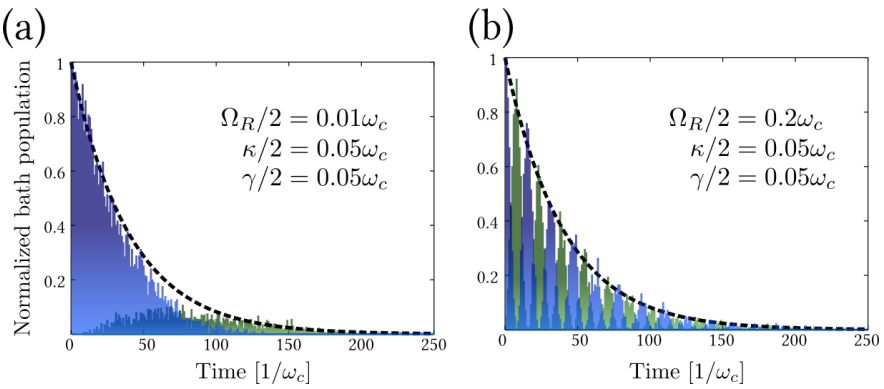

Figure 1.6 – 10^4 Quantum trajectory simulations of time evolution under the Jaynes-Cummings Hamiltonian 1.14 at resonance, in the presence of photon relaxation (at a rate $\gamma/2$) and absorber relaxation (at a rate $\kappa/2$), for weak (a) and strong (b) coupling regimes. The blue (green) histogram corresponds to the arrival time of excitation in the photonic (absorber) bath. The black dashed line is an exponential decay function of time constant $(2/\kappa + 2/\gamma)$.

We will complete this chapter by briefly exposing some more advanced models, aiming at understanding the strong coupling of a optical mode to complex molecular media.

1.2.4 *More complex models: toward cavity quantum chemistry*

A first extension of the Tavis-Cummings model to solid state systems was proposed by Houdré and coworkers [73], by accounting for the energetic disorder usually present in an ensemble of absorbers. There, it was shown that the Rabi splitting in such systems remained proportional the square root of the number of absorbers N, while the two polaritonic states were retaining their homogeneous linewidth $((\gamma + \kappa)/2)$. In this situation, the $(N-1)$ remaining states form linear combinations of purely material excitations with no mixing to the photonic mode, and thus constitute a pool of dark states, bounded to the energy span of the bare absorbers. Also not optically active, such states can have a profound impact on the dynamics of strongly coupled systems as they can be reached by internal relaxation of the polaritonic states. Moreover, it should be noted that despite their purely material character, they remain

nevertheless coherent superpositions [74], potentially linking together remote absorbers, something that is often a hurdle to achieve in material science [75, 76].

The first extension of this model toward the description of molecular strong coupling was proposed Agranovich and coworkers in 1997 [37] where they showed that organic and inorganic excitons could collectively participate in polaritonic states, allowing a versatile tuning of their character as a function of detuning. In a series of following papers [77–81], striking differences between organic and inorganic polaritons were pointed out, in particular due to the localized nature of organic materials excitons (so-called Frenkel excitons) and to their high level of disorder (energetic, positional and orientational). As a result of this translational symmetry breaking, the dispersion relation of strongly coupled disordered materials was shown to consists in both polariton states of well defined wave vector and other hybrid light-matter states for which the wave vector is not a 'good quantum number'. Moreover, these theoretical studies predicted the existence of a large number of uncoupled excitonic states where the excitations would accumulate before relaxing toward coherent polaritonic states, either via spontaneous emission in the coupled cavity mode structure or via non-radiative processes such as the emission of intramolecular phonons. By using a thermodynamical approach to this two-populations problem, Canaguier-Durand and coworkers [82] could determine a fractions of coupled molecules exceeding 60% in ultra-strongly coupled molecular systems.

In 2009, La Rocca and coworkers proposed a toy model to describe such intracavity polariton pumping [83, 84]. In their model, the effect of vibronic progressions present in typical organic materials was mimicked by including 4 electronic levels: two in the excited state manifold and two in the ground-state manifold. Including coherent coupling for the high oscillator strength transitions and scattering processes among the other energy levels, they could show numerically that the lower polaritonic branch could be strongly populated by resonant

phononic scattering from an exciton reservoir. This prediction was shortly followed by the first demonstration of organic polariton lasing in mono-crystalline anthracene, directly exploiting this resonant scattering mechanism [40]. This model is currently being extended, in a fully fermionic basis, to the case of two coherently coupled molecular ensembles in order to describe recently reported results on polariton energy transfer phenomenon [85–87].

In these extensions of strong coupling physics to molecular materials, a common feature is the fact that scattering rates are defined between coupled and uncoupled excitonic states. As pointed out by Canaguier-Durand and coworkers [88], such *ad-hoc* scattering terms naturally emerge when considering non-Markovian effects in the polariton dynamics. Indeed, with Rabi frequencies approaching optical transitions frequencies, the finite memory time of the vibronic bath prevents one from imparting bare material relaxation rates to the polaritons through a mere change of basis. Instead, the polariton relaxation rates have to be related to the uncoupled ones through integral equations [89–92], or can be directly defined on the dressed states diagram leading to genuine polaritonic scattering rates. Non-Markovian environment dynamics can lead to counter-intuitive results such as unbalanced lifetimes for the upper and lower polaritons, eventually exceeding both the bare molecule and the empty cavity photon lifetimes, as shown in the next chapter.

In order to better realize the implications of light-mater strong coupling in complex molecular systems, one however has to go beyond a purely vibronic states description of the material. This approach recently appeared in the field of density functional theory (DFT), where Tokatly and Rubio *et al.* successfully combined *ab initio* quantum mechanical calculations and cavity QED concepts [93, 94]. This new approach laid the ground for an accurate description of molecular strong coupling and for an understanding of the accumulating experimental results on new material and chemical properties under strong coupling [46]. Among the blossoming extensions of this approach over the last

two years [95–105], the redefinition of the Born-Oppenheimer surfaces and the profound modifications of conical intersections between potential energy surfaces appear to be key players in the observed and predicted properties of complex chemical matter under (ultra-)strong light-matter interaction.

Hence, given the current state of theoretical understanding of molecular strong coupling, some of the results presented in this thesis will only be discussed within the polariton basis, building up a self-consistent description of these new light-matter states and of the possibilities that they can offer. This way of reasoning remains so-far the only approach to understand *e.g.* modified chemical reactions under strong coupling [14, 15], where both the complex molecular landscape and the non-Markovian dynamics dictate the observed behavior. Whenever the studied phenomenon will only rely on a few well identified degrees of freedom, we will try to trace its description to the uncoupled basis and to develop toy models mimicking its behavior, thus providing insights into the physics at play. A general description of molecular polaritonic systems thus remains elusive so far, the underlying challenges being somewhat similar to those currently faced in the field of quantum biology, with the understanding of coherent and entangled dynamics near conical intersections of molecular potential energy surfaces.

2

DYNAMICS AND ENERGY FLOW IN STRONGLY COUPLED MOLECULES

In this chapter, we investigate different aspects of population dynamics and energy pathways in molecular ensembles strongly coupled to a cavity mode. The first section summarizes a photophysical study of a typical organic material used for light-molecules strong coupling: J-aggregates of TDBC. In particular, we report on the fluorescence quantum yield of its polariton emission and on its transient dynamics, as a function of the Rabi splitting. This is achieved by precisely tuning the TDBC layer position within the optical mode of a Fabry-Pérot (FP) microcavity. This section is followed by a comparative study of polariton photophysics in three archetypal molecular species, illustrating how chemical diversity can translate into rich polaritonic behavior.

Building upon this study of polariton dynamics, we demonstrate in the third section the possibility of transferring energy through hybrid light-matter states in which two different molecular species participate collectively. The efficiency of this new energy transfer mechanism is shown to be independent of the distance separating the energy donor and the energy acceptor molecules. To understand these results, we develop two different models, one based on a cavity modified Forster mechanism, and the other relying on a quantum trajectories algorithm.

This chapter is completed by an investigation of the nonlinear response of polaritonic states. In particular, we report on their remarkable efficiency for second harmonic generation.

2.1 FLUORESCENCE QUANTUM YIELD AND TRANSIENT DYNAMICS

Throughout this chapter we will study strongly coupled organic materials embedded into low finesse planar metallic FP cavities ($\mathcal{F} \simeq 30$). Such cavities, despite their poor photon storage time (*ca.* 50 fs), provide the very small mode volumes required to achieve large Rabi splittings, as discussed in the previous chapter. This can be illustrated by filling such a cavity with a polymer matrix doped with a high load of J-aggregates of TDBC cyanine dyes (0.1 mol/L, intermolecular distance of *ca.* 3 nm), having a J-band absorption peak at 588 nm. The resulting cavity transmission spectrum, shown in Fig. 2.1(c), clearly reveals the formation of two polaritonic states, separated in energy by a Rabi splitting of 325 meV, amounting to 15% of the J-band frequency. Such a large energy gap opening should impact the dynamical evolution of the system, and thus consitutes a case study of how collective strong coupling could modify molecular photophysical properties. Moreover, as a direct consequence of the dipolar coupling of molecules to the cavity mode, this Rabi splitting can be tuned by accurately positioning the molecules within the mode profile as we now demonstrate. Parts of this section are reproduced from already published work [106].

2.1.1 *Spatial tuning of strong coupling in FP cavities*

2.1.1.1 *Experimental methods*

We developed a bonding technique for the precise control of the position of a molecular layers in a FP cavity. First, a 30 nm thick silver film was sputtered on a glass substrate, forming the first cavity mirror. A dielectric layer of poly(methyl methacrylate) (PMMA) was then was spin-coated on top, forming a spacer of tunable thickness (referred to as 'slab A'). Meanwhile, another 30 nm thick silver mirror was deposited on a flexible 1 mm thick poly-(dimethylsiloxane) (PDMS) sub-

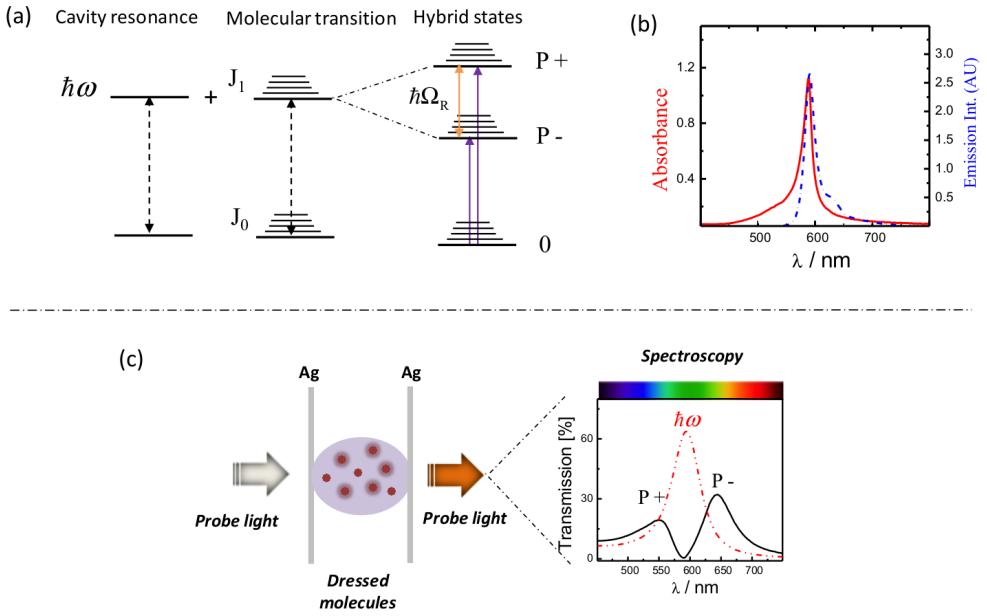

Figure 2.1 – (a) Energy level representation of the coupling of a molecular transition ($J_0 - J_1$) to an optical resonance forming the hybrid states P^+ and P^- separated in energy by the Rabi splitting ($\hbar\Omega_R$). (b) Absorption (red curve) and emission spectrum (blue dashed curve) of a layer of J-aggregate TDBC. (c) Schematic illustration of TDBC dispersed in a first mode FP cavity everywhere. Transmission spectrum of the empty cavity (red dashed curve) and of the cavity filled with polymer doped TDBC (back curve), giving rise to P+ and P-. Figure reproduced from reference [106].

strate by thermal evaporation. This mirror was also coated with a layer of PMMA of chosen thickness (labeled 'slab B'). The surface of the PMMA spacer of slab A was made hydrophilic by spin-coating a 2 nm thick PDMS layer on it from a 0.3 wt% PDMS solution in tert-butanol and exposing it to an oxygen plasma for 30 s. Next, alternated layers of TDBC J-aggregates (1,1'-diethyl-3,3'-bis(4-sulfobutyl)-5,5',6,6'-tetra-chlorobenzimidazolocarbocyanine, inner salt, sodium salt, few Chemicals) and of the polycation poly-(diallyldimethylammonium chloride) (PDDA, average molecular weight 200000—350000, 20 wt% in water, Aldrich) were adsorbed onto the surface via layer-by-layer (LBL) assembly [107, 108]. Polyelectrolyte layers were adsorbed by soaking slab A for 5 min in a solution of PDDA (6×10^{-2} M in deionized water), and J-aggregate layers were deposited by soaking it for 5 min in a solution of TDBC (1×10^{-4} M in deionized water) which was previously sonicated for 60 min at 35 °C. In order to reach the high absorption coefficient necessary for strong coupling, we repeated this bi-layers deposition process 10 times, thus forming a thin (*ca.* 25 nm) active layer absorbing close to 70% of the incident light at the maximum of the J-band. The surface of slab B was coated with a 2 nm thick film of PDMS. Finally, the polymer face of slab B was sealed to the molecular film surface of slab A to form the optical microcavity, as represented in Fig. 2.2. By controlling the thickness of the PMMA layers on slab A and slab B, the position of the J-aggregate layers could be moved from the edge of the cavity to its center with nanometric precision. The whole cavity length, including the PMMA and molecular films, could be tuned such that the J-aggregates absorption band at 588 nm was resonant with one of the optical modes of the FP cavity. The thickness of each layer was measured using an Alpha-step IQ surface profilometer.

2.1.1.2 *Results and discussion*

We show in Fig. 2.3 the transmission spectra of first and second mode cavities as the active layer is moved from the

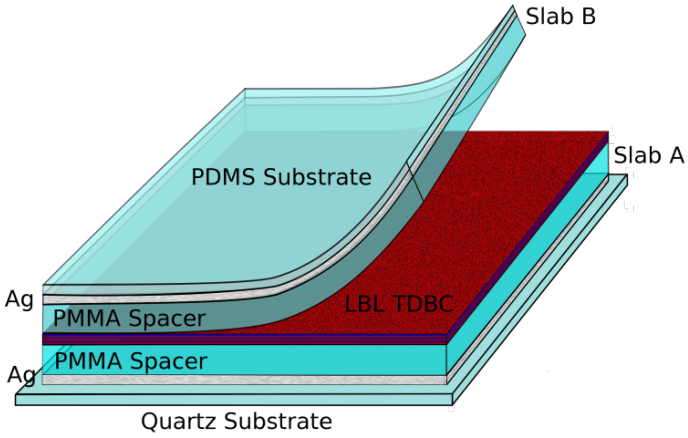

Figure 2.2 – Scheme of the layer-by-layer tunable microcavity. Figure reproduced from reference [106].

edge to the center. In the case of a first mode cavity, the Rabi splitting increases from 310 meV when the layer is close to the edge to 500 meV when it is positioned at the field antinode. In this configuration, the splitting increases by 60% over that obtained when the cavity is homogeneously filled with a layer of TDBC having the same absorption coefficient as the LBL assembly. Performing the same position tuning in a second mode cavity, we observe the transition from strong to weak coupling regime as the active layer reaches the central node of the cavity. Such position dependence of the Rabi splitting within the cavity mode are accurately reproduced by transfer matrix calculations, as shown in Fig. 2.3(c, f). Moreover, the reduction of the Rabi splitting in going from a first to a second mode cavity is consistent with the increase in the cavity mode volume (see Eq. (1.13)):

$$\frac{\Omega_R^{\lambda/2}}{\Omega_R^{\lambda}} \propto \sqrt{\frac{\mathcal{V}_\lambda}{\mathcal{V}_{\lambda/2}}} \simeq 1.6, \tag{2.1}$$

as estimated from transfer matrix calculations, with $\lambda/2$ and λ indices denoting the first and second mode cavities respectively.

The strong coupling to the cavity mode is further evidenced by measuring angle dependent transmission spectra, as

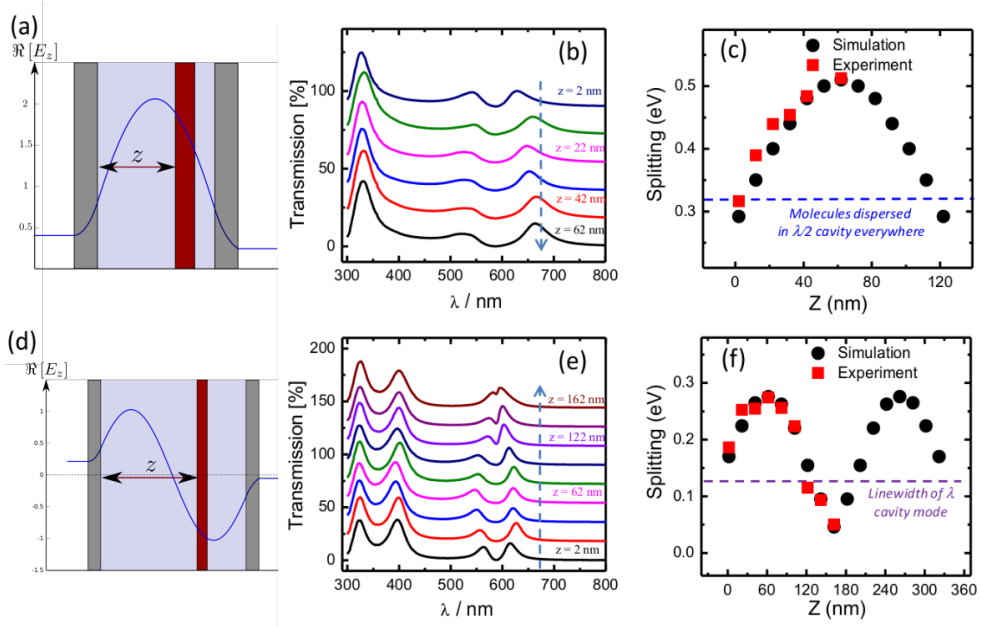

Figure 2.3 – Spectroscopy of the first (top row) and second mode (bottom row) cavities. (a,d) Schematic representation of the cavities and their calculated field amplitudes (real part of the electric field obtained by propagating a resonant monochromatic plan wave from the left side of the structure). (b,e) Transmission spectra of a set of cavities resonantly tuned to the TDBC J-band. The molecular layer is located at different positions inside the cavity (z from the edge to the center as indicated by the dashed blue arrow). The consecutive spectra are offset by 18% for clarity. The spectra were measured under 35° incident transverse electric polarized light. (c,f) Rabi splittings as a function of the LBL TDBC position inside the cavity mode (blue dashed line in (c) represents the splitting obtained when the molecules are dispersed evenly inside the cavity). The purple dashed line in (f) indicates the FWHM of the cavity mode (150 meV). Black dots in (c) and (f) are the calculated splittings using transfer matrix simulation where the complex refractive index of the TDBC J-aggregate film was extracted from its absorption spectrum via a Kramers-Kronig transformation and the thickness of the Ag mirrors and PMMA spacer layers were taken from experiments. Figure reproduced from reference [106].

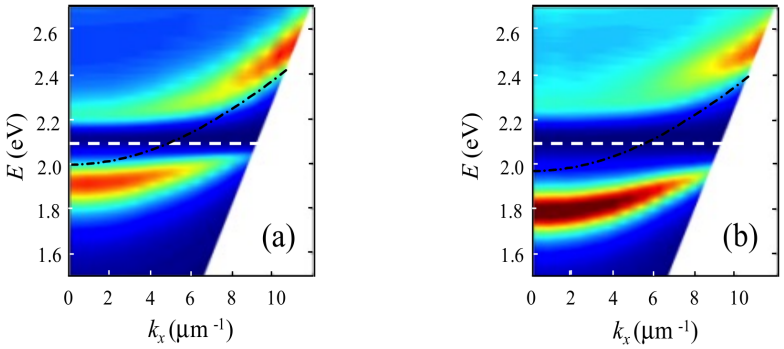

Figure 2.4 – Angular-dependent transmission spectra of a first mode cavity embedding the LBL TDBC layer at the mirror edge (a) and in the center (b) of the cavity. The angle of transverse electric polarized incident light was varied from 0° to 65°. The black dot-dashed curves and white dashed curves represent respectively the dispersion of the empty cavity mode and that of the bare TDBC J-band. Figure reproduced from reference [106].

exemplified for two different cavities in Fig. 2.4, where a clear anticrossing about the bare TDBC J-band is observed.

To go beyond these modal properties and investigate the excited states dynamics we first studied the photo-luminescence (PL) emission spectra of the LBL TDBC cavities upon off resonant monochromatic excitation (520 nm, filtered xenon lamp). We compare in Fig. 2.5 the normal incidence PL spectra of first and second mode cavities with the active layer placed at the nodes and anti-nodes of the field. A first striking observation from those spectral line shapes is that the upper polariton mode (expected at *ca.* 550 nm) does not emit. Instead, we obtain double peaked PL spectra where one contribution appears near the lower polariton state energy and the other at the bare J-band energy. Clearly, several mechanisms beyond the Tavis-Cummings model are at play here.

First, the absence of PL from the upper polariton state is reminiscent of what is observed in many aromatic molecules, where only the lower excited state emits, an effect known as Kasha's rule. This is due to the fact that higher molecular excited states are often lying within the vibronic manifolds of lower excited states. At room temperature, such non-radiative

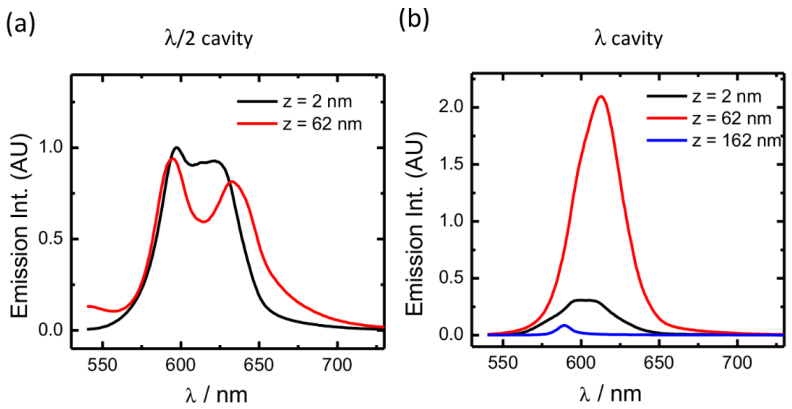

Figure 2.5 – Fluorescence emission spectra collected normal to the sample plan (0.1 collection and excitation numerical aperture, 520 nm excitation wavelength). (a) First mode cavity with the TDBC molecular layer placed at the edge ($z = 2$ nm, black curve) and at the center ($z = 62$ nm, red curve) of the cavity. (b) Second mode cavity with the layer placed at the edge ($z = 2$ nm, black curve), at the first antinode of the field ($z = 62$ nm, red curve) and at the center of the cavity ($z = 162$ nm, blue curve). Figure reproduced from reference [106].

decay pathways usually dominates the excited states dynamics, channeling the energy to the lowest energy excited state from which PL can eventually occur. As discussed above, the description of the vibronic structure of organic polariton systems is not trivial. However, the absence of upper polariton emission is a clear evidence of complex energy pathways within strongly coupled molecular systems. It should also be noted that upper polariton emission has been reported in low temperature experiments [109], further evidencing the role of vibrational modes in the polariton relaxation dynamics.

The presence of an emission peak at the J-band position in the spectra of Fig. 2.5 clearly shows that, even though all molecules are located at equivalent positions in the cavity mode volume, two different populations coexist: a strongly coupled one and an uncoupled one. In our system, this could be due to orientational and solvation disorder in the J-aggregates ensemble. As mentioned in the first chapter, the existence of uncoupled states and their impact on the polariton dynamics has been the subject of many theoretical [77–82] and experimental

works [110–113] as it is of fundamental importance for possible applications of strongly coupled systems.

In view of those observations, a clear advantage of our LBL cavity design is that the system can be continuously tuned from a mostly polaritonic emission (Fig. 2.5(b), red curve) to a completely uncoupled emission (Fig. 2.5(b), blue curve). Using this system, we now investigate in details the fluorescence quantum yield of the lower polaritonic state upon off-resonant excitation, thus obtaining key information on the polariton relaxation pathways.

2.1.2 *PL quantum yield and transient dynamics*

2.1.2.1 *Experimental methods*

The fluorescence quantum yield of the strongly coupled system was measured relative to a standard [114]. This approach amounts to comparing the emission over absorption ratio of the sample to that of a reference of known absolute quantum yield Φ_r:

$$\Phi_s = \Phi_r \frac{I_s}{f_s(\lambda_{ex})} \frac{f_r(\lambda_{ex})}{I_r} \frac{n_s^2(\lambda_{em})}{n_r^2(\lambda_{em})}, \tag{2.2}$$

where I refers to the integrated emission intensity, $f(\lambda_{ex})$ is the fraction of light absorbed at the pumping wavelength (λ_{ex}), $n(\lambda_{em})$ is the background refractive index of the medium at the emission wavelength (λ_{em}), and the indices (r, s) denote the reference and sample respectively. Our protocol consists in three steps. First, we measured the absolute quantum yield of a standard dye using a commercial integrating sphere setup (Hamamatsu C11347-11). This value was then used as a reference for computing the quantum yield of a thin polymer film (PMMA) containing the same standard dye. Finally, we obtained the quantum yield of strongly coupled TDBC by comparison to this new reference quantum yield. This calibration technique allows one to go in a controlled way from the measurements of dilute solutions to that of solid thin film samples.

The reference dye molecule (Lumogen F Red 300, LR) dissolved in spectroscopic grade chloroform was chosen for the overlap of both its absorption and emission spectra with that of the strongly coupled TDBC cavities, thus ensuring no wavelength sensitivity issues in the estimations of $f_{s(r)}$ and $I_{s(r)}$. Another important advantage of this LR dye is its very low sensitivity to environmental conditions. In particular, we measured a constant fluorescence lifetime of (5.8 ± 0.05) ns in dilute chloroform solutions after bubbling Ar for 10 minutes, indicating the absence of oxygen quenching. The same lifetime was also measured from the doped PMMA thin film, also constant upon successive degassing under Ar. The absorbance of the solution and of the thin film of LR was kept below 0.1 at maximum to limit fluorescence re-absorption effects. The absorption spectra were measured using a Shimadzu UV3101 spectrometer and the emission spectra were acquired on an Horiba Fluorolog-3 fluorimeter. The results are reported in Fig. 2.6(a,b).

The fluorescence quantum yield of coupled and uncoupled TDBC samples were measured under off-resonant excitation at 520 nm, and under resonant excitation of the upper polariton state at 550 nm. The results were the same in the two cases, in agreement with the Kasha rule stated above. The effect of the finite numerical aperture of collection on the measurement of the dispersive polariton emission band was corrected by an angle resolved analysis (see Fig. 2.6(c)).

2.1.2.2 *Results and discussion*

The fluorescence quantum yield is a direct measure of the relative importance of radiative relaxation pathways in the excited state dynamics, and can be expressed (in agreement with (2.2)) as

$$\Phi_f = \frac{k_r}{k_r + k_{nr}} = \tau \cdot k_r, \tag{2.3}$$

where k_r and k_{nr} are the radiative and nonradiative decay rates and τ is the lifetime of the emitting state. For a bare TDBC film outside the cavity, we measured a PL quantum yield of 0.02 by

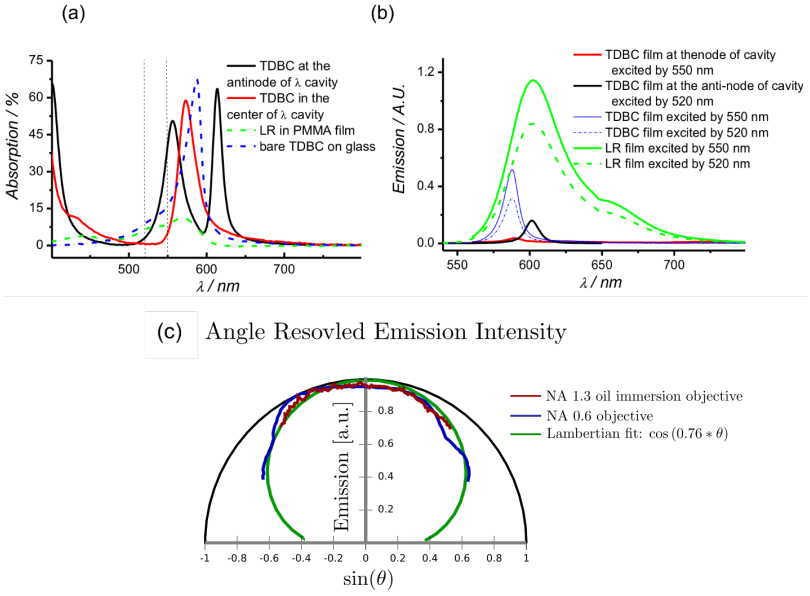

Figure 2.6 – Absorption (a) and emission spectra (b) of bare LBL TDBC film on quartz substrate, the TDBC film at the anti-node and in the center of the first mode cavity, and the reference LR in PMMA film. Normal incident angle was used for both the excitation beam (emission measurements) and the probe beam (absorption measurements). (c) Angle resovled emission intensity integrated over the lower polariton band for a LBL TDBC film placed at the anti-node of the first mode cavity. The angle resolved spectra were collected using high NA microscope objectives, the Fourier plan of which were imaged on a grating spectrometer. This optical setup will be detailed in a latter chapter. The emission intensity beyond the maximal collection angle was extrapolated from a Lambertian fit. Reproduced in part from reference [106].

the procedure detailed above. Placing the same LBL TDBC film at the central node of a second mode cavity, we measured a PL quantum yield of only 10^{-3}. This 20-fold reduction is due to the suppressed density of optical modes at the TDBC layer position, reducing the radiative decay rate by Purcell effect. When the J-aggregate layer was moved to the anti-node of the cavity, we measured a lower polariton quantum yield of 10^{-2}, while a slightly smaller value (8×10^{-3}) was obtained at the antinode of a first mode cavity.

The very low quantum yield values that we obtained implies that non-radiative relaxation is the dominant decay pathway in both coupled and uncoupled systems. This is likely due to the numerous molecular vibrational modes available to redistribute the energy (*ca.* 180 fundamental modes in the case of TDBC), as well as energy transfer to defects in the aggregates and perhaps formation of dimers [115, 116]. To go further in the assessment of the radiative and non-radiative decay rates, we undertook femtosecond transient absorption experiments.

2.1.2.3 *Transient polariton dynamics*

Femtosecond transient absorption spectra were recorded in a variable delay pump-probe configuration, under 585 nm pulsed excitation (chirped 150 fs pulses, 6 nm bandwidth, 500 Hz repetition rate, 50 $\mu J.cm^{-2}$). A broad band supercontinuum pulse train (180 fs, 1 kHz) was used as a probe to measure the transient evolution of the absorption spectrum. The intensity of this probe pulse was kept low enough to minimize stimulated emission from the excited populations. In this situation, the negative transient absorption features correspond to the transient bleach of the ground state absorption, while positive signals originate from excited states absorption [117, 118].

Figure 2.7(a,c) shows the differential absorption spectra recorded for the TDBC layer at the node and at the antinode of the second mode cavity, respectively. At the cavity node, the differential spectrum resembles that of the bare TDBC and it decays with the same lifetime ($\tau_{1/2} = 0.6$ ps, Fig. 2.7(b)), in

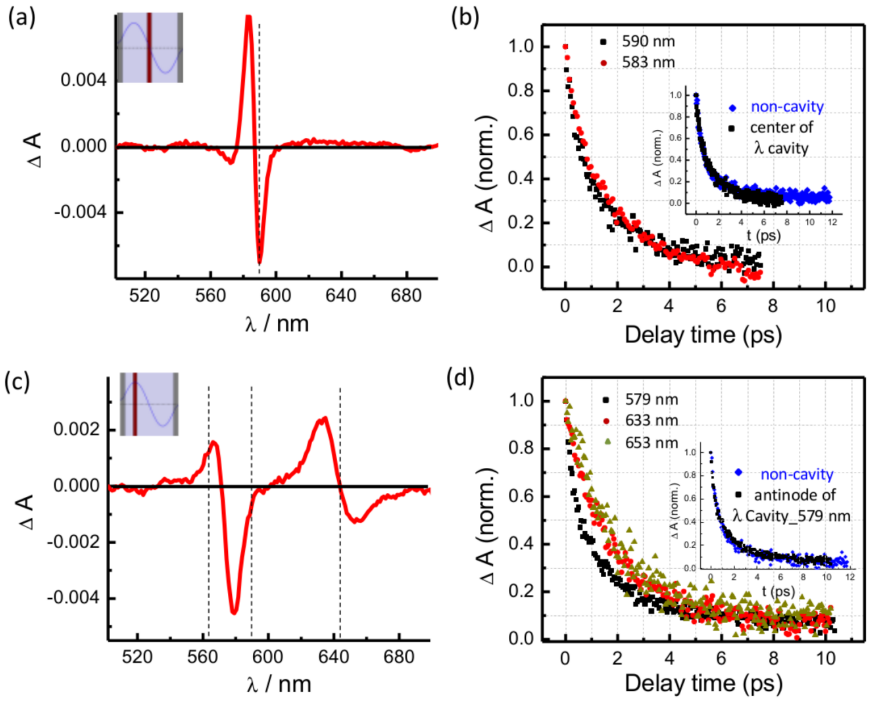

Figure 2.7 – (a) and (c) Transient absorption spectra of LBL TDBC layers in the center and at the antinode of the second mode cavity (as shown in insets). The vertical dashed lines indicate the absorption maxima of the J-band of the uncoupled molecules and of the upper and lower polaritons (only in (c)). (b) and (d) Decay kinetics for the two spatial positions of (a) and (c) respectively, measured at different wavelengths. The inset in (b) shows that the decay at the node of the cavity is identical to that of the bare TDBC layer (measured in the absence of the top mirror). The insert in (d) shows the decay at the uncoupled J-band wavelength (579 nm) for a TDBC layer placed at the anti-node of the cavity. Reproduced from reference [106].

agreement with the fact that this system is in the weak coupling regime.

At the cavity antinode, the transient dynamic depends on the detection wavelength. In the spectral region corresponding to the absorption of the uncoupled molecules (*ca.* 588 nm), the decay matches that measured on the bare TDBC ($\tau_{1/2} = 0.6$ ps), however in the region corresponding to the lower polariton state, the decay lifetime is surprisingly longer ($\tau_{1/2} = 1.4$ ps, Fig. 2.7(d)). The same lifetime was also measured in the lower polariton region of the first mode cavity. Such two-populations

	J-band, bare film	J-band, λ cavity, node	P^-, λ cavity, antinode	P^-, λ/2 cavity, antinode
$\tau_{1/2}$ (ps)	0.6	0.6	1.4	1.4
Φ_f	2×10^{-2}	1×10^{-3}	1×10^{-2}	8×10^{-3}
$k_r(s^{-1})$	3×10^{10}	1.7×10^{9}	7.1×10^{9}	5.7×10^{9}
$k_{nr}(s^{-1})$	1.6×10^{12}	1.7×10^{12}	7.1×10^{11}	7.1×10^{11}

Table 2.1 – Comparison of the properties of the excited states of the TDBC J-Aggregates outside the cavity (bare film) and at the cavity node with those of the lower polariton states P^- formed by placing the TDBC layer at the cavity anitnode.

dynamics are consistent with the results obtained above from steady-state emission spectroscopy. Moreover, the upper polariton lifetime in all cases could not be resolved, lying below the 180 fs resolution of our apparatus.

The independent measurements of the quantum yield and the lifetime of polariton states allows us to extract their radiative and non-radiative decay rates according to (2.3). The results are summarized in Table. 2.1. In order to verify the mutual consistency of these results, we have also calculated an approximate value for the radiative decay rate of each systems, based on Einstein's coefficients [119]:

$$k_r \simeq 2.9 n^2 \bar{\nu}^2 \int \epsilon d\nu, \tag{2.4}$$

where n is the background refractive index of the medium, $\bar{\nu}$ is the absorption peak wavenumber in inverse centimeters, and ϵ is the molar extinction coefficient. Using this approach, the radiative decay rate of bare TDBC was estimated to be $10^{10} s^{-1}$, while a value of $5 \times 10^{9} s^{-1}$ was obtained for the lower polariton states, both in remarkably good agreement with the results of Table. 2.1.

These results consistently show that the lifetime of the lower polariton state population upon off-resonant excitation is much longer than what would be expected from the Tavis-Cummings approach. In particular, with a cavity photon storage times of a few tens of femtoseconds, one would naively expect a similarly short dynamics for both upper and lower

polariton states. While long lived transients polariton populations have often been attributed to delayed scattering from an exciton reservoir [77], the present results demonstrate that this cannot be the only reason as the lower polariton lifetime even exceeds that of the bare molecules. This surprising result for polaritonic systems is however ubiquitous in molecular sciences where there are many examples of species whose lifetimes are longer than those of their constituents. The most notables are excimers formed from the coupling of an excited molecule (M^*) with another molecule in the ground state (M):

$$M^* + M \rightleftharpoons (MM^*). \tag{2.5}$$

The excimer is stabilized by the coupling interaction, leading to cases where the lifetime of (MM^*) is much longer than M^*. For instance, the excited naphthalene monomer has a lifetime of 52 ns at room temperature in ethanol, while its excimer has a lifetime of 380 ns [120].

Our results have been discussed in the context of a non-Markovian rate equation model by Canaguier-Durand and coworkers [88], in terms of genuine polaritonic vibrational relaxation pathways.

2.1.3 *Conclusions*

In this section, we demonstrated a method for precisely tuning the efficiency of light-molecule strong coupling by varying the spatial position of a thin layer of cyanine dye J-aggregates in a FP cavity. The resulting Rabi splitting follows the expected dependence on the cavity mode amplitude in the cavities, as expected from the Tavis-Cummings model.

By positioning the layer at the cavity mode maximum, a Rabi splitting of 503 meV was obtained, amounting to 24% of the J-band energy and placing the system in the ultrastrong coupling regime. The relatively long lifetime measured for the lower polaritonic state was shown to be consistent with its emission quantum yield. Moreover, this lifetime is longer

than any of the relevant timescales of the uncoupled molecules and of the empty cavity, an effect beyond traditional models of strongly coupled organic molecules.

The low polariton fluorescence quantum yield (*ca.* 10^{-2}) shows that the polariton decay is dominated by non-radiative processes.

In the next section, we further investigate the photophysics of molecular cavity polaritons by a comparative study of three different organic materials, exemplifying the rich and diverse excited states dynamics possible in such strongly coupled systems.

2.2 POLARITON PHOTOPHYSICS: A RICH CHEMICAL DIVERSITY

Even though light-matter strong coupling is often reduced to the coherent interaction of a single optically active transition with a cavity resonance, we saw in the previous section that collective molecular strong coupling yields a wealth of new phenomena that can only be described by more complex models, adapted to molecular materials. Thus, the results of the previous section must be contextualized in view of the extraordinarily rich dynamical behaviors reported for molecular systems. A first step in this direction is given here, by comparing the photophysical behavior of polaritons involving three different molecules with very distinct excited states properties. Parts of this section are reproduced from already published work [121].

2.2.1 *Systems under study*

The first molecule that we will discuss is the well-known TDBC in its J-aggregated form, which was already used in the previous section. The only difference here is that the aggregates are directly dispersed in the polymer matrix (PVA, Poly(vinyl alcohol)) by spin-coating instead of being deposited as layer-by-layer assemblies. This preparation method will allow a more

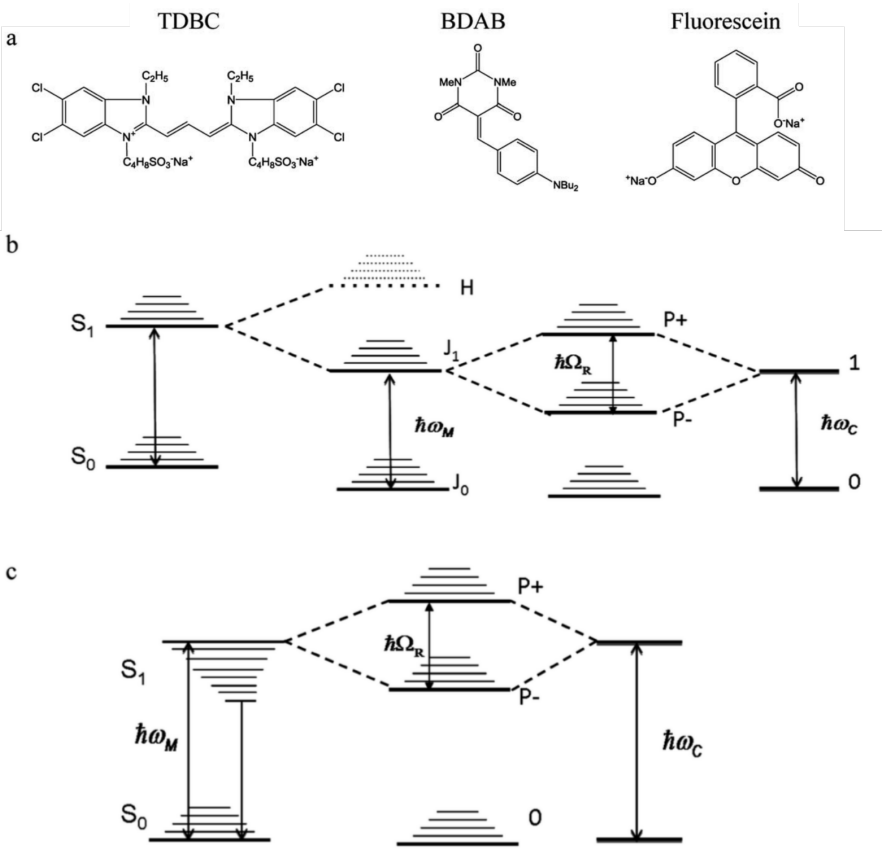

Figure 2.8 – (a) Molecular structures of the three compounds studied and the corresponding energy diagrams for (b) TDBC and (c) BDAB upon strong coupling. The TDBC monomers dipole–dipole coupling gives rise to aggregates states marked J and H. In the case of TDBC, only the J band is observed in the absorption spectrum as the transition to H band is optically forbidden [54]. The molecular Franck-Condon transitions are marked in bold. Reproduced from reference [121].

direct comparison with the two other systems for which a LBL preparation is not straightforward. The energy level diagram describing the coupling of this molecular aggregate to a cavity mode is schematically shown in Fig. 2.8(b), where we have also represented the monomeric coupling process giving rise to the molecular J-band.

The second molecule is a push–pull molecule, 5-(4- (dibutylamino) benzylidene)-1,3-dimethylpyrimidine-2,4,6 (1H,3H,5H)-trione (BDAB) with an unusually large Stokes shift of *ca.* 560 meV, due to excited state isomerization. The strong coupling energy level diagram for such molecular systems that undergo

significant electronic re-distribution in the excited state is illustrated in Fig. 2.8(b). Interestingly, the Franck–Condon transition involved in the strong coupling, corresponds in this case to the transition from the molecular ground state to a higher vibronic state of the excited state manifold. As a consequence, the resulting lower polariton branch may lie above, or be isoenergetic with, the relaxed excited state of the bare molecule. This may have consequences on the dynamics and the decay processes of the coupled system, as it has been shown by Törmä and co-workers [122].

The third molecule, fluorescein, as its name indicates, is a highly fluorescent dye in dilute solutions with a quantum yield of 0.9 and a Stoke shift of about 110 meV. It is a representative of standard organic dyes, with an excited state dynamics somewhat in between that of the very rigid J-aggregates rods and the very floppy BDAB molecules.

The strongly coupled samples were prepared by encasing polymer films doped with the molecular dyes in between two silver mirrors to form an optical cavity. The thickness of the polymer films, and thus the final separation between the Ag mirrors of the cavity, was chosen to give an optical mode resonant with the absorption maximum of the dye/aggregate (at 590 nm for TDBC, 470 nm for BDAB, and 510 nm for fluorescein). As in the previous section, the Q-factors of these cavities are low, typically between 10 and 20.

All the steady state measurements were performed on reflective cavities, in which the bottom Ag mirror, deposited on a glass substrate, was 200 nm thick, and the semitransparent top mirror was 30 nm thick. Pump–probe experiments were performed in transmission mode, on cavities for which both mirrors were 30 nm thick. The bottom Ag film was sputtered on borosilicate glass slide, followed by spin-coating of the molecules dispersed in a polymer to form a thin film. The second Ag film was then sputtering on top, thus closing the cavity. TDBC films were spin-cast from aqueous solution (Milli-Q) containing 0.5% TDBC and 5% PVA (molecular weight 205000) by weight. Fluorescein films were cast from aque-

ous solutions of 1% fluorescein disodium salt and 2% PVA by weight. BDAB films were cast from toluene solutions of 0.5% BDAB and 1% PMMA, (molecular weight 120000) by weight. Toluene (Sigma Aldrich), PVA (FLUKA), PMMA (Sigma Aldrich), fluorescein disodium salt (Exciton) and TDBC (Few Chemicals) were obtained commercially and used without further purification. BDAB was synthesized by G. Schaeffer in J.-M. Lehn's group as detailed in [121].

2.2.2 *Populating the lower polaritonic states*

The absorption and PL spectra of the FP cavities containing TDBC, fluorescein and BDAB are reported in Fig. 2.9 together with the bare molecules spectra. The two new absorption peaks corresponding to upper and lower polaritons (blue solid curves) have full width at half maxima (FWHM) that are mainly determined by the cavity mode finesse [73]. The Rabi splittings for these samples are 277, 554 and 720 meV for TDBC, BDAB and fluorescein respectively. It should be noted that for fluorescein the polariton splitting is more complex, due to the double peaked absorption of the bare molecule, as also reported for *e.g.* Rhodamine [122]. Careful observation of the emission spectra of the coupled systems shows that at least some fluorescence of the bare molecules is always present in these cavities. In other words, some of the molecules are not coupled to the cavity due to the disorder in the system, as also observed in the previous section. The lower polariton emission peak of the coupled BDAB is at higher energy than the bare molecule emission, in agreement with the schematic illustration of Fig. 2.8(c).

We report in Table. 2.2 the lifetime of the lower polariton state for the three systems studied, as measured by femtosecond pump-probe spectroscopy under high energy off-resonant excitation, as well as their fluorescence quantum yields obtained as described in the previous section. The extracted values of radiative and non-radiative decay rates are also reported.

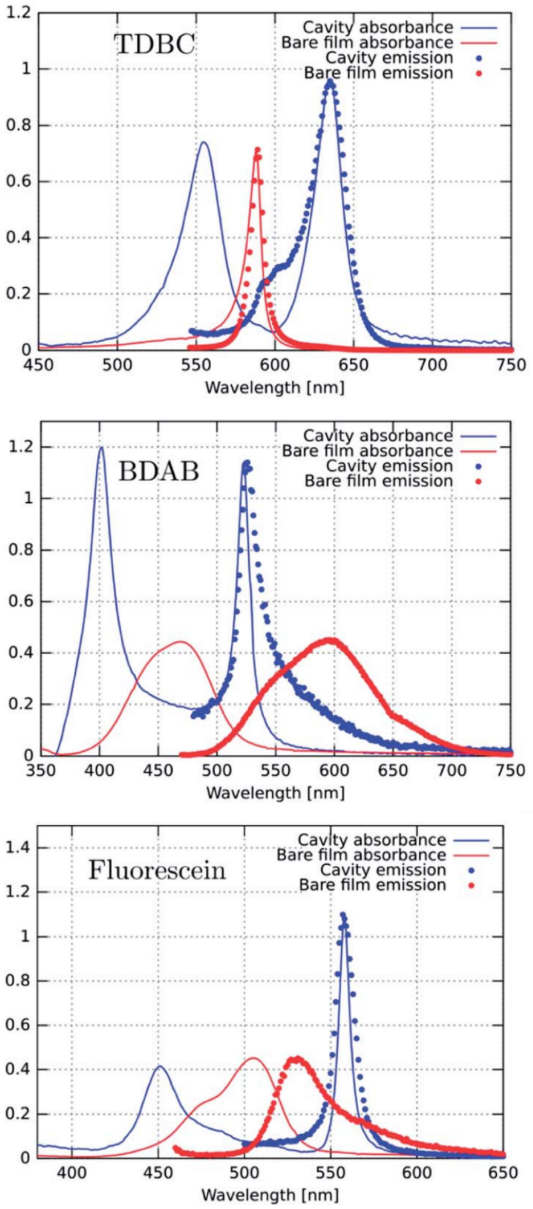

Figure 2.9 – Absorbance (solid lines) and emission (dotted lines) spectra of the bare molecules (red) and the corresponding coupled systems (blue). The excitation wavelengths were either 530 nm for TDBC or 450 nm for BDAB and fluorescein. Reproduced from reference [121].

	TDBC	BDAB	Fluorescein
$\tau_{1/2}$ (ps)	4.3	3.5	30
Φ_f	1×10^{-2}	4×10^{-2}	2×10^{-2}
$k_r(s^{-1})$	2×10^{9}	1×10^{10}	7×10^{8}
$k_{nr}(s^{-1})$	1×10^{11}	2×10^{11}	3×10^{10}

Table 2.2 – Comparison of the excited states properties of strongly coupled TDBC, BDAB and fluorescein, measured under high energy off-resonant excitation.

Overall, the results are comparable to what was found above for LBL TDBC cavities, pointing to the fact that vibrational relaxation remains a major decay channel in a broad class of organic polaritonic systems.

In view of these results, we would like to quantify the energy pathways that can channel population from higher excited states to the lower polariton branch. To do so, we will rely on pump-probe measurements and on fluorescence excitation spectroscopy, a technique that we briefly describe here.

2.2.2.1 *Fluorescence excitation spectroscopy*

Fluorescence excitation spectroscopy, also called action spectroscopy, is a technique routinely used in molecular science to reveal the states and mechanisms responsible for the PL. It consists in measuring the emission intensity, I_f, at a given wavelength λ_{em} while scanning the excitation wavelength λ_{ex} through the absorption spectrum of the sample. Since, assuming that the system follows Kasha's rule, $I_f(\lambda_{em}) \propto \Phi_f \sigma_A(\lambda_{ex}) I_0(\lambda_{ex}) c$, where σ_A is the absorption cross section of the molecule, c is the molecular concentration and $I_0(\lambda_{ex})$ is the excitation light intensity, one would expect that for a constant I_0, the excitation spectrum reproduces the absorbance spectrum of the system. The key element that makes excitation spectroscopy such a powerful technique is that it yields an absorption spectrum *conditioned* to the generation of a PL signal at the detection wavelength. In other words, it probes not only the relative intensity of the absorption bands, but also the efficiency of

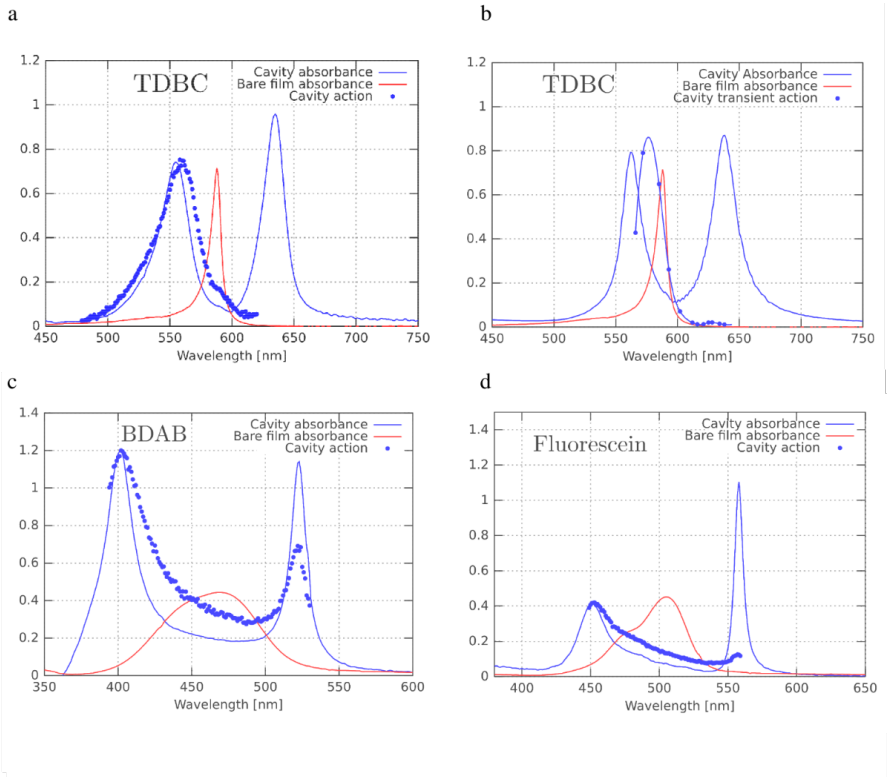

Figure 2.10 – Excitation spectra (blue dots) recorded at normal incidence from the lower polariton emission of (a) TDBC (at 680 nm), (c) BDAB (at 540 nm) and (d) fluorescein (at 576 nm). These spectra are compared to the absorbance spectra of the bare molecules (solid red lines) and to that of the strongly coupled systems (solid blue lines). (b) Lower polariton transient action spectrum of the TDBC cavity. Reproduced from reference [121].

their relaxation pathways toward the emitting state under study. This quantity will thus be extremely valuable in understanding the energy pathways in polaritonic systems, in particular when applied to the lower polariton state.

2.2.2.2 *Results and discussion*

We show in Fig. 2.10(a,c and d) the excitation spectra of the three molecules under study, recorded on the low energy side of their lower polariton emission, and compare it to their absorbance spectra.

The first striking feature in these spectra is the relative contribution of the upper and the lower polaritons to the emission

of P- (here all the excitation spectra have been normalized to the P+ absorbance peak). It thus appears that the direct excitation of the P- peak contributes very little to the P- emission, while when exciting into P+ or at the uncoupled molecules energy, the population rapidly relaxes to P-, from where emission can occur. As discussed before, this relaxation to P- can occur via energy transfer between the coupled and the uncoupled molecular reservoirs as well as by rapid internal vibrational relaxation. It is interesting to note that the ratio of P-/P+ excitation peaks is the smallest for TDBC (*ca.* 0.1) and the largest for BDAB (*ca.* 0.5). We show in Fig. 2.10(b) for the TDBC cavity that this steady state result is corroborated by transient excitation spectroscopy experiments. In this case instead of measuring a PL intensity, one monitors the amplitude of the transient absorption signal at the P- position as a function of the pumping wavelength. Surprisingly, in this experiment, the contribution of the upper polariton state to the transient signal at the lower polariton wavelength comes at a red-shifted position with respect to the static absorption spectrum of the cavity (blue curve in Fig. 2.10(b)).

To try to understand the origin of these observations, the PL excitation spectra were recorded for cavities of different detunings. As can be seen from Fig. 2.11, the excitation spectra of both BDAB and fluorescein cavities get closer to their absorption spectra as the cavity is detuned to the blue of the bare molecules absorption maxima. In particular, the relative P-/P+ intensity of the absorbance spectra is accurately reproduced by the excitation spectra in those two systems under blue detuning. At the same time, the excitation spectra intensity in between the two polariton peaks significantly increases, indicating that uncoupled molecules contribute more to the emission of a blue-detuned lower polariton peak. The dependence of the excitation spectra upon cavity detuning seems to be more pronounced for fluorescein, where the P- contribution suddenly develops (red spectrum), as compared to BDAB for which the P- signal steadily increases from red to blue detuned cavities.

Interestingly, we do not observe any contribution from P- in the TDBC cavities, regardless of the detuning.

At this point, it should be reemphasized that excitation spectra are not probing the existence of the states, but rather the possibility for those states to transfer population to the emitting state under study, here the bottom of the lower polaritonic branch. When measuring the 'resonant' contribution from P-, *i.e.* the possibility of getting emission from the red tail of P- while exciting at the P- absorption peak, one needs a relaxation mechanism by which a polariton can lower its energy before fluorescing at the detection wavelength. In other words the fluorescence of P- has to undergo a finite Stokes shift. As evidenced by the data shown here, this relaxation mechanism strongly depends on the overlap between the polaritonic states and the vibronic manifold of the bare molecular material, and also possibly on the excited state rearrangement involved in the molecular Stokes shift.

2.2.3 *Conclusions*

In this section, we reported on a first step toward the exploration of chemical diversity in the context of polariton photophysics. By strong coupling three different species to FP cavity modes, we could carry on a comparative study, revealing some common features of molecular strong coupling, such as the presence of uncoupled molecules in the cavity emission spectra, or the low PL quantum yield.

The very different excited states dynamics of the three molecules under study was however found to profoundly affect the energy pathways among the excited states of the coupled system in the case of resonant excitation of the lower polariton state. This effect was shown to strongly depend on the overlap between the lower polaritonic state and the vibronic levels of the bare molecules allowing polaritons to undergo a Stokes shifted radiative relaxation. Clearly more experiments and theory that can handle such complex materials and the

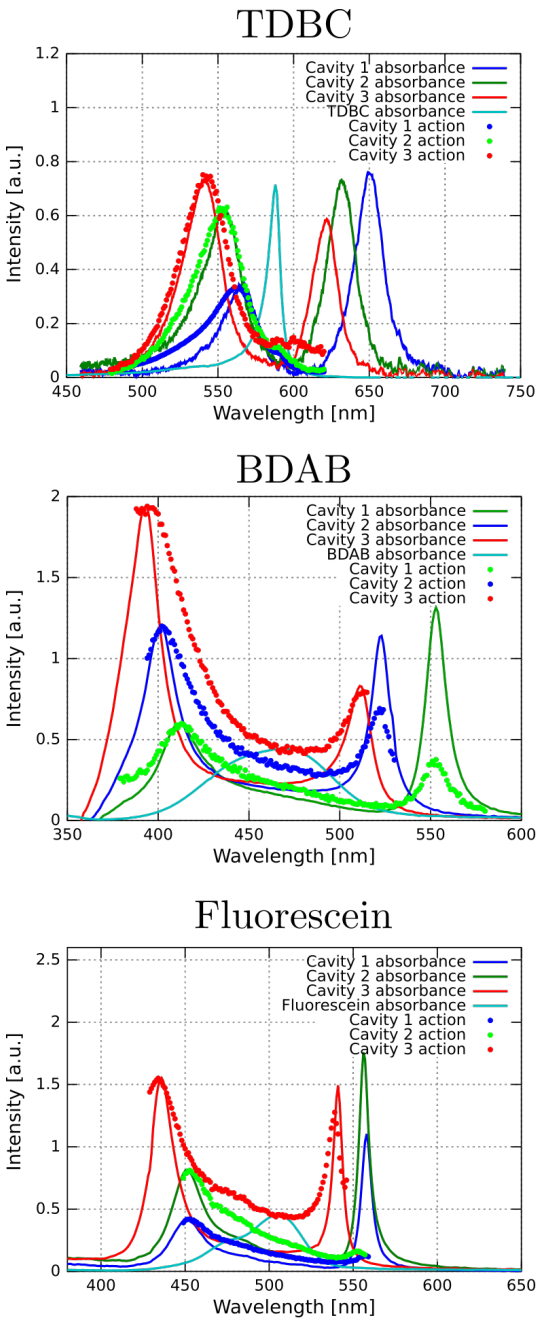

Figure 2.11 – Normal incidence excitation spectra (dotted lines) of TDBC, BDAB and fluorescein cavities for different detunings, compared to the corresponding absorbance spectra of the coupled systems and the bare molecules. In each cases, the PL detection wavelength lies 5 nm to the red of the last point of the excitation spectrum. Reproduced from reference [121].

particularities associated with individual molecular structures need to be developed to elucidate these strongly interacting and dissipative systems.

In the next section, we build upon these results to design a two-species polaritonic system offering a new and efficient energy transfer channel between the coupled entities.

2.3 ENERGY TRANSFER THROUGH LIGHT-MATTER HYBRID STATES

As we saw throughout the two previous sections, non-radiative relaxation within the excited state vibronic manifold usually constitutes the dominant mechanism by which polaritons can relax their energy. When, as in the case of TDBC, the lower polariton states lie below the bottom of the excited state manifold, such an energy relaxation process is suppressed and the polariton can either decay by an isoenergetic photon emission or relax to the ground state manifold by molecular internal relaxation.

By collectively coupling two different molecular species to a common cavity mode, we will show in this section that the excited state polaritonic energy relaxation can be recast into an efficient energy transfer mechanism between the two species. As it involves the formation of delocalized light-matter states, this collective energy transfer mechanism will be shown to be independent of the separation distance between the two coupled populations, provided that the coupling strength is maintained. Parts of this section are reproduced from already published work [86, 87].

2.3.1 *Energy transfer in a cascade coupling configuration*

Looking back at the cavity excitation spectra of Fig. 2.10, it is clear that the energy can efficiently flow from the upper to the lower polaritonic states. Moreover, the analysis of the resonant excitation spectra of P- in different molecular

systems showed that this polaritonic relaxation mechanism was sensitive to the presence of isoenergetic vibronic states in the molecular excited state manifold. Building upon this result, we decided to engineer a system in which the density of vibronic states at the lower polariton energy would belong to a different molecule than the one giving rise to this lower polaritonic state. The corresponding cascade coupling diagram is schematically shown in Fig. 2.12(a). In this situation, the efficient energy flow from the upper to the lower polaritonic states would effectively translate into an energy transfer from one molecular species to the other.

2.3.1.1 *System under study*

We will use TDBC J-aggregates as the energy-donor since we already know that its lower polariton lies below the bottom of its excited states vibronic manifold. Another J-aggregated dye (BRK) will be used as the energy acceptor, having a strong absorption band in the wavelength range where the TDBC lower polariton should appear (*ca.* 650 nm, see Fig. 2.12(c)). A toy model for the resulting energy levels diagram can be derived from the following three-by-three coupling matrix:

$$\mathcal{H} = \begin{pmatrix} E_\gamma(\theta) & \hbar\Omega_D/2 & \hbar\Omega_A/2 \\ \hbar\Omega_D/2 & E_D & 0 \\ \hbar\Omega_A/2 & 0 & E_A \end{pmatrix}, \tag{2.6}$$

where $E_\gamma(\theta) = E_0(1 - \sin^2\theta/n_c^2)^{-1/2}$ is the angle dependent (dispersive) cavity mode energy, E_0 is the cavity cutoff energy, n is the background refractive index, $E_{D(A)}$ is the donor (acceptor) exciton energy, and $\hbar\Omega_{D(A)}$ is the donor (acceptor) Rabi splitting. By solving the eigenvalues problem in the case where the cavity is resonant with the donor and with the acceptor lying at a lower energy, one obtains three dispersive polariton branches with Hopfield coefficients gradually going from a donor-like P+ to an acceptor-like P-, as sketched in Fig. 2.12(b). This is precisely the configuration that we are looking for in view of a polariton mediated energy transfer.

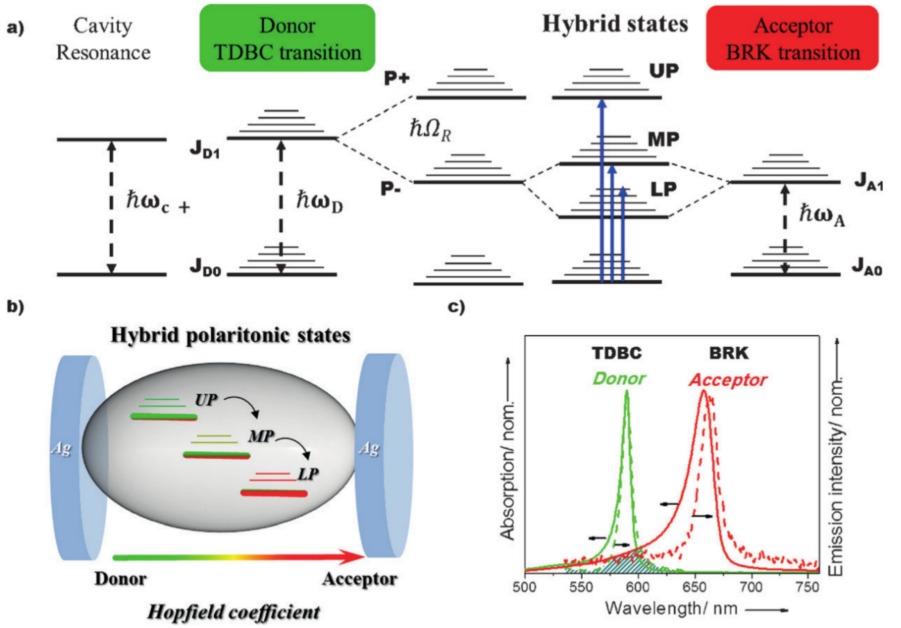

Figure 2.12 – (a) Schematic representation of the cascade strong coupling with the energy-donor molecules resonant with a FP cavity mode, and the energy-acceptor molecules resonant with the donor's lower polariton. The consecutive splitting of this lower polariton results in the formation of three hybrid light-matter states: the upper (UP), middle (MP), and lower (LP) polaritonic states. (b) Schematic diagram of the different donor and acceptor contents (Hopfield coefficient) of UP, MP, and LP states in the strongly coupled cavity with UP having the largest donor character while LP is mostly acceptor-like. (c) Normalized spectroscopic data for the donor and acceptor materials. The green solid and dash curves are the TDBC absorption and emission spectra on top of a 30 nm Ag film, while the red solid and dash curves are for the BRK acceptor. The shadowed part is the overlap between the donor emission and acceptor absorption spectra. Reproduced from reference [86].

The samples were prepared by mixing various weight percentages of TBDC and BRK (BRK5714, Organica Feinchemie GmbH) in a water-PVA solution that was then spin coated onto a 30 nm thick silver mirror to form a 140 nm thick active layer. The deionized water solutions used for spin-coating contained 0.25% TDBC and 2.5% PVA by weight, and weight percentages of BRK ranging from 0.075% to 0.25%. Since the molecular weights of the two species are nearly equal ($M_{TDBC} = 762.53$ g/mol, $M_{BRK} = 782.067$ g/mol), these weight ratios approximately correspond to the molecular population ratios. After spin-coating, another 30 nm thick silver mirror was sputtered upon the film to close the microcavities.

The resulting cavity absorption spectra, calculated as $1 - R - T$ from the measured cavity reflection (R) and transmission (T) spectra, are show in Fig. 2.13(a) for different mass ratio of TDBC and BRK. In the absence of the BRK (acceptor), the cavity absorption spectrum displays two polariton peaks at 549 nm (2.27 eV) and 637 nm (1.95 eV), separated by a Rabi splitting of 320 meV. As the quantity of BRK increases, we clearly see how its absorption peak splits the original P- band of the TDBC cavity. This effect is also revealed by the angle resolved cavity absorption spectra shown in (c) and (d) for the 1:0 and 1:1 cavities respectively. These dispersion relations can be accurately fitted by a coupled oscillators model involving either one or two different absorbing species (black dots in (c,d)), and yields in for the 1:1 cavity the Hopfield coefficients shown in (b). As expected, the upper polaritonic state is mostly donor-like, with a donor/acceptor mixing coefficient $|\alpha_{exD}|^2/|\alpha_{exA}|^2 = 7.3$, the middle polariton is also quite donor-like with $|\alpha_{exD}|^2/|\alpha_{exA}|^2 = 2$, while the lower polariton is dominated by the acceptor component with $|\alpha_{exD}|^2/|\alpha_{exA}|^2 = 0.1$.

2.3.1.2 *Hints of energy transfer in steady state spectra*

We show in Fig. 2.14(a) the emission and excitation spectra of bare films containing different donor to acceptor ratios. While two well resolved emission peaks can be observed in the

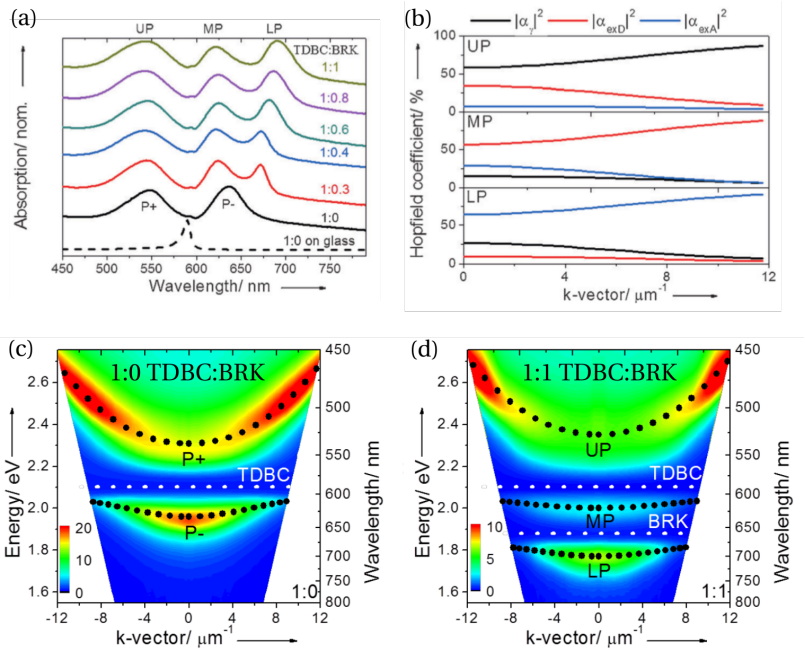

Figure 2.13 – (a) Normalized absorption spectra for various weight ratios (1:0 to 1:1) of donor (TDBC) and acceptor (BRK) inside strongly coupled cavities. The absorption spectra A is determined after recording the transmission T and the reflection spectra R of the samples ($A = 1 - T - R$). The black dash curve shows the donor absorbance spectrum on top of a glass substrate. (b) Hopfield coefficients of the three hybrid light-matter states for the 1:1 donor–acceptor cavity, obtained by fitting the peaks of the angle resolved absorption spectrum (d) to the eigenvalues of (2.6). (c) Shows the angle resolved absorption spectrum of the TDBC cavity (1:0 ratio) for comparison. Reproduced from reference [86].

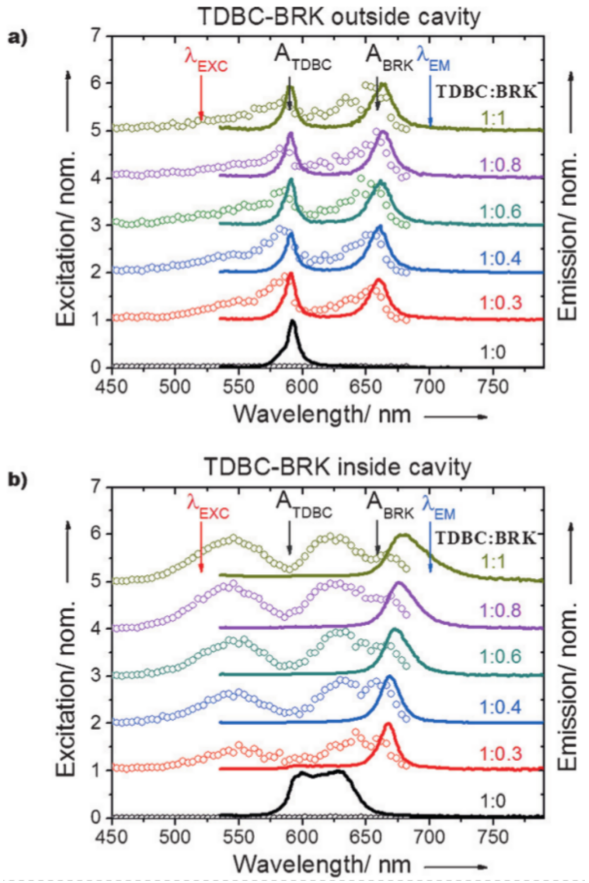

Figure 2.14 – Normalized excitation and emission spectra from varying weight ratios between donor and acceptor. (a) in the absence of the top Ag mirror (outside cavity) and (b) in the strongly coupled system. The emission spectra are recorded upon excitation at 520 nm while the excitation spectra are collected at 700 nm. Reproduced from reference [86].

presence of TDBC and BRK molecules, the excitation spectra acquired from the red tail of the BRK emission (700 nm) reveal that some energy transfer is already at play here. Indeed, even though TDBC alone emit very weakly at 700 nm, it strongly contribute to the collected PL at this wavelength, implying an energy transfer process to the BRK molecules. The presence of such an energy transfer channel in the bare film should not be too surprising. The conditions stated above that we want to fulfill to observe a polaritonic energy transfer naturally led us to chose two dyes with overlapping absorption and emission spectra (see Fig. 2.12(c)), a favorable condition to observe usual Förster type energy transfer outside the cavity [123].

The emission and excitation spectra of the corresponding cavity samples are shown in Fig. 2.14(b). Strikingly, while the 1:0 TDBC cavity shows its usual coupled-uncoupled emission spectrum, the cavities containing TDBC and BRK display a single emission peak at their lower polariton energy. Moreover, this lower polariton emission is largely fueled by upper and middle polaritons as shown by the excitation spectra. These two observations, constitute strong evidences for a very efficient energy channel from the donor-like to the acceptor-like polaritonic states. In other words, the collective hybridization via a common cavity mode seems to have boosted the ability of the donor molecules to transfer energy to the acceptor molecules.

2.3.1.3 *Time-resolved polaritonic energy transfer*

Such static findings, also reported by Lidzey and coworkers in a similar system [85], however do not constitute an indisputable proof of polaritonic energy transfer. To go beyond these steady-state measurements and demonstrate that the system is truly undergoing enhanced energy transfer under strong coupling, the dynamics of the system was studied by femtosecond transient transmission spectroscopy. The transient spectra under 530 nm excitation, are shown for the donor–acceptor inside and outside the cavity in Fig. 2.15(a). As can be seen from the black curve, we mostly excite the donor at this pumping wavelength, with just a small transient signal at the acceptor position coming from both its finite absorption at the pump wavelength and Förster energy transfer in the bare film. Inside the cavity, even though the transient spectrum is complicated by the overlapping ground-states bleach and excited states absorption from the different polaritonic states, the highly efficient polaritonic energy transfer process discussed above is still visible through a large increase of the transient signal in the acceptor-like LP region upon excitation of the donor-like UP state.

The decay kinetics of the transient spectra are shown in Fig. 2.15(b) for the donor–acceptor system inside and outside

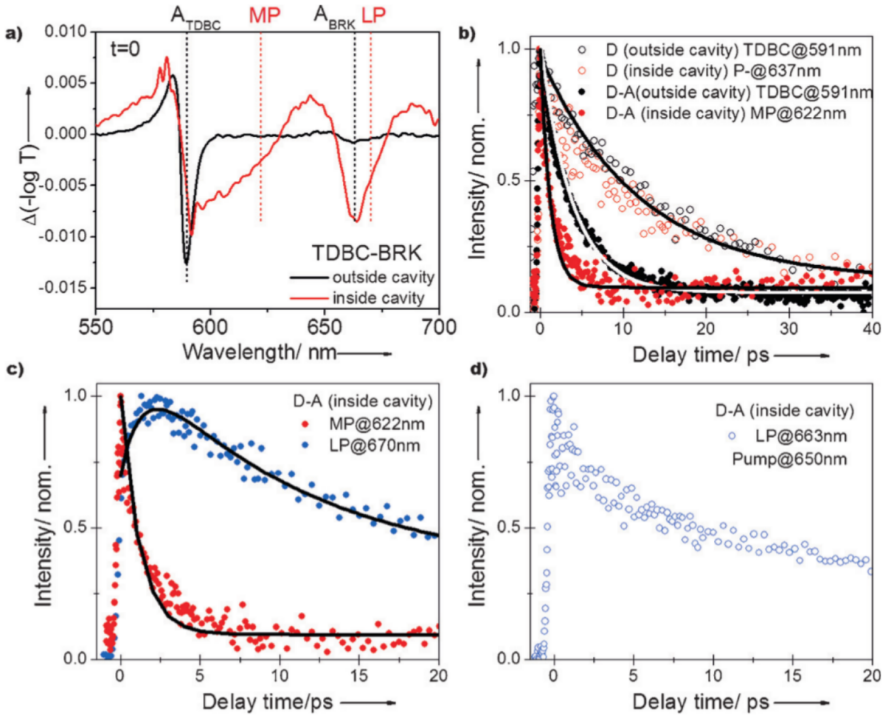

Figure 2.15 – (a) Transient absorption spectra of the donor–acceptor films (1:0.3 ratio) inside the cavity (red curve) and on top of a single Ag mirror (black curve). The 150 fs pump was set at 530 nm. The black dash lines indicate the TDBC and BRK absorption maximum and the red dash lines correspond to MP and LP. (b) Decay kinetics of the donor only film outside cavity at the TDBC absorption maximum 591 nm (black open circles) and of its P- in the 1:0 strongly coupled system at 637 nm (red open circles). The decay kinetics of the donor–acceptor film (1:0.3) outside the cavity at 591 nm is shown as black filled circles, and that of the MP in the strongly coupled system at 622 nm is shown as red filled circles. (c) Kinetics recorded at different wavelengths for the strongly coupled donor–acceptor (1:0.3) showing the decay of the signal at wavelengths where MP absorbs and the concomitant rise of the LP population. (d) Decay kinetics recorded at 663 nm for the coupled donor–acceptor (1:0.3) with the pump at 650 nm. The solid lines overlapping the data points in (b) and (c) are the exponential fits as described in the text. Reproduced from reference [86].

the cavity (red and black filled circles, respectively). Control experiments with only the donor molecules show a long lifetime of *ca.* $\tau_D = 12$ ps both inside and outside the cavity (red and black open circles, respectively), a much larger value than what we obtained for the same J-aggregates in the previous section due to the reduced molecular self-quenching at the densities used here.

In the presence of the acceptor in the bare film, the lifetime in the spectral region of the donor decreases to $\tau_{DA} = 5.5$ ps. Remarkably, it further drops down to $\tau_{DA}^c = 1.2$ ps in the strongly coupled system. From these values, the energy transfer rates $R_{ET} = k_{ET}[A]$ for a given concentration of acceptor $[A]$ can be extracted since $R_{ET} = 1/\tau_{DA} - 1/\tau_D$, and it is found to be much higher in the strongly coupled system ($0.68 \times 10^{12} s^{-1}$) than outside the cavity ($0.10 \times 10^{12} s^{-1}$) under these experimental conditions. The shorter decay lifetimes in the presence of the acceptor are a direct evidence of energy transfer in both the strongly coupled system and the bare film outside the cavity. Since $[A]$ is the same in both cases, it is the energy transfer rate constant inside the cavity k_{ET}^c that is enhanced by a factor of nearly 7 as compared to its value in the bare film.

In addition, this efficient flow of energy through the polaritonic states can also be evidenced by the delayed rise time of the LP population concomitant with the decay of the MP population, as can be seen in Fig. 2.15(c). These energy transfer kinetics can be well reproduced by the following rate equations, typical of bipartite energy transferring systems [124]:

$$\begin{cases} \dfrac{dD(t)}{dt} = -(k_D + k_{ET}) & (2.7) \\ \dfrac{dA(t)}{dt} = k_{ET} D(t) - k_A A(t), & (2.8) \end{cases}$$

where $D(t)$ is the time dependent concentration of excited state donors, $A(t)$ is the time dependent concentration of excited state acceptors and $k_{D(A)}$ is the decay rate constant of the donors (acceptors) alone. As discussed above, the MP (or UP) plays here

the role of the energy donor, and the LP is the energy acceptor. The solutions of this rate model:

$$\begin{cases} D(t) = D_0 e^{-(k_D + k_{ET})t} & (2.9) \\ A(t) = \dfrac{D_0 k_{ET}}{k_D + k_{ET} - k_A} \left(e^{-k_A t} - e^{-(k_D + k_{ET})t} \right) & (2.10) \end{cases}$$

yield transient populations $D(t)$ and $A(t)$ that closely fit the decays of Fig. 2.15(b,c) as shown by the solid curves. When the excitation wavelength is changed to 650 nm (Fig. 2.15(d)), at the blue edge of the LP absorption band, no rise time in the LP population is seen, as expected in the absence of energy transfer.

The above experiments were carried out on samples containing donor–acceptor ratios of 1:0.3. At higher acceptor concentrations, that is, when the acceptor is more and more strongly hybridized with the donor and cavity photon, the energy transfer dynamics are so fast that it is beyond the limit of our temporal resolution and at least 10 times faster than outside the cavity for the same conditions. Although we excited directly into UP at 530 nm, its decays to the MP is in all cases faster than our time resolution of *ca.* 150 fs.

The enhanced energy transfer rate constant in the strongly coupled system will lead to an increase in the energy transfer efficiency η^c_{ET} and therefore in the efficiency of emission η^c_{EM} of the acceptor state upon excitation of the donor as

$$\eta^c_{EM} = \eta^c_{ET} \cdot \Phi_{LP} = \frac{k^c_{ET}[A]}{k^c_r + k^c_{nr} + k^c_{ET}[A]} \Phi_{LP}, \qquad (2.11)$$

where Φ_{LP} is the emission quantum efficiency of the LP acceptor-like state, k^c_r and k^c_{nr} are the radiative and non-radiative decay rate constants of the donor-like state. Because $k_r \ll k_{nr}$ both for the coupled and uncoupled donor molecules, we can estimate that the energy transfer efficiency increases from its value of $\eta_{ET} \simeq 0.55$ outside the cavity to $\eta^c_{ET} \simeq 0.90$ in the strongly coupled system. This difference is in qualitative agreement with the variations seen in the emission spectra of Fig. 2.14 where outside the cavity both the donor and the acceptor fluorescence

peaks are observed while in the strongly coupled case the emission is dominated by the LP. This implies that the emission quantum yields are comparable inside and outside the cavity, in agreement to what was found in the previous section in other systems.

In our strongly coupled system, the delocalized nature of the hybrid polaritonic states is most likely responsible for enhanced energy transfer rate. By this collective hybridization of donor and acceptor molecules, the new eigenstates of the system result in an effective giant delocalized molecule through which energy can cascade from donor-like to acceptor-like states, an effect somewhat reminiscent of recently discovered phenomena in photosynthetic complexes [125]. To push this idea further, we now demonstrate that this energy transfer process can also occur when the collectively coupled donor and acceptor molecules are spatially separated on either sides of the cavity.

2.3.2 *Energy transfer between spatially separated entangled molecules*

From our toy model (2.6) describing the cascade coupling that leads to the polaritonic energy transfer, it is remarkable that the spatial separation between the donor and the acceptor molecules does not appear explicitly. Indeed, the argument carried above was only concerned with the spectral features of the coupled and uncoupled systems, and it seems that, as long as the light-molecules coupling strength is maintained, the same effects would be observable regardless of the distance between the two species.

2.3.2.1 *Static and transient signatures*

In order to see how far this surprising implication could be verified, we developed a different cavity design in which the donor molecules can be separated from the acceptor molecules by a PMMA spacer of tunable thickness. Moreover, we used a second mode optical cavity such that this dielectric spacer

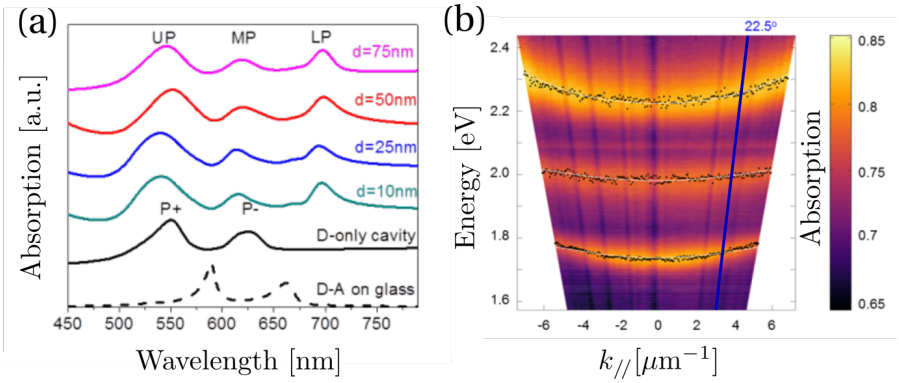

Figure 2.16 – (a) Normalized absorption spectra for various spacer thickness (10 nm to 75 nm) of donor (TDBC) and acceptor (BRK) in the strongly coupled cavity. The absorption A is determined after recording the transmission T and the reflection R of the samples (A = 1−T−R). The black dash curve shows the absorbance spectrum of spatially separated donor and acceptor on a glass substrate. (b) Example of angular dispersion spectrum for the 50 nm spacer strongly coupled cavity. The white curves are the coupled oscillators fits from the model (2.6). The blue line indicates the 22.5° direction with respect to the sample normal, from where we collected the excitation spectra. Reproduced from reference [87].

occupied the central region of the cavity where the electric field is the weakest, thus inducing a minor degradation of the overall coupling strength as the thickness of this layer was increased. The resulting cavity absorption spectra are shown in Fig. 2.16(a) for spacer thicknesses ranging from 10 to 75 nm, and a fixed total cavity thickness of 330 nm. As expected, we observe the three polaritonic branches resulting from the same cascade coupling as in the previous experiment (see *e.g.* Fig. 2.16(b)), with minor variations as the spacer thickness is varied.

The emission and excitation spectra of the donor-acceptor system under strong coupling are compared with those taken outside the cavity in Fig. 2.17 for different spacer thicknesses. Outside the cavity, the results are much different from what we observed in Fig. 2.14(a) when the donor and acceptor molecules were blended together in the same polymer film. In this spatially separated configuration, the 530 nm excitation gives rise to a strong emission from the donor molecules, with only a tiny amount of light emitted at the acceptor wavelength. This

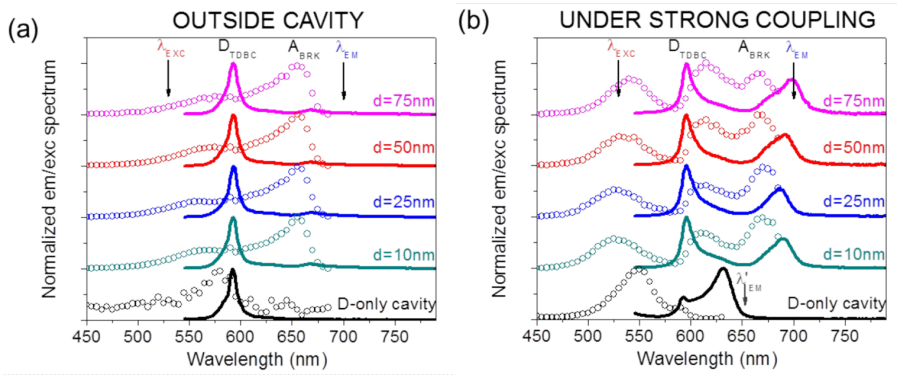

Figure 2.17 – Normalized excitation (dots) and emission (solid curves) spectra for varying spacer thickness from 10 nm to 75 nm, (a) for a film on a single Ag mirror (outside cavity) and (b) in the strongly coupled system. The emission spectra are recorded upon excitation at 530 nm at normal incidence while the excitation spectra are collected at 700 nm with a detection angle of 22.5° from the normal to the sample plan. Reproduced from reference [87].

very weak emission, also revealed by the acceptor excitation spectra is independent of the spacer thickness, showing that it probably originates from tails of absorption from the acceptor at the pumping wavelength. Thus, already with a spacer of 10 nm, we observe no energy transfer in the bare film, as expected from the strong distance dependence of Förster energy transfer [123].

In striking contrast to these bare films results, the strongly coupled cavities show a clear emission from the LP state, to which all the three polaritonic states contribute with comparable intensities. We also observe near 600 nm some emission from the bare donor molecules convoluted with the MP state, indicating that, contrary to what we saw in *e.g* Fig. 2.14(b), the energy transfer process efficiency does not reach unity in such systems. Despite this lower efficiency, the opening of a genuine long distance energy transfer pathway via the collective hybridization of remote donor and acceptor molecules to a cavity mode remains a very appealing result.

These steady state results were further confirmed by transient absorption experiments where the decay kinetics inside and outside the cavity for different spacer thicknesses were

compared. With spacer thicknesses larger than 10 nm, the lifetime of the donor molecules outside the cavity (*ca.* 12 ps) is not modified by the presence of the acceptor molecules, as expected from the uncoupled excitation spectra results, and as shown in Fig. 2.18(a, black circles). Inside the cavity (red circles), the decay dynamics is shortened to 9 ps as observed by monitoring the spectral region corresponding to the middle polariton MP which is the intermediate state through which the energy transfer occurs. As before, the UP is so short lived that we cannot resolve its lifetime with our 150 fs time resolution. From these values, an energy transfer rate $R_{ET} = k_{ET}[A] = 1/\tau_{DA} - 1/\tau_D = 0.04 \times 10^{12} s^{-1}$ can be extracted, yielding an energy transfer efficiency $\eta_{ET}^c \simeq 0.37$ in the spatially separated strongly coupled system. The lower value obtained here, as compared to the one obtained above for donors and acceptors homogeneously mixed inside the cavity, is reasonable since short range dipole-dipole energy transfer does not contribute at such spacer thicknesses. Moreover, the competition between the decay of the donor and this energy transfer process is in qualitative agreement with the ratios of the emission peaks corresponding to the donor and LP in Fig. 2.17(b).

Remarkably, when the spacer thickness is varied from 10 nm to 75 nm the dynamics does not change as shown in Fig. 2.18(b). This result is also consistent with the static experiments of Fig. 2.17(b). We emphasise again that, for this range of spacer thicknesses, the strong coupling strength remains nearly constant (see Fig. 2.16(a)) because the spacer occupies the central region of our second mode cavity.

2.3.2.2 *Cavity Förster model of polaritonic energy transfer*

In order to link this new polaritonic energy transfer mechanism to the reported processes in donor-acceptor systems [123], we developed a very simplified model of cavity modified Förster theory. This model describes the elementary energy transfer process between a donor molecule (D) initially in its excited state, and an assembly of acceptor molecules (A)

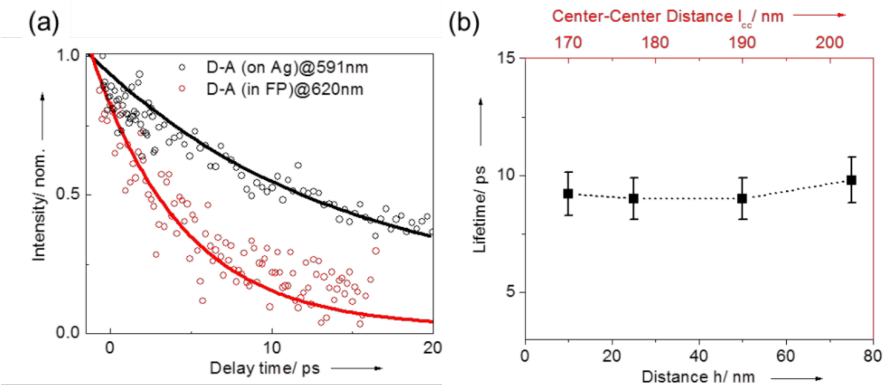

Figure 2.18 – (a) Decay kinetics of the donor–acceptor system inside and outside the cavity for a spacer thickness $h = 50$ nm. The decay outside the cavity is taken at the TDBC absorption peak (591 nm, black circles). Inside the cavity, the decay is taken at the MP energy at 620 nm (red circles). (b) Lifetimes of MP recorded at different spacer thicknesses for the strongly coupled donor– acceptor cavity. Reproduced from reference [87].

initially in their ground-states, mediated by a resonant optical cavity mode. Like in our experiment, the D and A molecules are distributed in either side of a FP cavity having its 2^{nd} optical mode resonantly tuned to the D absorption peak, and are spatially separated by a dielectric spacer of variable thickness d as shown in Fig. 2.19(a).

Following a multipolar approach [126], we can write the probability amplitude of a coherent excitation transfer between D and A as

$$M = \langle g_D, e_A | H_{int} | e_D, g_A \rangle , \tag{2.12}$$

where $g(e)_{D(A)}$ denotes the ground-state (excited-state) of the donor (acceptor) molecule. The dipole-dipole interaction Hamiltonian H_{int} couples the D and A transition dipole operators $\mathcal{D}_{D(A)}$ (1.9) via the cavity electric field operator $\mathcal{E}(z)$ (1.5), and is given by

$$H_{int} = -\mathcal{D}_D \cdot \mathcal{E}(z_D) - \mathcal{D}_A \cdot \mathcal{E}(z_A), \tag{2.13}$$

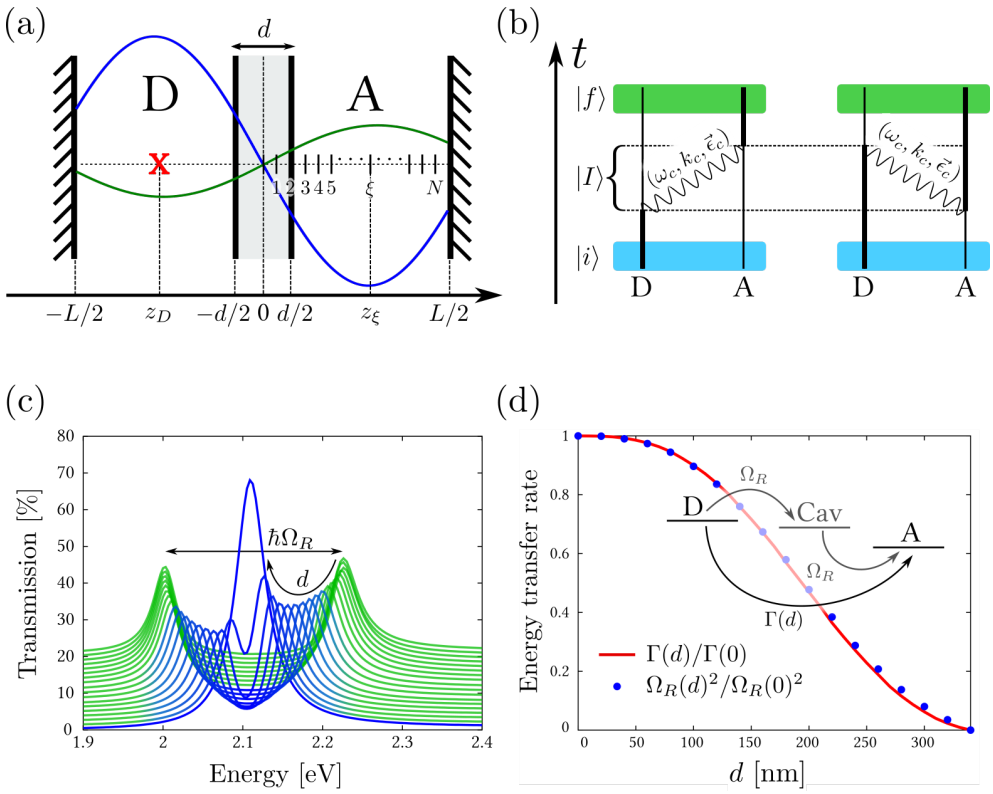

Figure 2.19 – (a) Schematic representation of the 2nd mode cavity of length L embedding the donor (D) and acceptor (A) molecules, separated by a dielectric spacer of thickness d. The initially excited D at position z_D can transfer its energy to any A molecule at position z_ξ. The blue (green) curve represents the real (imaginary) part of the electric field in the cavity as calculated by transfer matrix method. (b) Temporal picture of the dipole allowed energy transfer processes from an initial state $|i\rangle$ where D is excited and A is in the ground state, to a final state $|f\rangle$ where A is excited and D is in the ground state. Those processes involve an intermediate state $|I\rangle$ in which a cavity photon of frequency ω_c, wave-vector $\vec{k}_c$ and polarization, $\vec{\epsilon}_c$ is exchanged. (c) Calculated transmission spectrum of the cavity embedding the D and A molecules for different spacer thicknesses. (d) Energy transfer rate $\Gamma(d)$ as a function of spacer thickness, normalized to the energy transfer rate without spacer $\Gamma(0)$. The blue dots represent the normalized Rabi splitting squared, as extracted from panel (c). The scheme represents the energy transfer process involving two Rabi oscillations. Reproduced from reference [87].

where $z_{D(A)}$ is the position of the D (A) molecule along the optical z axis. At second order in the coupling, M reads

$$M = \sum_I \frac{\langle f|H_{int}|I\rangle\langle I|H_{int}|i\rangle}{E_i - E_I}, \tag{2.14}$$

where the initial state $|i\rangle = |e_D, g_A, 0_c\rangle$ of energy E_i and final state $|f\rangle = |g_D, e_A, 0_c\rangle$ are linked by all the possible intermediate states $|I\rangle$ of energy E_I. In this notation, $|0(1)_c\rangle$ indicates the number of photons occupying the cavity mode of energy $E_c = \hbar\omega_c$, wave-vector $\vec{k}_c$ and polarization $\vec{\epsilon}_c$. The key point of our approach is to impose in the summation over all states $|I\rangle$ that they respect the cavity dispersion relation $\omega_c(\vec{k})$. In particular, this single mode restriction suppresses the near field D-A energy transfer, as it should be the case due the presence of the dielectric spacer. In other words, the transfer of energy will be restricted to occur via 'on-shell' cavity photons. The two possible intermediate states for the energy transfer process are those represented in Fig. 2.19(b), and correspond to the rotating and counter-rotating contributions to the dipolar coupling Hamiltonian (1.12). Upon summation over those intermediate states, we obtain the following expression for the energy transfer probability amplitude

$$M = d_A d_D \frac{\hbar\omega_c}{2\epsilon_0 \mathcal{V}} \vec{\epsilon}_A^* \cdot \left[\vec{\epsilon}_c \cdot \vec{\epsilon}_D \cdot \vec{\epsilon}_c^* \frac{f(z_A) f^*(z_D)}{E_D - \hbar\omega_c} + \vec{\epsilon}_c^* \cdot \vec{\epsilon}_D \cdot \vec{\epsilon}_c \frac{f^*(z_A) f(z_D)}{-E_A - \hbar\omega_c} \right], \tag{2.15}$$

where, as in Chapter 1, $\mathcal{V}$ is the cavity mode volume, $f(z_{D(A)})$ is the field amplitude at the donor (acceptor) position, $\vec{\epsilon}_c$ is the polarization unit vector of the cavity mode, $\vec{\epsilon}_{D(A)}$ is the polarization unit vector of the transition dipole moment $d_{D(A)}$ of the donor (acceptor), $E_{D(A)}$ is the corresponding transition energy, and * indicates the complex conjugation. We note that this amplitude only depends on the light-matter coupling strength at the D and A positions in the field of the cavity and not on their relative distance as it would in the standard Förster theory.

Following our analogy with Förster mechanisms, we can express the net rate of energy transfer from an initially exited

donor to an assembly of ground states acceptors using Fermi golden rule

$$\Gamma(d) = \frac{2\pi}{\hbar}\rho \sum_{d/2<z_A<L/2} |M(z_A)|^2, \tag{2.16}$$

where ρ is the density of acceptor states. Of course, such a Fermi golden rule argument, imposing the net flow of energy from donor to acceptors, comes at odd with respect to the usual Rabi dynamics of strongly coupled systems. However, it can be taken as a rough way to account for the relaxational (non-Markovian) polariton dynamics that we investigated in the previous sections of this chapter.

In the language of strong coupling, this energy transfer process is thus achieved via two Rabi oscillations as sketched in Fig. 2.19(d). As the spacer thickness d increases, less and less molecules participate in the energy transfer process, while the Rabi splitting decreases accordingly (see Fig. 2.19(c)). We show in Fig. 2.19(d) that as expected, the calculated energy transfer rate $\Gamma(d)$ drops as the square of the Rabi frequency Ω_R, confirming this intuitive picture. Thus, as long as the strong coupling strength is preserved, this model predicts a constant polaritonic energy transfer rate regardless of the separation distance between donor and acceptor molecules. It should however be noted that sustaining a high coupling strength in large cavities can be problematic due to the increase in the cavity mode volume.

From our toy model, we can thus anticipate that this energy transfer process will be favored by using a high quantum yield (low k_{nr}) donor, and a low quantum yield (large k_{nr}) acceptor. In this situation, the vibronic sink of the acceptors would bias the otherwise reversible Rabi exchange, driving the energy transfer process in a similar way as thermal trapping of a product can displace the equilibrium of a reversible photochemical reaction [127]. The linewidth of the acceptors should however not become too large either as this might deteriorate the Rabi frequency and hence the energy transfer

rate. There must then exist an optimal energy transfer situation, for which the acceptor states are highly dissipative, while the Rabi exchange remains fast. Clearly, this situation does not corresponds to the ideal undamped strong coupling regime, in which no energy transfer would be observed.

In order to gain further insights into the mechanisms ruling polaritonic energy transfer, we are currently developing a more advanced model of such systems, in collaboration with D. Hagenmuller in G. Pupillo's group. This model, sketched in Fig. 2.20(a), relies on the explicit description of the vibronic manifolds of both the donor and acceptor molecules in a fermionic basis. As opposed to working in a (bosonized) excitonic picture, this approach allows for the independent tunning of scattering rates within the ground and excited states vibronic manifolds. We stress that the strength of this model lies in the fact that it is only concerned with fermions evolving in the uncoupled basis. In particular, no *ad hoc* exciton-to-polariton scattering rates are invoked.

In our model, a single cavity mode (shown in blue) is coherently coupled to two vibronic levels of both the donor (green) and acceptor (red) molecules. The energy levels of both molecules are labeled $|ij\rangle$, with $i = 1(2)$ for the donor (acceptor) and $j = 0(1,2)$ for the ground state (first, second excited states). The coupling frequency of each transition is correspondingly labeled Ω_{ij}. All frequencies will be given in units of the cavity mode frequency. The incoherent relaxation rates $\gamma_{nr1,2} = 0.01$ correspond to the vibrational relaxation within the donor and acceptor excited states manifolds. The cavity mode is incoherently pumped via a Lindblad term [128] at a rate $\gamma_p = 0.01$ and it decays at a rate $\kappa = 0.05$.

In view of mimicking the experimental situation of [86, 87], the $|10\rangle \rightarrow |11\rangle$ is strongly coupled, with $\Omega_{11} = 0.1$, giving rise in the dressed states basis to the two polaritonic states $|P^{\pm}\rangle$ shown in gray. The $|P^{-}\rangle$ state then comes close in energy of the $|22\rangle$ state, to which it can in turn couple provided that Ω_{22} is made large enough. Ω_{12} and Ω_{21} are always weakly coupled, both being equal to 0.01 in our units.

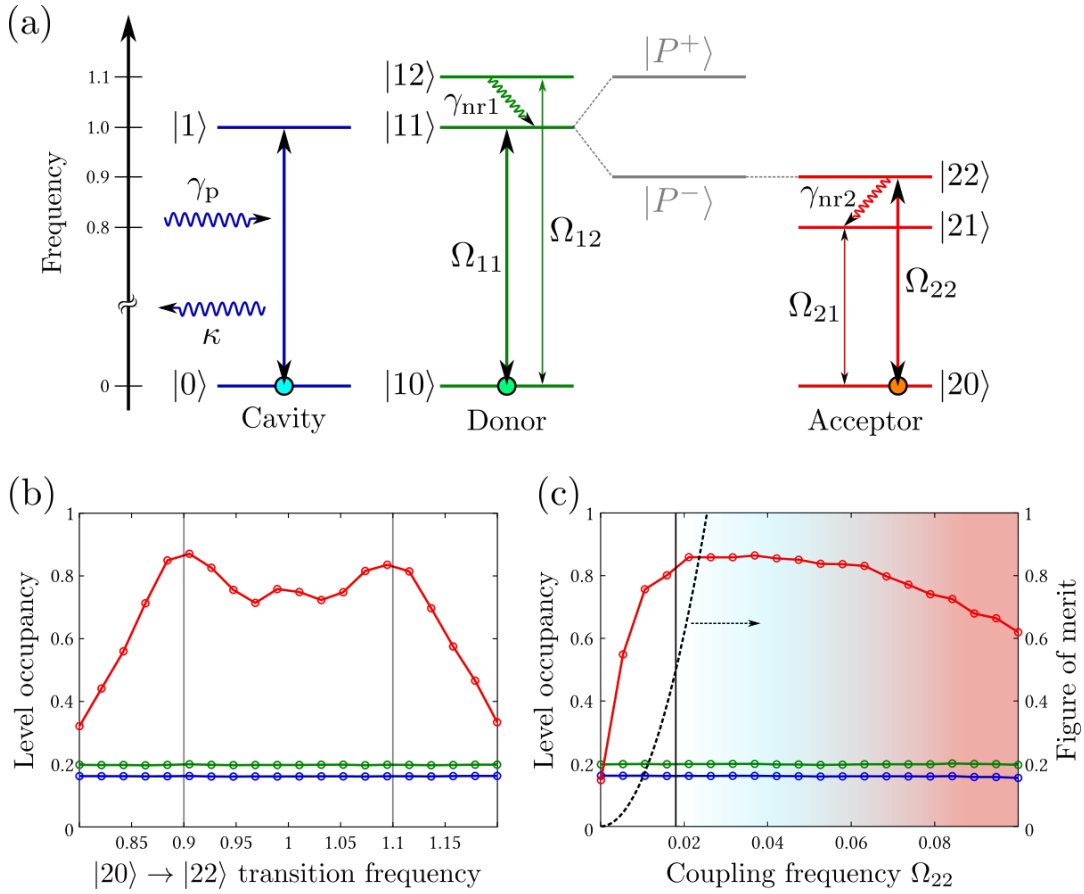

Figure 2.20 – (a) Schematic representation of the fermionic toy model of energy transfer under strong coupling (notations detailed in the main text). (b) Steady state occupancy of the cavity mode (blue), the donor $|11\rangle$ level (green) and the acceptor $|21\rangle$ level (red) as function of the $|20\rangle \rightarrow |22\rangle$ transition frequency, when $\Omega_{22} = 0.01$. (c) Steady state occupancy of the same states (same color code as in (b)) as a function of the coupling frequency Ω_{22}, and for a transition frequency $|20\rangle \rightarrow |22\rangle$ of 0.9. The black dashed curve is a figure of merit of strong coupling for the $|20\rangle \rightarrow |22\rangle$ transition (see main text), and it exceeds the threshold value of 0.5 at the position indicated by the vertical black line. All frequencies are given in units of the cavity mode frequency.

Starting from an initial ground state and letting γ_p drive the system incoherently, we apply a quantum trajectories algorithm [129, 130] to extract the steady state populations of the donor, acceptor and photon states, for various coupling parameters and different vibronic bath structures. This approach also allows us to compute two-times correlation functions in the steady state, directly related to emission spectra, as well as off-diagonal correlations between the different species.

Following our original idea of tailoring a dissipative bath at the $|P^-\rangle$ energy that would belong to an energy acceptor molecule, we plot in Fig. 2.20(b) the steady state populations of the donor, acceptor and cavity modes as a function of the acceptor detuning. Strikingly, we observe an increase in the $|22\rangle$ energy level occupancy when its energy matches that of either $|P^+\rangle$ or $|P^-\rangle$. Such resonances are a direct confirmation of our intuitive picture, and are here readily obtained in the most simplistic configuration of strongly coupled molecular energy transfer process. The slight increase in the acceptor population observed at a frequency of 1, equal to that of the donor, could be due to the participation of the acceptor in formation of a collective Dicke state with the donor.

In order to identify the most favorable conditions for energy transfer under light-matter strong coupling, we now keep the $|20\rangle \rightarrow |22\rangle$ transition at a frequency of 0.9, and vary its coupling frequency Ω_{22} to the cavity mode. As shown in Fig. 2.20(c), the energy transfer efficiency starts near zero for a weakly active transition before rising to an optimal efficiency near $\Omega_{22} = 0.02$, and then decreasing in the 'ideal' strong coupling limit. We also report on this graph (black dashed curve) a figure of merit of the strong coupling regime for the acceptor transition $(2\Omega_{22})^2/(\gamma_{nr2}^2 + \kappa^2)$, a quantity that exceeds 0.5 when strong coupling is reached [36]. Interestingly, the optimal energy transfer efficiency is reached just beyond this threshold (vertical black line), in the bad cavity limit of strong coupling. We will encounter again, in the last chapter of this thesis, a similarly optimal 'bad strong coupling condition' in the context of cavity protection effects.

2.3.3 *Conclusions*

In this section, we presented direct evidence of enhanced non-radiative energy transfer between two J-aggregated cyanine dyes strongly coupled to the vacuum field of a cavity. Excitation spectroscopy and femtosecond pump–probe measurements show that the energy transfer is highly efficient when both the donor and acceptor form light-matter hybrid states with the cavity vacuum field. The rate of energy transfer is increased by a factor of seven under those conditions as compared to the normal situation outside the cavity, with a corresponding effect on the energy transfer efficiency.

By spatially separating the donor and acceptor molecules inside the cavity, we demonstrated that polaritonic energy transfer can emerge in systems that would otherwise not exchange energy. Moreover, this energy transfer rate remains distant independent, provided that the donor-acceptor-cavity coupling strength is maintained.

Strongly coupled molecular systems thus offer a convenient way to try to mimic coherent photosynthetic light harvesting systems by providing a cascade of coherent extended hybrid light-matter states.

In the last section of this chapter, we investigate polaritonic signatures in the nonlinear response of strongly coupled systems. In particular, we report on their remarkable efficiency in generating second harmonic optical signals under femtosecond excitation.

2.4 SECOND HARMONIC GENERATION FROM POLARITONIC STATES

Second-harmonic generation (SHG) remains one of the most widely applied nonlinear optical (NLO) effects since its first observation over a half-century ago [131–134]. In particular, organic SHG active materials have attracted considerable attention due to the diverse choice of molecular ma-

terials and their efficient second-order NLO response [135]. Furthermore, the supramolecular self-assembly of these molecular systems offers opportunities for the construction of NLO materials with well defined architectures at the subwavelength scale, with potential applications in integrated photonic circuits [136]. However, photodegradation and harmonic reabsorption have so far limited their use in devices. Moreover, the effective translation of the molecular hyperpolarizabilities of the NLO dyes to the corresponding material susceptibilities remains a great challenge.

To date, studies on nonlinear optics involving exciton polaritonic states have focused on their third-order optical nonlinearity and the resulting polariton-polariton interactions [17]. However, the impact of light-matter strong coupling on SHG remains mostly unexplored. To our knowledge, resonant SHG signals from polariton states have only been studied in the context of 2p exciton generation for terahertz lasing devices with GaAs-based microcavities. In view of previously reported results on the modification of energy and populations dynamics in strongly coupled molecular materials, we undertook the investigation of potential polaritonic signatures in the second-order nonlinear response of NLO active dyes in cavities.

2.4.1 *Systems under study*

Here we study both the efficiency and wavelength dependence of the resonant SHG process [137, 138] from strongly coupled single crystalline nanofibers, self-assembled from chiral porphyrin molecules (c-Porphyrin, Fig. 2.21). To ensure the non-centrosymmetric molecular arrangement required for generating second order NLO signal, the model porphyrin molecule was functionalized with four chiral alkyl tails (namely the (S)-3,7-dimethyloctyl groups, Fig. 2.21(a)), and crystallized into nanofibers. The synthetic route to this compound, developed by X. Xu and coworkers in T. Rasing's group, is detailed in [139]. The crystalline nanofibers were obtained by dissolving 1 mg

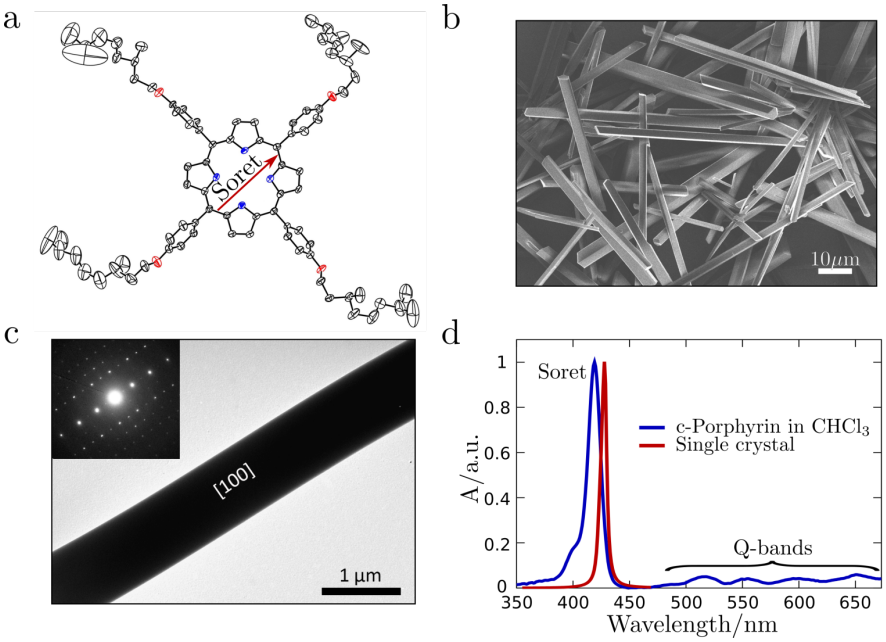

Figure 2.21 – (a) Oak Ridge Thermal Ellipsoid Plot (ORTEP) of the c-Porphyrin molecule at 50% ellipsoid probability. The red arrow indicates the orientation of a Soret band transition dipole moment. (b) SEM image of an ensemble of single crystal c-Porphyrin nanofibers. (c) Transmission electron microscope (TEM) image of a typical c-Porphyrin nanofiber and its corresponding selected area electron diffraction (SAED) patterns in inset. The fiber axis is identified to be along the crystallographic a-axis. (d) Absorbance spectrum of the c-Porphyrin dissolved in chloroform ($CHCl_3$, blue curve) and of the single crystal (red curve) as reconstructed from polarized reflectometric measurements. Reproduced from reference [139].

of c-Porphyrin in 10 mL of heptane under sonication at room temperature. Upon sudden cooling in a dry-ice/acetone bath and stabilization at -80°C for 1 h, the compound precipitated as nanofibers. The suspension with the as-prepared c-Porphyrin nanofibers was mixed with 50 mL of ethanol and was left aging for 1 h until it reached room temperature. The crystals were then transferred onto substrates by simply drop-casting the nanofiber suspensions.

As seen in the scanning electron microscope (SEM) image of Fig. 2.21(b), those fibers typically have thicknesses of hundreds of nanometers and lengths up to hundreds of micrometers. Selected area electron diffraction (SAED) patterns taken

from a typical fiber under a transmission electron microscope (TEM) clearly suggest its single crystalline nature with the fiber axis along the crystallographic a-axis (Fig. 2.21(c) and inset). Moreover, single crystal and powder X-ray diffraction (XRD, see details in [139]) of a as-grown crystals suggests that the c-Porphyrin molecules indeed crystallize with a non-centrosymmetric triclinic P1 space group, allowing for a potentially non-zero second order optical response [135].

When dissolved in chloroform ($CHCl_3$), c-Porphyrin shows a sharp and intense Soret absorption band (S_0 to S_2 transition) at 420 nm and a vibronic progression of Q-bands (S_0 to S_1 transitions) spanning the visible spectrum (Fig. 2.21(d), blue curve) [140]. The spectroscopic study of the nanofiber crystal phase is experimentally challenging due to the very high extinction coefficient of the Soret band, and the strong optical birefringence ($|n_e - n_o| = 0.2$) and dichroism of the crystal. To measure the single crystal absorption spectrum, we followed a reported procedure [141] consisting in refractive index reconstruction from polarized specular reflectance spectroscopy on a single crystal. By probing different polarization angles, we could selectively maximize the Soret or the Q-bands contributions to the absorption spectrum, in agreement with their relative orientation [140]. Throughout the rest of this study, we always fix the incident polarization of all beams to the angle that maximizes the Soret band absorption, which will be the targeted transition for strong coupling. The reconstructed absorption line shape shows a strong Soret band red-shifted to 430 nm, suggesting a J-type packing of the c-Porphyrin molecules, in agreement with the crystal XRD observations reported in [139].

The nanosized molecular crystals were then deposited on a glass substrate coated with a 30 nm thick Ag mirror. Sputtering another 50 nm mirror of Ag on top of the crystals led to the formation of FP cavities as the one shown in Fig. 2.22(a). In this way, a variety of FP cavities were obtained, each defined by the thickness of the embedded c-Porphyrin single crystal and further characterized optically under a microscope.

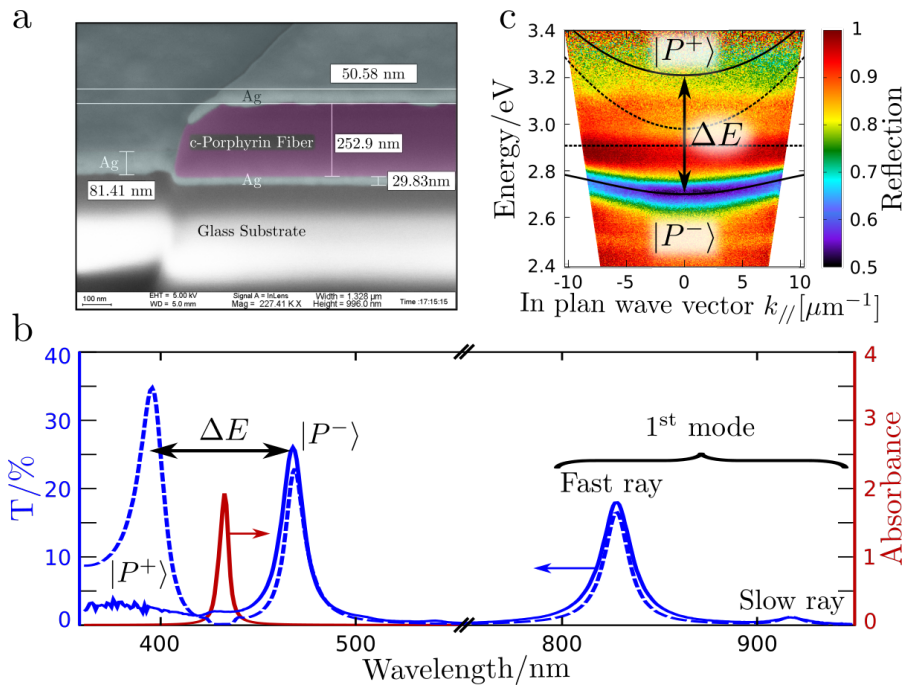

Figure 2.22 – (a) Scanning electron microscopy image of a cross-cut through the fiber cavity used for SHG measurements. The cut was made using focused ion beam lithography. (b) Absorbance spectrum of a bare crystal outside the cavity (red curve) and transmission spectrum of a 250 nm thick crystal in the FP cavity (blue curve) with its transfer matrix fit (dashed blue curve). The two modes in the near IR are the first cavity modes for the two refractive indices of the birefringent crystal. The ratio of their intensities is determined by the chosen polarization axis. The mode splitting between the two polaritonic states ΔE is *ca.* 510 meV. (c) Angle-resolved reflection spectrum of the FP cavity showing the dispersive behavior of the polaritonic states. The solid black curves are coupled oscillators fit to the polaritonic branches, and the dashed ones correspond to the uncoupled exciton and optical resonances. Reproduced from reference [139].

The transmission spectra were monitored in order to identify a suitable FP cavity with the signature of strong coupling of the Soret band. Fig. 2.22(b) compares the spectrum of a bare crystal (red curve) with that of a coupled system (blue curve) for the 250 nm thick fiber cavity shown in Fig. 2.22(a), displaying a mode splitting ΔE of *ca.* 510 meV. Transfer matrix calculations are in very good agreement with the measured spectrum (Fig. 2.22(b), blue dashed curve), except in the region below 420 nm where our microscope works very poorly due to a combination of low source power and antireflection coatings. Unfortunately, the microscopic size of the fiber cavity does not allow the use of a conventional large beam spectrophotometer to overcome this measurement problem.

The angle-resolved reflection spectrum of the cavity fiber of interest is shown in Fig. 2.22(c) clearly demonstrating the dispersive behavior of the lower polariton branch. By fitting the dispersion data to a coupled oscillators model (see *e.g.* (2.6)), we obtained a resonant Rabi splitting of 500 meV, amounting to 17% of the energy of the coupled Soret band. In this cavity, the Soret band was coupled to the second optical mode. As described below, this has the advantage that the first FP mode in the near infrared (NIR) can be used as a transparency window to pump the SHG process.

2.4.2 *SHG measurements*

A home built setup [136] was used for the investigation of the NLO properties of c-Porphyrin nanofibers inside and outside the cavities. A femtosecond laser (Spectra physics Mai Tai), with a pulse duration of 100 fs and a repetition rate of 82 MHz was used as the pump, with tunable wavelengths from 720 nm to 990 nm. The laser pulses were focused by a gradient index lens of 3 centimeters working distance onto a spot about 6µm diameter. The angle of incidence and detection could be tuned with a rotation stage. The samples were mounted on an automatic XY—scanning stage. The signal generated from the

microfibers was collected through a multimode fiber and sent to a monochromator (Princeton instruments), followed by a CCD detector to register the spectra, or by a lock-in amplified photomultiplier tube (PMT) to register the response at a particular wavelength. The detection part could be switched from CCD to PMT by using a flip-mirror. The pump laser was linearly polarized and its polarization angle was tuned by rotating a half-wave plate.

By exciting a single c-Porphyrin nanofiber crystal on an opaque silver substrate (no top mirror), with femto-second pulses at 840 nm, we observe an intense SHG peak at 420 nm (Fig. 2.23(a), spectrum indicated by the arrow). The quadratic dependence of this signal on the pump intensity (inset) and its sharp linewidth confirms that this signal originates from the second harmonic response of the crystal, and not from other NLO process such as two-photons absorption induced fluorescence. The SHG spectra recorded for different pumping wavelengths from 740 to 980 nm are shown in the same panel (a). Very importantly, the polarization of the incident laser with respect to the fiber orientation was again set to the angle that maximizes the Soret transition at the second harmonic wavelength. Under those conditions, the wavelength dependent profile of the SHG intensity $I_{2\omega}$ reproduces the Soret absorption band at 430 nm, which is a direct demonstration of the resonance enhanced SHG effect. Indeed, it can be shown (see *e.g.* [138]) that in the electric-dipole approximation, the non-linear polarizability tensor for a resonance of the second harmonic frequency with a transition from a ground state $|g\rangle$ to an excited state $|n\rangle$ of a molecule can be expressed as

$$\begin{aligned}\alpha^{(2)}_{ijk}(2\omega=\omega+\omega) &= \left(\alpha^{(2)}_{ijk}\right)_{NR} - \left(1/\pi\hbar^2\right)\tilde{\alpha}^{(1)}(2\omega)\,\langle g|p_i|n\rangle \\ &\quad\times\sum_{n'}\frac{\langle n|p_j|n'\rangle\langle n'|p_k|g\rangle + \langle n|p_k|n'\rangle\langle n'|p_j|g\rangle}{\omega-\omega_{n'g}},\end{aligned} \tag{2.17}$$

where $\left(\alpha^{(2)}_{ijk}\right)_{NR}$ is the non-resonant part of $\alpha^{(2)}_{ijk}$, $\langle n'|\vec{p}|n\rangle$ and $\omega_{n'n}$ denote, respectively, the dipole-matrix element and the

frequency of the $|n\rangle$ to $|n'\rangle$ transition, and $\tilde{\alpha}^{(1)}(2\omega)$ represents the linear polarizability of the molecule at 2ω. Since the SHG efficiency is proportional to $|\alpha^{(2)}_{ijk}(2\omega)|^2$, the measured spectrum $I_{2\omega}$ is expected to show resonant contributions from both the real and imaginary parts of $\tilde{\alpha}^{(1)}(2\omega)$.

Performing the wavelength-dependent SHG measurement under the same conditions for the c-Porphyrin nanofiber inside the FP cavity, and correcting for the cavity filtering function acting on the incident pump beam in the NIR (see Fig. 2.22(b) and discussion below), we obtain a very different intensity profile as shown in Fig. 2.23(b). Instead of reaching one maximum at 430 nm, the SHG intensity from the nanofiber in the cavity has two maxima at 390 and 455 nm (pump at 780 and 910 nm, respectively) corresponding to the resonant SHG from the polaritonic states. Interestingly, the SHG signal from $|P-\rangle$ is more than 5 times larger than that from $|P+\rangle$, even though the linear absorption spectrum (black dashed curve) shows a higher contribution from $|P+\rangle$. As shown in the inset, the measured signal grows quadratically with the pump intensity, confirming its second harmonic origin. Moreover, the polarization dependent SHG signal, shown in Fig. 2.23(c), follows a cosine fourth curve as expected for resonantly enhanced SHG.

By raster scanning the sample under a fixed pump wavelength (910 nm), we obtain the SHG intensity map shown in Fig. 2.23(d). It clearly outlines the structure of the resonant fiber cavity (red dashed rectangle), which gives a much higher SHG signal than the nearby non-resonant (thicker) cavity fibers imaged in the inset, showing that the SHG efficiency is strongly enhanced by the polaritonic states at resonance.

To better estimate the magnitude of this effect, we now compare the SHG efficiency of c-Porphyrin fibers inside and outside the cavity. A quantitative comparison between those two systems can only be made by accounting accurately for the filtering function $F_{exc}(\omega)$ acting on the pump in both cases. Moreover, the second harmonic field collection efficiency $F_{det}(2\omega)$ must also be precisely computed [142]. For a pump

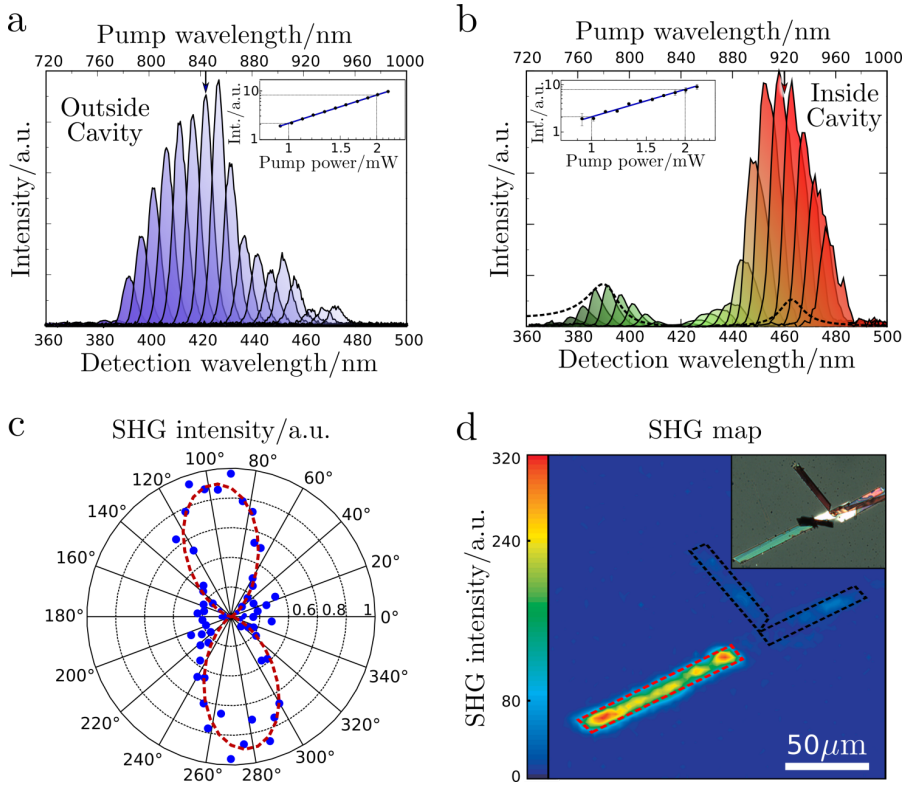

Figure 2.23 – SHG spectra measured at different pump wavelengths for a c-Porphyrin fiber outside (a) and inside (b) the cavity. The cavity data are normalized by the filtering function acting on the pump in the NIR (Fig. 2.22(b)). The color code is just a visual guide. The dashed curve is the transfer matrix fit to the linear transmission spectrum. The power dependence of the SHG intensity obtained at the wavelength indicated by the arrows in (a) and (b) are shown in insets (logarithmic plots, black dots) together with fits of slope 2.0 (blue lines). (c) Polar plot of the polarization dependent SHG signal from the fiber inside the cavity (blue) and its cosine fourth fit (red). (d) SHG intensity scan map ($200 \times 200\mu m^2$) of a region around the coupled fiber (red dashed rectangle) and nearby non-resonant fibers (black dashed rectangles). The inset shows the transmission image taken from the same area showing the two thicker fibers (purple in the transmission image) near the resonant fiber (bluish in transmission). Reproduced from reference [139].

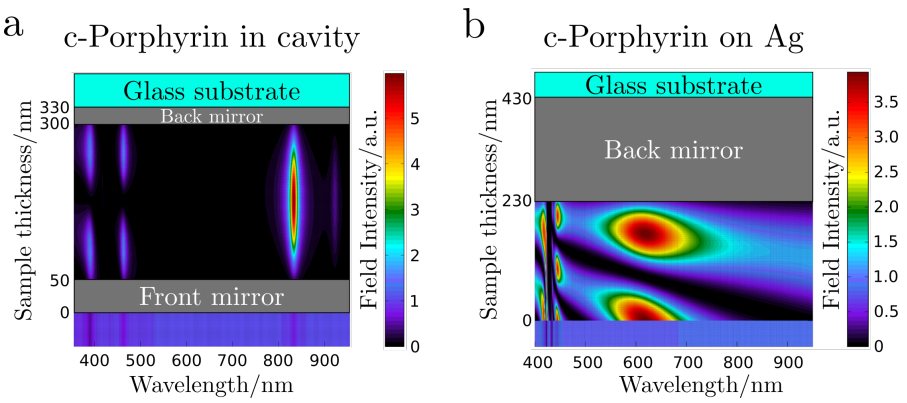

Figure 2.24 – Transfer matrix calculation of the electric field intensity distribution inside (a) and outside (b) the cavity as a function of wavelength. Reproduced from reference [139].

intensity I_ω, the measured second harmonic intensity can be written in the electric-dipole approximation as

$$I_{2\omega} = (F_{exc}(\omega)I_\omega)^2 J(2\omega = \omega + \omega)F_{det}(2\omega), \tag{2.18}$$

where $J(2\omega = \omega + \omega)$ contains the square of the second order nonlinear polarizability tensor of the material $|\alpha^{(2)}_{ijk}(2\omega)|^2$.

The transfer matrix calculation of the electric field intensity profiles in the cavity and in the bare crystal as a function of wavelength are shown in Fig. 2.24. These intensity profiles are obtained by propagating incident fields of given frequencies and of normalized intensities through the multilayered structure using discrete propagators. The average intensity in the active layer thus directly yields the excitation filtering factors F_{exc} inside (0.47 a.u.) and outside (1.2 a.u.) the cavity at the resonant pumping wavelengths (910 nm and 860 nm, respectively).

To obtain the SHG filtering factors F_{det} inside and outside the cavity, we follow the derivation made in [142]. It amounts to solving the FP multiple reflection problem for a field at the second harmonic (SH) wavelength generated in the active layer by the pump beam. Since the cavity is not resonant at the pump frequency, the intracavity pump field does not build up (hence the excitation filtering factor of only 0.47 a.u.), and the SH field can be assumed to be generated by a single pass of

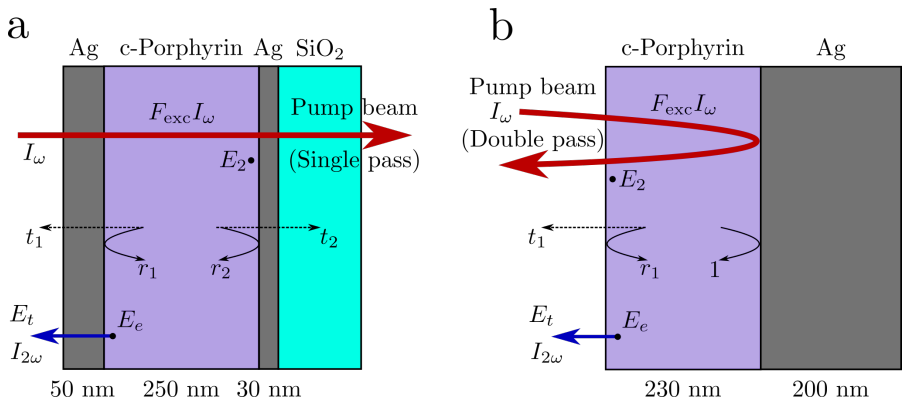

Figure 2.25 – (a) Schematic representation of the c-Porphyrin in a cavity with the multiple reflections of the second harmonic (SH) field. The SH field E_2 is generated along the pass of the pump beam (red arrow) and is reflected on the first (second) mirror with a coefficient $\sqrt{r_{1(2)}}$ and transmitted through the first (second) mirror with a coefficient $\sqrt{t_{1(2)}}$. These FP interference build up the intracavity SH field E_e. The SH intensity $I_{2\omega}$ transmitted outside the cavity is indicated by a blue arrow. (b) Corresponding scheme for the case of c-Porphyrin on opaque Ag. Reproduced from reference [139].

the pump (Fig. 2.25(a)). In the case of c-Porphyrin on opaque silver, outside the cavity, the double pass of the pump through the active layer has to be accounted for (Fig. 2.25(b)).

Defining E_e as the complex harmonic electric field in the active layer, at the exit surface of the crystal, we can write the transmitted SH intensity as

$$I_{2\omega} = |E_t|^2 = n t_2 |E_e|^2, \tag{2.19}$$

where n is the refractive index of the crystal at the SH frequency, and t_2 is the power transmission coefficient, as defined in Fig. 2.25. The SH field E_e is given by the self-consistency equation

$$E_e = E_2 \sqrt{r_2} e^{-\alpha_2/2} + E_e \sqrt{r_1 r_2} e^{-\alpha_2} e^{i\phi}, \tag{2.20}$$

where $r_{1(2)}$ is the power reflection coefficient, as defined in Fig. 2.25, α_2 is the single pass power absorption coefficient at the SH frequency, ϕ is the SH round-trip phase accumulation

and E_2 is the SH field generated along the pass of the fundamental beam, as obtain by integrating

$$\frac{dE_2}{dz} = i\, J F_{exc} I_\omega, \tag{2.21}$$

along the fundamental beam propagation length. The perfect phase matching condition assumed here is justified by the sub-wavelength thickness of the active layer, and the low finesse of the FP cavity. Solving (2.20) for E_e and injecting into (2.19), we obtain a relation between the measurable SH intensity exiting the system $I(2\omega)$ and the *in situ* SHG efficiency J inside and outside the cavity, where all the parameters can be straightforwardly computed from the transfer matrix simulations.

Using the measured SH intensities from the cavity and bare fiber samples, we obtain a polaritonic SHG efficiency J_{cav} two orders of magnitude larger than the bare fiber efficiency $J_{non\text{-}cav}$, confirming what is qualitatively seen in Fig. 2.23(d).

2.4.3 *Conclusions*

Remarkably, the enhanced polaritonic SHG efficiency that we measured must stem from a genuine modification of the polaritonic states hyperpolarizability since both the pump and the harmonic field filtering factors have been corrected for. Comparable polaritonic enhancement of the molecular susceptibility has recently been reported for the Raman scattering efficiency in the context of vibrational strong coupling (VSC), a regime that we will investigate in the next chapter. There, it was argued that the enhancement effect could originate either from the macroscopic coherence that is established in the molecular ensemble by its interaction with a common cavity mode [143, 144], or alternatively from the modification of the nonlinear response at the single molecule level. Even though the energy scales in VSC are reduced by an order of magnitude as compared to electronic strong coupling, the same arguments are indeed also applicable here. In particular, it is striking

that for comparable relative coupling strengths, both systems exhibit polaritonic enhancement effects of similar magnitudes. Moreover, in both systems the signal at $|P-\rangle$ dominates over that of $|P+\rangle$.

This proof of principle that SHG is enhanced for lower exciton polaritons opens the door for further studies on the use of strongly coupled systems for NLO of organic materials. The system design needs to be optimized, in particular by using different electromagnetic resonators such as distributed Bragg reflectors, or plasmonic structures which could also be resonant at the pump wavelength. Such structures are however more demanding to design as the molecules must be properly aligned with respect to the polarization of the field. Nevertheless these results indicate that the potential is worth the challenge and could lead to highly efficient NLO organic devices.

3

VIBRATIONAL LIGHT-MATTER STRONG COUPLING

In view of the fascinating possibilities offered by electronic strong coupling for modifying the excited states properties of complex systems, achieving similar behaviors within the electronic ground state manifold - *i.e.* strong coupling a vibrational transitions (VSC) [22, 145–151]- would be a key step toward new material science and chemistry under light-matter strong coupling. Indeed, since most chemical reactions occur through the vibrational manifold of the electronic ground state, strong coupling an ensemble of molecular vibrations to a common cavity mode should have immediate consequences for chemical reactivity, catalysis, site-selective reactions and biochemistry. The idea of a chemistry under collective vibrational light-matter strong coupling is currently emerging as a new interdisciplinary frontier of science, and the first experimental demonstration has recently been reported by our group in the context of the deprotection reaction of a simple alkynylsilane [15]. Further extensions of VSC toward biochemical systems are also being explored [152].

Due to their relatively high oscillation frequencies ω_v, and the tiny mass of the atoms involved, molecular vibrations also constitute ideal systems for cavity QED experiments. Indeed, with room temperature thermal occupancy factors $n_v \sim e^{-\hbar\omega_v/k_B T} \sim 10^{-4}$, they can safely be approximated by assemblies of two level systems in their quantum ground states, a hurdle to achieve in microfabricated optomechanical systems [153, 154].

In this chapter, we explore different aspects of this recently demonstrated regime of VSC [22]. In particular, we show that such systems can enter the regime of ultra-strong coupling, with a Rabi splitting reaching 24% of the vibrational transition frequency. We also demonstrate polaritonic IR emission under thermal excitation. Ongoing experiments on the modification of chemical reaction pathways, protein folding and superconducting phase transitions will not be covered here. Large parts of the first section are taken from already published work [155].

3.1 MULTIPLE RABI SPLITTINGS UNDER ULTRASTRONG VIBRATIONAL COUPLING

When the light-matter coupling strength approaches the energy of the coupled transition, the rotating wave approximation made in the Hamiltonian (1.14) of Chapter 1 breaks down, and one has to keep the anti-resonant and quadratic terms stemming from the full light-matter dipolar Hamiltonian. This ultra-strong coupling regime (USC) recently, predicted [67] and observed [68, 156], yields new fascinating effects such as dynamical Casimir effect [157, 158], superradiance phase transition [159, 160], enhanced light emission [161–163] and modified photon blockade [164].

In this section, we demonstrate that USC can also be reached, at room temperature, with ground-state molecular vibrations coupled to FP modes in the IR. Inherent features of the USC regime, antiresonant and self-energy contributions to the coupling, are measured on vibrational polaritonic states. Moreover, the concurrence of very large Rabi splitting and small cavity free spectral range leads to the formation of a ladder of ultra-strongly coupled levels. These results reveal totally different dynamics than the one previously reported under vibrational strong coupling [22].

3.1.1 *System under study*

To reach this vibrational USC regime, we exploit unique features of molecular liquids with a high vibrational dipolar strength. At room temperature, such liquids resemble assemblies of ground-state mechanical oscillators where one is able to reach dipolar strength densities far beyond the quenching densities in the solid phase. These combined features naturally set the conditions for collective coupling strengths up to the USC regime.

Our system consists of a microfluidic FP flow cell which can be filled with any given molecular liquid. It is made of two zinc selenide (ZnSe) windows coated with 13 nm thick Au layers to form the FP mirrors, and closing them with a Mylar spacer of the appropriate thickness produces a microcavity with IR modes of quality factors $Q \simeq 50$ [146]. By varying the spacer thickness, one of the optical modes is brought into resonance with the targeted molecular vibration. Different concentrations of molecules are injected in the cell, and the system is spectroscopically characterized using a commercial Fourier transform IR spectrophotometer (FTIR, Nicolet-6700).

The molecule chosen for this study is the iron pentacarbonyl $Fe(CO)_5$, a molecular liquid at room temperature. $Fe(CO)_5$ liquid has a very strong oscillator strength with three equatorial and two axial CO-stretching degenerate modes having a fundamental frequency ω_v corresponding to a spectroscopic wave number of *ca.* 2000 cm^{-1} [165]. The IR absorption band of a dilute $Fe(CO)_5$ solution (10 wt.% in toluene) is shown in Fig. 3.1(a). We inject the same solution into a FP cavity tuned to have its fourth-order longitudinal mode resonant with the CO-stretching band. This resonant coupling splits the fundamental vibrational mode into an upper and lower mode separated by $\hbar\Omega_{10\%} \simeq 135$ cm^{-1} (Fig. 3.1(c)).

Injecting the pure $Fe(CO)_5$ liquid in the cavity under the same resonant conditions expectedly leads to an increase in the mode splitting, reaching $\hbar\Omega_{100\%} \simeq 480$ cm^{-1}, as shown in the last column of Fig. 3.2. In these conditions, the vibra-

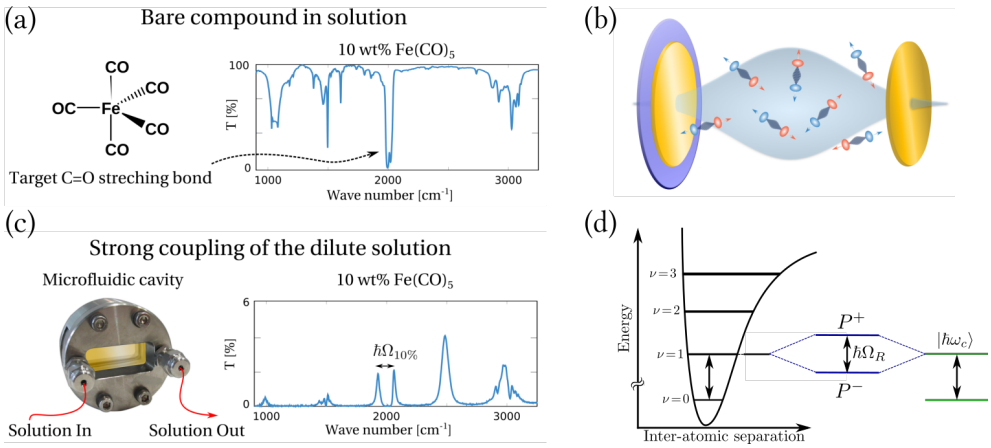

Figure 3.1 – (a) IR transmission spectrum of a dilute solution of iron pentacarbonyl $Fe(CO)_5$ (10 wt.% in toluene) showing a strong CO-stretching mode at *ca.* 2000 cm^{-1}. This solution can be injected in the resonantly tuned microfluidic IR cavity (sketch in (b)) to yield a vacuum Rabi splitting $\hbar\Omega_{10\%}$, as shown in the cavity transmission spectrum (c). (d) Schematic energy level diagram of the formation of upper and lower vibro-polaritonic states in the electronic ground state manifold. Adapted from reference [155].

tional spectrum of the coupled $Fe(CO)_5$ liquid also displays a series of sharp resonances that, as we explain below, stem from the coupling of the CO-stretching band with successive longitudinal modes of the FP cavity. This multimode splitting theoretically predicted by Meiser and Meystre [166] is similar to that reported in the case of electronic strong coupling [167, 168].

3.1.2 *Vibrational multimode coupling*

In order to understand the multipeaked structure of the spectrum, we first perform transfer matrix simulations. As already mentioned in the previous chapters, this technique amounts to solving the classical problem of a multi-layered stack of dispersive media in terms of forward and backward propagating electric field amplitudes. Thus for a given system to simulate, one needs to know the complex refractive indices and the thicknesses of each of the layers.

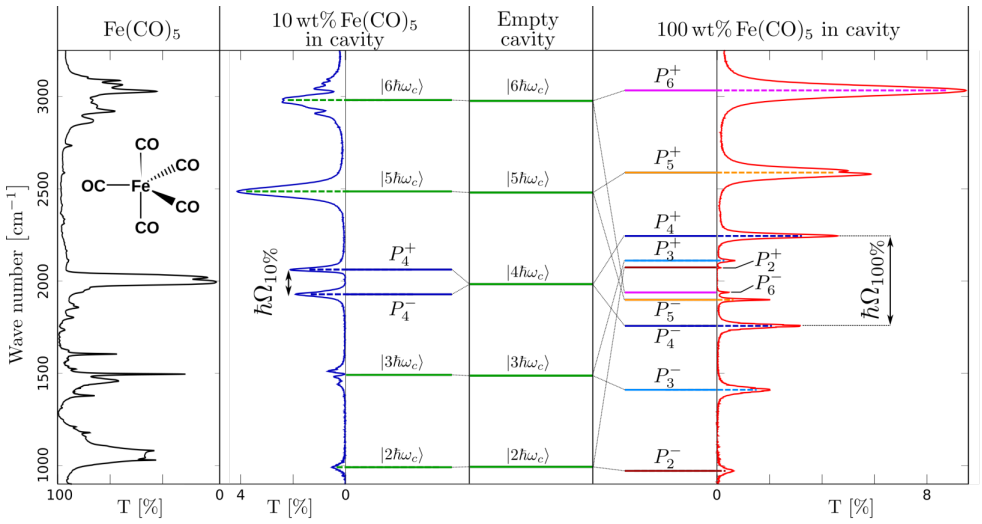

Figure 3.2 – $Fe(CO)_5$ data are shown in columns for clarity, starting with the IR spectrum of 10 wt.% $Fe(CO)_5$ in toluene, the transmission spectrum of the FP cavity filled with the same solution (blue curve) with a Rabi splitting $\hbar\Omega_{10\%} \simeq 135$ cm^{-1}, followed by the mode diagram of the system under the corresponding coupling. The middle column shows the bare cavity modes with, on the right-hand side, the coupled diagram of the multiple polaritonic states when the cavity is filled with 100 wt.% $Fe(CO)_5$. The last column on the right shows the corresponding experimental IR spectrum of the filled cavity with a resonant Rabi splitting $\hbar\Omega_{100\%} \simeq 480\,cm^{-1}$. Reproduced from reference [155].

We first measure the IR transmission spectrum of the dilute $Fe(CO)_5$ solution (10 wt.% in toluene) injected in a barium fluoride BaF_2 flow cell. BaF_2 windows were preferred to ZnSe for this experiment as their lower refractive index minimizes FP modulations on the flow cell transmission spectrum. We recover in the transmission spectrum of Fig. 3.3(a) the strong, inhomogeneously broadened, absorption peak at 2000 cm^{-1} of $Fe(CO)_5$. In order to model the complex refractive index of $Fe(CO)_5$, we fit this transmission spectrum to the transfer matrix result for a flow cell containing a medium of complex multi-Lorentzian refractive index:

$$\tilde{n}(k) = \sqrt{n_b^2 - \sum_{j=1}^{N} \mathcal{L}(f_j, k_{0j}, \Gamma_j)}, \tag{3.1}$$

where n_b is a background refractive index, and $\mathcal{L}(f_j, k_{0j}, \Gamma_j) = f_j/(k^2 - k_{0j}^2 + ik\Gamma_j)$, with f_j the oscillator strength, k_{oj} the resonance wave vector and Γ_j a phenomenological damping constant. It should be noted that no specific meaning can be attributed to these individual Lorentzians since the only criterion here is to reproduce accurately the flow cell transmission spectrum. A good fit to the measured spectrum is obtained using 7 Lorentzians as shown in Fig. 3.3(a). In this fitting process, the length of the BaF_2 cell is also left a free parameter. Moreover, the calculations are performed assuming semi-infinite BaF_2 cell windows, their actual thickness being ~ 3 mm (see Fig. 3.3(b)). Corrections for the front air/BaF_2 and rear BaF_2/air interfaces are applied, based on the bare BaF_2 window transmission spectrum. The resulting fitted parameters are reported in Table 3.1.

We now use the fitted refractive index of $Fe(CO)_5$ to model the transmission spectrum of the ZnSe cavity flow cell, again using the transfer matrix method. The cavity Au mirrors are 13 nm thick as fixed by the sputtering parameters and their refractive indices are modelled by a Drude-Lorenz equation with an additional damping correction originating from the thickness confinement of the conduction electrons [22, 169]. This time the

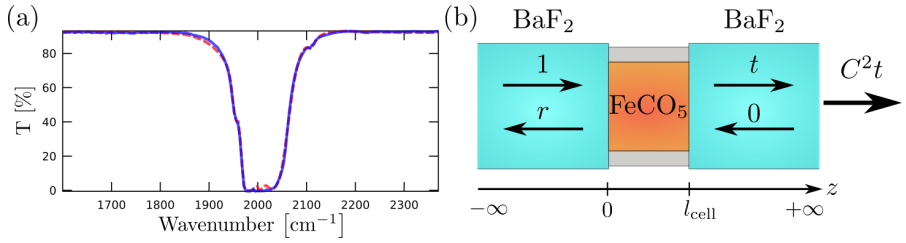

Figure 3.3 – (a) Measured transmission spectrum of the BaF_2 flow cell filled with $Fe(CO)_5$ (solide blue curve) compared to its transfer matrix fit (dashed red curve). (b) Schematic representation of the modelled flow cell of thickness l_{cell} for transfer matrix calculations. The gray rectangles represent the Mylar spacer separating the cell windows. The incident field to the left of the structure has an amplitude of 1. By definition, the reflected field has an amplitude r while the field propagating to the right of the structure has an amplitude t. The transmitted field outside the flow cell has an amplitude C^2t, where C is the transmission coefficient of a bare BaF_2 window measured at the considered wave vector. Reproduced from reference [155].

l_{cell}	n_b	f_1	k_{01}	Γ_1	f_2	k_{02}	Γ_2	f_3	k_{03}	Γ_3	f_4
2.00	1.46	3.02	1.98	5.31	0.69	2.02	22.2	0.16	1.95	15.4	0.70
k_{04}	Γ_4	f_5	k_{05}	Γ_5	f_6	k_{06}	Γ_6	f_7	k_{07}	Γ_7	
1.99	41.6	0.36	2.00	9.43	0.01	2.10	20.0	4.32	19.8	$4.17 \cdot 10^4$	

Table 3.1 – Fitted parameters for the transmission spectrum of the BaF_2 flow cell filled with $Fe(CO)_5$. Cell length l_{cell} in µm, oscillator strengths f_j in $10^5\,cm^{-2}$, resonant wave vectors k_{0j} in $10^3\,cm^{-1}$, phenomenological damping constants Γ_j in cm^{-1}.

only adjustable parameter is the exact cavity length l, starting from a value of $6\,\mu m$ given by the manufacturer of the Mylar spacer. A very good fit is obtained for a thickness $l = 6.850\,\mu m$, resulting in the spectrum shown in Fig. 3.4(a, black curve).

The free spectral range (FSR) of the fitted cavity transmission spectrum, as determined by the peak-to-peak spacing in a non-dispersive spectral region (*e.g.* $5000 - 7000\,cm^{-1}$), is $\Delta\nu = 492\,cm^{-1}$. We note that this FSR is *not* directly related to the cavity length by the usual formula FSR $= 1/2n_b l$ because of the finite skin-depth of the Au cavity mirrors. Indeed, using this expression and the value of the FSR, we would expect a cavity thickness $\tilde{l} = 6.932\,\mu m$. The over-estimation factor with respect to the actual cavity thickness is $\alpha = \tilde{l}/l = 1.012$. This factor only depends on the refractive indices of the Au/$Fe(CO)_5$ interface and on the Au mirror thickness. Thus, we will use it to correct the relationship between FSR and cavity thickness in what follows: $\Delta\nu = 1/2\alpha n_b l$.

Using the parameter obtained from the transmission fit, we calculate in Fig. 3.4(b) the electric field distribution inside the cavity. As can be seen from the field distributions, the CO-stretching mode of $Fe(CO)_5$ resonantly coupled to the 4^{th} mode of the FP cavity gives rise to an upper and a lower mode, at $2245\,cm^{-1}$ and $1756\,cm^{-1}$ respectively. The other four new resonances on either sides of the fundamental CO-stretching mode are at $2110, 2071, 1938, 1898\,cm^{-1}$ (the other peaks outside this spectral window can be seen in Fig. 3.2). The nodes and antinodes of the field distribution allow us to identify the modes at higher energy as originating from the coupling between the vibrational band and lower optical modes of the cavity and vice versa for the modes at lower energy, as sketched in the energy diagram of Fig. 3.2.

The positions of these modes is directly given by computing the round trip phase accumulation $\delta\phi = 2l\omega n/c + 2\phi_r = 2\alpha l\omega n/c$ for the electromagnetic field in the cavity, where ω is the vacuum frequency of light, c is the speed of light, n is real part of the refractive index of the intracavity medium and ϕ_r is the reflection phase due to the finite metal skin depth

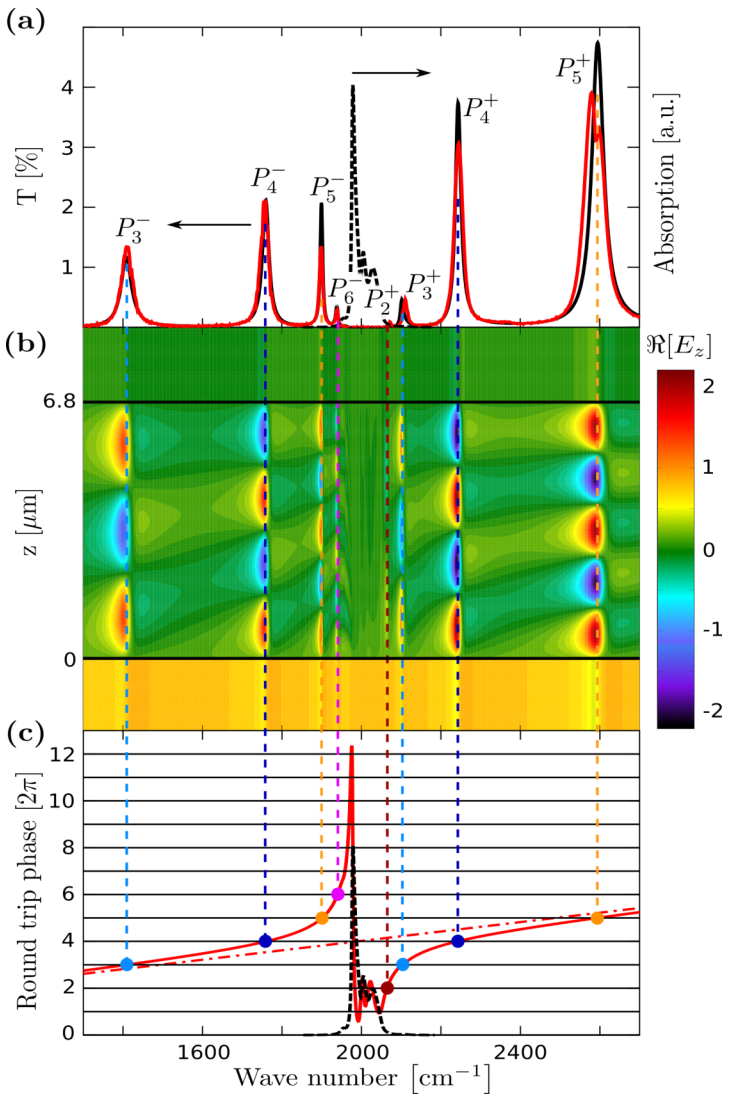

Figure 3.4 – (a) Experimental (red line) and transfer matrix simulated (black line) IR transmission spectra of pure $Fe(CO)_5$ coupled to the 4^{th} mode of a flow cell FP cavity. The black dashed curve is the simulated absorbance of the CO-stretching mode of pure $Fe(CO)_5$. (b) Transfer matrix simulation of the electric field distribution inside the FP cavity. Asymmetric field distribution on either side of the vibrational band is an indication of higher and lower mode folding effects due to strongly dispersive refractive index. (c) Round trip phase accumulation of the electromagnetic field in the cavity with (red curve) and without (red dashed line) absorber. Optical resonances occur for phase accumulation equal to integer multiples of 2π (horizontal black lines). The dispersion of the refractive index of the intra-cavity medium allows multiple solutions for various mode indices (vertical dashed lines, same color code as in Fig. 3.2). The fitted absorption lineshape of $Fe(CO)_5$ is also shown in black dashed curve. The resonances lying in the strong absorption region are over damped solutions and do not appear in the transmission spectra. Reproduced from reference [155].

[61]. As shown in Fig. 3.4(c), the refractive index of the pure molecular liquid disperses so strongly that optical modes of different m^{th}-orders can satisfy simultaneously the resonant phase condition $\delta\phi = 2\pi m$, with two solutions P_m^+, P_m^- for each mode m. The observed resonances ladder is characterized by very large multi-mode splittings, with $\Omega_{100\%}$ reaching *ca.* 24% of the vibrational mode frequency. Such a high relative coupling strength is often encountered in USC systems, and in order to confirm that our molecular liquid has indeed entered this regime, we now show that the spectral structure of the coupled vibrational ladder *cannot* be described outside the framework of ultra-strong light-matter interaction.

3.1.3 *Signatures of multimode vibrational USC*

The involvement of specific features of the USC regime can be revealed most directly at the level of polaritonic dispersion diagrams. We have measured the dispersions of our coupled vibrational modes as a function of the cavity thickness (*i.e.* as a function of cavity detuning). This is done by varying the cavity thickness around a value determined by the spacer inserted in our flow cell cavity. The results are gathered in Fig. 3.5. Using a thicker spacer of *ca.* 12.5 µm, we obtain asymptotic positions of the coupled modes. These experimental data are now compared to vibro-polariton models in the strong and ultra-strong coupling regimes, showing that only the later accurately fits these dispersion data. We emphasize that in the two models, the only free parameter is the Rabi splitting $\hbar\Omega_R$.

3.1.3.1 *Collective vibrational coupling: a model for ultra-strongly coupled oscillators*

We describe our molecular liquid as an ensemble of N individual ground-state mechanical oscillators to each of which is associated a localized vibrational dipole $\vec{p}_i$. This yields an effective density of polarization $\vec{P}(\vec{r}) = \sum_{i=1}^{N} \vec{p}_i \delta(\vec{r})$ which corresponds to a collective dipole $\vec{P}(\vec{0}) = \sum_{i=1}^{N} \vec{p}_i$ localized

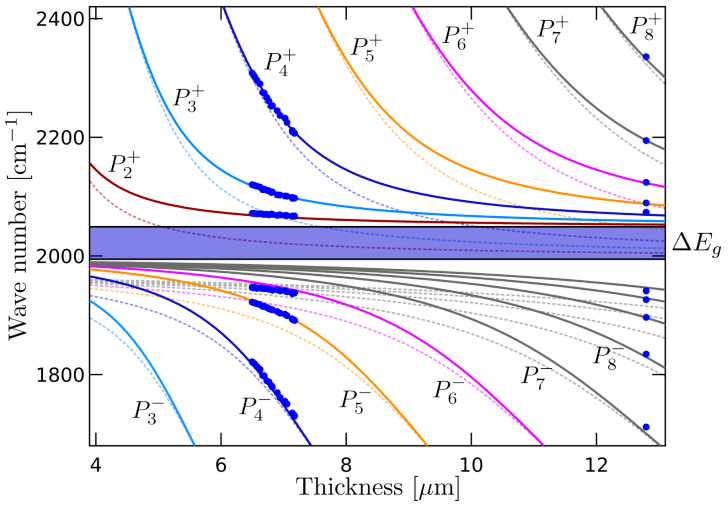

Figure 3.5 – Polaritonic dispersion diagram as a function of the cavity thickness. Experiental transmission peaks positions are reported as blue dots. The exact cavity thickness is determined from the free spectral range of the cavity by using the correction factor α. The solid curves are the best fit to the data using the full (non-RWA) Hamiltonian model, while the dashed curves are solutions of the RWA model. Same color code as in Fig. 3.2. The vibrational polaritonic bandgap ΔE_g only appears in the full Hamiltonian model. Reproduced from reference [155].

on $\vec{r} = \vec{0}$. This collective dipole is coupled to the electric displacement $\vec{D}(\vec{r})$ of a single m^{th}-order longitudinal cavity mode of volume $\mathcal{V}$. A natural framework to describe this effective dipolar coupling is to write the usual minimal coupling Hamiltonian in the '$\vec{D}\cdot\vec{P}$' representation. This can be done by a Göppert-Mayer transformation [68, 170, 171] which, neglecting the inhomogeneity of the cavity mode profile, yields the full dipolar Hamiltonian

$$\mathcal{H} = \mathcal{H}_{cav}^{m} + \mathcal{H}_{vib} - \frac{1}{\epsilon_0}\vec{D}(\vec{0})\cdot\vec{P}(\vec{0}) + \frac{1}{2\epsilon_0\mathcal{V}_v}\vec{P}(\vec{0})^2 \tag{3.2}$$

where $\mathcal{V}_v$ corresponds to the intra-cavity volume occupied by the molecules. The $\vec{P}^2$ term appearing in this expression results from the Göppert-Mayer transformation of the transverse field energy. In our representation, it corresponds to a polarization self-energy, renormalizing the dipole energy by its own radiated field. As we show below, this term usually neglected in light-matter coupling models will play a key role in the ultra-strong coupling regime.

With a background refractive index n inside the cavity of length l, the dispersion of the m^{th}-order mode writes as

$$\omega_c^m = \frac{c}{n}\sqrt{\left(\frac{m\pi}{l}\right)^2 + \left|\vec{k}_{\parallel}\right|^2} \tag{3.3}$$

and is therefore parametrized by the conserved in-plane component $\vec{k}_{\parallel}$ of the light wavevector. This leads to define the cavity field Hamiltonian:

$$\mathcal{H}_{cav}^{m} = \frac{1}{4}\hbar\omega_c^m\left(Q_c^2 + P_c^2\right) \tag{3.4}$$

where the optical position Q_c and momentum P_c quadratures are introduced, built from the $a(a^\dagger)$ annihilation (creation) photon operators as

$$\begin{pmatrix} Q_c \\ P_c \end{pmatrix} = \begin{pmatrix} 1 & 1 \\ -i & i \end{pmatrix}\begin{pmatrix} a \\ a^\dagger \end{pmatrix}, \tag{3.5}$$

with $[Q_c, P_c] = 2i$ considering that $[a, a^\dagger] = 1$.

Putting aside the rotational excitations which are not resolved in our experiment, the Born-Oppenheimer (BO) approximation enables us to separate the electronic and vibrational intra-molecular modes. We can thus consider that the vibrational dipole associated with each of the CO-stretching mode i of one $Fe(CO)_5$ molecule is merely defined from the dependence of the dipole moment $\langle\vec{p}\rangle_e(Q)_i$ on nuclear coordinates Q within the electronic state e considered. The BO approximation also insures that the vibrational dynamics is performed within the same electronic quantum state -in our case, the electronic ground state of $Fe(CO)_5$. Within this approximation, each of the N molecular vibrations are treated in the harmonic approximation [22] and we thus define the collective vibrational Hamiltonian as

$$\mathcal{H}_{vib} = \frac{1}{4}\sum_{i=1}^{N} \hbar\omega_{\nu,i}\left(Q_{\nu,i}^2 + P_{\nu,i}^2\right) \tag{3.6}$$

with ω_ν^i the vibrational transition associated with a single oscillator and

$$\begin{pmatrix} Q_{\nu,i} \\ P_{\nu,i} \end{pmatrix} = \begin{pmatrix} 1 & 1 \\ -i & i \end{pmatrix}\begin{pmatrix} b_i \\ b_i^\dagger \end{pmatrix}, \tag{3.7}$$

the vibrational position and momentum quadratures related to the $b_i(b_i^\dagger)$ annihilation (creation) operators of the vibrational mode of the i^{th} molecule. The commutators simply write as $[b_i, b_j^\dagger] = \delta_{i,j}$ and $[Q_{\nu,i}, P_{\nu,j}] = 2i\delta_{i,j}$.

At room temperature, one only retains low vibrational excitation levels so that the vibrational dipole moment is given by a first-order expansion on the nuclear coordinates

$$\langle\vec{p}\rangle(Q)_i = \langle\vec{p}_i\rangle_0 + \left(\frac{\partial\langle\vec{p}\rangle}{\partial Q_i}\right)_0 \cdot Q_i \tag{3.8}$$

This expansion is taken with respect to the equilibrium nuclear configuration (indicated by the subscript 0) in the harmonic mean potential of the electronic ground state of the $Fe(CO)_5$ molecule. The first term corresponds to the static dipole mo-

ment of the molecule at this equilibrium nuclear position. This static term cancels out due to the D_{3h} point group symmetry of the $Fe(CO)_5$ molecule.

The nuclear coordinate associated with the harmonic molecular vibration is described in our model by a position quadrature operator

$$\mathcal{Q}_i = \sqrt{\frac{\hbar}{2\mu_i\omega_{v,i}}}Q_{v,i} \tag{3.9}$$

where μ_i is the reduced mass of the vibrational mode and $Q_{zpf,i} = \sqrt{\hbar/2\mu_i\omega_{v,i}}$ the zero-point fluctuation amplitude of the molecular oscillator.

At this stage, we now assume that all vibrational modes are strictly degenerate in energy and mass $\omega_{v,i} = \omega_{v,j}, \mu_i = \mu_j$. This leads us to the definition of the collective dipole operator

$$\mathcal{P}(\vec{0}) = \left(\frac{\partial\langle\vec{p}\rangle}{\partial Q}\right)_0 Q_{zpf}\sum_{i=1}^{N} Q_{v,i}. \tag{3.10}$$

The operator corresponding to the electric displacement of the m^{th}-order mode is given by [172]

$$\frac{1}{\epsilon_0}\mathcal{D}(\vec{0}) = i\sqrt{\frac{\hbar\omega_c^m}{2\epsilon_0\mathcal{V}}}\left(a\vec{\epsilon}_m - a^\dagger\vec{\epsilon}_m^\star\right) \tag{3.11}$$

For the sake of the model's simplicity, we will also assume *(i)* that the dipoles are all perfectly aligned with the polarization $\vec{\epsilon}_m$ of the intracavity field and *(ii)* that the molecules entirely fill the cavity: $\mathcal{V}_v = \mathcal{V}$. Under these assumptions, the Hamiltonian (3.2) becomes

$$\begin{aligned}\mathcal{H} \;=\; & \mathcal{H}_{cav}^m + \mathcal{H}_{vib} \\ & -i\hbar\Omega(a - a^\dagger)\sum_{i=1}^{N} Q_{v,i} \\ & +\kappa^2\sum_{i=1}^{N} Q_{v,i}\sum_{j=1}^{N} Q_{v,j}\end{aligned} \tag{3.12}$$

with

$$\hbar\Omega = \left(\frac{\partial\langle\vec{p}\rangle}{\partial Q}\right)_0 \sqrt{\frac{\hbar\omega_c}{2\epsilon_0\mathcal{V}}} Q_{zpf} \tag{3.13}$$

$$\begin{aligned}\kappa^2 &= \frac{1}{2\epsilon_0\mathcal{V}}\left(\frac{\partial\langle\vec{p}\rangle}{\partial Q}\right)_0^2 Q_{zpf}^2 \\ &= \frac{\hbar\Omega^2}{\omega_\nu}\end{aligned} \tag{3.14}$$

when at resonance $\omega_c^m = \omega_\nu$.

While the dipolar self-energy term $\vec{P}(\vec{0})^2/2\epsilon_0\mathcal{V}$ is neglected in the standard strong coupling regime, we see from (3.14) that it must be fully accounted for in the equation of motion of the vibrational polaritonic states in the ultra-strong coupling regime. To do so, we adapt the original procedure of Hopfield [67, 72] to the case of an ensemble of vibrational modes. This procedure consists in writing down the equation of motion of a polaritonic annihilation operator defined as a normal mode operator $P^\pm$ of the system

$$[P^\pm, \mathcal{H}] = \omega_\pm P^\pm \tag{3.15}$$

where $\omega_\pm$ are the energies associated with the upper $+$ and lower $-$ polaritonic states.

Dealing with an ensemble of vibrational modes coupled to the cavity field, the definition of the normal mode operator

$$P^\pm = w_\pm a + x_\pm B + y_\pm a^\dagger + z_\pm B^\dagger \tag{3.16}$$

involves collective operators defined as

$$\begin{aligned}B(B^\dagger) &= \frac{1}{\sqrt{N}}\sum_{i=1}^{N} b_i(b_i^\dagger) \\ B + B^\dagger &= \frac{1}{\sqrt{N}}\sum_{i=1}^{N} Q_{\nu,i}.\end{aligned} \tag{3.17}$$

From $[b_i, b_j^\dagger] = \delta_{i,j}$, these collective operators obey canonical commutation relations

$$[B, B^\dagger] = 1. \tag{3.18}$$

This implies that the normal mode operators will have the simple commutation relations

$$\begin{aligned} [P^\pm, P^\pm] &= [P^{\pm\dagger}, P^{\pm\dagger}] = 0 \\ [P^\pm, P^{\pm\dagger}] &= 1. \end{aligned} \tag{3.19}$$

These definitions also lead to the following commutation rules

$$\begin{aligned} &[B, \sum_{i=1}^{N} Q_{\nu,i}] = \sqrt{N}, \\ &[B^\dagger, \sum_{i=1}^{N} Q_{\nu,i}] = -\sqrt{N}, \\ &[B, \sum_{i=1}^{N} Q_{\nu,i} \cdot \sum_{j=1}^{N} Q_{\nu,j}] = 2N\left(B + B^\dagger\right), \\ &[B^\dagger, \sum_{i=1}^{N} Q_{\nu,i} \cdot \sum_{j=1}^{N} Q_{\nu,j}] = -2N\left(B + B^\dagger\right). \end{aligned} \tag{3.20}$$

Using these rules, we derive the matrix for the equation of motion (Hopfield matrix)

$$\frac{1}{2}\begin{pmatrix} 2\hbar\omega_c^m & i\hbar\Omega_R & 0 & i\hbar\Omega_R \\ -i\hbar\Omega_R & 2\hbar\omega_\nu + \hbar D & i\hbar\Omega_R & \hbar D \\ 0 & i\hbar\Omega_R & -2\hbar\omega_c & i\hbar\Omega_R \\ i\hbar\Omega_R & -\hbar D & -i\hbar\Omega_R & -2\hbar\omega_\nu - \hbar D \end{pmatrix} \tag{3.21}$$

where $\hbar\Omega_R = \hbar\Omega\sqrt{N}$ corresponds to the well-known fact that the collective coupling strength is $\sqrt{N}$ time stronger than in the case of a single vibrational mode. The self-energy term is also enhanced by N since we have $\hbar D = N\kappa^2 = \hbar(\Omega_R^2/\omega_\nu)$.

The rotating wave approximation (RWA) of the Hamiltonian (3.12) amounts to neglecting the off-diagonal blocks of the Hopfield matrix [67]. Moreover, the polarization self-interaction

term must also be neglected in this regime, since it is a $\mathcal{O}(\Omega_R^2/\omega_v)$ order term. The resulting Hopfield matrix reads

$$\begin{pmatrix} \hbar\omega_c & i\hbar\Omega_R/2 & 0 & 0 \\ -i\hbar\Omega_R/2 & \hbar\omega_v & 0 & 0 \\ 0 & 0 & -\hbar\omega_c & i\hbar\Omega_R/2 \\ 0 & 0 & -i\hbar\Omega_R/2 & -\hbar\omega_v \end{pmatrix}_{\text{RWA}} . \quad (3.22)$$

The energies of the measured transmission peaks, reported in Fig. 3.5 for different cavity thicknesses, are then successively fitted to the eigenvalues of (3.21) and (3.22) for the different mode orders and thicknesses. The cavity thickness for each spectrum is directly accessible from the value of its FSR, and using the correction factor α. The cavity mode energy $\hbar\omega_c^m$ is calculated from the mode order, the cavity FSR and the background refractive index, and the vibrational energy $\hbar\omega_v$ corresponds to the energy of maximal extinction in the dilute solution transmission spectrum of Fig. 3.1(a). The Rabi splitting $\hbar\Omega_R$ is thus the unique free parameter in both fittings. In the two cases, we search for a minimum of the following quantity [173]:

$$\chi^2 = \sum_m \sum_l (E_{P_m^\pm}(l) - \hat{E}_{P_m^\pm}(l))^2 \quad (3.23)$$

where $P_m^\pm$ is the upper (lower) polaritonic branch of m^{th} order, l is the cavity thickness, E is the measured polariton energy and $\hat{E}$ is the calculated polariton energy which depends on the fitting parameter.

3.1.3.2 *Results and discussion*

While both the RWA and full Hamiltonian models closely fit the data far away from resonance (Fig. 3.6, top row), the RWA model clearly fails to reproduce the measured dispersions close to the bare vibrational mode energy (Fig. 3.6, bottom row). The comparison of the two model is also shown in Fig. 3.5, demonstrating the crucial importance of the polarization self-interaction and counter-rotating terms in the description of our ultra-strongly coupled system.

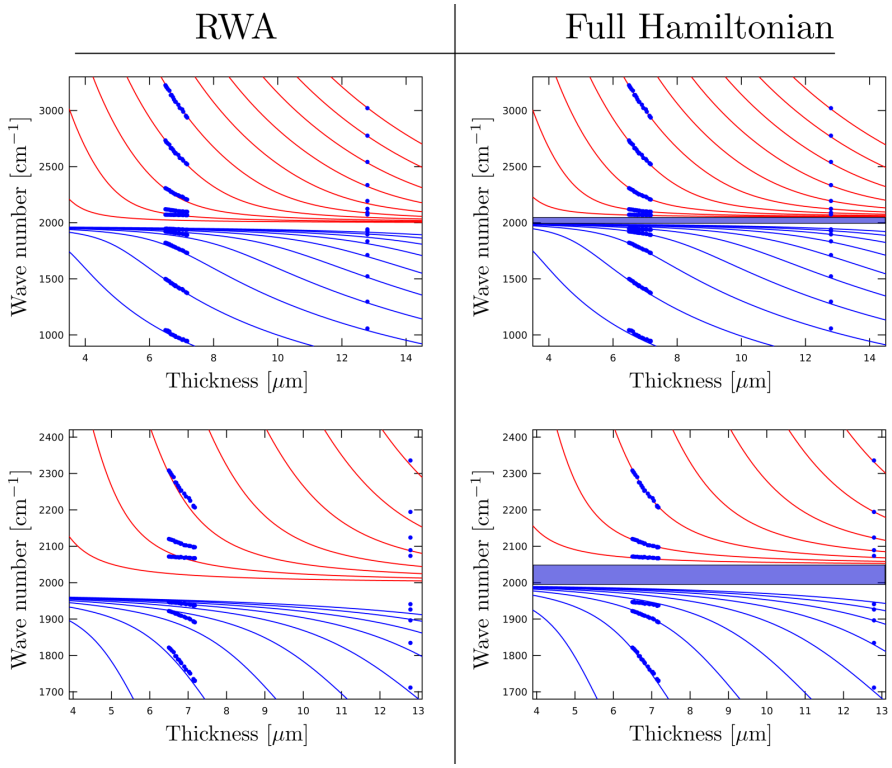

Figure 3.6 – Comparison between the fitting results using the RWA and full Hamiltonian models. In both cases, the 10 observable polaritonic branches are simultaneously fitted via the Rabi splitting $\hbar\Omega_R$. The bottom row is a blown up on around the bare molecular vibrational mode energy. See also Fig. 3.5. Reproduced from reference [155].

Remarkably, the asymptotic values of the full Hamiltonian model yield a vibrational polaritonic bandgap of ~ 60 cm^{-1}. As we show in Fig. 3.7(a) the angle resolved dispersion spectrum of a 492 cm^{-1} FSR cavity although displays this forbidden energy gap in the polaritonic spectrum, which thus exist for any cavity thickness and at any angle. The solid curves correspond to the predictions of our ultra-strong coupling model using the parameters previously determined and the experimentally measured angles. As pointed out in the context of intersubband electronic transition systems [70, 71], the opening of such a bandgap, originating from destructive interference between the dipolar polarization field and the bare cavity mode, also constitutes an indisputable signature of the USC regime.

The extracted Hopfield coefficients for the polaritonic branches P_4^- and P_6^- are shown in Fig. 3.7(b). As expected, the vibrational content of the states increases as they approach the energy of the bare vibrational mode. It is interesting to note the non-trivial evolution of the Hopfield coefficients calculated for the lower P_4^- polaritonic states which is more photon-like at resonance. This unbalanced matter- vs. photon-like mixing fraction at resonance is another remarkable feature of the USC regime that comes in clear contrast with the usual regime of strong coupling.

Between P_4^+ and P_4^-, the polaritonic ladder consists of heavy (*i.e.* large vibrational content) states. Surprisingly, these heavy polaritons show very high Q factors, up to 5 times higher than that of the bare cavity mode, and linewidths up to 6 times smaller than that of the bare molecular vibration, leading in principle to an enhanced coherence time, longer than any of the coherence times of the uncoupled system. Because of the opening of the vibrational polaritonic band gap, these heavy states are pushed away from the dissipative region of the bare vibration, therefore remaining perfectly resolved with their narrow linewidths, a major hurdle encountered in the regime of electronic strong coupling [174].

Even though the model discussed here assumes no interaction between the vibrational polaritonic branches of different

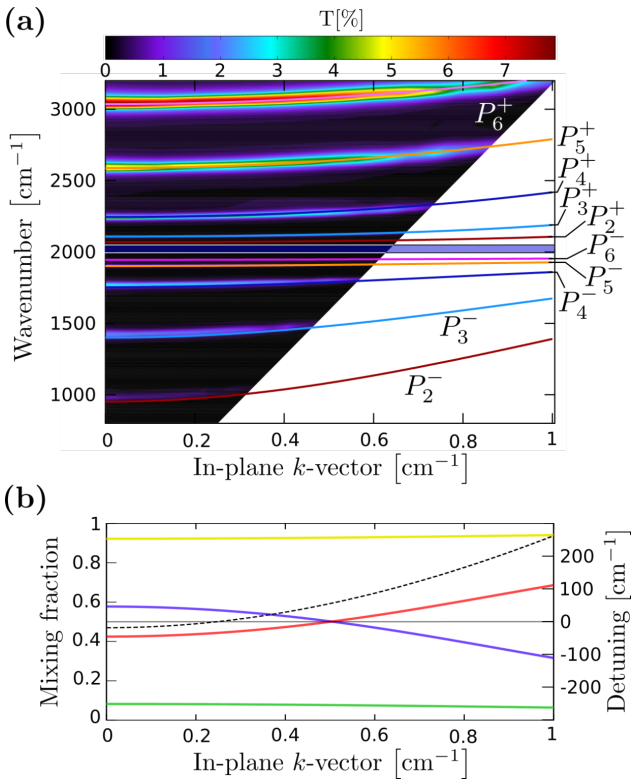

Figure 3.7 – (a) Polaritonic dispersion diagram measured by angle dependent IR transmission spectroscopy (unpolarized, 0−28°). The solid lines are the solutions of the full Hamiltonian model, using the same parameters and color code as in Fig. 3.5. The vibrational polaritonic band-gap is again clearly observed (blue horizontal band). (b) Photonic and vibrational fractions of the 4^{th} polaritonic branch (blue and red curves respectively) and of the 6^{th} polaritonic branch (green and yellow curves respectively). The photon-vibration energy detuning for the 4^{th} cavity mode is shown in black dashes (right axis). Reproduced from reference [155].

cavity mode orders, nontrivial cross talk between the branches should be expected when accounting for the non-Markovian dissipative dynamics of our system [88, 175]. Indeed, with Rabi frequencies exceeding the memory time of the vibrational 'heat bath' (rotational and translational degrees of freedom, relaxing over few picoseconds timescales [176]), qualitatively new non-Markovian effects might arise. Moreover, the possibility of vibrational excitonic features in pure molecular liquids [175] might be a new route to explore in the context of strongly correlated vibro-polaritons.

3.1.4 *Conclusions*

We have demonstrated in this section that it is possible to reach the regime of room temperature USC in the vibrational realm, by embedding high oscillator strength molecular liquids in FP cavities. We have revealed direct signatures of the USC regime, showing how the features inherent to the USC regime can be also found at the level of molecular vibrational modes. Remarkably, the multimode vibrational polaritonic ladder shown here is a practical way for generating heavy polaritonic states with smaller linewidths than both the optical transition and the molecular vibration, potentially leading to an enhanced coherence time.

Interestingly, the USC regime also implies that the vibrational ground state must shift to lower energies while acquiring a photonic admixture [67]. Such modifications, analogous to those described at the level of electronic transitions, have perhaps even deeper implications in the case of vibrational strong coupling, as they correspond to a redefinition the whole vibronic landscape of the dressed molecules through which chemistry occurs. In particular, these results point to the potential impact of the USC regime in the context of bond-selective chemistry.

In the next section, we present preliminary results on the excited state properties of vibro-polaritons by measuring

their IR emission which, together with recent results on IR transient spectroscopy [177], paves the way to the study of vibro-polaritonic energy transfer and many-body interactions.

3.2 VIBRO-POLARITONIC IR EMISSION IN THE STRONG COUPLING REGIME

Here we investigate the polaritonic emissivity from a typical molecular system used in the VSC regime, an organic polymer (poly(methyl methacrylate), PMMA) embedded in a metallic FP cavity, resonantly tuned to one of its IR vibrational transitions. When targeting the high oscillator strength CO-stretching band of the polymer, we reach the strong coupling regime, resulting in the formation of the hybrid light-matter states $|P^+\rangle$ and $|P^-\rangle$. By heating up the strongly coupled system, we thermally excite a population of vibro-polaritons, the radiative decay of which is directly measured using IR emission spectroscopy. Angle-resolved emission spectra allow us to assess the steady-state thermalization of the vibro-polaritons.

3.2.1 *System under study*

We show in Fig. 3.8(a) the IR transmission spectrum of a thin film of PMMA, spin-coated on top of a Ge substrate. To obtain this film, a concentrated solution of PMMA (16 wt%) was first prepared in trichloroethylene. Both PMMA ($M_w = 996000$) and trichloroethylene were purchased from Sigma Aldrich and used without further purification. The solution was then spin-coated at a high speed (*ca.* 5000 rpm) to form a 2µm thick film. The FTIR transmission spectrum reveals multiple sharp lines, associated with different IR active intra-molecular vibrational modes of the polymer. Superimposed on these lines, we observe a slowly varying envelope which corresponds to FP interferences in the PMMA layer, between the air and the Ge substrate. The strong vibrational band at 1732 cm^{-1} (27 cm^{-1} full width at half maximum) originates from the CO-stretching

mode of the polymer backbone (see structure in Fig. 3.8(a), inset), and is the molecular resonance that we will target to achieve VSC. The black dashed curve superimposed on this spectrum is the result of transfer matrix calculation obtained by solving Maxwell's equations for the air-Ge-PMMA-air multilayer and fitting the PMMA dielectric function to a Lorenz model with multiple resonances, as explained in the previous section.

The IR cavity is fabricated by first sputtering a 10 nm Au mirror onto a Si wafer. A thin PMMA layer is then spin-coated on the Au mirror and baked for 1 hour at 100°C to relax the strain in the polymer film and to evaporate the remaining solvent. Finally, a 10 nm layer of Au is sputtered on the film to form the FP cavity, whose modes are determined by the thickness of the PMMA layer. By spin-coating a 2μm thick PMMA film, we obtain a FP cavity with a 866 cm^{-1} free spectral range (FSR), and a quality factor of *ca.* 25. The resonant coupling between the second cavity mode and the CO-stretching band of PMMA results in a cavity transmission spectrum displaying normal modes splitting of 142 cm^{-1} (Fig. 3.8(b), green curve), amounting to *ca.* 8% of the bare vibrational transition frequency and firmly placing our system in the VSC regime. This behavior is accurately reproduced by the transfer matrix calculation using the previously determined dielectric function of PMMA (dashed black curves). The slight Gaussian broadening of the experimental cavity spectrum is due to inhomogeneities in the PMMA film thickness, averaged over the region probed by the spectrometer (*ca.* 9 mm^2).

In order to further establish the hybrid light-matter nature of the new normal modes, we now investigate the dispersion diagram of the coupled system, using angle dependent transmission spectroscopy. As shown in Fig. 3.8(c) in units of the conserved in-plane light momentum $k_{\parallel}$ and under transverse electric (TE) polarization, the two vibro-polaritonic eigenstates undergo an avoided crossing about the vibrational C=O resonance energy (1732 cm^{-1}, white horizontal dashed line) as they disperse toward asymptotically uncoupled molecular and

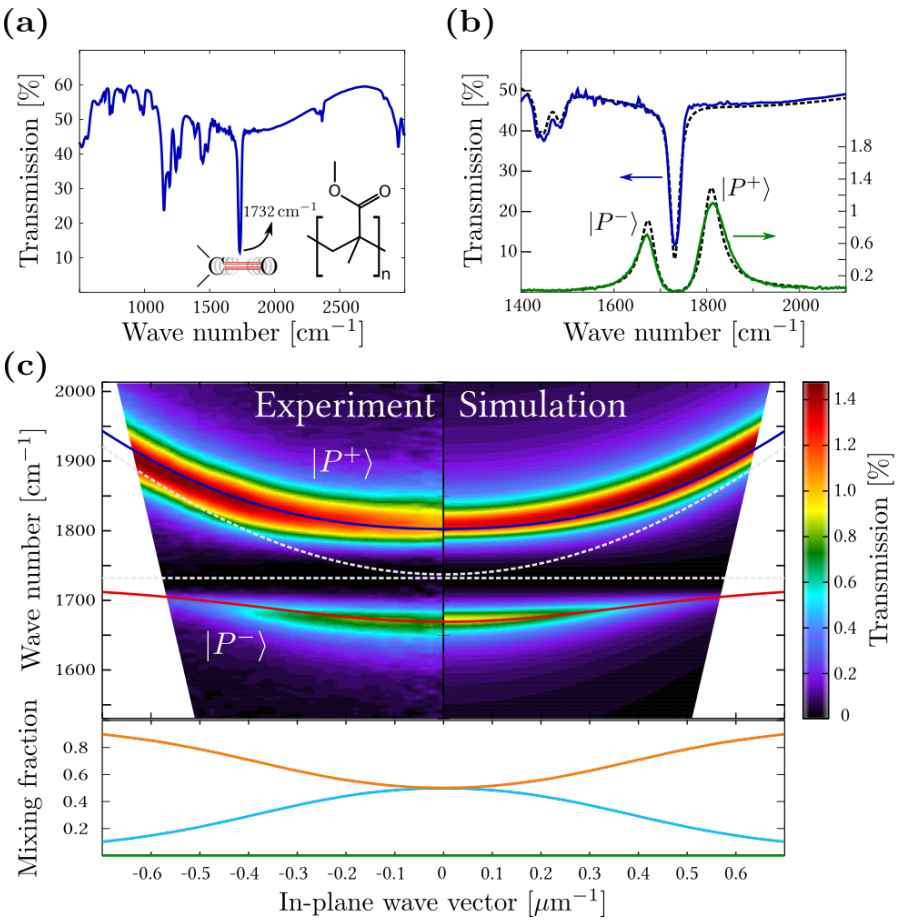

Figure 3.8 – (a) IR transmission spectrum of a 2µm thick PMMA layer (molecular structure in inset) spin-coated on top of a Ge substrate. (b) IR transmission spectra of the resonantly coupled PMMA cavity (green curve), compared to the bare PMMA transmission spectrum (blue curve). The transfer matrix predictions are shown by the black dashed curves. (c) Angle-resolved transmission spectra measured under TE illumination (left) and the corresponding transfer matrix prediction (right). The solid curves are the fitted solution of the coupled oscillators model (3.21) and the white dashed curves are the dispersions of the corresponding uncoupled modes. The lower panel shows the photonic ($|w_-|^2$, cyan curve) and the vibrational fractions ($|x_-|^2$, orange curve) composing the lower polaritonic state. The non-RWA terms $|y_-|^2, |z_-|^2$ are shown in green.

optical modes. The corresponding angle-dependent transfer matrix simulations, shown in the right panel of Fig. 3.8(c) is again in close agreement with the measured data, albeit yielding slightly sharper modes.

The expression of these new eigenstates in terms of the bare molecular and cavity modes can be derived from the same dipolar Hamiltonian model (3.21) as in the previous section. The resulting dispersive vibro-polaritonic energy branches are fitted to the experimental data as shown by the blue and red curves in Fig. 3.8(c), yielding a coupling strength of 133 cm^{-1}. In this fitting process, the coupling strength is the only free parameter since both the CO-vibration and the cavity mode energies can be experimentally determined independently. The squared modulus of the mixing coefficients $(w,x,y,z)_{\pm}$, reported in the lower panel of Fig. 3.8(c), show that the vibro-polaritonic states share a 50:50 light-vibration character at normal incidence. Moreover, with a relative coupling strength $\Omega_R/\omega_\nu \simeq 8\%$, the anti-resonant contributions $y_\pm$ and $z_\pm$ usually neglected in the rotating wave approximation (RWA) remain close to zero.

3.2.2 *FTIR emission spectroscopy of vibro-polaritons*

Given this vibro-polaritonic mode structure, as revealed by IR transmission spectroscopy, we now demonstrate that polariton populations in such systems can be conveniently characterized by thermal emission spectroscopy. This technique, firmly established in various research fields ranging from polymer sciences [178, 179] to mineralogy [180, 181] and astronomy [182], has yet to be applied to the study of strongly coupled systems. This holds, in part, to the fact that materials traditionally used for strong coupling are not compatible with the high temperatures needed to thermally excite a sizable population of polaritons, and one has to rely on optical or electrical excitation to study their excited states properties. In this respect, VSC of polymer films offers a unique combination

of low energy vibrations and relatively high thermal stability. For instance, the unzipping of PMMA polymer chains only occurs around a temperatures of 155°C [179].

The measurement presented here were performed on a Bruker FTIR Vertex 70 spectrometer, by keeping the sample of interest on the side input port. Emission spectra were recorded using a liquid nitrogen cooled mercury-cadmium-telluride detector, at a resolution of 4 cm^{-1}. The sample was mounted on a computer controlled rotating stage to allow for angle-resolved measurements, and it was heated from the back by a Peltier stage. The surface temperature of the sample was kept constant throughout the study, and was continuously monitored by a thermocouple.

The thermal emissivity spectrum ϵ of a 2 µm thick PMMA film spin-coated onto a Si wafer and heated up to 100°C is shown in Fig. 3.9(a), together with the bare PMMA IR transmission spectrum already presented in Fig. 3.8. The emissivity spectrum is obtained after correcting the measured emission of the sample L by the emission of a bare Si substrate L^{ref}, and normalizing to the emission of an approximate blackbody L^{BB} made of a Si substrate coated with a thick layer of carbon soot. The emission of the sample, of the reference and of the approximate blackbody were all measured at the same temperature:

$$\epsilon = \frac{L - L^{ref}}{L^{BB}}. \tag{3.24}$$

We clearly see in this figure that the emissivity spectrum reproduces the vibrational features observed in transmission, as expected from Kirchhoff's law of thermal radiation in a system with a Boltzmann occupancy of excited states [183].

When measuring at normal incidence the thermal emission from the strongly coupled cavity, heated up to the same temperature of 100°C, we obtain the emissivity spectrum displayed in Fig. 3.9(b). This spectrum shows a series of asymmetric peaks at the different cavity modes energies, as well as vibro-polaritonic emission near 1700 cm^{-1}. The asymmetric line shape, although surprising at the first glance, correlates

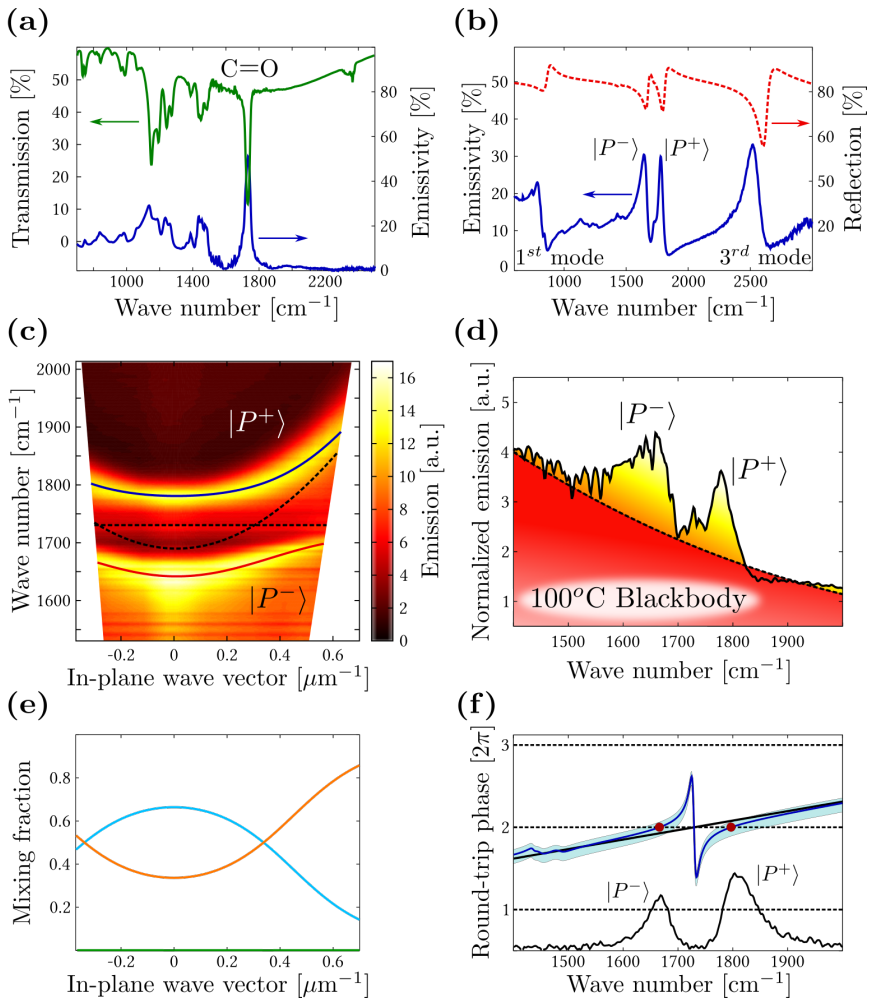

Figure 3.9 – (a) Emissivity spectrum of a 2 µm thick film of PMMA on a Si substrate at 100°C (blue curve). The transmission spectrum of PMMA on a Ge substrate is shown for comparison (green curve). (b) Emissivity spectrum of the strongly coupled cavity at 100°C (blue curve), and simulated cavity reflection spectrum using the transfer matrix calculation of Fig. 3.8(b). (c) Angle-resolved TE emission spectrum of the strongly coupled cavity and coupled-oscillators dispersions obtained from the previously determined parameters with a thermal expansion of 0.115 µm of the 2 µm thick active layer. The corresponding Hopfield coefficients for $|P^-\rangle$ are shown in (e), with the photonic fraction (cyan), the vibrational fraction (orange) and the non-RWA terms (green). (d) Normal incidence emission over absorption ratio (black curve), compared to the expected blackbody distribution (black dashed curve). The absorption is calculated from the fit of the cavity transmission spectrum measured at 100°C. (f) Round-trip phase accumulation of the cavity photon with (blue curve) and without (black line) the absorber. The polaritonic resonances (black transmission spectrum) occurs at the positions indicated by the red dots, where the phase accumulation equals 4π.

well with the simulated cavity reflection spectrum obtained using the same parameters as in Fig. 3.8(b). From the transfer matrix simulations, we can trace back this asymmetry to the frequency dependence of the refractive index of the Au mirrors. Moreover, the small spectral shift in the emission peaks toward lower energies as compared to the room temperature simulations can be attributed to a mere thermal expansion of the PMMA intra-cavity layer, and can be accounted for by a 0.115 μm increase of the simulated layer thickness of 2 μm. The measured thermal emission from the bare cavity modes is also expected from Kirchhoff's law, given the finite energy dissipation occurring at these modes energies in the polymer and in the Au mirrors. Hence, the emission from uncoupled cavity modes can be attributed to the filtered polymer film emission, as well as to thermal emission from the Au mirrors, a contribution that could be minimized by using dielectric mirror cavities [148].

The angle-resolved TE emission spectrum of the vibro-polaritons is shown in Fig. 3.9(c), together with the coupled oscillator fit of Fig. 3.8(c), accounting for the thermal expansion of the polymer. Contrary to the data presented in panels (a-b), this dispersion diagram is not normalized to a blackbody spectrum, thus allowing the observation of the actual vibro-polaritons populations. Dispersive contributions from both the upper and lower vibro-polaritons are clearly identified, with a stronger emission coming from the bottom of the $|P^-\rangle$ branch. Such an intensity distribution is already quite suggestive of an interaction-mediated polariton relaxation mechanism, akin to those required for polariton condensation in other strongly coupled systems [40, 184]. Alternatively, it could be related to the angle-dependent photonic and vibrational mixture composing the polaritonic states (see Fig. 3.9(e)) [112].

The non-thermal population distribution of vibro-polaritons is further evidenced by comparing their normalized emission-over-absorption spectrum to the theoretical blackbody distribution expected from Kirchhoff's law. The absorption spectrum $A = 1 - R - T$ used in this normalization is computed by

transfer matrix calculations, based on the fit of the transmission spectrum measured at 100°C. As shown in Fig. 3.9(d), while this comparison works fairly well for the non-zero background emission of the system, it clearly fails near the vibro-polaritons energies, as well as at the energy of the bare C=O vibration. By comparing this normalized emission spectrum to the cavity transmission spectrum shown in Fig. 3.9(f), we also observe a slight offset with respect to the measured $|P^+\rangle$ position. This offset suggests that $|P^+\rangle$ is inhomogeneously broadened in our system, with a thermally relaxed population at higher energy and a non-thermal occupancy of lower energy states, a signature that could be confirmed by IR transient absorption experiments. The observation of thermally excited emission from both upper and lower polaritons, and their intensity distributions along the branches, points toward new mechanisms of vibro-polariton interactions, the details of which is subject to ongoing experiments. It is worth noting however that such observations lay the ground for the investigation of vibro-polariton condensation.

3.2.3 *Conclusions*

We have demonstrated in this section the first steps toward a detailed study of IR emissivity from vibro-polaritonic states in a strongly coupled polymer microcavity. By thermally promoting a broadband population of vibro-polaritons, we characterized their emissivity and angular distribution. Our preliminary results show that the polaritonic emission is not thermalized. This observation points toward vibro-polariton interactions leading to non-Boltzmann state occupancy, the study of which requires further investigation. This work thus offers a complementary approach to the recent experiments on time-resolved vibro-polariton dynamics [177], opening the possibility of investigating energy transfer processes in the vibrational strong coupling regime, as well as non-equilibrium vibro-polariton condensation.

4

CHIRAL LIGHT-CHIRAL MATTER STRONG COUPLING

Throughout the previous chapters, we have been investigating how collective light-matter strong coupling can modify specific molecular and material properties. A complementary approach, which we will follow in this chapter, is to look for specific properties of the uncoupled systems as ways to tailor new behaviors of the hybrid light-matter states. To illustrate this point, we will explore the strong coupling regime between surface plasmons and excitons in a class of semiconductor materials, atomically thin layers of transition metal dichalcogenides (TMDs). These materials, long known in there few layers forms [185, 186], have recently triggered a huge interest due to the many exotic properties that they display when thinned down to the monolayer limit [187–190]. On the other hand, plasmonic structures are well known to constitute highly versatile electromagnetic resonators, enabling the design of a rich variety of near field optical modes [191–198].

In this chapter, we explore the interplay between the optical chirality of plasmonic near fields and the valley chirality of 2D TMDs, an excitonic property emerging from the TMD crystal symmetries. After an introductory section on the strong coupling of 2D TMDs to simple surface plasmon resonators, we demonstrate the generation of spin-momentum locked polaritonic states, yielding surprisingly robust valley polarization and intervalley coherences. These chiral polaritons are found to propagate over several microns distances, opening new routes toward chiral optical networks. Parts of this chapter

are reproduced from already published work [199, 200] that has been carried in collaboration with the groups of G. Pupillo and S. Berciaud.

4.1 STRONG COUPLING OF WS_2 MONOLAYERS WITH PLASMONIC NANOSTRUCTURES

Over the past seven years, it has been demonstrated that group VI TMDs with structures MX_2 (where M is Mo or W and X is S or Se) transition from an indirect to a direct band gap when going from multilayers to a monolayer. The resulting strongly allowed excitonic resonances, occurring at two inequivalent momenta K and K′ of the Brillouin zone, dominate the visible and near-IR absorption spectra of these systems, and give rise to orders of magnitude enhanced photo-luminescence [201]. The absorption coefficient in 2D TMDs monolayers can reach up to 10^6 cm^{-1}, much higher than in typical colloidal cadmium selenide quantum dots (*ca.* 0.2×10^5 cm^{-1}), and comparable to what is found in very high density layers of organic molecular aggregates (*e.g.* cyanine J-aggregates, 0.5×10^6 cm^{-1}).

Thanks to the strong in-plane confinement of the electrons and holes, and to their reduced dielectric screening in the 2D limit, tightly bound excitons of *ca.* 1 nm Bohr radii and binding energies exceeding 300 meV, remain stable up to room temperature [202]. Moreover, those excitons exhibit a great diversity of many-body interactions and correlations, leading to the formation of different kinds of trions and bi-excitons, enriching the possibilities offered by TMDs for fundamental research and device applications in material sciences [203–211] as well as in the context of light-matter strong coupling [212–216].

Another fascinating feature of 2D TMDs is the concomitance of large spin-orbit splitting and lack of crystal inversion symmetry (see *e.g.* Fig. 4.1(a)). These combined features lead to coupled spin and valley degrees of freedom [217, 218]. In particular, the spin-orbit splitting of the valence band at the K and K′ points results in two excitonic states, denoted

A and B and separated in energy by up to 400 meV in W dichalcogenides. In addition to this large energy splitting, the broken inversion symmetry of the crystal packing gives rise to a different valley index at those two inequivalent points of the Brillouin zone [219]. As a result, low energy direct transitions undergo chiral optical selection rules, with the K valley coupled to σ^+ polarized light, and the K′ valley to σ^- polarized light [220–222]. This peculiar spin-valley excitonic behavior opens new possibilities in the context of Hall effect physics [217]. It also strengthens both the spin and valley indices by forbidding the transformation of one without the simultaneous transformation of the other [223]. Recently, the robust valley index of TMDs has led to the demonstration and manipulation of coherent superpositions of valley excitons, resulting in co-linearly polarized PL under linearly polarized excitation [224, 225]. In the second section of this chapter, we will show how such spin-valley properties of TMDs can also enrich the physics of strongly coupled systems.

4.1.1 *WS_2, a natural candiate for light-matter strong coupling*

The first reports of strong light-matter coupling with monolayer TMDs appeared very recently in the literature, originally involving MoX_2 monolayers. Menon and co-workers [226] and Tartakovskii and co-workers [227] incorporated MoS_2 and $MoSe_2$, respectively, into DBR cavities, while Agarwal and co-workers [228] studied the coupling of MoS_2 to both local and surface lattice modes of metal nanoparticle arrays. While these studies showed the potential of MoX_2 TMDs for achieving strong coupling, the observed Rabi splittings were limited by the absorption of the materials with a maximum reported splitting of 86 meV at room temperature [228]. Furthermore, in MoX_2 monolayers, the spin-orbit splitting of the excitonic transition is limited to *ca.* 150 meV such that both the A and B exciton could simultaneously interact with cavity modes, complicating the studies of such systems. In this respect, WS_2

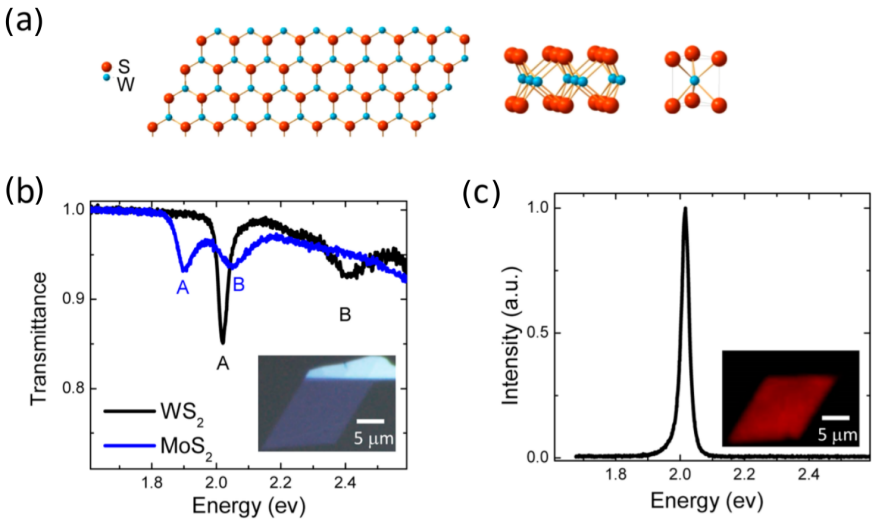

Figure 4.1 – (a) Structure of a WS_2 monolayer showing, from left to right, out-of-plane view, in-plane view, and the unit cell. (b) Transmittance of monolayers of WS_2 (black curve) and MoS_2 (blue curve) on quartz substrates, displaying the spin-orbit splitted A and B excitons. The inset shows an optical micrograph of the WS_2 flake in which the dark blue region is a monolayer and the bright region is a multilayer. (c) Emission spectrum taken from the monolayer region of WS_2 under continuous wave 532 nm (2.330 eV) excitation. The inset displays the fluorescence image of the WS $_2$ flake in which bright emission is observed only from the monolayer region (image taken under 470 nm (2.64 eV)) excitation. Reproduced from reference [199].

monolayers have the advantage of presenting a much stronger and isolated *A* exciton absorption band [229], as can be seen in Fig. 4.1(b), two favorable aspects for room temperature light-matter strong coupling.

To illustrate this point, we show in Fig. 4.2 the TE-polarized angle-resolved transmission, reflection and emission spectra of a FP cavity embedding a single monolayer of WS_2, clearly displaying the anticrossing behavior of strongly coupled systems with a Rabi splitting of 101 meV, as measured in transmission. To prepare this FP cavity sample, WS_2 flakes were first exfoliated from a synthetic bulk single crystal (Hq graphene, The Netherlands), and the monolayers were identified by optical contrast, and PL microscopy. The monolayers were then deposited on a flexible PDMS slab before being transferred onto the cavity substrate. This substrate consists of a 50 nm thick Ag mirror coated with a 86 nm thick LiF spacer, both thermally evaporated, allowing the WS_2 monolayer to sit in the center of the final FP cavity. Subsequent evaporation of another 90 nm thick LiF spacer and of a top 50 nm thick Ag mirror finalized the first mode FP cavity, and yields a bare optical mode linewidth of *ca.* 80 meV.

4.1.2 *Light-matter strong coupling at the 2D limit*

One disadvantage in using FP cavities to achieve strong coupling with 2D TMDs is their dimensional mismatch, resulting in the fact that the active layer only occupies a tiny fraction of the available mode volume of the resonator. In this respect, coupling TMDs to surface plasmon resonances seems like a natural path to follow. In addition, as we will discuss in the next section, the versatility of plasmonic resonators for tailoring near field mode structures opens a wealth of possibilities in the context of light-matter strong coupling.

Surface plasmon (SP) modes are electromagnetic resonances that exist at the interface between a metal and a dielectric [230–232]. These resonances result from coupled os-

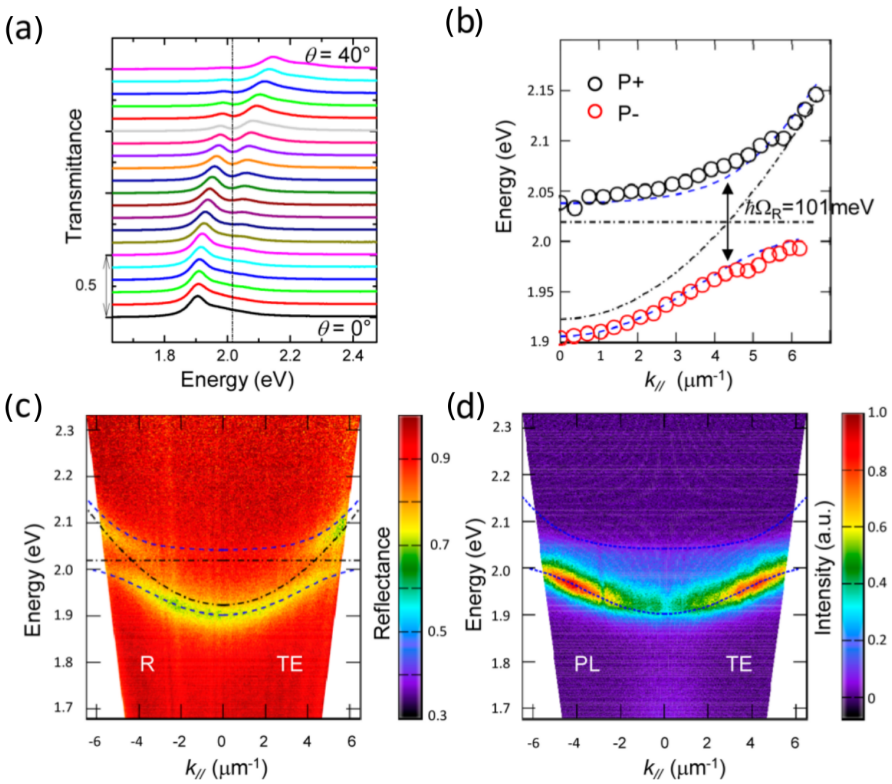

Figure 4.2 – (a) Transmission spectra as a function of angle (θ from 0° to 40°) for a FP cavity embedding the WS_2 monolayer. (b) Peak transmission energies as a function of in-plane angular momentum for the same FP cavity. Black and red circles correspond, respectively, to the measured positions of the P+ and P- extracted from the data displayed in (a). Black horizontal dot-dashed line and curves show, respectively, the dispersion of the A exciton transition energy and empty cavity mode. The P+ and P- dispersions are fitted (blue dashed curves) to a standard Jaynes-Cummings model (see *e.g.* (1.14)). (c) Energy in-plane momentum dispersion for the same FP cavity taken in TE polarized reflection. (d) Dispersion of the photoluminescence from the same FP cavity under continuous wave 532 nm excitation. The dashed curves represent the dispersions of P+ and P- as obtained from (c). Reproduced from reference [199].

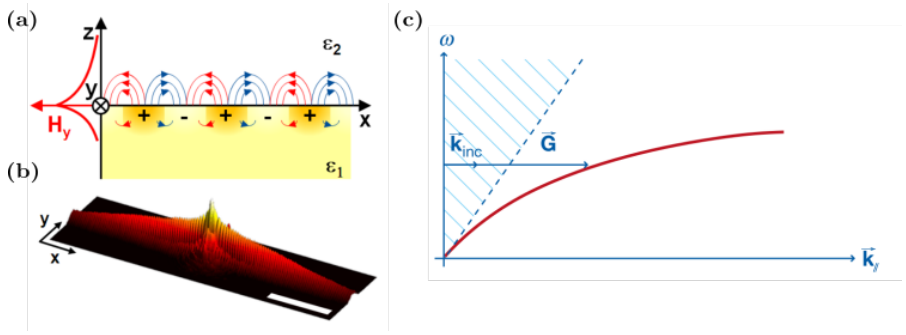

Figure 4.3 – (a) Sketch of a propagating SP at the interface of a metal with the permittivity ϵ_1 and a dielectric ϵ_2. The field is transverse magnetic (TM) polarized and exponentially decays in the direction normal to the interface. (b) 3D plot of logarithmic SP intensity, launched by a point source at the field maximum. The scale bar corresponds to 50 µm. (c) Sketch of the SP dispersion relation on a flat metal-dielectric interface. The real part of the SP wave vector $\vec{k}_{SP}$ is shown in red. The blue dashed region represents the light cone in the dielectric medium from where the excitation beam is shinned, with an in-plane wave vector $\vec{k}_{inc}$. The missing in-plane momentum $\vec{G}$, necessary to match the plasmonic dispersion, can be provided by *e.g.* scattering on a periodic grating. Figure adapted from reference [233].

cillations of the electromagnetic field and of the free electrons gas at the metal surface, and can thus propagate as density waves along the interface. For such intrinsically 2D excitations, the electromagnetic field exponentially decays with distance in both media, and is maximum at the interface, as sketched in Fig. 4.3(a,b).

Being evanescent waves in the direction normal to the interface to which they are bound, SP cannot be directly excited by shinning a far-field source at the interface. Instead, one has to rely on one of the excitation schemes shown in Fig. 4.4, in which the large SP in-plane momentum is provided to the incident photon either by evanescent reflection or by scattering on surface corrugations. We will focus here on the case of SP excitation by periodic diffraction gratings, a scheme of excitation that has several advantages in the context of strong coupling as we will see in the following.

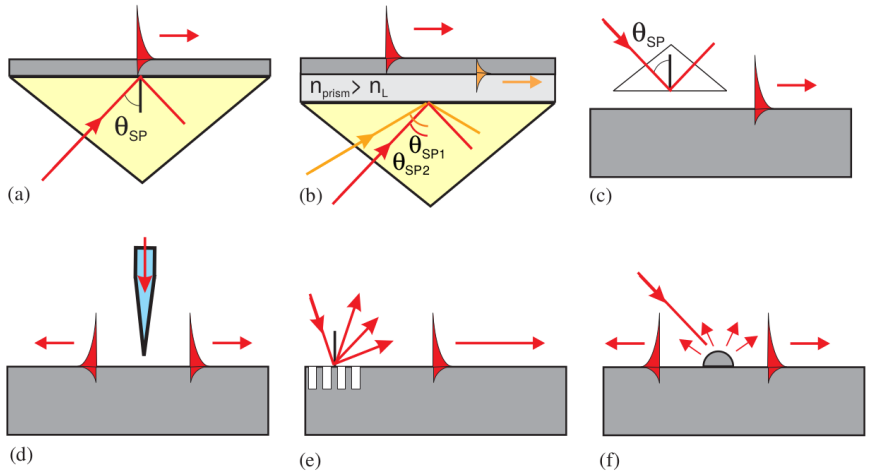

Figure 4.4 – Different excitation schemes of SPs: (a) Kretschmann geometry, (b) two-layer Kretschmann geometry, (c) Otto geometry, (d) excitation with a scanning near-field optical microscope probe, (e) diffraction on a periodic grating, and (f) diffraction on surface defect. Figure reproduced from reference [231].

Upon scattering off a periodic corrugation, ruled onto an otherwise flat metallic surface, an incident photon can change its wave vector according to the gratings law. The coupling condition for exciting a SP then translates into the matching of one of the diffractive orders of the grating with the in-plane momentum of the SP:

$$k_{SP} = \frac{\omega}{c}\sqrt{\frac{\epsilon_d \epsilon_m}{\epsilon_d + \epsilon_m}}, \tag{4.1}$$

where ϵ_d and ϵ_m are the frequency dependent complex dielectric functions of the dielectric and of the metal, respectively. For a grating period Λ and a photon incidence angle θ, the k-vector matching condition read:

$$\vec{k}_{SP} = \frac{\omega}{c} n_s \sin\theta \hat{u} \delta_p \pm n\frac{2\pi}{\Lambda}\hat{x} \pm m\frac{2\pi}{\Lambda}\hat{y}, \tag{4.2}$$

where $\delta_d = 1(0)$ for TM (TE) polarized light, n_s is the refractive index of the dielectric medium, $\hat{u}$ is the in-plane unit vector of the incident photon, $\hat{x}$ and $\hat{y}$ are the unit lattice vectors of the periodic grating and (m,n) are integers defining the propagation direction of the excited SP. In other words, the

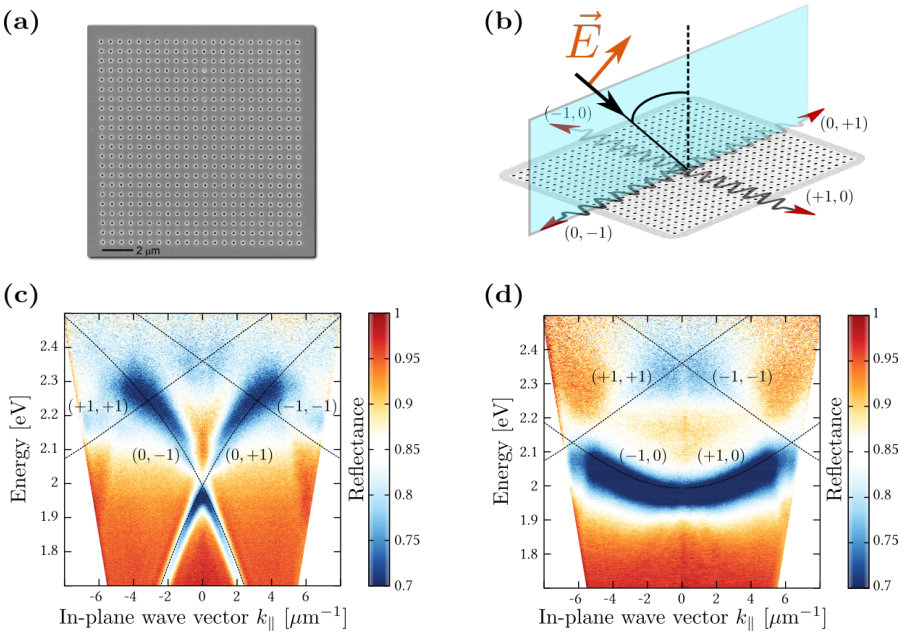

Figure 4.5 – (a) Scanning electron microscope image of a square plasmonic hole array ($\Lambda = 530$ nm, hole diameter of 120 nm). (b) Definition of the diffractive orders of the plasmonic grating with respect to the plane of incidence (shown in cyan). The incident electric field, shown in orange corresponds here to a TM incidence. (c-d) Angle-resolved reflection dispersion measured above the hole array under TM and TE polarization, respectively. The different plasmonic branches, calculated from (4.2) are reported as black dashed curves. Adapted from reference [199].

diffraction grating folds the evanescent plasmonic dispersion back into the light cone by an integer number of times the grating reciprocal lattice vector $\vec{G}$, thus allowing the resonant excitation of SP waves from the far field [192]. We show in Fig. 4.5(c,d) the angle-resolved reflection spectrum in TM and TE polarization respectively, measured on a typical square array of circular nano-holes ($\Lambda = 530$ nm, hole diameter of 120 nm, SEM image in Fig. 4.5(a)).

When covering such a plasmonic surface with an highly absorbing medium, the typical anti-crossing behavior of light-matter strong coupling can be observed about the crossing point of SP modes with the absorbing state. Such signatures have been experimentally reported in a rich variety of plasmonic-absorbers systems, including the first demonstration

of strong coupling in 1975 [31], and have recently led to several breakthrough in establishing long range coherences in molecular systems [44, 143, 144, 234]. Some of the recent experimental developments in this field have been reviewed in [235], and a theoretical description of strong coupling in such geometry can be found in [236].

In order to experimentally demonstrate the possibility of strongly coupling TMDs with such plasmonic gratings, we transferred a WS_2 monolayer onto a square hole array milled by focused ion beam lithography in a 260 nm thick sputtered Au mirror. A 5 nm thick PMMA film was spin coated onto the array before this transfer to reduce both the quenching in the metal lossy waves [237], and hot electron transfer between Au and the semiconductor [238, 239]. With a hole array period of 530 nm and a hole diameter of 120 nm, the folded surface plasmon resonances corresponding to the $(0,\pm1)$ and $(\pm1,0)$ modes of the grating could be brought in resonance with the A exciton of WS_2. An optical micrograph of the sample and its photo-luminescence (PL) image are shown in Fig. 4.6(a,b), clearly revealing how the monolayer flake covers the plasmonic grating. We also observe that the emission is enhanced by *ca.* 2.5 folds above the holes, possibly due to two factors: first, the plasmonic field has a maximum above the holes, enhancing the photonic mode density at this point and thereby increasing the excitonic radiative rate [237, 240], and second, the different dielectric screening at the positions where the monolayer is suspended over the holes rather than above the metal could enhance the emission [187].

The optical setup used to measure angle-resolved dispersion diagrams from such microscopic samples is sketched in Fig. 4.6(c). A source (deuterium-halogen white light for reflectometry or continuous wave 533 nm laser for PL) is injected via a beam splitter (BS) into a 40x objective (NA 0.6). The reflected beam or PL signal from the sample is collected by the same objective and passes through a broadband half-wave plate (HWP) and a linear polarization analyzer (LP). Adjustable slits (AS) placed in the image plane of the tube lens (TL) allow

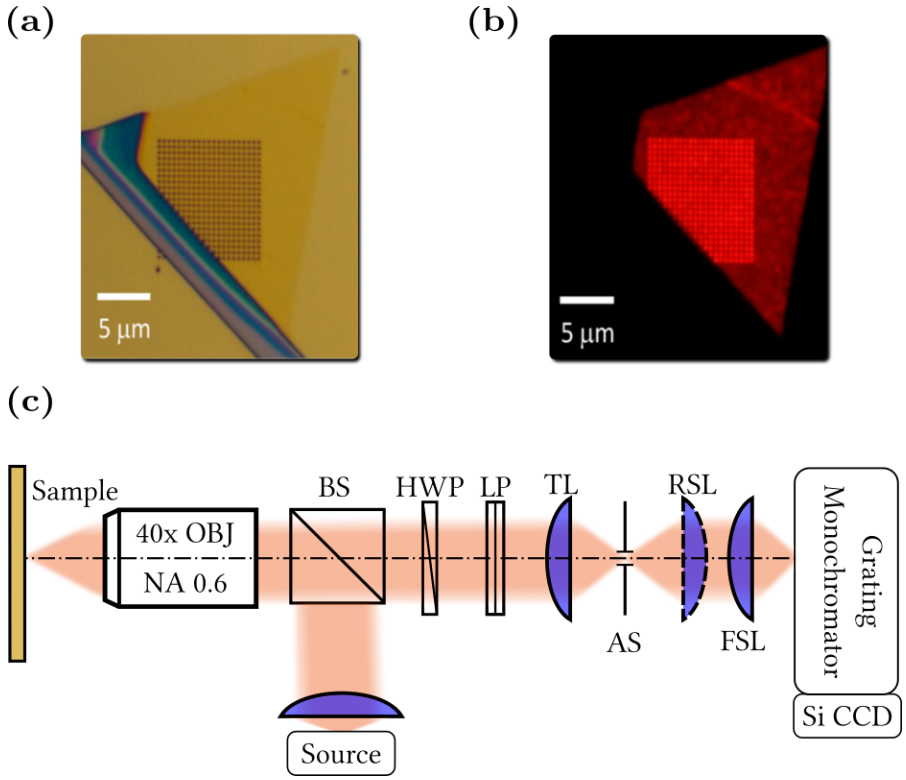

Figure 4.6 – (a) Optical micrograph of the sample and (b) its wide field PL image under 405 nm excitation. The monolayer region appears red in the PL image. (c) Schematic of home built optical setup used for angle resolved spectroscopy. Its description is given in the main text. Adapted from reference [199].

to spatially select the signal coming only from a desired area of the sample, whose Fourier-space (or real space) spectral content can be imaged onto the entrance slits of a spectrometer by a Fourier-space lens (FSL), or adding a real-space lens (RSL). The resulting image is recorded by a cooled CCD Si camera.

The dispersion diagram of the plasmonic hole array covered with the WS_2 monolayer is shown in Fig. 4.7(a,d), for TM and TE polarization, respectively. Under TM polarization, the anticrossing between the $(0,\pm1)$ SP modes (black dot-dashed curves in Fig. 4.7(a)) and the A exciton (horizontal black dot-dashed line) is again clear, giving a Rabi splitting of 60 meV. This value is smaller than the one observed above for the FP cavity but still easily observable given the width of the SP resonance at 2.010 eV (*ca.* 36 meV). This reduction of Rabi splitting in going from FP cavities to plasmonic hole arrays is much greater than that observed in previous studies with disordered molecular layers [241], and illustrates the importance of the orientation of the transition dipole moments of the crystalline materials, relative to the SP polarization.

The light-matter mixing coefficients of the strongly coupled $(0,-1)$ TM mode and the exciton, shown in Fig. 4.7(b) shows that the interaction between them is limited to an in-plane momentum range of -1 to $1\,\mu m^{-1}$ due to the strongly dispersive behavior of the TM mode. This has consequences for the emission of such systems as can be seen in Fig. 4.7(c). At the anticrossing, the emission is a mixture of the bare and coupled WS_2, while it is pinned to the bare exciton energy at larger $k_{\|}$ values.

In the TE case (Fig. 4.7(d-f)), a Rabi splitting of 60 meV is also observed for the interaction of the $(\pm1,0)$ SP mode with the WS_2 exciton, despite the slightly lower quality factor of the bare SP mode ($Q \simeq 20$ at 2.010 eV). The dispersion of the TE mode has a parabolic shape as shown in Fig. 4.7(d) (dot-dashed curves). The weaker dispersion of this mode as compared to the $(0,\pm1)$ modes results in a larger range of interacting in-plane momenta, from -5 to 5 μm^{-1}. In the range -2 to 2 μm^{-1}, the measured $|P^+\rangle$ and $|P^-\rangle$ bands are well fitted by the coupled

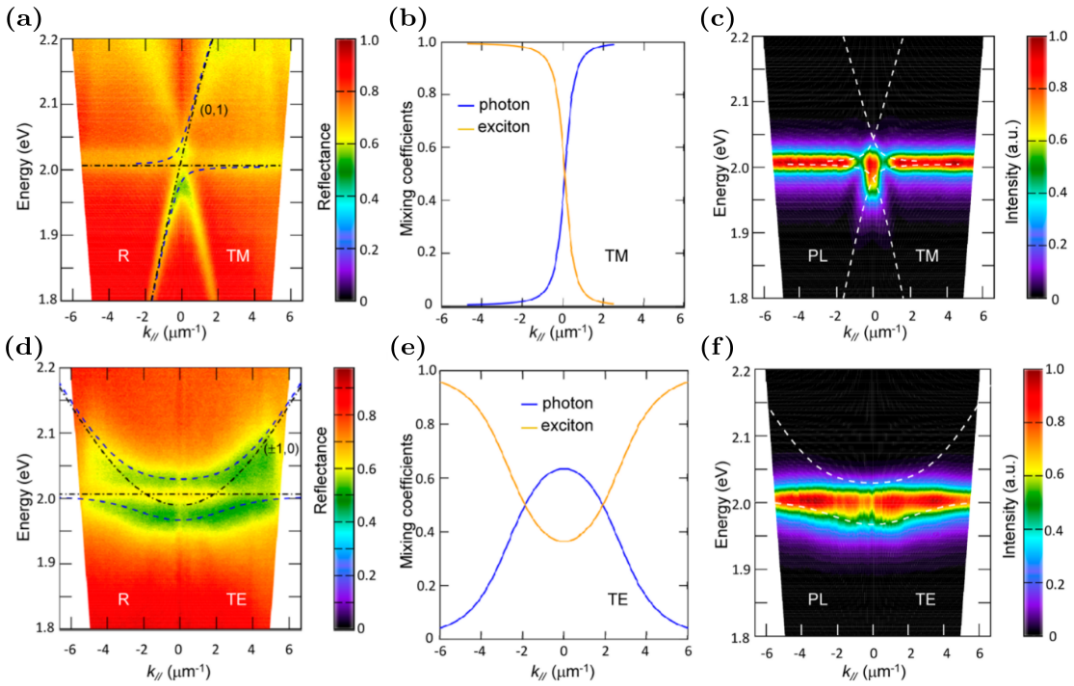

Figure 4.7 – (a,d) Energy/in-plane momentum dispersion for the plasmonic hole array covered with WS_2 monolayer, in TM and TE reflection mode, respectively. The black horizontal dot-dashed line and dispersive curves show, respectively, the energy of the A exciton and the bare SP modes $(0,1)$ and $(\pm1,0)$. The $|P^+\rangle$ and $|P^-\rangle$ band are fitted by the blue dashed curves using a coupled oscillator model. For clarity, (a) only shows the results for the (0, 1) branch. (b,e) The plasmonic (blue) and excitonic (yellow) contents of $|P^-\rangle$ for the $(0,-1)$ and $(\pm1,0)$ branches, respectively. (c,f) Dispersion of the PL measured from the same region. The white dashed curves indicate the coupled oscillators fits obtained from (a) and (d). Reproduced from reference [199].

oscillator model. However, beyond this range $|P^+\rangle$ bends toward lower energies due to its interactions with the higher lying $(\pm1,\pm1)$ SP modes (see Fig. 4.5(d)), which are not included in the fit model. As shown in Fig. 4.7(f), the PL emission is also distributed between the bare exciton and the dispersive $|P^-\rangle$ state.

We have shown in this section clear signatures of room temperature strong coupling by incorporating a WS_2 monolayers into a metallic FP cavity. The system was characterized by transmission, reflection, and emission at room temperature. While the metallic FP cavity gives a larger Rabi splittings for this material, plasmonic resonators also allow one to reach the strong coupling regime, as we demonstrated using a simple square array of circular nano-holes. In the next section, we design chiral plasmonic resonators and explore their interplay with the valley degree of freedom of TMDs.

4.2 SPIN-MOMENTUM LOCKED POLARITONS UNDER CHIRAL STRONG COUPLING

The versatility of plasmonic resonators in tailoring optical near field can be understood from a simple Huygens-Fresnel perspective. Considering each hole of a plasmonic grating as a point source for 2D cylindrical waves of wave vector k_{SP}, the plasmonic launching condition (4.2) becomes a condition for constructive interference for the multiple secondary waves. We show in Fig. 4.8(a,b) a comparison between such a Huygens-Fresnel simulation and the measured SP near field above a square array of holes. This near field measurement was performed on a home built leakage microscopy setup, the details of which can be found in [233]. A direct consequence of this point source description of plasmonic resonators is the possibility to engineer non-trivial SP fields by playing on the distribution of point sources, which amounts to tailoring the phases of the multiple interfering secondary waves, as sketched in Fig. 4.8(c) and discussed in *e.g.* [242]. A striking example

of this is given in Fig. 4.8(d) where a chiral plasmonic vortex is obtained by arranging the SP sources in the form of an Archimedean spiral [195].

Another possibility for tailoring plasmonic near fields is to use dichroic elements, *e.g.* nano-rectangles, as the motif of the periodic grating. In this situation, each point source has a launching efficiency for secondary waves that depends on its orientation with respect to the incident polarization state. In this section, we will make use of this effect by designing a plasmonic grating of rotating nano-rectangles, that allows for the selective launching of SP waves in counter-propagating directions, as determined by the optical spin state of the incident beam [243, 244]. Such an optical spin-orbit (OSO) interaction, that couples the polarization of a light field with its propagation direction has recently attracted considerable attention [245]. An important body of work has described how OSO interactions can be exploited at the level of nano-optical devices, involving dielectric [246–249] or plasmonic architectures [250–255], all able to confine the electromagnetic field below the optical wavelength. Optical spin-momentum locking effects have also been used to spatially route the flow of photoluminescence (PL) depending on the spin of the polarization of the emitter transition [256]. Such directional coupling, also known as chiral coupling, has been demonstrated in both the classical and in the quantum regimes [257–262]. Chiral coupling thus opens new possibilities in the field of light-matter interactions with the design of non-reciprocal devices, ultrafast optical switches, non destructive photon detector, and quantum memories and networks (see [263] and references therein).

In this section, we propose a new platform in which the spin-polarized valleys of a TMD monolayer are strongly coupled to a plasmonic OSO mode, at room temperature (RT). In this strong coupling regime, each spin-polarized valley exciton is hybridized with a single plasmonic mode of specific momentum, as sketched in Fig. 4.9(c). The chiral nature of this interaction generates spin-momentum locked polaritonic states, which we will refer to with the portmanteau *chiralitons*.

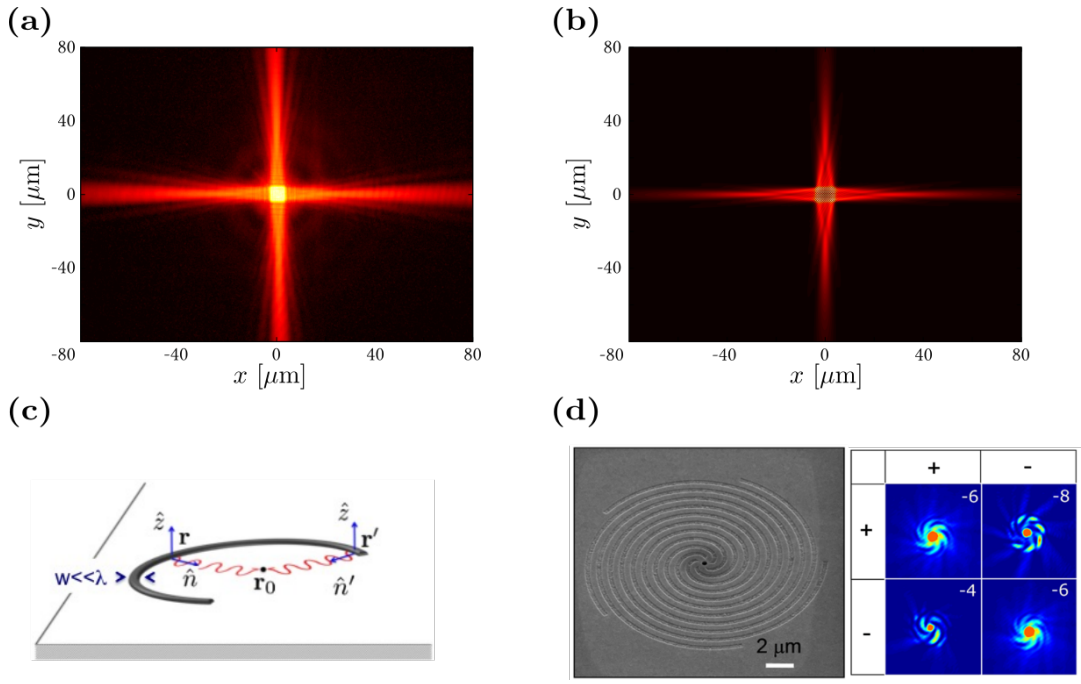

Figure 4.8 – (a) Propagating SP at a Au-air interface, launched by a square array of circular nano-holes (765 nm period, 120 nm diameter) under normal incidence excitation at 785 nm and 45° polarization. This image is acquired using a leakage microscopy setup, with a crossed analyser at −45°. (b) Corresponding Huygens-Fresnel simulation. (c) Sketch of the plasmonic field build-up as a result of multiple contributions from distributed secondary sources. Each segment of the nano-groove launches secondary waves along its local normal vector $\hat{n}$. The variation of this local normal vector along the structure imprints a global topology on the resulting plasmonic field. (d) Example of an Archimedean plasmonic spiral, and the resulting far-field intensity patterns for different circular states of excitation and analysis, as explained in [195].

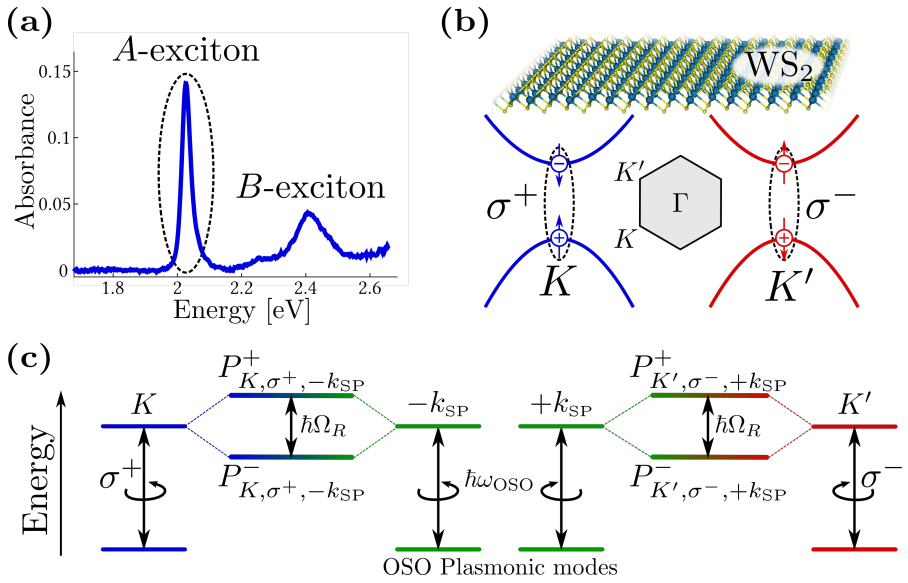

Figure 4.9 – (a) Absorbance spectrum of a WS_2 monolayer as obtained from its transmission spectrum.(b) Crystal packing of a tungsten disulfide (WS_2) monolayer, and sketch of its electronic band structure around the points K and K′ of the Brillouin zone, with the corresponding optical selection rules for band-edge excitons formation under left (σ^+) and right (σ^-) circular excitation. (c) Energy level diagram of the K and K′ excitons of WS_2 strongly coupled to OSO plasmonic modes at energy $\hbar\omega_{OSO}$ and wavevector $\pm k_{SP}$. Reproduced from reference [200].

A striking feature of our platform is its capacity to induce RT robust valley contrasts, enabling the directional transport of chiralitons over micron scale distances. Surprisingly, the strong coupling regime also yields coherent intervalley dynamics whose contribution can still be observed in the steady-state. We hence demonstrate the generation of coherent superpositions of chiralitons flowing in opposite directions. These results, unexpected from the bare TMD monolayer at RT [264–266], point towards the importance of the strong coupling regime where fast Rabi oscillations compete with the TMD valley relaxation dynamics, as very recently discussed in the literature [267–269].

4.2.1 *System under study*

Our system, shown in Fig. 4.10(a), consists of a mechanically exfoliated monolayer of WS_2 covering a plasmonic OSO hole array, with a 5 nm thick dielectric spacer of PMMA. The array, imaged in Fig. 4.10(b), is designed on a (x,y) square lattice with a grating period Λ, and consists of rectangular nano-apertures (160×90 nm^2) rotated stepwise along the x-axis by an angle $\phi=\pi/6$. The associated orbital period $6\times\Lambda$ defines a rotation vector $\vec{\Omega}=(\phi/\Lambda)\hat{z}$, which combines with the spin σ of the incident light into a geometric phase $\Phi_g=-\Omega\sigma x$ [270]. The gradient of this geometric phase imparts a momentum $\vec{k}_g=-\sigma(\phi/\Lambda)\hat{x}$ added to the matching condition on the array between the plasmonic $\vec{k}_{SP}$ and incidence in-plane $\vec{k}_{in}$ momenta:

$$\vec{k}_{SP}=\vec{k}_{in}+(2\pi/\Lambda)(n\hat{x}+m\hat{y})+\vec{k}_g. \tag{4.3}$$

The dispersive properties of such a resonator thus combines two modal responses: plasmon excitations directly determined on the square Bravais lattice of the grating for both σ^+ and σ^- illuminations via $(2\pi/\Lambda)(n\hat{x}+m\hat{y})$, and spin-dependent plasmon OSO modes launched by the additional geometric momentum $\vec{k}_g$. The period of our structure $\Lambda=480$ nm is optimized to have $n=+1$ and $n=-1$ TM modes resonant with the absorption energy of the A-exciton of WS_2 at 2.01 eV for σ^+ and σ^- illuminations respectively. This strict relation between $n=\pm1$ and $\sigma=\pm1$ is the OSO mechanism that breaks the left vs. right symmetry of the modal response of the array, which in this sense becomes chiral. Plasmon OSO modes are thus launched in counter-propagating directions along the x-axis for opposite spins σ of the excitation light. In the case of a bare plasmonic OSO resonator, this is clearly observed in Fig. 4.10 (c). We stress that similar arrangements of anisotropic apertures have previously been demonstrated to allow for spin-dependent surface plasmon launching [194, 252, 255, 271].

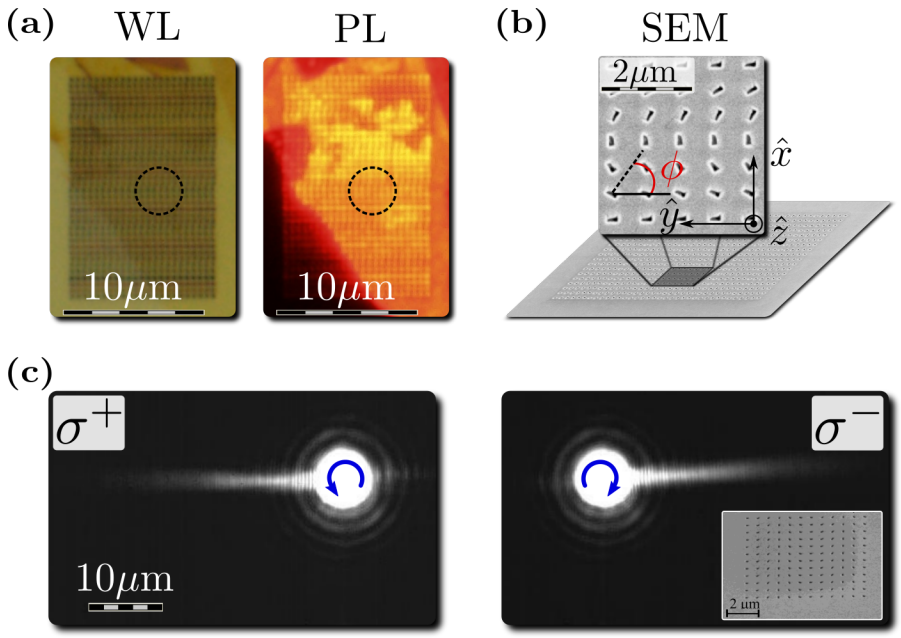

Figure 4.10 – (a) White light (WL) microscope image of the sample and photoluminescence (PL) image of the same area under 2.58 eV excitation. (b) SEM image of the plasmonic OSO resonator fabricated by sputtering 200 nm of gold on a glass substrate coated by a 5 nm thick chromium adhesion layer. The array with ϕ-rotated rectangular apertures is milled through the metallic layers using a focused ion beam (FIB). (c) Real-space leakage radiation microscope images of the surface plasmons launched by σ^+ and σ^- excitations on a OSO plasmonic resonator similar to the one of panel (b). Reproduced from reference [200].

4.2.2 *Results and discussion*

Angle-resolved white light reflection spectra are recorded and shown in Fig. 4.11(a) and (b) in left and right circular polarizations, respectively. In each case, two strongly dispersing branches are observed, corresponding to upper and lower chiralitonic states. Due to the negligible transmission through the structure, those reflection dispersion diagrams are directly giving the absorption dispersion by $A = 1 - R$.

In order to highlight the polaritonic contribution in the absorption spectra, we calculate the first derivative of the reflectivity dispersions $d\left[R_{sample}/R_{substrate}\right]/dE$. The derivative was approximated by interpolating the reflectivity spectra on an equally spaced wavelength grid of step $\Delta\lambda = 0.55$ nm and using the following finite difference expression valid up to fourth order in the grid step:

$$\frac{dR}{d\lambda}(\lambda_0) \simeq \frac{\frac{1}{12}R(\lambda_{-2}) - \frac{2}{3}R(\lambda_{-1}) + \frac{2}{3}R(\lambda_{+1}) - \frac{1}{12}R(\lambda_{+2})}{\Delta\lambda}, \quad (4.4)$$

where $R(\lambda_n)$ is the reflectivity evaluated n steps away from λ_0. The resulting first derivative reflectivity spectra were then converted to an energy scale and plotted as dispersion diagrams in Fig. 4.11(c) and (d).

In these first derivative reflectivity maps, the zero-crossing points correspond to the peak positions of the modes, and the maxima and minima indicate the inflection points of the reflectivity lineshapes. At the excitonic asymptotes of the dispersion curves, where the polaritonic linewidth is expected to match that of the bare WS_2 exciton, we read a linewidth of 26 meV from the maximum to minimum energy difference of the derivative reflectivity maps. This value is equal to the full width at half maximum (FWHM) $\hbar\gamma_{ex}$ that we measured from the absorption spectrum of a bare WS_2 flake on a dielectric substrate, and corresponds to the inhomogeneously broadened A-exciton transition [272].

On the low energy plasmonic asymptotes, we clearly observe the effect of the Bravais and OSO modes, partially over-

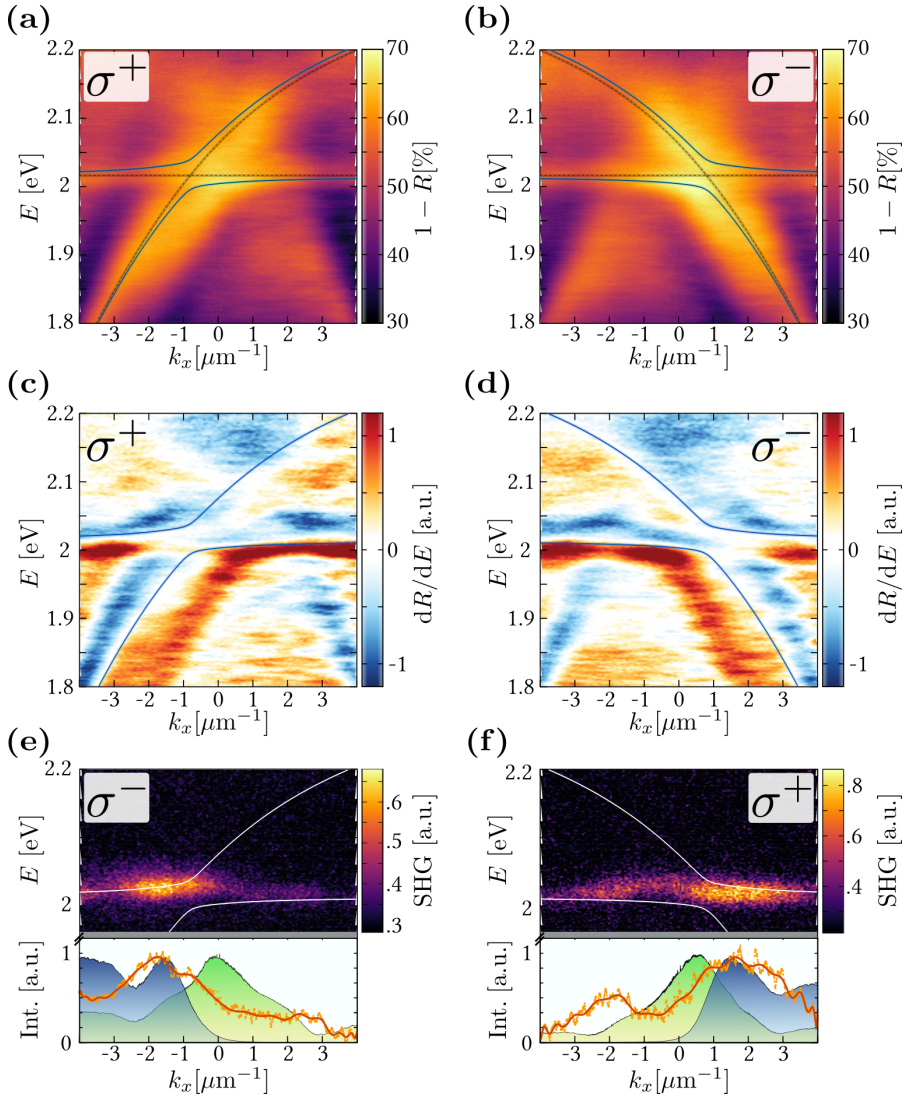

Figure 4.11 – Angle-resolved absorption spectrum of the sample analyzed in (a) left and (b) right circular polarizations, with the best fit coupled oscillator model drawn. First derivative reflectivity maps in (b) left and (c) right circular polarizations, with the best fit coupled oscillator model drawn. Angle-resolved resonant second harmonic spectrum for (e) right and (f) left circular excitations at 1.01eV. Corresponding crosscuts are displayed with the angular profile of the SH signal (red curves), of the absorption spectra at 2 eV (green shades) and of the product (blue shades) between the absorption and the 4^{th} power of the excitonic Hopfield coefficient of the chiralitonic state. Reproduced from reference [200]. .

lapping in an asymmetric broadening of the branches. In this situation, a measure of the mode half-widths can be extracted from the (full) widths of the positive or negative regions of the first differential reflectivity maps. This procedure yields an energy half-width for the plasmonic modes of $\hbar\Gamma_{OSO}/2 = 40$ meV. This width in energy can be related to an in-plane momentum width of ca. 0.5 μm^{-1} via the plasmonic group velocity $v_G = \partial E/\partial k = 87$ meV·μm, that we calculate from the branch curvature at 1.85 eV. This in-plane momentum width results in a plasmonic propagation length of about 4 μm. This value is in very good agreement with the measured PL extension above the structure, as can be seen in Fig. 4.10(b), thus validating our estimation of the mode linewidth $\hbar\Gamma_{OSO} = 80$ meV.

The dispersive modes of the system can be modeled by a dipolar Hamiltonian, where excitons in each valley are selectively coupled to degenerated OSO plasmonic modes of opposite wave vectors $\pm\vec{k}_{SP}$, as depicted in Fig. 4.9(c):

$$\mathcal{H} = \sum_{k_x} \left[\mathcal{H}_{OSO}(k_x) + \mathcal{H}_{ex} + \mathcal{H}_{int}(k_x)\right], \tag{4.5}$$

which consists of three different contributions:

$$\mathcal{H}_{OSO}(k_x) = \hbar\omega_{OSO}(k_x)\left(a^\dagger_{k_x} a_{k_x} + a^\dagger_{-k_x} a_{-k_x}\right), \tag{4.6}$$

$$\mathcal{H}_{ex}(k_x) = \hbar\omega_{ex}\left(b^\dagger_{K-k_x} b_{K-k_x} + b^\dagger_{K'+k_x} b_{K'+k_x}\right), \tag{4.7}$$

$$\begin{aligned}\mathcal{H}_{int}(k_x) \;=\; & \hbar g\left(a^\dagger_{k_x} + a_{k_x}\right)\left(b^\dagger_{K'+k_x} + b_{K'+k_x}\right) \\ & + \hbar g\left(a^\dagger_{-k_x} + a_{-k_x}\right)\left(b^\dagger_{K-k_x} + b_{K-k_x}\right),\end{aligned} \tag{4.8}$$

where $a(a^\dagger)$ are the lowering (raising) operators of the OSO plasmonic modes of energy $\hbar\omega_{OSO}(k_x)$, $b(b^\dagger)$ are the lowering (raising) operators of the exciton fields of energy $\hbar\omega_{ex}$, and $g = \Omega_R/2$ is the light-matter coupling frequency. The dispersion of the exciton energy can be safely neglected on the scale of

the plasmonic wave vector $\vec{k}_{SP}$. In this hamiltonian the chiral light-chiral matter interaction is effectively accounted for by coupling excitons of the valley $K'(K)$ to plasmons propagating with wave vectors $k_x(-k_x)$. A microscopic description of this spin-selective coupling process in the near-field is currently being developed in collaboration with S. Schutz and D. Hagenmuller in G. Pupillo's group, as we will briefly discuss in the outlooks of this thesis.

Using the Hopfield procedure, we can diagonalize the total Hamiltonian by finding polaritonic normal mode operators $P^{\pm}_{K(K')}$ associated with each valley, and obeying the following equation of motion at each k_x

$$\left[P^{\pm}_{K(K')}, \mathcal{H}\right] = \hbar\omega_{\pm} P^{\pm}_{K(K')}, \tag{4.9}$$

with $\omega_{\pm} > 0$. In the rotating wave approximation (RWA), justified here by the moderate coupling strength, $P^{j}_{\lambda} \simeq \alpha^{j}_{\lambda} a + \beta^{j}_{\lambda} b$, $j \in \{+,-\}$ and $\lambda \in \{K, K'\}$. The plasmonic and excitonic Hopfield coefficients $\alpha^{j}_{\lambda}(k_x)$ and $\beta^{j}_{\lambda}(k_x)$ are obtained by diagonalizing the following matrix for every k_x

$$\begin{pmatrix} \hbar\omega_{OSO} & i\hbar\Omega_R/2 & 0 & 0 \\ -i\hbar\Omega_R/2 & \hbar\omega_{ex} & 0 & 0 \\ 0 & 0 & -\hbar\omega_{OSO} & i\hbar\Omega_R/2 \\ 0 & 0 & -i\hbar\Omega_R/2 & -\hbar\omega_{ex} \end{pmatrix}. \tag{4.10}$$

The dynamics of the coupled system will be ruled by the competition between the coherent evolution described by the Hamiltonian (4.5) and the different dissipative processes contributing to the uncoupled modes linewidths. This can be taken into account by including the measured linewidths as imaginary parts in the excitonic and plasmonic mode energies (Weisskopf-Wigner approach). Under such conditions, the equation of motion (4.9) leads us to evaluate the eigenvalues $\omega_{\pm}$ which real parts are fitted to the dispersions shown in

Fig. 4.11(a) and (b). A best fit yields the polaritonic branch splitting

$$\hbar(\omega_+ - \omega_-) = \sqrt{(\hbar\Omega_R)^2 - (\hbar\gamma_{ex} - \hbar\Gamma_{OSO})^2} \tag{4.11}$$

which equals 40 meV. From the determination of the FWHM of the excitonic $\hbar\gamma_{ex}$ and plasmonic $\hbar\Gamma_{OSO}$ modes, we evaluate a Rabi energy $\hbar\Omega_R = 70$ meV. These values allow us to recover the strong coupling criterion [36]

$$(\hbar\Omega_R)^2 / \left((\hbar\gamma_{ex})^2 + (\hbar\Gamma_{OSO})^2\right) = 0.69 > 0.5, \tag{4.12}$$

which demonstrates that our system is operating in the strong coupling regime.

In view of chiral light-chiral matter interactions, we further investigate the interplay between the OSO plasmonic chirality and the valley-contrasting chirality of the WS_2 monolayer. A first demonstration of such an interplay is found in the resonant second harmonic (SH) response of the strongly coupled system. Indeed, monolayer TMDs have been shown to give a high valley contrast in the generation of a SH signal resonant with their A-excitons [273]. As we show in Fig. 4.12, such high SH valley contrasts are measured on a bare WS_2 monolayer. The valley optical selection rules for SH generation are opposite to those in linear absorption since the process involves two excitation photons, and are more robust since the SH process is instantaneous.

The angle resolved resonant SH signals from the strongly coupled system are shown in Fig. 4.11(e) and (f) for right and left circularly polarized excitation, respectively. The SH signals are angularly exchanged when the spin of the excitation is reversed with a right vs. left contrast (ca. 20%) close to the one measured on the reflectivity maps (ca. 15%). In view of the behavior observed on a bare flake in Fig. 4.12, this result unambiguously demonstrates the selective coupling of excitons in one valley to surface plasmons propagating in one direction,

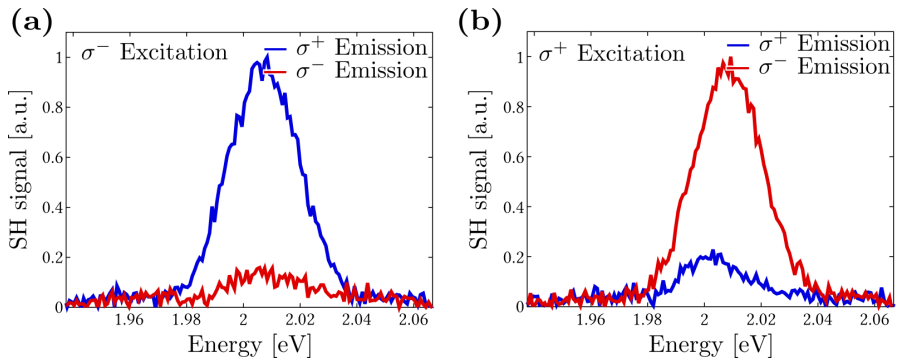

Figure 4.12 – Resonant SH spectrum for left and right circular analysis, for (a) left and (b) right circular excitation at 1.01eV. Reproduced from reference [200]. .

thus realizing valley-contrasting chiralitonic states with spins locked to their propagation wavevectors:

$$|P^{\pm}_{K,\sigma^+,-k_{SP}}> = |g_K, 1_{\sigma^+}, -k_{SP}> \pm |e_K, 0_{\sigma^+}, -k_{SP}>$$
$$|P^{\pm}_{K',\sigma^-,+k_{SP}}> = |g_{K'}, 1_{\sigma^-}, +k_{SP}> \pm |e_{K'}, 0_{\sigma^-}, +k_{SP}>,$$

where $e_i(g_i)$ corresponds to the presence (absence) of an exciton in the valley $i = (K, K')$ of WS_2, and $1_j(0_j)$ to 1 (0) plasmon in the mode of polarization $j = (\sigma^+, \sigma^-)$ and wavevector $\pm k_{SP}$.

The detailed features of SH signal (crosscuts in Fig. 4.11(e) and (f)) reveal within the bandwidth of our pumping laser the contributions of both the uncoupled excitons and the upper chiraliton to the SH enhancement. The key observation, discussed bellow, is the angular dependence of the main SH contribution. This contribution, shifted from the anticrossing region, is a feature that gives an additional proof of the strongly coupled nature of our system because it is determined by the excitonic Hopfield coefficient of the spin-locked chiralitonic state. In contrast, the residual SH signal related to the uncoupled (or weakly coupled) excitons simply follows the angular profile of the absorption spectra taken at 2 eV, and is thus observed over the anticrossing region. Resonant SH spectroscopy of our system therefore confirms the presence of the chiralitonic states, with the valley contrast of WS_2 and the spin-locking property

of the OSO plasmonic resonator being imprinted on these new eigenstates of the system.

In general, the resonant SH signal writes as [137, 139]:

$$I(2\omega) \propto (\rho_\omega I_\omega)^2 \cdot |\chi^{(2)}(2\omega)|^2 \cdot \rho_{2\omega} \tag{4.13}$$

where I_ω is the pump intensity, $\chi^{(2)}(2\omega)$ the second order susceptibility, ρ_ω the optical mode density of the resonator related to the fraction of the pump intensity that reaches WS_2 and $\rho_{2\omega}$ the optical mode density of the resonator that determines the fraction of SH intensity decoupled into the far field. While ρ_ω can safely be assumed to be non-dispersive at $\hbar\omega = 1$ eV, the dispersive nature of the resonator leads to $\rho_{2\omega}$ strongly dependent on the in-plane wave vector k_x. The optical mode density being proportional to the absorption, $\rho_{2\omega}(k_x)$ is given by the angular absorption spectrum crosscut at $2\hbar\omega = 2$ eV, displayed in the lower panels of Fig. 4.11(e) and (f).

Under the same approximations of [138], the resonant second order susceptibility can be written as

$$\chi^{(2)}(2\omega) = \alpha^{(1)}(2\omega) \sum_n \frac{K_{eng}}{\omega_{ng} - \omega} \tag{4.14}$$

where $\sum_n$ sums over virtual electronic transitions, and $K_{eng} = \langle e|\vec{p}|g\rangle \otimes \langle e|\vec{p}|n\rangle \otimes \langle n|\vec{p}|g\rangle$ is a third-rank tensor built on the electronic dipole moments $\vec{p}$ taken between the e, n, g states. The prefactor $\alpha^{(1)}(2\omega)$ is the linear polarizability of the system at frequency 2ω, yielding resonantly enhanced SH signal at every allowed $|g\rangle \rightarrow |e\rangle$ electronic transitions of the system.

With two populations of uncoupled and strongly coupled WS_2 excitons, the SH signal is therefore expected to be resonantly enhanced when the SH frequency matches the transition frequency of either uncoupled or strongly coupled excitons. When the excited state is an uncoupled exciton associated with a transition energy fixed at frequency $2\hbar\omega = 2$ eV for all angles, the tensor K_{eng} is non-dispersive and the SH signal is simply determined and angularly distributed from $\rho_{2\omega}(k_x)$.

When the excited state is a strongly coupled exciton, the resonant second order susceptibility becomes dispersive with $\chi^{(2)}(2\omega, k_x)$. This is due to the fact that the tensor K_{eng} incorporates the excitonic Hopfield coefficient of the polaritonic state involved in the electronic transition $|g\rangle \rightarrow |e\rangle$ when the excited state is a polaritonic state. In our experimental conditions with a pump frequency at 1 eV, this excited state is the upper polaritonic state with $|e\rangle \equiv |P^{+}_{K(K'),\sigma^{\pm}}, \mp k_{SP}\rangle$ and therefore $K_{eng} \propto [\beta^{+}_{K(K')}(k_x)]^2$. This dispersive excitonic Hopfield coefficient is evaluated by the procedure described in details above, Sec. A. The profile of the SH signal then follows the product between the optical mode density $\rho_{2\omega}(k_x)$ and $|\chi^{(2)}(2\omega, k_x)|^2 \propto [\beta^{+}_{K(K')}(k_x)]^4$.

These two contributions are directly resolved in the SH data displayed in Fig. 4.11(e) and (f). A residual signal is measured in particular within the anticrossing region, as expected from the angular profile of $\rho_{2\omega}(k_x)$, while the angular distribution of the main SH signal clearly departs from $\rho_{2\omega}(k_x)$, revealing the dispersive influence of $\beta^{+}_{K(K')}(k_x)$. This feature is thus a direct proof of the existence of chiralitonic states, *i.e.* of the strongly coupled nature of our system.

Revealed by these resonant SH measurements, the spin-locking property of chiralitonic states incurs however different relaxation mechanisms through the dynamical evolution of the chiralitons. In particular, excitonic intervalley scattering erases valley contrast in bare WS_2 at RT [274]. In our configuration, this would transfer chiraliton population from one valley to the other, generating via optical spin-locking, a reverse flow, racemizing the chiraliton population. This picture however does not account for the possibility of more robust valley contrasts in strong coupling conditions, as recently reported with $MoSe_2$ in Fabry-Pérot cavities [267]. Interestingly, the intervalley scattering rate $\hbar\gamma_{KK'}$ does not enter in this strong coupling criterion discussed above. Indeed, such events corresponding to an inversion of the valley indices $K \leftrightarrow K'$ do not directly determine the measured inhomogeneous excitonic linewidth [223], and are thus not detrimental to the observation

of strong coupling. In the $\hbar\Omega_R \ll \hbar\gamma_{KK'}$ limit, the Hamiltonian (4.5) would simply reduce to the usual RWA Hamiltonian and the valley contrasting chiralitonic behavior would be lost. The results presented below clearly show that this is not the case for our system, allowing us to conclude that the Rabi frequency overcomes such intervalley relaxation rates. Remarkably, strong coupling thus allows us to quantitatively estimate those rates, in close relation with [275].

The chiralitonic flow is measured by performing steady-state angle resolved polarized PL experiments, averaging the signal over the PL lifetime of ca. 200 ps, corresponding to a spontaneous decay rate of $\hbar\gamma_0 = 3.3\mu$eV. For these experiments, the laser excitation energy is chosen at 1.96 eV, slightly below the WS_2 band-gap. At this energy, the measured PL results from a phonon-induced up-convertion process that minimizes intervalley scattering events [276]. The difference between PL dispersions obtained with left and right circularly polarized excitations is displayed in Fig. 4.13(a), showing net flows of chiralitons with spin-determined momenta. This is in agreement with the differential white-light reflectivity map $R_{\sigma^-} - R_{\sigma^+}$ of Fig. 4.13(b). Considering that this map gives the sorting efficiency of our OSO resonator, such correlations in the PL implies that the effect of the initial spin-momentum determination of the chiralitons (see Fig. 4.11) is remnant after 200 ps at RT. After this PL lifetime, a net chiral flow $\mathcal{F} = I_{\sigma^-} - I_{\sigma^+}$ of $\sim 6\%$ is extracted from Fig. 4.13(a). This is the signature of a chiralitonic valley polarization, in striking contrast with the absence of valley polarization that we observe for a bare WS_2 monolayer at RT [200]. The extracted net flow is however limited by the finite optical contrast $\mathcal{C}$ of our OSO resonator, which we measure at a 15% level from a cross-cut taken on Fig. 4.13(b) at 1.98 eV. It is therefore possible to infer that a chiralitonic valley contrast of $\mathcal{F}/\mathcal{C} \simeq 40\%$ can be reached at RT for the strongly coupled WS_2 monolayer. As mentioned above, we understand this surprisingly robust contrast by invoking the fact that under strong coupling conditions, valley relaxation is outweighed by the faster Rabi energy exchange between the

exciton of each valley and the corresponding plasmonic OSO mode, a cavity protection mechanism that we quantitatively assess below. From the polaritonic point of view, the local dephasing and scattering processes at play on bare excitons that erase valley contrasts on a bare WS2 flake are reduced by the delocalized nature of the chiralitonic state, a process akin to motional narrowing and recently observed on other polaritonic systems [267–269, 277].

As a consequence of this motional narrowing effect, such a strongly coupled system involving atomically thin crystals of TMDs could then provide new ways to incorporate intervalley coherent dynamics [264, 266, 278–280] into the realm of polariton physics. To illustrate this, we now show that two counter-propagating flows of chiralitons can evolve coherently. It is clear from the sketch of Fig. 4.9(c) that within such a coherent superposition of counter-propagating chiralitons

$$|\Psi>=|P^{\pm}_{K,\sigma^+,-k_{SP}}>+|P^{\pm}_{K',\sigma^-,+k_{SP}}> \tag{4.15}$$

flow directions and spin polarizations become non-separable.

Intervalley coherence is expected to result in a non-zero degree of linearly polarized PL when excited by the same linear polarization. As detailed in the Methods section below, this can be monitored by measuring the $S_1 = I_{TM} - I_{TE}$ coefficient of the PL Stokes vector, where $I_{TM(TE)}$ is the emitted PL intensity analyzed in TM (TE) polarization. This coefficient is displayed in the k_x-energy plane in Fig. 4.13(c) for an incident TM polarized excitation at 1.96 eV. Fig. 4.13(e) displays the same coefficient under TE excitation. A clear polarization anisotropy on the chiraliton emission is observed for both TM and TE excitation polarizations, both featuring the same symmetry along the $k_x = 0$ axis as the differential reflectivity dispersion map $R_{TM} - R_{TE}$ shown in Fig. 4.13(d). The degree of chiralitonic intervalley coherence -see details below- can be directly quantified by the difference $(S_1^{out}|_{TM} - S_1^{out}|_{TE})/2$, which measures the PL linear depolarization factor displayed (as m_{11}) in Fig. 4.13(f). By this procedure, we retrieve a chiralitonic intervalley coherence that

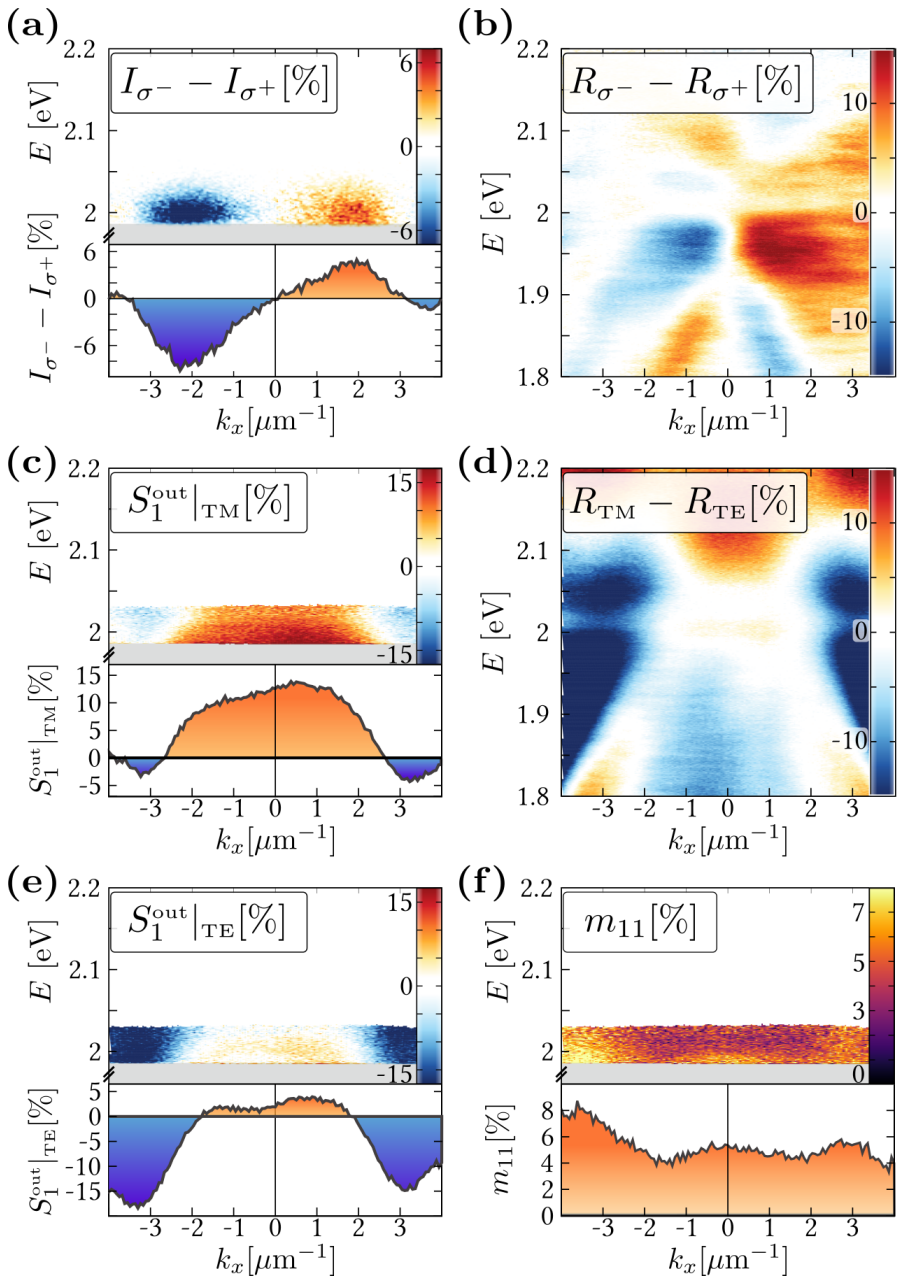

Figure 4.13 – (a) Differential PL dispersion spectrum for left and right circularly polarized excitations. The shaded regions in all panels are removed by the laser line filter, and the cross-cuts are taken at 2 eV. (b) Differential angle-resolved reflection spectrum for left and right circularly polarized light. (c), (e) Angle-resolved spectrum of the normalized coefficient $S_1^{out}|_{TM(TE)}/S_0$ of the PL Stokes vector for a TM(TE) polarized excitation (see text for details). Note that we have put a detection threshold below 100 photon counts that cuts the signal above ~ 2.03 eV in panels (a), (c), (e) and (f). (d) Differential angle-resolved reflection spectrum obtained from analyzed TM and TE measurements. (f) k_x-energy dispersion of the degree of chiralitonic inter-valley coherence m_{11} computed from (c) and (e). Reproduced from reference [200].

varies between 5% and 8% depending on k_x. Interestingly, these values that we reach at RT have magnitudes comparable to those reported on a bare WS_2 monolayer at 10 K [281]. Our results directly show how such strongly coupled TMD systems can sustain RT coherent dynamics robust enough to be observed despite the long exciton PL lifetimes and plasmonic propagation distances.

In view of assessing the competition between such RT cavity protection effects and the relaxational dynamics of the TMD valleys, we present here preliminary results on the steady state resolution of the model sketched in Fig. 4.14(a). This model, developed in collaboration with S. Schutz and D. Hagenmuller in G. Pupillo's group, builds upon a recently proposed model by Stern and coworkers [268] and is currently being extended and confronted to more experimental results, as discussed in the outlooks chapter. Briefly, it amounts to finding the steady state solutions of a quantum master equation, in which excitons in the K valley are incoherently pumped at a small rate ($\hbar\gamma_p = 0.1\mu eV$). Those excitons can then undergo coherent Rabi dynamics with a coupling frequency $\hbar g = 35$ meV (equal to that measured experimentally above), or undergo incoherent relaxational processes toward the ground state (with a rate $\hbar\gamma_0 = 3.3\mu eV$) or toward the other excitonic valley (with a rate $\hbar\gamma_{KK'}$). The dephasing rate of the excitonic ensemble, given by their inhomogeneously broadened spectroscopic linewidth $\hbar\gamma_{ex} = 26$ meV, is described by a Lindblad term applying random jumps to the exciton phase [236]. Both OSO plasmonic modes decay at a rate $\Gamma_{OSO} = 80$ meV.

We show in Fig. 4.14(b) the evolution of the steady state valley contrast C as a function of the intervalley scattering rate $\gamma_{KK'}$, defined as

$$C = \frac{n_K - n_{K'}}{n_K + n_{K'}}, \tag{4.16}$$

where $n_{K(K')}$ is the exciton population in the $K(K')$ valley. Interestingly, the valley contrast of 40%, that we inferred from the experimentally measured valley contrast and the finite optical contrast of our OSO resonator, is obtained at $\hbar\gamma_{KK'} =$

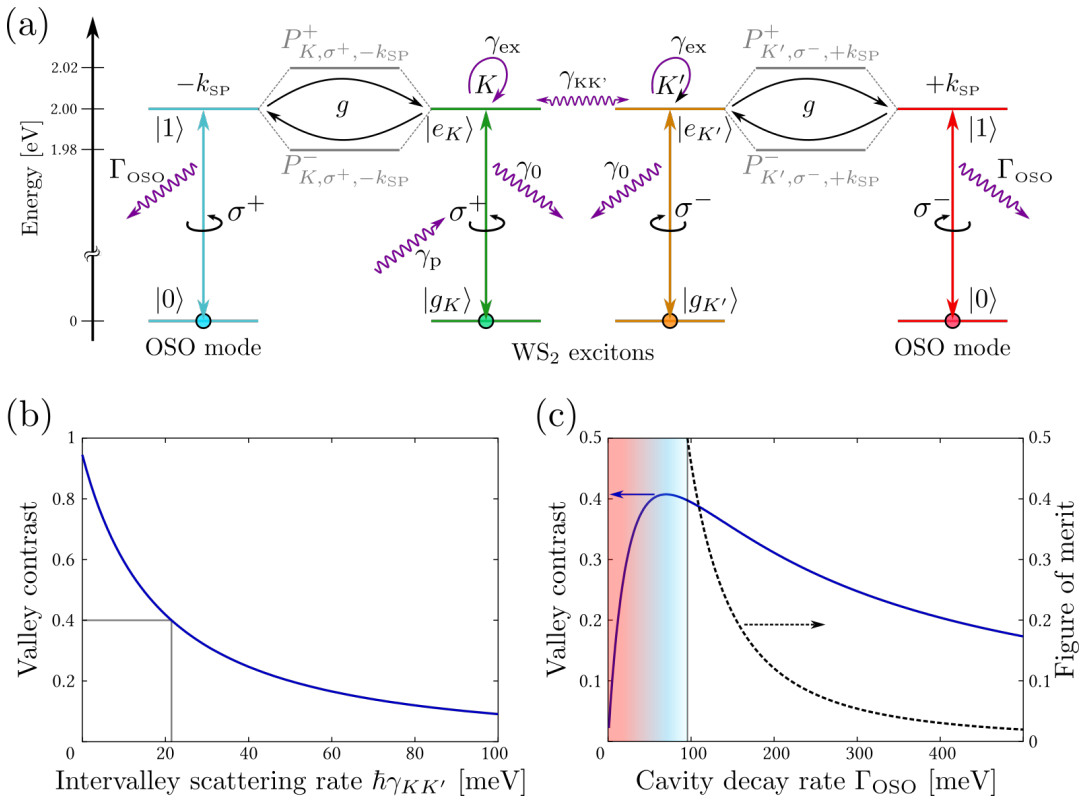

Figure 4.14 – (a) Schematic representation of the toy model for valley protection under chiral strong coupling (notations detailed in the main text). (b) Steady state valley contrast as a function of the intervalley scattering rate $\hbar\gamma_{KK'}$. The valley contrast of 40%, inferred from our measurements is obtained at $\hbar\gamma_{KK'} = 22$ meV. (c) Valley contrast as a function of the plasmonic decay rate Γ_{OSO}. The black dashed curve is a figure of merit of strong coupling (see main text), and it exceeds the threshold value of 0.5 at the position indicated by the vertical gray line. Strong coupling is thus achieved in the colored region.

22 meV. This value of intervalley scattering rate, close to $k_B T$ at room temperature, is of the order of magnitude of the typical phononic scattering rates contributing to the relaxation of valley polarization in the bare material [223]. This model is currently being extended to assess the dynamics of intervalley coherences under coherent pumping.

Along the same lines as what was done in chapter 1 for finding the optimal conditions of the polaritonic energy transfer mechanism, we now investigate the conditions that maximize the valley contrast of chiralitons. Again this optimal cavity protection regime cannot correspond to the ideal undamped strong coupling regime, in which the population would oscillate between the plasmonic mode and the exciton until being racemized between the two valleys. The ideal condition that we are looking for is that of a very fast Rabi oscillation, transferring the initial exciton population to the OSO plasmonic mode, followed by the rapid radiative decay of this plasmon toward the detection system. In this situation, the irreversible decay of the plasmon leaks the valley index information out of the system before the reversible Rabi exchange brings back the population on the exciton state where $\gamma_{KK'}$ can act. One however cannot afford a too large radiative linewidth for the plasmonic mode either, as this would deteriorate the Rabi exchange process by a quantum Zeno effect [282]. Indeed, it is the energy splitting of the polaritonic states (4.11) that determines -by Fourier transformation- the period of the population exchange between the coupled modes; and this energy splitting requires Γ_{OSO} not too different from γ_{ex} to sustain a branch splitting. The optimal curve of chiraliton valley contrast is shown in Fig. 4.14(c, blue curve), together with the figure of merit of strong coupling $(\hbar\Omega_R)^2 / \left((\hbar\gamma_{ex})^2 + (\hbar\Gamma_{OSO})^2\right)$. In striking analogy with the results obtained for optimal polariton energy transfer, this curve predicts an optimal chiraliton valley contrast for systems lying at the 'bad cavity' edge of strong coupling regime. In particular, this optimum is found for a cavity linewidth of *ca.* 70 meV, close to the experimental value of 80 meV.

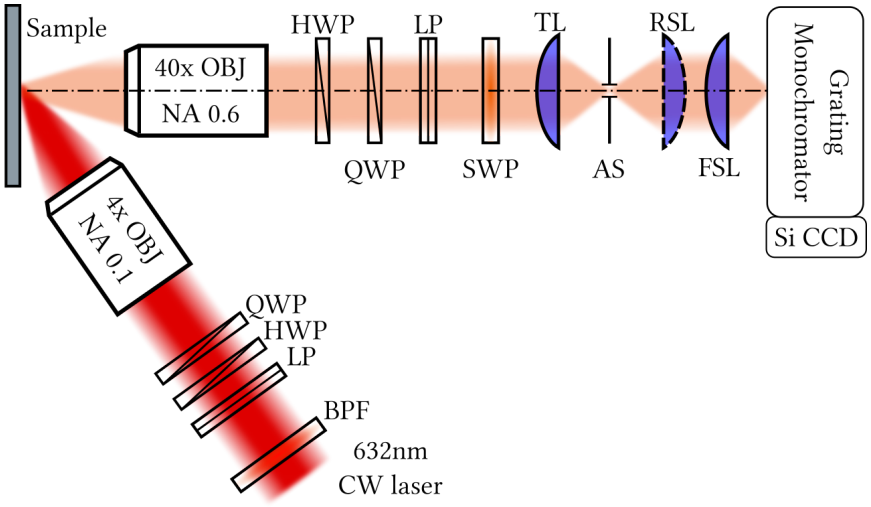

Figure 4.15 – Optical setup used for the angle-resolved polarimetric measurements. See the corresponding paragraph for details. Reproduced from reference [200].

4.2.3 *Methods*

The optical setup used for PL polarimetry experiments is shown in Fig. 4.15. The continous-wave HeNe pumping laser is filtered by a bandpass filter (BPF) and its polarization state is controlled by a set of polarization optics: a linear polarizer (LP), a half-wave plate (HWP) and a quarter-wave plate (QWP). The beam is focused onto the sample surface at oblique incidence angle by a microscope objective to a typical spot size of 100 μm^2, corresponds to an optical flux of 10 $W{\cdot}cm^{-2}$. In such conditions of irradiation, the PL only comes from the A—exciton. The emitted PL signal is collected by a high numerical aperture objective, and its polarization state is analyzed by another set of broadband polarization optics (HWP, QWP, LP). A short-wavelength-pass (SWP) tunable filter is placed on the optical path to stop the laser light scattered. The rest of the detection line is identical to the one described in Fig. 4.6(c). This side-excitation configuration allows us to work without a beam splitter, avoiding its detrimental effect on polarization states.

Using this optical setup, we measure the angle-resolve PL spectra for different combinations of excitation and detection

polarizations. Such measurements allow us to retrieve the coefficients of the Mueller matrix $\mathcal{M}$ of the system, characterizing how the polarization state of the excitation beam affects the polarization state of the chiralitons PL. As discussed above, the spin-momentum locking mechanism of our chiralitonic system relates such PL polarization states to specific chiraliton dynamics. An incident excitation in a given polarization state is defined by a Stokes vector $\vec{S}^{in}$, on which the matrix $\mathcal{M}$ acts to yield an output PL Stokes vector $\vec{S}^{out}$:

$$\vec{S}^{out} = \begin{pmatrix} I \\ I_V - I_H \\ I_{45} - I_{-45} \\ I_{\sigma^+} - I_{\sigma^-} \end{pmatrix}_{out} = \mathcal{M} \begin{pmatrix} I_0 \\ I_V - I_H \\ I_{45} - I_{-45} \\ I_{\sigma^+} - I_{\sigma^-} \end{pmatrix}_{in}, \qquad (4.17)$$

where $I_{(0)}$ is the emitted (incident) intensity, $I_V - I_H$ is the relative intensity in vertical and horizontal polarizations, $I_{45} - I_{-45}$ is the relative intensity in $+45^o$ and -45^o polarizations and $I_{\sigma^+} - I_{\sigma^-}$ is the relative intensity in σ^+ and σ^- polarizations. We recall that for our specific alignment of the OSO resonator with respect to the slits of the spectrometer, the angle-resolved PL spectra in V and H polarizations correspond to transverse-magnetic (TM) and transverse-electric (TE) dispersions respectively (see Fig. 4.10(b)). Intervalley chiraliton coherences, revealed by a non-zero degree of linear polarization in the PL upon the same linear excitation, are then measured by the $S_1 = I_V - I_H$ coefficient of the PL output Stokes vector. This coefficient is obtained by analysing the PL in the linear basis, giving an angle-resolved PL intensity $\left(S_0^{out} + (-)S_1^{out}\right)/2$, for TM (TE) analysis. In order to obtain the polarization characteristics of the chiralitons, we measure the four possible

combinations of excitation and detection polarization in the linear basis:

$$I_{TM/TM} = (m_{00} + m_{01} + m_{10} + m_{11})/2 \quad (4.18)$$
$$I_{TM/TE} = (m_{00} + m_{01} - m_{10} - m_{11})/2 \quad (4.19)$$
$$I_{TE/TM} = (m_{00} - m_{01} + m_{10} - m_{11})/2 \quad (4.20)$$
$$I_{TE/TE} = (m_{00} - m_{01} - m_{10} + m_{11})/2, \quad (4.21)$$

where $I_{p/a}$ is the angle-frequency resolved intensity measured for a pump polarization p = (TE,TM) and analysed in a = (TE,TM) polarization, and $m_{i,j}$ are the coefficients of the 4x4 matrix $\mathcal{M}$. By solving this linear system of equations, we obtain the first quadrant of the Mueller matrix: m_{00}, m_{01}, m_{10} and m_{11}. The $S_1^{out}|_{TM}$ coefficient of the output Stokes vector for a TM excitation is then directly given by $m_{10} + m_{11}$ as can be seen from (4.17) by setting $I_V = 1, I_H = 0$ and all the other input Stokes coefficients to zeros. This quantity, normalized to S_0^{out}, is displayed in the k_x—energy plane in Fig. 4.13(c). Similarly, the $S_1^{out}|_{TE}$ coefficient is given by $m_{10} - m_{11}$, which is the quantity displayed in Fig. 4.13(d).

As the dispersion of the OSO resonator is different for TE and TM polarizations, the pixel-to-pixel operations performed to obtain S_1^{out} do not directly yield the chiraliton inter-valley contrast. In particular, the observation of negative value regions in $S_1^{out}|_{TM}$ only reveals that the fraction of chiralitons that lost inter-valley coherence contributes more strongly to the PL in regions where the TE mode dominates over the TM mode (see Fig. 4.13(c) and (e)). It *does not* correspond to genuine anti-correlation of the chiraliton PL polarization with respect to the pump polarization. To correct for such dispersive effects and obtain the degree of chiraliton intervalley coherence, the appropriate quantity is $(S_1^{out}|_{TM} - S_1^{out}|_{TE})/(2S_0^{out}) = m_{11}$, resolved in the k_x—energy plane in Fig. 4.13(f). This quantity can also be refered to as a chiraliton linear depolarization factor.

4.2.4 *Conclusions*

In summary, we demonstrate valley contrasting spin-momentum locked chiral polaritonic states in an atomically thin TMD semiconductor strongly coupled to a plasmonic OSO resonator. Likely, the observation of such contrasts even after 200 ps lifetimes is made possible by the unexpectedly robust RT coherences inherent to the strong coupling regime. Exploiting such robust coherences, we measure chiralitonic flows that can evolve as superpositions over micron scale distances. Our results show that the combination of OSO interactions with TMD valleytronics is an interesting path to follow in order to explore and manipulate RT coherences in chiral quantum architectures under strong coupling [262, 283].

5

CONCLUSIONS AND OUTLOOKS

In this thesis, we have explored different facets of light-matter strong coupling in complex materials, revealing how collective polaritonic states can redefine energetic landscapes and dynamics in the coupled system.

The photophysical properties within such polaritonic landscapes are in general complex, and cannot be simply deduced from those of the uncoupled systems through a mere change of basis. Instead, the interplay between coupled and uncoupled degrees of freedom as well as the non-Markovian nature of the coupling process leads to distinct polaritonic properties, hence behaving as a new kind of supramolecular entity. In particular, we show that such states can be longer lived than their uncoupled constituents, and can display surprisingly intense non-linear optical response. Moreover, the tremendous diversity of chemical species that can be used in the context of light-matter strong coupling allows us to tailor specific polaritonic landscapes, as we show in the context of energy transfer mechanism. At this stage, a deeper understanding of such polaritonic landscapes becomes crucial, in particular in the vicinity of conical intersections of potential energy surfaces where Born-Oppenheimer approximations fail. This topic is the subject of current efforts from different theoretical [95–105] and experimental perspectives [46].

The possibilities offered by strong coupling in modifying chemical landscapes is most directly revealed when coupling light to a molecular vibration of the electronic ground state manifold. New chemical reaction rates have recently been re-

ported by our group in this vibrational strong coupling regime (VSC) [15], and other experiments are currently ongoing in view of modifying solvation mechanisms and proteins folding. In a similar perspective, we are currently investigating the possibility of modifying superconductivity phase transitions by perturbing molecular vibrations under VSC. Another topic that is being explored is the non-linear behavior of vibro-polaritons, potentially leading to the formation of an out of equilibrium Bose-Einstein condensate in such systems. The possibility of a chemical reaction on such a quantum degenerated states of matter is a most stimulating perspective.

In view of imprinting specific properties of the coupled materials on the polaritonic states, we explore the interplay between optical chirality and material chirality in the strong coupling regime. By coupling the valley polarized transitions of an atomically thin crystal of transition metal dichalcogenide (TMD) to spin-momentum locked plasmonic resonances, we reach this chiral light-chiral matter strong coupling regime, in which the electronic valley coherences of the material are found to be surprisingly strengthened. One particularly intriguing aspect of these results is the fact that the in-plane orientation of the bright excitons in the TMD, combined with the transverse magnetic nature of plasmonic modes, does not *a priori* allow for such a valley selective cavity protection effect. The details of this coupling mechanism, involving the transverse spin of surface plasmons [284] and the contribution of dark TMD excitons [285–288] is currently being explored both theoretically and experimentally. This work also opens a wealth of possible perspectives in the context of the topological engineering of polaritonic fields. Singular fluorescence and polaritonic vortices are currently under study in TMDs coupled to plasmonic Archimedean spirals.

6

RÉSUMÉ DE LA THÈSE

6.1 CONTEXT

Depuis ses premiers développements expérimentaux dans le domaine des atomes froids dans les années 1980[1], le régime de couplage fort de l'électrodynamique quantique de cavité (cQED) s'est imposé comme une des nouvelles frontières de la science, en offrant un contrôle sans précédent sur les propriétés de la lumière et de la matière. Les développements récents en condensation de Bose-Einstein, en superfluidité, en manipulation et transfert de l'intrication quantique, en production de champs de jauge synthétiques et en modification de réaction chimique dans les systèmes fortement couplés promettent de fascinantes applications technologiques et ouvrent de nouvelles voies de recherche fondamentale[16, 46].

Ce régime de couplage fort a récemment été atteint dans une grande variété de systèmes, dont les puits quantiques dans les semi-conducteurs inorganiques, les bits quantiques supraconducteurs, les transitions nucléaires, ainsi que dans les transitions électroniques et vibrationnelles de semi-conducteurs organiques. Dans toutes ces différentes réalisations du couplage fort, la dynamique du système peut être décrite sur la base d'un même Hamiltonien effectif, rendant compte du couplage entre la lumière et la matière, toutes deux idéalisées comme des systèmes à deux niveaux[2]. Lorsque l'interaction lumière-matière devient suffisamment intense, ce modèle prédit l'apparition de nouveaux états pour le système couplé, dont les propriétés sont à la fois héritées de la lumière et de la matière. Ces

états hybrides lumière-matière, également appelés 'états polaritoniques' offrent des possibilités inédites tant pour l'optique que pour les sciences des matériaux, en particulier en tirant profit du caractère non-local et propageant de la lumière ainsi que du caractère local, interagissant et potentiellement non-linéaire de la matière. Ainsi, malgré leur équivalence formelle, les spécificités de chaque système en termes de leurs couplages à l'environnement et de leurs non-linéarités intrinsèques donnent lieu à une grande variété de directions de recherche dans les différentes réalisations du couplage fort lumière-matière.

Dans ce travail de thèse, nous nous sommes intéressés au régime de couplage fort lumière-matière dans des ensembles moléculaires macroscopiques couplés collectivement au même mode optique d'une micro-cavité. Dans de tels systèmes, les nouvelles propriétés chimiques et matérielles offertes par ces états polaritoniques ouvrent la voie au domaine émergeant de la chimie de cavité[46]. Notre travail dans ce domaine s'est articulé en trois directions.

Dans le domaine du visible d'abord, en couplant les transitions électroniques d'ensembles moléculaires à des champs de cavités optiques, nous avons étudié la photo-physique et les transferts d'énergie au sein de ces états polaritoniques. De plus, nous nous sommes intéressés à la réponse optique non-linéaire de ces systèmes.

En vue de modifier les réactions chimiques, qui typiquement ont lieu dans l'état électronique fondamental des molécules, nous nous sommes ensuite tournés vers le couplage fort de transitions vibrationnelles à des cavités résonantes dans l'infrarouge. Dans ce domaine où les forces de couplage peuvent atteindre des énergies comparables à l'énergie des transitions couplées, nous avons conduit une étude approfondie des propriétés d'absorption et d'émission des vibro-polaritons dans la limite dite de 'couplage ultra-fort'[67].

Finalement, nous avons mis en évidence un nouvel aspect du couplage fort lumière-matière entre des plasmons de surface et des excitons dans une classe émergente de semi-conducteurs inorganiques sous forme de couches atomiquement fines de

dichalcogénures de métaux de transition (TMD). Dans ces systèmes, la chiralité optique de résonances plasmons de surface peut être couplée à la chiralité de vallée des TMD pour donner naissance à de nouveaux modes de polaritons chiraux.

6.2 RÉSULTATS ET DISCUSSIONS

La première partie de ce travail de thèse porte sur différents aspects de la dynamique des populations et des chemins énergétiques dans les ensembles moléculaires fortement couplés, via leurs transitions électroniques, aux modes optiques de cavités Fabry-Pérot. Ces systèmes, relativement simples à fabriquer, permettent d'atteindre des forces de couplage remarquables, de l'ordre du dixième de l'énergie des transitions électroniques couplées. Dans cette situation, les fréquences des différents processus régissant la photo-physique de ces molécules peuvent êtres dominés par la fréquence à laquelle les molécules échangent leur énergie avec le champ de la cavité via des processus cohérents d'émission et d'absorption, appelés 'oscillations de Rabi'. Ainsi, le couplage fort peut profondément redéfinir la dynamique de l'état excité des molécules en cavité. Cet effet est au cœur de cette première partie, et se retrouvera au travers de plusieurs autres expériences dans ce travail de thèse.

Afin de mener une étude de la photo-physique des molécules fortement couplées en fonction de la force du couplage, nous avons mis au point une technique par laquelle une couche fine de molécules est placée, avec une précision nanométrique, à une certaine distance des miroirs de la cavité (voir Figure 6.1). En déplaçant cette couche du bord de la cavité jusqu'en son centre, la force de couplage a pu être variée en conservant les même densités surfaciques de molécules, garantissant ainsi la possibilité de comparer les différentes dynamiques entre elles.

Cette étude a permis de mesurer le rendement quantique de fluorescence de ces systèmes en fonction de la force de couplage, ainsi que le temps de vie de leurs états polaritoniques. De façon surprenante, ces temps de vies peuvent aller de quelques

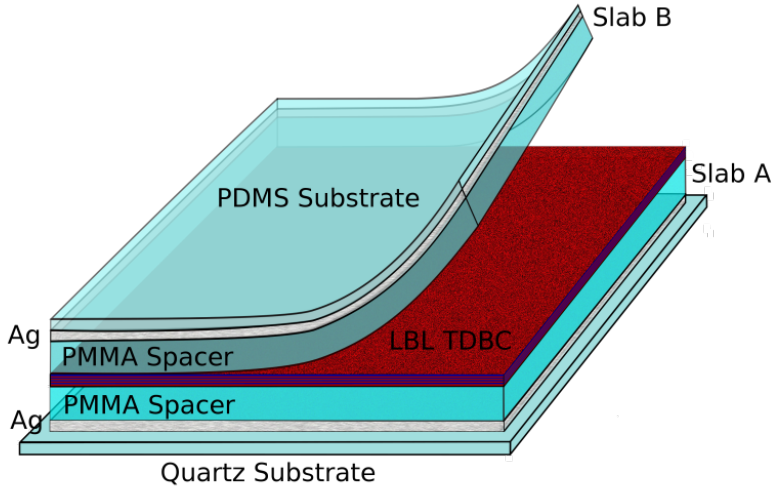

Figure 6.1 – Schéma d'une cavité Fabry-Pérot contenant une fine couche de molécules (20 nm) placée à une distance choisie des deux miroirs. Les couches de poly(methyl methacrylate) (PMMA) d'épaisseurs variables permettent d'ajuster la position de la couche de molécules optiquement actives (TDBC). Le mirroir supérieur fermant la cavité Fabry-Pérot est préparé sur un substrat flexible de poly-(dimethylsiloxane) (PDMS), permettant d'ouvrir et de fermer la cavité de façon réversible.

picosecondes à quelques nanosecondes, bien plus longs que ce qui pourrait être attendu par l'approche hamiltonienne évoquée plus haut. De telles durées de vie impliquent une dynamique relaxationnelle complexe, dans laquelle le feuillet vibrationnel des molécules est redéfini par le couplage au champ de la cavité. Nous avons développé un modèle numérique afin de modéliser de tels comportements.

Même si le couplage fort lumière-matière est souvent réduit à l'interaction cohérente d'une seule transition optiquement active avec une résonance optique de cavité, nous avons vu par cette étude photophysique que le couplage fort dans des milieux moléculaire complexes donne lieu à de nouveaux phénomènes qui ne peuvent être décrits que par des modèles plus élaborés, adapté aux matériaux moléculaires. Ainsi, les résultats de cette section doivent-il être contextualisés en vue de l'extraordinaire diversité photophysique de ces systèmes moléculaires. Afin d'illustrer ce propos, nous avons comparé les comportement photophysique des polaritons impliquant

trois différents molécules avec des dynamique d'état excité très distinctes: un aggrégat J de cyanine (1,1'-diethyl-3,3'-bis(4-sulfobutyl)-5,5',6,6'- tetra-chlorobenzimidazolocarbocyanine), une molécule 'push-pull' à grand décalage de Stokes (5-(4- (dibutylamino) benzylidene)-1,3-dimethylpyrimidine-2,4,6 (1H,3H,5H)-trione) et un colorant organique de fluoresceine à décalage de Stokes modéré.

Cette étude a démontrée que les différentes dynamiques des états excités des trois molécules étudiées affectent profondément les chemins énergétiques dans l'état excité polaritonique. Cet effet dépend fortement du recouvrement entre l'état polaritonique de plus basse énergie et les niveaux vibroniques des molécules 'nues', permettant aux polaritons de relaxer de manière non-radiative.

En se basant sur les résultats de cette étude photo-physique, nous avons fabriqué un nouveau type de cavités dans lesquelles deux espèces moléculaires différentes se couplent collectivement au même champ de cavité. Dans ce système, une des espèces moléculaires est donneur d'énergie et l'autre en est accepteur. En couplant collectivement ces deux espèces au même mode optique, nous avons pu démontrer l'ouverture d'un nouveau canal de transfert d'énergie, réduisant ainsi le temps de vie du donneur et augmentant l'efficacité du processus de transfert.

De plus, comme ce transfert est médié par des modes polaritoniques délocalisés, nous avons pu montrer qu'il est indépendant de la distance séparant les molécules donneurs et accepteurs, à condition que leurs forces de couplage à la cavité soient maintenues (voir Figure 6.2). Ces résultats ont également pu être décrits par notre modèle numérique évoqué plus haut.

La réponse collective des systèmes fortement couplés, à l'origine des comportements photo-physiques observés ouvre des possibilités fascinantes pour de nombreuses applications. L'une d'entre elles est la génération de second harmonique (SHG) sous pompage optique intense. En effet, ce phénomène central dans de nombreuses applications technologiques repose sur la capacité à faire fluctuer en phase les nuages électroniques

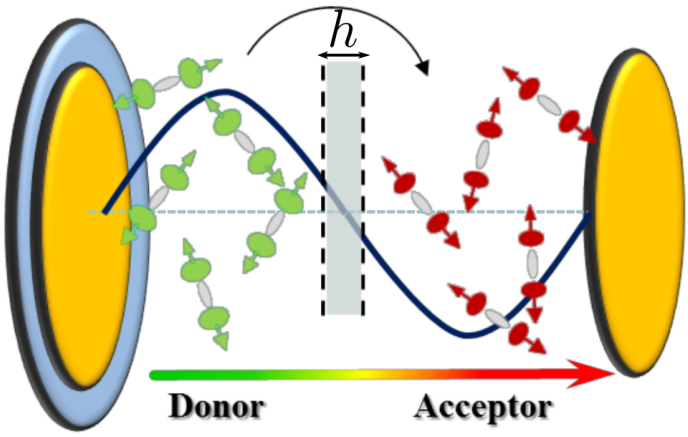

Figure 6.2 – Schéma d'une cavité Fabry-Pérot contenant deux ensembles moléculaires distincts: des donneurs d'énergie (en vert) et des accepteurs d'énergie (en rouge). Les deux ensembles sont séparés par une couche diélectrique de Poly(vinyl alcohol) (PVA) d'épaisseur variable. Le deuxième mode longitudinal de la cavité (schématisé en bleu) est résonant avec l'absorption des donneurs.

des molécules. En étudiant ce processus en et hors couplage fort, nous avons pu mettre en évidence une augmentation de deux ordres de grandeurs de l'efficacité de SHG par le mode polaritonique de plus basse énergie.

Cette preuve de concept a été effectuée sur un mono-cristal de porphyrine dont la bande Soret constitue la transition cible pour réaliser le couplage fort lumière-matière. La conception du système peut clairement être optimisée, en particulier en utilisant différents résonateurs électromagnétiques tels que des miroirs de Bragg, ou des structures plasmoniques qui pourraient également être résonantes à la longueur d'onde de pompe pour maximiser l'efficacité du système. De telles structures sont cependant plus exigeantes de concevoir, en particulier dût au fait que les molécules doivent être correctement alignées vis-à-vis de la polarisation du champ. Néanmoins, ces résultats indiquent que de tels dispositifs pourraient conduire à des plateformes organiques non-linéaires très efficaces.

Suite à ces études dans le domaine des transitions électroniques, nous nous sommes tournés vers le régime de couplage fort vibrationnel. Dans ce cadre, nous avons démontré la

possibilité d'atteindre le régime dit de couplage ultra-fort, où non seulement les états moléculaires vibrationnels sont fortement modifiés, mais l'état fondamental du système lui aussi est affecté. En particulier, dans ce régime, l'état fondamental devient également un état hybride lumière-matière, ouvrant de nouvelles possibilités dans le cadre de l'effet Casimir dynamique [67]. Par une étude spectroscopique approfondie et un modèle vibro-polaritonique adapté, nous avons pu mettre en évidence les signatures d'un tel régime. En particulier, nous avons observé l'ouverture d'un gap polaritonique existant à tous les angles d'incidence et à tous les désaccords de la cavité infrarouge. De plus, le rapport entre l'intervalle spectral libre de la cavité Fabry-Pérot et la force de couplage dans nos structures a permis l'observation de plusieurs branches polaritoniques émergeant du couplage non résonant de différents modes longitudinaux de la cavité à la même transition vibrationnelle. Ces différentes branches polaritoniques portent également les signatures du couplage ultra-fort lumière-matière.

En vue d'explorer davantage le régime de couplage ultra-fort vibrationnel, nous avons également rapporté, pour la première fois, des signatures polaritoniques dans les spectres d'émission thermique de ces systèmes. Cette nouvelle fenêtre d'observation donne directement accès aux populations thermiques de vibro-polaritons, et permet d'observer d'éventuels effets non-linéaires dus à leurs interactions à haute densité. De telles interactions sont notamment à l'origine du phénomène de condensation de Bose-Einstein que nous cherchons encore à démontrer dans ces systèmes en couplage fort vibrationnel. En excitant thermiquement une large distribution énergétique de polaritons, nous avons pu caractériser leur émissivité spectrale ainsi que la distribution angulaire de cette émission. Nos résultats montrent que l'émission polaritonique n'est pas thermalisée. Cette observation révèle ainsi la présence d'interactions entre vibro-polaritons et pose les bases d'une étude de la condensation de Bose-Einstein de vibro-polaritons. Cette étude établit également la spectroscopie d'émission IR de polaritons comme une approche complémentaire aux expériences récentes de dy-

namique résolue en temps, offrant la possibilité d'étudier les processus de transfert d'énergie dans le régime de couplage fort vibrationnelle.

Finalement, nous nous sommes intéressés au couplage fort de monocouches atomiques de dichalcogénures de métaux de transition (TMDs). L'étude de ces TMDs est un domaine de recherche particulièrement actif, et de nombreuses propriétés fascinantes ont récemment été rapportées. En particulier, leurs structures en nid d'abeille avec deux sites adjacents non-équivalents implique des règles de sélection optiques différentes aux points K et K' de la zone de Brillouin, impliquant des processus optique spin-vallée dépendants. Dans ce contexte, nous nous sommes intéressés au régime de couplage fort entre de tels transitions optiques et des résonances plasmons de surface (voir Figure 6.3). Ces résonances plasmons de surface, façonnables par la nano-structuration d'une surface métallique, permettent de designer différents modes optiques chiraux auxquels les transitions de vallée du TMD se couplent fortement. Les nombreuses configurations exploitants de tels couplages chiral-chiral entre des plasmons de surface et les excitons de vallée dans des monocouches atomiques de TMDs constituent un domaine émergeant de recherche (voir Figure 6.3).

Nous nous sommes intéressés ici à des modes plasmons spin-orbites qui ont la particularité d'associer de manière univoque le spin d'un faisceau optique incident à la direction de propagation du plasmon à la surface du métal. D'un autre côté, l'effet de vallée dans certaines monocouches de TMDs correspond à exciter de manière sélective une sous-population d'excitons par un spin optique d'excitation donné. En combinant le caractère spin-orbite des plasmons et la polarisation de vallée des TMDs dans le régime de couplage fort, nous avons pu démontrer la formation de polaritons chiraux pour lesquels un spin lumineux est associé à une vallée et à une direction de propagation. Dans de telles conditions, le couplage au champ électromagnétique du plasmon domine la dynamique du système, avec comme résultat une robustesse accrue du

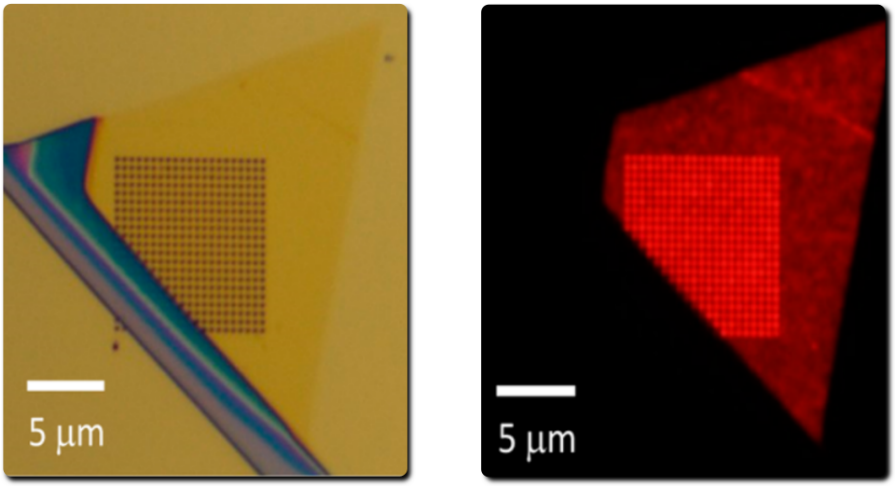

Figure 6.3 – Monocouche atomique de disulfure de tungstène (WS_2) recouvrant un réseau plasmonique sur une surface métallique. Le panel de gauche correspond à l'image sous microscope à lumière blanche. Le panel de droite correspond à la même région de l'échantillon, observé en microscopie à fluorescence (excitation en lumière continue à 400 nm).

degré de polarisation de vallée, en comparaison avec celui d'un TMD non couplé. En effet, dans ce régime de couplage fort chiral, nous avons démontré un maintient de polarisation de vallée de l'ordre de 10% à température ambiante, correspondant à un maintient de la direction de propagation des polaritons chiraux à la surface du résonateur plasmonique. De plus, nous avons montré un maintient de polarisation linéaire (cohérence inter-vallées) également de l'ordre de 10%, indiquant un maintient de relation de phase entre des flux contra-propageants de polaritons chiraux.

Ces résultats montrent que la combinaison d'interactions spin-orbite optique avec les propriétés de vallées des TMDs est un chemin prometteur en vue explorer et de manipuler les cohérences électroniques à température ambiante, dans le cadre des réseaux quantiques chiraux.

6.3 CONCLUSION

Dans cette thèse, nous avons exploré différentes facettes du couplage fort lumière-matière dans des matériaux com-

plexes, révélant ainsi comment les états polaritoniques collectifs peuvent redéfinir les paysages énergétiques et la dynamique dans le système couplé. Les propriétés photophysiques dans de telles paysages énergétiques sont en général complexes et ne peuvent pas être simplement déduites de celles des systèmes non-couplés, via un simple changement de base. Au lieu de cela, l'interaction entre les degrés de liberté couplés et non-couplés ainsi que la nature non-markovienne du processus de couplage conduit à des propriétés polaritoniques distinctes, constituant ainsi un nouveau type d'entité supramoléculaire. En particulier, nous montrons que ces états peuvent avoir des durées de vie plus longues que leurs constituants non-couplés, et peuvent révéler d'étonnantes réponses optique non-linéaire. De plus, la formidable diversité des espèces chimiques pouvant être utilisées dans le contexte de couplage fort lumière-matière nous permet de façonner des paysages polaritoniques spécifiques, comme nous le montrons dans le contexte des mécanisme de transfert d'énergie. À ce stade, une meilleure compréhension de de tels paysages polaritoniques nécessaire, notamment le voisinage des intersections coniques de surfaces d'énergie potentielles où l'approximation de Born-Oppenheimer n'est plus valide.

Les possibilités offertes par le couplage fort pour la modification des paysages chimiques sont directement révélées lors du couplage d'un mode de cavité infra-rouge à une vibration moléculaire de l'état fondamental électronique. De nouveaux taux de réactions chimiques ont récemment été rapporté par notre groupe dans ce régime de couplage fort vibrationnel, et d'autres expériences sont actuellement en cours vue de la modification des mécanismes de solvatation et de repliement des protéines. Dans une perspective similaire, nous étudions actuellement la possibilité de modifier les transitions de phase de supraconductrices par perturbation des vibrations moléculaires sous VSC. Un autre sujet en cours d'exploration est le comportement non linéaire des vibro-polaritons, ouvrant la voie à la formation d'un condensat de Bose-Einstein hors équilibre

dans de tels systèmes et offrant la perspective d'une réaction chimique impliquant de tels états quantiques macroscopiques.

En vue d'imprimer des propriétés spécifiques des matériaux couplés sur les états polaritoniques, nous explorons l'interaction entre la chiralité optique et la chiralité matérielle dans le régime de couplage fort. En couplant les transitions polarisées de vallées d'un cristal atomiquement mince de TMD à des résonances plasmoniques verrouillées en spin-impulsion, nous atteignons le régime de couplage fort chiral. Dans ce régime, les cohérences de vallée électroniques du matériau se trouvent être étonnamment renforcées. Un aspect particulièrement intéressant de ces résultats est le fait que l'orientation des excitons brillants dans le TMD, combinée à la nature transverse magnétique des modes plasmons, ne permet a priori pas une telle protection de vallée. Les détails de ce mécanisme de couplage, impliquant le spin transverse des plasmons de surface et la contribution des excitons sombres du TMD sont actuellement en cours d'exploration à la fois d'un point de vue théorique et expérimental. Ce travail ouvre également de nombreuses perspectives dans le contexte de la topologie des champs polaritoniques. Les effets de fluorescence singulière et de vortex polaritoniques sont actuellement étudiés dans les TMD couplés à des spirales d'Archiméde plasmoniques.

ACKNOWLEDGMENTS

First and foremost, I thank my supervisor Prof. Thomas W. Ebbesen for his guidance throughout these years of PhD. His door has always been opened for discussing any kind of topics, and his constant enthusiasm have been key to the good development of this thesis work.

I would also like to thank Prof. Angel Rubio, Prof. Jaime Gómez Rivas, Prof. Guido Pupillo and Prof. Ataç Imamoğlu for accepting to participate in my thesis jury, and for their constructive comments on this work.

I thank Dr. Cyriaque Genet for our *polaritonic* relationship: may our excitement be long lived, and our delocalized interaction resist the fluctuations of life, even at room temperature!

Many thanks to Dr. James Hutchison and Dr. Eloïse Devaux for making the nanostructures lab such a nice place to work. Even purging the water chillers of a femtosecond laser can be great fun in such good company!

Thanks a lot to all the former and current group members for sharing this time with me. I keep in mind many good memories: the enthusiasm of Gabriel Schnoering, home made layer-by-layer depositions with Shaojun Wang, pump-probe alignment with Xiaolan Zhong, the cigarette chats with Atef Shalabney, biryani parties with Jino George and his familly, a week in Venice with the Great Stefano Azzini to balance several other great weeks in the dark room, traditional polarimetry measurements with Anoop Thomas, IPCMS-ISIS Experimental Jazz Nights with Etienne Lorchat and the Chervazzinat trio, bi-linguistic theoretico-experimental discussions with David Hagenmueller, the chocolate mouse of Robrecht Vergauwe, chicha evenings with Hadi Bahsoun. Many thanks to Marie-Claude Jouati, to the Team Force members: Oussama Sentissi, Yoseline

Rosales-Cabrara and Ming-Hao Li and to our new colleagues Kalaivanan Nagarajan and Marcus Seidel.

I am also indebted to several extraordinary persons with whom I had the chance to work: Chunliang Wang, Jialiang Xu, Loïc Mager Antoine Canaguier-Durand, Stefan Berciaud, Yuri Gorodetski, Elias Akiki and Manuel Hertzog.

Many thanks to the climbing crew: keep it up, we have to train for our outdoor expedition!

Thanks to the old friends from the Monday *groupe lectures*, and in particular to Ziyad Chaker for remaining so inspirational after so many years.

Many thoughts to my family: Meltem, Fifi, Laurence and Pedro, Nicole, Jaja et mon petit Daniel!

BIBLIOGRAPHY

[1] Y. Kaluzny, P. Goy, M. Gross, J.-M. Raimond, and S. Haroche, "Observation of self-induced Rabi oscillations in two-level atoms excited inside a resonant cavity: the ringing regime of superradiance", Phys. Rev. Lett. **51**, 1175 (1983) (cit. on pp. 6, 9, 158).

[2] S. Haroche and J.-M. Raimond, *Exploring the quantum: atoms, cavities, and photons* (Oxford university press, 2006) (cit. on pp. 6, 9, 22, 24, 158).

[3] J. Kasprzak, M Richard, S Kundermann, A Baas, P Jeambrun, J. Keeling, F. Marchetti, M. Szymańska, R Andre, J. Staehli, et al., "Bose-Einstein condensation of exciton polaritons", Nature **443**, 409–414 (2006) (cit. on pp. 6, 10).

[4] R. Balili, V. Hartwell, D. Snoke, L. Pfeiffer, and K. West, "Bose-Einstein condensation of microcavity polaritons in a trap", Science **316**, 1007–1010 (2007) (cit. on pp. 6, 10).

[5] W. H. Nitsche, N. Y. Kim, G. Roumpos, C. Schneider, M. Kamp, S. Höfling, A. Forchel, and Y. Yamamoto, "Algebraic order and the Berezinskii-Kosterlitz-Thouless transition in an exciton-polariton gas", Phys. Rev. B **90**, 205430 (2014) (cit. on pp. 6, 10).

[6] K. S. Daskalakis, S. A. Maier, and S. Kéna-Cohen, "Spatial coherence and stability in a disordered organic polariton condensate", Phys. Rev. Lett. **115**, 035301 (2015) (cit. on pp. 6, 10).

[7] K. G. Lagoudakis, M. Wouters, M. Richard, A. Baas, I. Carusotto, R. André, L. S. Dang, and B Deveaud-Plédran, "Quantized vortices in an exciton-polariton condensate", Nat. Phys. **4**, 706–710 (2008) (cit. on pp. 6, 11).

[8] A. Amo, J. Lefrère, S. Pigeon, C. Adrados, C. Ciuti, I. Carusotto, R. Houdré, E. Giacobino, and A. Bramati, "Superfluidity of polaritons in semiconductor microcavities", Nat. Phys. **5**, 805–810 (2009) (cit. on pp. 6, 11).

[9] D Sanvitto, F. Marchetti, M. Szymańska, G Tosi, M Baudisch, F. Laussy, D. Krizhanovskii, M. Skolnick, L Marrucci, A Lemaitre, et al., "Persistent currents and quantized vortices in a polariton superfluid", Nat. Phys. **6**, 527–533 (2010) (cit. on pp. 6, 11).

[10] Á. Cuevas, B. Silva, J. C. L. Carreno, M. de Giorgi, C. S. Munoz, A. Fieramosca, D. G. S. Forero, F. Cardano, L. Marrucci, V. Tasco, et al., "Entangling a polariton with one photon: effect of interactions at the single-particle level", arXiv preprint arXiv:1609.01244 (2016) (cit. on p. 6).

[11] T. Karzig, C.-E. Bardyn, N. H. Lindner, and G. Refael, "Topological polaritons", Phys. Rev. X **5**, 031001 (2015) (cit. on pp. 6, 11).

[12] H. Terças, H. Flayac, D. D. Solnyshkov, and G. Malpuech, "Non-abelian gauge fields in photonic cavities and photonic superfluids", Phys. Rev. Lett. **112**, 066402 (2014) (cit. on pp. 6, 11).

[13] H.-T. Lim, E. Togan, M. Kroner, J. Miguel-Sanchez, and A. Imamoglu, "Electrically tunable artificial gauge potential for polaritons", arXiv preprint arXiv:1610.07358 (2016) (cit. on pp. 6, 11).

[14] J. A. Hutchison, T. Schwartz, C. Genet, E. Devaux, and T. W. Ebbesen, "Modifying chemical landscapes by coupling to vacuum fields", Angew. Chem., Int. Ed. **51**, 1592–1596 (2012) (cit. on pp. 6, 31).

[15] A. Thomas, J. George, A. Shalabney, M. Dryzhakov, S. J. Varma, J. Moran, T. Chervy, X. Zhong, E. Devaux, C. Genet, J. A. Hutchison, and T. W. Ebbesen, "Ground-state chemical reactivity under vibrational coupling to the vacuum electromagnetic field", Angew. Chem., Int. Ed. **128**, 11634–11638 (2016) (cit. on pp. 6, 31, 91, 157).

[16]D. Sanvitto and S. Kéna-Cohen, "The road towards polaritonic devices", Nat. Mater. **15**, 1061–1073 (2016) (cit. on pp. 6, 11, 158).

[17]I. Carusotto and C. Ciuti, "Quantum fluids of light", Rev. Mod. Phys. **85**, 299–366 (2013) (cit. on pp. 6, 79).

[18]C. Weisbuch, M. Nishioka, A. Ishikawa, and Y. Arakawa, "Observation of the coupled exciton-photon mode splitting in a semiconductor quantum microcavity", Phys. Rev. Lett. **69**, 3314–3317 (1992) (cit. on pp. 6, 10).

[19]A. Wallraff, D. I. Schuster, A. Blais, L Frunzio, R.-S. Huang, J Majer, S Kumar, S. M. Girvin, and R. J. Schoelkopf, "Strong coupling of a single photon to a superconducting qubit using circuit quantum electrodynamics", Nature **431**, 162–167 (2004) (cit. on p. 6).

[20]J. Haber, K. S. Schulze, K. Schlage, R. Loetzsch, L. Bocklage, T. Gurieva, H. Bernhardt, H.-C. Wille, R. Rüffer, I. Uschmann, et al., "Collective strong coupling of X-rays and nuclei in a nuclear optical lattice", Nat. Photon. (2016) (cit. on p. 6).

[21]I. Pockrand, A. Brillante, and D. Möbius, "Exciton–surface plasmon coupling: an experimental investigation", J. Chem. Phys. **77**, 6289–6295 (1982) (cit. on pp. 6, 11).

[22]A. Shalabney, J. George, J Hutchison, G. Pupillo, C. Genet, and T. W. Ebbesen, "Coherent coupling of molecular resonators with a microcavity mode", Nat. Commun. **6** (2015) (cit. on pp. 6, 91, 92, 96, 103).

[23]E. T. Jaynes and F. W. Cummings, "Comparison of quantum and semiclassical radiation theories with application to the beam maser", Proc. IEEE **51**, 89–109 (1963) (cit. on pp. 6, 10, 12, 24).

[24]A. Ourjoumtsev, A. Kubanek, M. Koch, C. Sames, P. W. Pinkse, G. Rempe, and K. Murr, "Observation of squeezed light from one atom excited with two photons", Nature **474**, 623–626 (2011) (cit. on p. 8).

[25]H. Gorniaczyk, C. Tresp, J. Schmidt, H. Fedder, and S. Hofferberth, "Single-photon transistor mediated by interstate Rydberg interactions", Phys. Rev. Lett. **113**, 053601 (2014) (cit. on p. 8).

[26]D. Tiarks, S. Baur, K. Schneider, S. Dürr, and G. Rempe, "Single-photon transistor using a Förster resonance", Phys. Rev. Lett. **113**, 053602 (2014) (cit. on p. 8).

[27]T. Tiecke, J. D. Thompson, N. P. de Leon, L. Liu, V Vuletić, and M. D. Lukin, "Nanophotonic quantum phase switch with a single atom", Nature **508**, 241–244 (2014) (cit. on p. 8).

[28]G. Rempe, "A photon steers a photon with an atom", Science **345**, 871–871 (2014) (cit. on p. 8).

[29]E. M. Purcell, H. C. Torrey, and R. V. Pound, "Resonance absorption by nuclear magnetic moments in a solid", Phys. Rev. **69**, 37–38 (1946) (cit. on p. 8).

[30]K. H. Drexhage, "Interaction of light with monomolecular dye layers", Prog. Optics **12**, 163 –232 (1974) (cit. on p. 8).

[31]V. Yakovlev, V. Nazin, and G. Zhizhin, "The surface polariton splitting due to thin surface film LO vibrations", Opt. Commun. **15**, 293 –295 (1975) (cit. on pp. 9, 129).

[32]V. Agranovich and A. Malshukov, "Surface polariton spectra if the resonance with the transition layer vibrations exist", Opt. Commun. **11**, 169 –171 (1974) (cit. on p. 9).

[33]S. Zeytinoğlu, A. Imamoğlu, and S. Huber, "Engineering matter interactions using squeezed vacuum", Phys. Rev. X **7**, 021041 (2017) (cit. on p. 9).

[34]M. Tavis and F. W. Cummings, "Exact solution for an n-molecule-radiation-field hamiltonian", Phys. Rev. **170**, 379–384 (1968) (cit. on pp. 10, 25).

[35]I. Shomroni, S. Rosenblum, Y. Lovsky, O. Bechler, G. Guendelman, and B. Dayan, "All-optical routing of single photons by a one-atom switch controlled by a single photon", Science **345**, 903–906 (2014) (cit. on p. 10).

[36]R. Houdré, "Early stages of continuous wave experiments on cavity-polaritons", Phys. Status Solidi B **242**, 2167–2196 (2005) (cit. on pp. 10, 77, 143).

[37]V. Agranovich, H. Benisty, and C. Weisbuch, "Organic and inorganic quantum wells in a microcavity: Frenkel-Wannier-Mott excitons hybridization and energy transformation", Solid State Commun. **102**, 631 –636 (1997) (cit. on pp. 11, 29).

[38]T. Fujita, Y. Sato, T. Kuitani, and T. Ishihara, "Tunable polariton absorption of distributed feedback microcavities at room temperature", Phys. Rev. B **57**, 12428–12434 (1998) (cit. on p. 11).

[39]D. G. Lidzey, D. D. C. Bradley, M. S. Skolnick, T. Virgili, S. Walker, and D. M. Whittaker, "Strong exciton-photon coupling in an organic semiconductor microcavity", Nature **395**, 53–55 (1998) (cit. on p. 11).

[40]S Kéna-Cohen and S. Forrest, "Room-temperature polariton lasing in an organic single-crystal microcavity", Nat. Photon. **4**, 371–375 (2010) (cit. on pp. 11, 30, 118).

[41]J. D. Plumhof, T. Stöferle, L. Mai, U. Scherf, and R. F. Mahrt, "Room-temperature Bose-Einstein condensation of cavity exciton–polaritons in a polymer", Nat. Mater. **13**, 247–252 (2014) (cit. on p. 11).

[42]K. Daskalakis, S. Maier, R. Murray, and S. Kéna-Cohen, "Nonlinear interactions in an organic polariton condensate", Nat. Mater. **13**, 271–278 (2014) (cit. on p. 11).

[43]C. P. Dietrich, A. Steude, L. Tropf, M. Schubert, N. M. Kronenberg, K. Ostermann, S. Höfling, and M. C. Gather, "An exciton-polariton laser based on biologically produced fluorescent protein", Science Advances **2** (2016) (cit. on p. 11).

[44]M. Ramezani, A. Halpin, A. I. Fernández-Domínguez, J. Feist, S. R.-K. Rodriguez, F. J. Garcia-Vidal, and J. G. Rivas, "Plasmon-exciton-polariton lasing", Optica **4**, 31–37 (2017) (cit. on pp. 11, 129).

[45]G. Lerario, A. Fieramosca, F. Barachati, D. Ballarini, K. S. Daskalakis, L. Dominici, M. De Giorgi, S. A. Maier, G. Gigli, S. Kena-Cohen, and D. Sanvitto, "Room-temperature superfluidity in a polariton condensate", Nat. Phys. (2017) (cit. on p. 11).

[46]T. W. Ebbesen, "Hybrid light–matter states in a molecular and material science perspective", Acc. Chem. Res. **49**, 2403–2412 (2016) (cit. on pp. 11, 30, 156, 158, 159).

[47]M. Skolnick, T. Fisher, and D. Whittaker, "Strong coupling phenomena in quantum microcavity structures", Semicond. Sci. Technol. **13**, 645 (1998) (cit. on p. 12).

[48]R. Holmes and S. Forrest, "Strong exciton–photon coupling in organic materials", Org. Elect. **8**, 77–93 (2007) (cit. on p. 12).

[49]H. Deng, H. Haug, and Y. Yamamoto, "Exciton-polariton Bose-Einstein condensation", Rev. Mod. Phys. **82**, 1489–1537 (2010) (cit. on p. 12).

[50]M. Chachisvilis, H. Fidder, T. Pullerits, and V. Sundström, "Coherent nuclear motions in light-harvesting pigments and dye molecules, probed by ultrafast spectroscopy", J. Ram. Spectro. **26**, 513–522 (1995) (cit. on p. 12).

[51]V. Sundström, T. Pullerits, and R. van Grondelle, "Photosynthetic light-harvesting: reconviling dynamics and structure of purple bacterial LH2 reveals function of photosynthetic unit", J. Phy. Chem. B **103**, 2327–2346 (1999) (cit. on p. 12).

[52]G. D. Scholes, G. R. Fleming, A. Olaya-Castro, and R. Van Grondelle, "Lessons from nature about solar light harvesting", Nat. Chem. **3**, 763–774 (2011) (cit. on p. 12).

[53]E. Romero, V. I. Novoderezhkin, and R. van Grondelle, "Quantum design of photosynthesis for bio-inspired solar-energy conversion", Nature **543**, 355–365 (2017) (cit. on p. 12).

[54]M. Kasha, "Energy transfer mechanisms and the molecular exciton model for molecular aggregates", Rad. Res. **20**, 55–70 (1963) (cit. on pp. 12, 48).

[55]F. Würthner, T. E. Kaiser, and C. R. Saha-Möller, "J-aggregates: from serendipitous discovery to supramolecular engineering of functional dye materials", Angew. Chem. Int. Ed. **50**, 3376–3410 (2011) (cit. on p. 12).

[56]E. Knapp, "Lineshapes of molecular aggregates, exchange narrowing and intersite correlation", Chem. Phys. **85**, 73 –82 (1984) (cit. on p. 13).

[57]J. Knoester, "Nonlinear optical line shapes of disordered molecular aggregates: motional narrowing and the effect of intersite correlations", J. Chem. Phys. **99**, 8466–8479 (1993) (cit. on p. 13).

[58]F. C. Spano, "The spectral signatures of Frenkel polarons in H- and J-aggregates", Acc. Chem. Res. **43**, 429–439 (2010) (cit. on p. 13).

[59]W. Moerner, *Persistent spectral hole-burning: science and applications* (Springer-Verlag New York Inc.,New York, NY, 1988) (cit. on pp. 14, 16).

[60]J. S. Toll, "Causality and the dispersion relation: logical foundations", Phys. Rev. **104**, 1760–1770 (1956) (cit. on p. 18).

[61]Y. Zhu, D. J. Gauthier, S. E. Morin, Q. Wu, H. J. Carmichael, and T. W. Mossberg, "Vacuum Rabi splitting as a feature of linear-dispersion theory: analysis and experimental observations", Phys. Rev. Lett. **64**, 2499–2502 (1990) (cit. on pp. 21, 100).

[62]J. J. Childs, K. An, R. R. Dasari, and M. S. Feld, *Cavity quantum electrodynamics*, edited by P. R. Berman (Academic Press, Boston, 1994) (cit. on p. 21).

[63]V. Savona, L. Andreani, P. Schwendimann, and A. Quattropani, "Quantum well excitons in semiconductor microcavities: unified treatment of weak and strong coupling regimes", Solid State Commun. **93**, 733 –739 (1995) (cit. on pp. 21, 27).

[64]R. Houdré, "Early stages of continuous wave experiments on cavity-polaritons", Phys. Status Solidi B **242**, 2167–2196 (2005) (cit. on p. 21).

[65]D. O. Krimer, B. Hartl, and S. Rotter, "Hybrid quantum systems with collectively coupled spin states: suppression of decoherence through spectral hole burning", Phys. Rev. Lett. **115**, 033601 (2015) (cit. on p. 21).

[66]C. Sauvan, J. P. Hugonin, I. S. Maksymov, and P. Lalanne, "Theory of the spontaneous optical emission of nanosize photonic and plasmon resonators", Phys. Rev. Lett. **110**, 237401 (2013) (cit. on p. 23).

[67]C. Ciuti, G. Bastard, and I. Carusotto, "Quantum vacuum properties of the intersubband cavity polariton field", Phys. Rev. B **72**, 115303 (2005) (cit. on pp. 24, 92, 105, 106, 111, 159, 164).

[68]Y. Todorov, A. M. Andrews, R. Colombelli, S. De Liberato, C. Ciuti, P. Klang, G. Strasser, and C. Sirtori, "Ultrastrong light-matter coupling regime with polariton dots", Phys. Rev. Lett. **105**, 196402 (2010) (cit. on pp. 24, 92, 102).

[69]G. Scalari, C. Maissen, D. Turčinková, D. Hagenmüller, S. De Liberato, C. Ciuti, C. Reichl, D. Schuh, W. Wegscheider, M. Beck, and J. Faist, "Ultrastrong coupling of the cyclotron transition of a 2D electron gas to a THz metamaterial", Science **335**, 1323–1326 (2012) (cit. on p. 24).

[70]B Askenazi, A Vasanelli, A Delteil, Y Todorov, L. C. Andreani, G Beaudoin, I Sagnes, and C Sirtori, "Ultra-strong light–matter coupling for designer Reststrahlen band", New J. Phys. **16**, 043029 (2014) (cit. on pp. 24, 109).

[71]S. Gambino, M. Mazzeo, A. Genco, O. Di Stefano, S. Savasta, S. Patanè, D. Ballarini, F. Mangione, G. Lerario, D. Sanvitto, and G. Gigli, "Exploring light–matter interaction phenomena under ultrastrong coupling regime", ACS Photonics **1**, 1042–1048 (2014) (cit. on pp. 24, 109).

[72]J. J. Hopfield, "Theory of the contribution of excitons to the complex dielectric constant of crystals", Phys. Rev. **112**, 1555–1567 (1958) (cit. on pp. 25, 105).

[73]R. Houdré, R. P. Stanley, and M. Ilegems, "Vacuum-field rabi splitting in the presence of inhomogeneous broadening: resolution of a homogeneous linewidth in an inhomogeneously broadened system", Phys. Rev. A **53**, 2711–2715 (1996) (cit. on pp. 28, 50).

[74]C. Gonzalez-Ballestero, J. Feist, E. Gonzalo Badía, E. Moreno, and F. J. Garcia-Vidal, "Uncoupled dark states can inherit polaritonic properties", Phys. Rev. Lett. **117**, 156402 (2016) (cit. on p. 28).

[75]K. Bergmann, H. Theuer, and B. W. Shore, "Coherent population transfer among quantum states of atoms and molecules", Rev. Mod. Phys. **70**, 1003–1025 (1998) (cit. on p. 28).

[76]H. J. Kimble, "The quantum internet", Nature **453**, 1023–1030 (2008) (cit. on p. 28).

[77]V. M. Agranovich, M. Litinskaia, and D. G. Lidzey, "Cavity polaritons in microcavities containing disordered organic semiconductors", Phys. Rev. B **67**, 085311 (2003) (cit. on pp. 29, 39, 46).

[78]M. Litinskaya, P. Reineker, and V. Agranovich, "Fast polariton relaxation in strongly coupled organic microcavities", J. Lumin. **110**, 364 –372 (2004) (cit. on pp. 29, 39).

[79]V. Agranovich and G. L. Rocca, "Electronic excitations in organic microcavities with strong light–matter coupling", Solid State Commun. **135**, 544 –553 (2005) (cit. on pp. 29, 39).

[80]P. Michetti and G. C. La Rocca, "Polariton states in disordered organic microcavities", Phys. Rev. B **71**, 115320 (2005) (cit. on pp. 29, 39).

[81]M. Litinskaya, P. Reineker, and V. Agranovich, "Exciton–polaritons in organic microcavities", J. Lumin. **119–120**, 277 –282 (2006) (cit. on pp. 29, 39).

[82]A. Canaguier-Durand, E. Devaux, J. George, Y. Pang, J. A. Hutchison, T. Schwartz, C. Genet, N. Wilhelms, J.-M. Lehn, and T. W. Ebbesen, "Thermodynamics of molecules strongly coupled to the vacuum field", Angew. Chem. Int. Ed. **125**, 10727 –10730 (2013) (cit. on pp. 29, 39).

[83]L. Fontanesi, L. Mazza, and G. C. La Rocca, "Organic-based microcavities with vibronic progressions: linear spectroscopy", Phys. Rev. B **80**, 235313 (2009) (cit. on p. 29).

[84]L. Mazza, L. Fontanesi, and G. C. La Rocca, "Organic-based microcavities with vibronic progressions: photoluminescence", Phys. Rev. B **80**, 235314 (2009) (cit. on p. 29).

[85]D. M. Coles, N. Somaschi, P. Michetti, C. Clark, P. G. Lagoudakis, P. G. Savvidis, and D. G. Lidzey, "Polariton-mediated energy transfer between organic dyes in a strongly coupled optical microcavity", Nat. Mater. **13**, 712–719 (2014) (cit. on pp. 30, 63).

[86]X. Zhong, T. Chervy, S. Wang, J. George, A. Thomas, J. A. Hutchison, E. Devaux, C. Genet, and T. W. Ebbesen, "Non-radiative energy transfer mediated by hybrid light-matter states", Angew. Chem. Int. Ed. **55**, 6202–6206 (2016) (cit. on pp. 30, 57, 59, 61, 62, 64, 75).

[87]X. Zhong, T. Chervy, L. Zhang, A. Thomas, J. George, C. Genet, J. A. Hutchison, and T. W. Ebbesen, "Energy transfer between spatially separated entangled molecules", Angew. Chem. Int. Ed. (cit. on pp. 30, 57, 68, 69, 71, 72, 75).

[88]A. Canaguier-Durand, C. Genet, A. Lambrecht, T. W. Ebbesen, and S. Reynaud, "Non-Markovian polariton dynamics in organic strong coupling", Eur. Phys. J. D **69**, 24 (2015) (cit. on pp. 30, 46, 111).

[89]Z. Kurucz, J. H. Wesenberg, and K. Mølmer, "Spectroscopic properties of inhomogeneously broadened spin ensembles in a cavity", Phys. Rev. A **83**, 053852 (2011) (cit. on p. 30).

[90] I. Diniz, S. Portolan, R. Ferreira, J. M. Gérard, P. Bertet, and A. Auffèves, "Strongly coupling a cavity to inhomogeneous ensembles of emitters: potential for long-lived solid-state quantum memories", Phys. Rev. A **84**, 063810 (2011) (cit. on p. 30).

[91] D. O. Krimer, S. Putz, J. Majer, and S. Rotter, "Non-Markovian dynamics of a single-mode cavity strongly coupled to an inhomogeneously broadened spin ensemble", Phys. Rev. A **90**, 043852 (2014) (cit. on p. 30).

[92] G. Hornecker, A. Auffèves, and T. Grange, "Influence of phonons on solid-state cavity-QED investigated using nonequilibrium Green's functions", Phys. Rev. B **95**, 035404 (2017) (cit. on p. 30).

[93] I. V. Tokatly, "Time-dependent density functional theory for many-electron systems interacting with cavity photons", Phys. Rev. Lett. **110**, 233001 (2013) (cit. on p. 30).

[94] M. Ruggenthaler, J. Flick, C. Pellegrini, H. Appel, I. V. Tokatly, and A. Rubio, "Quantum-electrodynamical density-functional theory: bridging quantum optics and electronic-structure theory", Phys. Rev. A **90**, 012508 (2014) (cit. on p. 30).

[95] F. C. Spano, "Optical microcavities enhance the exciton coherence length and eliminate vibronic coupling in j-aggregates", J. Chem. Phys. **142**, 184707 (2015) (cit. on pp. 30, 156).

[96] J. Galego, F. J. Garcia-Vidal, and J. Feist, "Cavity-induced modifications of molecular structure in the strong-coupling regime", Phys. Rev. X **5**, 041022 (2015) (cit. on pp. 30, 156).

[97] P. E. Trevisanutto and M. Milletarì, "Hedin equations in resonant microcavities", Phys. Rev. B **92**, 235303 (2015) (cit. on pp. 30, 156).

[98] C. Pellegrini, J. Flick, I. V. Tokatly, H. Appel, and A. Rubio, "Optimized effective potential for quantum electrodynamical time-dependent density functional theory", Phys. Rev. Lett. **115**, 093001 (2015) (cit. on pp. 30, 156).

[99]K. Bennett, M. Kowalewski, and S. Mukamel, "Novel photochemistry of molecular polaritons in optical cavities", Farad. Discuss. **194**, 259–282 (2016) (cit. on pp. 30, 156).

[100]J. A. Ćwik, P. Kirton, S. De Liberato, and J. Keeling, "Excitonic spectral features in strongly coupled organic polaritons", Phys. Rev. A **93**, 033840 (2016) (cit. on pp. 30, 156).

[101]F. Herrera and F. C. Spano, "Cavity-controlled chemistry in molecular ensembles", Phys. Rev. Lett. **116**, 238301 (2016) (cit. on pp. 30, 156).

[102]M. Kowalewski, K. Bennett, and S. Mukamel, "Cavity femtochemistry: manipulating nonadiabatic dynamics at avoided crossings", J. Phys. Chem. Lett. **7**, 2050–2054 (2016) (cit. on pp. 30, 156).

[103]N. Wu, J. Feist, and F. J. Garcia-Vidal, "When polarons meet polaritons: exciton-vibration interactions in organic molecules strongly coupled to confined light fields", Phys. Rev. B **94**, 195409 (2016) (cit. on pp. 30, 156).

[104]J. Galego, F. J. Garcia-Vidal, and J. Feist, "Suppressing photochemical reactions with quantized light fields", Nat. Commun. **7**, Article, 13841 – (2016) (cit. on pp. 30, 156).

[105]J. Flick, M. Ruggenthaler, H. Appel, and A. Rubio, "Atoms and molecules in cavities, from weak to strong coupling in quantum-electrodynamics (QED) chemistry", Proc. Nat. Acad. Sci. **114**, 3026–3034 (2017) (cit. on pp. 30, 156).

[106]S. Wang, T. Chervy, J. George, J. A. Hutchison, C. Genet, and T. W. Ebbesen, "Quantum yield of polariton emission from hybrid light-matter states", J. Phys. Chem. Lett. **5**, 1433–1439 (2014) (cit. on pp. 33, 34, 36–39, 42, 44).

[107]G. Decher, "Fuzzy nanoassemblies: toward layered polymeric multicomposites", Science **277**, 1232–1237 (1997) (cit. on p. 35).

[108]M. Bradley, J. Tischler, and V. Bulović, "Layer-by-layer J-aggregate thin films with a peak absorption constant of $10^6 \mathrm{cm}^{-1}$", Adv. Mater. **17**, 1881–1886 (2005) (cit. on p. 35).

[109]D. M. Coles, P. Michetti, C. Clark, A. M. Adawi, and D. G. Lidzey, "Temperature dependence of the upper-branch polariton population in an organic semiconductor microcavity", Phys. Rev. B **84**, 205214 (2011) (cit. on p. 39).

[110]T. Virgili, D. Coles, A. M. Adawi, C. Clark, P. Michetti, S. K. Rajendran, D. Brida, D. Polli, G. Cerullo, and D. G. Lidzey, "Ultrafast polariton relaxation dynamics in an organic semiconductor microcavity", Phys. Rev. B **83**, 245309 (2011) (cit. on p. 40).

[111]T. Schwartz, J. A. Hutchison, J. Léonard, C. Genet, S. Haacke, and T. W. Ebbesen, "Polariton dynamics under strong light–molecule coupling", ChemPhysChem **14**, 125 –131 (2013) (cit. on p. 40).

[112]D. M. Coles, R. T. Grant, D. G. Lidzey, C. Clark, and P. G. Lagoudakis, "Imaging the polariton relaxation bottleneck in strongly coupled organic semiconductor microcavities", Phys. Rev. B **88**, 121303 (2013) (cit. on pp. 40, 118).

[113]D. Ballarini, M. De Giorgi, S. Gambino, G. Lerario, M. Mazzeo, A. Genco, G. Accorsi, C. Giansante, S. Colella, S. D'Agostino, P. Cazzato, D. Sanvitto, and G. Gigli, "Polariton-induced enhanced emission from an organic dye under the strong coupling regime", Adv. Opt. Mater. **2**, 1076 –1081 (2014) (cit. on p. 40).

[114]C. Würth, M. Grabolle, J. Pauli, M. Spieles, and U. Resch-Genger, "Relative and absolute determination of fluorescence quantum yields of transparent samples", Nat. Protoc. **8**, 1535–1550 (2013) (cit. on p. 40).

[115]A. A. Muenter, D. V. Brumbaugh, J. Apolito, L. A. Horn, F. C. Spano, and S. Mukamel, "Size dependence of excited-state dynamics for J-aggregates at silver bromide interfaces", J. Phys. Chem. **96**, 2783–2790 (1992) (cit. on p. 43).

[116]P. J. Reid, D. A. Higgins, and P. F. Barbara, "Environment-dependent photophysics of polymer-bound J aggregates determined by time-resolved fluorescence spectroscopy and

time-resolved near-field scanning optical microscopy", J. Phys. Chem. **100**, 3892–3899 (1996) (cit. on p. 43).

[117]R. Berera, R. van Grondelle, and J. T. M. Kennis, "Ultrafast transient absorption spectroscopy: principles and application to photosynthetic systems", Photo. Res. **101**, 105–118 (2009) (cit. on p. 43).

[118]W. T. Pollard, S. Lee, and R. A. Mathies, "Wave packet theory of dynamic absorption spectra in femtosecond pump–probe experiments", J. Chem. Phys. **92**, 4012–4029 (1990) (cit. on p. 43).

[119]M. Sharnoff, "Photophysics of aromatic molecules", J. Lumin. **4**, 69–71 (1971) (cit. on p. 45).

[120]G. Andric, J. F. Boas, A. M. Bond, G. D. Fallon, K. P. Ghiggino, C. F. Hogan, J. A. Hutchison, M. A. P. Lee, S. J. Langford, J. R. Pilbrow, G. J. Troup, and C. P. Woodward, "Spectroscopy of naphthalene diimides and their anion radicals", Aust. J. Chem. **57**, 1011–1019 (2004) (cit. on p. 46).

[121]J. George, S. Wang, T. Chervy, A. Canaguier-Durand, G. Schaeffer, J.-M. Lehn, J. A. Hutchison, C. Genet, and T. W. Ebbesen, "Ultra-strong coupling of molecular materials: spectroscopy and dynamics", Farad. Discuss. **178**, 281–294 (2015) (cit. on pp. 47, 48, 50, 51, 53, 55).

[122]T. K. Hakala, J. J. Toppari, A. Kuzyk, M. Pettersson, H. Tikkanen, H. Kunttu, and P. Törmä, "Vacuum Rabi splitting and strong-coupling dynamics for surface-plasmon polaritons and rhodamine 6G molecules", Phys. Rev. Lett. **103**, 053602 (2009) (cit. on pp. 49, 50).

[123]G. D. Scholes, "Long-range resonance energy transfer in molecular systems", Annu. Rev. Phys. Chem. **54**, 57–87 (2003) (cit. on pp. 62, 69, 70).

[124]S. P. Laptenok, J. W. Borst, K. M. Mullen, I. H. M. van Stokkum, A. J.W. G. Visser, and H. van Amerongen, "Global analysis of forster resonance energy transfer in live cells measured by fluorescence lifetime imaging microscopy ex-

ploiting the rise time of acceptor fluorescence", Phys. Chem. Chem. Phys. **12**, 7593–7602 (2010) (cit. on p. 65).

[125]F. Fassioli, R. Dinshaw, P. C. Arpin, and G. D. Scholes, "Photosynthetic light harvesting: excitons and coherence", J. R. Soc. Interface **11** (2013) (cit. on p. 67).

[126]D. P. Craig and T. Thirunamachandran, *Molecular quantum electrodynamics: an introduction to radiation-molecule interactions* (Courier Corporation, 1984) (cit. on p. 71).

[127]R. D. Richardson, M. G. Baud, C. E. Weston, H. S. Rzepa, M. K. Kuimova, and M. J. Fuchter, "Dual wavelength asymmetric photochemical synthesis with circularly polarized light", Chem. Sci. **6**, 3853–3862 (2015) (cit. on p. 74).

[128]G. Lindblad, "On the generators of quantum dynamical semigroups", Comm. Math. Phys. **48**, 119–130 (1976) (cit. on p. 75).

[129]J. Dalibard, Y. Castin, and K. Mølmer, "Wave-function approach to dissipative processes in quantum optics", Phys. Rev. Lett. **68**, 580–583 (1992) (cit. on p. 77).

[130]K. Mølmer, Y. Castin, and J. Dalibard, "Monte Carlo wave-function method in quantum optics", J. Opt. Soc. Am. B **10**, 524–538 (1993) (cit. on p. 77).

[131]P. A. Franken, A. E. Hill, C. W. Peters, and G. Weinreich, "Generation of optical harmonics", Phys. Rev. Lett. **7**, 118–119 (1961) (cit. on p. 78).

[132]Z. Sekkat and W. Knoll, *Photoreactive organic thin films* (Academic Press, 2002) (cit. on p. 78).

[133]S. R. Marder, "Organic nonlinear optical materials: where we have been and where we are going", Chem. Commun., 131–134 (2006) (cit. on p. 78).

[134]J. Leuthold, C. Koos, and W. Freude, "Nonlinear silicon photonics", Nat. Photon. **4**, 535–544 (2010) (cit. on p. 78).

[135]S. R. Marder, J. E. Sohn, and G. D. Stucky, *Materials for nonlinear optics chemical perspectives*, Vol. 455 (American Chemical Society, 1991) (cit. on pp. 79, 81).

[136]J. Xu, S. Semin, D. Niedzialek, P. H. J. Kouwer, E. Fron, E. Coutino, M. Savoini, Y. Li, J. Hofkens, H. Uji-I, D. Beljonne, T. Rasing, and A. E. Rowan, "Self-assembled organic microfibers for nonlinear optics", Adv. Mater. **25**, 2084–2089 (2013) (cit. on pp. 79, 83).

[137]T. F. Heinz, C. K. Chen, D. Ricard, and Y. R. Shen, "Spectroscopy of molecular monolayers by resonant second-harmonic generation", Phys. Rev. Lett. **48**, 478–481 (1982) (cit. on pp. 79, 144).

[138]S. H. Lin, R. G. Alden, A. A. Villaeys, and V. Pflumio, "Theory of second-harmonic generation of molecular systems: the steady-state case", Phys. Rev. A **48**, 3137–3151 (1993) (cit. on pp. 79, 84, 145).

[139]T. Chervy, J. Xu, Y. Duan, C. Wang, L. Mager, M. Frerejean, J. A. W. Münninghoff, P. Tinnemans, J. A. Hutchison, C. Genet, A. E. Rowan, T. Rasing, and T. W. Ebbesen, "High-efficiency second-harmonic generation from hybrid light-matter states", Nano Lett. **16**, 7352–7356 (2016) (cit. on pp. 79–82, 86–88, 144).

[140]M. Gouterman, "Spectra of porphyrins", J. Mol. Spectrosc. **6**, 138 –163 (1961) (cit. on p. 81).

[141]B. G. Anex, "Optical properties of highly absorbing crystals", Mol. Cryst. Liq. Cryst. **1**, 1–36 (1966) (cit. on p. 81).

[142]A. Ashkin, G. Boyd, and J. Dziedzic, "Resonant optical second harmonic generation and mixing", IEEE J. Quantum Electron. **2**, 109–124 (1966) (cit. on pp. 85, 87).

[143]S. Aberra Guebrou, C. Symonds, E. Homeyer, J. C. Plenet, Y. N. Gartstein, V. M. Agranovich, and J. Bellessa, "Coherent emission from a disordered organic semiconductor induced by strong coupling with surface plasmons", Phys. Rev. Lett. **108**, 066401 (2012) (cit. on pp. 89, 129).

[144]L. Shi, T. K. Hakala, H. T. Rekola, J.-P. Martikainen, R. J. Moerland, and P. Törmä, "Spatial coherence properties of organic molecules coupled to plasmonic surface lattice reso-

nances in the weak and strong coupling regimes", Phys. Rev. Lett. **112**, 153002 (2014) (cit. on pp. 89, 129).

[145]J. P. Long and B. S. Simpkins, "Coherent coupling between a molecular vibration and Fabry-Pérot optical cavity to give hybridized states in the strong coupling limit", ACS Photonics **2**, 130–136 (2015) (cit. on p. 91).

[146]J. George, A. Shalabney, J. A. Hutchison, C. Genet, and T. W. Ebbesen, "Liquid-phase vibrational strong coupling", J. Phys. Chem. Lett. **6**, 1027–1031 (2015) (cit. on pp. 91, 93).

[147]B. S. Simpkins, K. P. Fears, W. J. Dressick, B. T. Spann, A. D. Dunkelberger, and J. C. Owrutsky, "Spanning strong to weak normal mode coupling between vibrational and Fabry–Pérot cavity modes through tuning of vibrational absorption strength", ACS Photonics **2**, 1460–1467 (2015) (cit. on p. 91).

[148]M. Muallem, A. Palatnik, G. D. Nessim, and Y. R. Tischler, "Strong light-matter coupling between a molecular vibrational mode in a PMMA film and a low-loss mid-IR microcavity", Ann. Phys. **528**, 313–320 (2016) (cit. on pp. 91, 118).

[149]S. R. Casey and J. R. Sparks, "Vibrational strong coupling of organometallic complexes", J. Phys. Chem. C **120**, 28138–28143 (2016) (cit. on p. 91).

[150]H. Memmi, O. Benson, S. Sadofev, and S. Kalusniak, "Strong coupling between surface plasmon polaritons and molecular vibrations", Phys. Rev. Lett. **118**, 126802 (2017) (cit. on p. 91).

[151]J. del Pino, J. Feist, and F. J. Garcia-Vidal, "Quantum theory of collective strong coupling of molecular vibrations with a microcavity mode", New J. Phys. **17**, 053040 (2015) (cit. on p. 91).

[152]R. M. A. Vergauwe, J. George, T. Chervy, J. A. Hutchison, A. Shalabney, V. Y. Torbeev, and T. W. Ebbesen, "Quantum strong coupling with protein vibrational modes", J. Phys. Chem. Lett. **7**, 4159–4164 (2016) (cit. on p. 91).

[153]A. D. O'Connell, M. Hofheinz, M. Ansmann, R. C. Bialczak, M. Lenander, E. Lucero, M. Neeley, D. Sank, H. Wang, M. Weides, J. Wenner, J. M. Martinis, and A. N. Cleland, "Quantum ground state and single-phonon control of a mechanical resonator", Nature **464**, 697–703 (2010) (cit. on p. 91).

[154]P. Roelli, C. Galland, N. Piro, and T. J. Kippenberg, "Molecular cavity optomechanics as a theory of plasmon-enhanced raman scattering", Nat. Nanotech. (2015) (cit. on p. 91).

[155]J. George, T. Chervy, A. Shalabney, E. Devaux, H. Hiura, C. Genet, and T. W. Ebbesen, "Multiple Rabi splittings under ultrastrong vibrational coupling", Phys. Rev. Lett. **117**, 153601 (2016) (cit. on pp. 92, 94, 95, 97, 99, 101, 108, 110).

[156]G. Gunter, A. A. Anappara, J. Hees, A. Sell, G. Biasiol, L. Sorba, S. De Liberato, C. Ciuti, A. Tredicucci, A. Leitenstorfer, and R. Huber, "Sub-cycle switch-on of ultrastrong light-matter interaction", Nature **458**, 178–181 (2009) (cit. on p. 92).

[157]S. D. Liberato, C. Ciuti, and I. Carusotto, "Quantum vacuum radiation spectra from a semiconductor microcavity with a time-modulated vacuum Rabi frequency", Phys. Rev. Lett. **98**, 103602 (2007) (cit. on p. 92).

[158]A. Auer and G. Burkard, "Entangled photons from the polariton vacuum in a switchable optical cavity", Phys. Rev. B **85**, 235140 (2012) (cit. on p. 92).

[159]P. Nataf and C. Ciuti, "No-go theorem for superradiant quantum phase transitions in cavity QED and counter-example in circuit QED", Nat. Commun. **1**, 72 (2010) (cit. on p. 92).

[160]S. De Liberato and C. Ciuti, "Quantum phases of a multimode bosonic field coupled to flat electronic bands", Phys. Rev. Lett. **110**, 133603 (2013) (cit. on p. 92).

[161]C. Ciuti and I. Carusotto, "Input-output theory of cavities in the ultrastrong coupling regime: the case of time-independent cavity parameters", Phys. Rev. A **74**, 033811 (2006) (cit. on p. 92).

[162]S. De Liberato and C. Ciuti, "Quantum model of microcavity intersubband electroluminescent devices", Phys. Rev. B **77**, 155321 (2008) (cit. on p. 92).

[163]S. De Liberato and C. Ciuti, "Quantum theory of electron tunneling into intersubband cavity polariton states", Phys. Rev. B **79**, 075317 (2009) (cit. on p. 92).

[164]A. Ridolfo, M. Leib, S. Savasta, and M. J. Hartmann, "Photon blockade in the ultrastrong coupling regime", Phys. Rev. Lett. **109**, 193602 (2012) (cit. on p. 92).

[165]R. Cataliotti, A. Foffani, and L. Marchetti, "Infrared spectrum of crystalline iron pentacarbonyl", Inorg. Chem. **10**, 1594–1597 (1971) (cit. on p. 93).

[166]D. Meiser and P. Meystre, "Superstrong coupling regime of cavity quantum electrodynamics", Phys. Rev. A **74**, 065801 (2006) (cit. on p. 94).

[167]E. Dupont, J. A. Gupta, and H. C. Liu, "Giant vacuum-field Rabi splitting of intersubband transitions in multiple quantum wells", Phys. Rev. B **75**, 205325 (2007) (cit. on p. 94).

[168]X. Yu, D. Xiong, H. Chen, P. Wang, M. Xiao, and J. Zhang, "Multi-normal-mode splitting of a cavity in the presence of atoms: a step towards the superstrong-coupling regime", Phys. Rev. A **79**, 061803 (2009) (cit. on p. 94).

[169]A. D. Rakić, A. B. Djurišić, J. M. Elazar, and M. L. Majewski, "Optical properties of metallic films for vertical-cavity optoelectronic devices", Appl. Opt. **37**, 5271–5283 (1998) (cit. on p. 96).

[170]R. Loudon, *The quantum theory of light* (OUP Oxford, 2000) (cit. on p. 102).

[171]A. Vasanelli, Y. Todorov, and C. Sirtori, "Ultra-strong light–matter coupling and superradiance using dense electron gases", C. R. Phys. **17**, 861 –873 (2016) (cit. on p. 102).

[172]C. Cohen-Tannoudji, J. Dupont-Roc, and G. Grynberg, *Photons and atoms: introduction to quantum electrodynamics* (Wiley-VCH, 1997) (cit. on p. 104).

[173]S. G. Johnson, "The NLopt nonlinear-optimization package", http://ab-initio.mit.edu/nlopt (cit. on p. 107).

[174]A. Trichet, E. Durupt, F. Médard, S. Datta, A. Minguzzi, and M. Richard, "Long-range correlations in a 97% excitonic one-dimensional polariton condensate", Phys. Rev. B **88**, 121407 (2013) (cit. on p. 109).

[175]D. W. Oxtoby, "Vibrational relaxation in liquids: quantum states in a classical bath", J. Phys. Chem. **87**, 3028–3033 (1983) (cit. on p. 111).

[176]K. D. Rector and M. D. Fayer, "Vibrational dephasing mechanisms in liquids and glasses: vibrational echo experiments", J. Chem. Phys. **108**, 1794–1803 (1998) (cit. on p. 111).

[177]A. Dunkelberger, B. Spann, K. Fears, B. Simpkins, and J. Owrutsky, "Modified relaxation dynamics and coherent energy exchange in coupled vibration-cavity polaritons", Nat. Commun. **7**, 13504 (2016) (cit. on pp. 112, 119).

[178]P. F. Bernath, "Infrared emission spectroscopy", Annu. Rep. Prog. Chem., Sect. C: Phys. Chem. **96**, 177–224 (2000) (cit. on p. 115).

[179]M. Celina, D. Ottesen, K. Gillen, and R. Clough, "FTIR emission spectroscopy applied to polymer degradation", Polym. Degrad. Stab. **58**, 15 –31 (1997) (cit. on pp. 115, 116).

[180]S. W. Ruff, P. R. Christensen, P. W. Barbera, and D. L. Anderson, "Quantitative thermal emission spectroscopy of minerals: a laboratory technique for measurement and calibration", J. Geophys. Res. **102**, 14899–14913 (1997) (cit. on p. 115).

[181]P. R. Christensen, G. L. Mehall, S. H. Silverman, S. Anwar, G. Cannon, N. Gorelick, R. Kheen, T. Tourville, D. Bates, S. Ferry, T. Fortuna, J. Jeffryes, W. O'Donnell, R. Peralta, T. Wolverton, D. Blaney, R. Denise, J. Rademacher, R. V. Morris, and S. Squyres, "Miniature thermal emission spectrometer for the Mars exploration rovers", J. Geophys. Res. **108**, 8064 (2003) (cit. on p. 115).

[182] A Léger, L d'Hendecourt, and D Defourneau, "Physics of IR emission by interstellar PAH molecules", Astron. Astrophys. **216**, 148–164 (1989) (cit. on p. 115).

[183] J. W. Salisbury, A. Wald, and D. M. D'Aria, "Thermal-infrared remote sensing and Kirchhoff's law: 1. laboratory measurements", J. Geophys. Res. **99**, 11897–11911 (1994) (cit. on p. 116).

[184] P. Corfdir, J. Levrat, G. Rossbach, R. Butté, E. Feltin, J.-F. Carlin, G. Christmann, P. Lefebvre, J.-D. Ganière, N. Grandjean, and B. Deveaud-Plédran, "Impact of biexcitons on the relaxation mechanisms of polaritons in III-nitride based multiple quantum well microcavities", Phys. Rev. B **85**, 245308 (2012) (cit. on p. 118).

[185] R. Tenne, L. Margulis, M. Genut, and G. Hodes, "Polyhedral and cylindrical structures of tungsten disulphide", Nature **360**, 444–446 (1992) (cit. on p. 120).

[186] L. Margulis, G. Salitra, R. Tenne, and M. Talianker, "Nested fullerene-like structures", Nature **365**, 113–114 (1993) (cit. on p. 120).

[187] K. F. Mak, C. Lee, J. Hone, J. Shan, and T. F. Heinz, "Atomically thin MoS_2: a new direct-gap semiconductor", Phys. Rev. Lett. **105**, 136805 (2010) (cit. on pp. 120, 129).

[188] A. Splendiani, L. Sun, Y. Zhang, T. Li, J. Kim, C.-Y. Chim, G. Galli, and F. Wang, "Emerging photoluminescence in monolayer MoS_2", Nano Lett. **10**, 1271–1275 (2010) (cit. on p. 120).

[189] H. S. S. Ramakrishna Matte, A. Gomathi, A. K. Manna, D. J. Late, R. Datta, S. K. Pati, and C. N. R. Rao, "MoS_2 and WS_2 analogues of graphene", Angew. Chem. Int. Ed. **122**, 4153–4156 (2010) (cit. on p. 120).

[190] A. Castellanos-Gomez, "Why all the fuss about 2D semiconductors?", Nat. Photon. **10**, 202–204 (2016) (cit. on p. 120).

[191] W. L. Barnes, A. Dereux, and T. W. Ebbesen, "Surface plasmon subwavelength optics", Nature **424**, 824–830 (2003) (cit. on p. 120).

[192]C. Genet and T. W. Ebbesen, "Light in tiny holes", Nature **445**, 39–46 (2007) (cit. on pp. 120, 128).

[193]G. M. Lerman, A. Yanai, and U. Levy, "Demonstration of nanofocusing by the use of plasmonic lens illuminated with radially polarized light", Nano Lett. **9**, 2139–2143 (2009) (cit. on p. 120).

[194]N. Shitrit, I. Bretner, Y. Gorodetski, V. Kleiner, and E. Hasman, "Optical spin Hall effects in plasmonic chains", Nano Lett. **11**, 2038–2042 (2011) (cit. on pp. 120, 137).

[195]Y. Gorodetski, A. Drezet, C. Genet, and T. W. Ebbesen, "Generating far-field orbital angular momenta from near-field optical chirality", Phys. Rev. Lett. **110**, 203906 (2013) (cit. on pp. 120, 134, 135).

[196]A. Canaguier-Durand and C. Genet, "Chiral near fields generated from plasmonic optical lattices", Phys. Rev. A **90**, 023842 (2014) (cit. on p. 120).

[197]P. Genevet and F. Capasso, "Holographic optical metasurfaces: a review of current progress", Rep. Prog. Phys. **78**, 024401 (2015) (cit. on p. 120).

[198]G. Spektor, D. Kilbane, A. K. Mahro, B. Frank, S. Ristok, L. Gal, P. Kahl, D. Podbiel, S. Mathias, H. Giessen, F.-J. Meyer zu Heringdorf, M. Orenstein, and M. Aeschlimann, "Revealing the subfemtosecond dynamics of orbital angular momentum in nanoplasmonic vortices", Science **355**, 1187–1191 (2017) (cit. on p. 120).

[199]S. Wang, S. Li, T. Chervy, A. Shalabney, S. Azzini, E. Orgiu, J. A. Hutchison, C. Genet, P. Samorì, and T. W. Ebbesen, "Coherent coupling of WS_2 monolayers with metallic photonic nanostructures at room temperature", Nano Lett. **16**, 4368–4374 (2016) (cit. on pp. 121, 123, 125, 128, 130, 132).

[200]T. Chervy, S. Azzini, E. Lorchat, S. Wang, Y. Gorodetski, J. A. Hutchison, S. Berciaud, T. W. Ebbesen, and C. Genet, "Spin-momentum locked polariton transport in the chiral strong coupling regime", arXiv preprint arXiv:1701.07972 (2017) (cit. on pp. 121, 136, 138, 140, 143, 147, 148, 153).

[201] F. A. Rasmussen and K. S. Thygesen, "Computational 2D materials database: electronic structure of transition-metal dichalcogenides and oxides", J. Phys. Chem. C **119**, 13169–13183 (2015) (cit. on p. 121).

[202] A. Chernikov, T. C. Berkelbach, H. M. Hill, A. Rigosi, Y. Li, O. B. Aslan, D. R. Reichman, M. S. Hybertsen, and T. F. Heinz, "Exciton binding energy and nonhydrogenic rydberg series in monolayer WS_2", Phys. Rev. Lett. **113**, 076802 (2014) (cit. on p. 121).

[203] K. F. Mak, K. He, C. Lee, G. H. Lee, J. Hone, T. F. Heinz, and J. Shan, "Tightly bound trions in monolayer MoS_2", Nat. Mater. **12**, 207–211 (2013) (cit. on p. 121).

[204] J. S. Ross, S. Wu, H. Yu, N. J. Ghimire, A. M. Jones, G. Aivazian, J. Yan, D. G. Mandrus, D. Xiao, W. Yao, and X. Xu, "Electrical control of neutral and charged excitons in a monolayer semiconductor", Nat. Commun. **4**, 1474 (2013) (cit. on p. 121).

[205] T. C. Berkelbach, M. S. Hybertsen, and D. R. Reichman, "Theory of neutral and charged excitons in monolayer transition metal dichalcogenides", Phys. Rev. B **88**, 045318 (2013) (cit. on p. 121).

[206] A. Singh, G. Moody, S. Wu, Y. Wu, N. J. Ghimire, J. Yan, D. G. Mandrus, X. Xu, and X. Li, "Coherent electronic coupling in atomically thin $MoSe_2$", Phys. Rev. Lett. **112**, 216804 (2014) (cit. on p. 121).

[207] Y. You, X.-X. Zhang, T. C. Berkelbach, M. S. Hybertsen, D. R. Reichman, and T. F. Heinz, "Observation of biexcitons in monolayer WSe_2", Nat. Phys. **11**, 477–481 (2015) (cit. on p. 121).

[208] J. Shang, X. Shen, C. Cong, N. Peimyoo, B. Cao, M. Eginligil, and T. Yu, "Observation of excitonic fine structure in a 2D transition-metal dichalcogenide semiconductor", ACS Nano **9**, 647–655 (2015) (cit. on p. 121).

[209]E. J. Sie, A. J. Frenzel, Y.-H. Lee, J. Kong, and N. Gedik, "Intervalley biexcitons and many-body effects in monolayer MoS_2", Phys. Rev. B **92**, 125417 (2015) (cit. on p. 121).

[210]A. M. Jones, H. Yu, J. R. Schaibley, J. Yan, D. G. Mandrus, T. Taniguchi, K. Watanabe, H. Dery, W. Yao, and X. Xu, "Excitonic luminescence upconversion in a two-dimensional semiconductor", Nat. Phys. (2015) (cit. on p. 121).

[211]A. Singh, G. Moody, K. Tran, M. E. Scott, V. Overbeck, G. Berghäuser, J. Schaibley, E. J. Seifert, D. Pleskot, N. M. Gabor, J. Yan, D. G. Mandrus, M. Richter, E. Malic, X. Xu, and X. Li, "Trion formation dynamics in monolayer transition metal dichalcogenides", Phys. Rev. B **93**, 041401 (2016) (cit. on p. 121).

[212]C. Grenier, C. Ciuti, and A. Imamoğlu, "Trion-polaritons : how strong coupling to a cavity changes the orbital and spin properties of trions", ArXiv e-prints (2015) (cit. on p. 121).

[213]O. Cotlet, S. Zeytinoğlu, M. Sigrist, E. Demler, and A. Imamoğlu, "Superconductivity and other collective phenomena in a hybrid bose-fermi mixture formed by a polariton condensate and an electron system in two dimensions", Phys. Rev. B **93**, 054510 (2016) (cit. on p. 121).

[214]S. Ravets, S. Faelt, M. Kroner, W. Wegscheider, and A. Imamoğlu, "Polaron-polaritons in the integer and fractional quantum hall regimes", arXiv preprint arXiv:1701.01029 (2017) (cit. on p. 121).

[215]M. Sidler, P. Back, O. Cotlet, A. Srivastava, T. Fink, M. Kroner, E. Demler, and A. Imamoğlu, "Fermi polaron-polaritons in charge-tunable atomically thin semiconductors", Nat. Phys. **13**, 255–261 (2017) (cit. on p. 121).

[216]N Lundt, P Nagler, A Nalitov, S Klembt, M Wurdack, S Stoll, T. H. Harder, S Betzold, V Baumann, A. V. Kavokin, C Schüller, T Korn, S Höfling, and C Schneider, "Valley polarized relaxation and upconversion luminescence from tamm-plasmon trion–polaritons with a $MoSe_2$ monolayer", 2D Mater. **4**, 025096 (2017) (cit. on p. 121).

[217]D. Xiao, G.-B. Liu, W. Feng, X. Xu, and W. Yao, "Coupled spin and valley physics in monolayers of MoS_2 and other group-VI dichalcogenides", Phys. Rev. Lett. **108**, 196802 (2012) (cit. on pp. 121, 122).

[218]X. Xu, W. Yao, D. Xiao, and T. F. Heinz, "Spin and pseudospins in layered transition metal dichalcogenides", Nat. Phys. **10**, 343–350 (2014) (cit. on p. 121).

[219]W. Yao, D. Xiao, and Q. Niu, "Valley-dependent optoelectronics from inversion symmetry breaking", Phys. Rev. B **77**, 235406 (2008) (cit. on p. 122).

[220]K. F. Mak, K. He, J. Shan, and T. F. Heinz, "Control of valley polarization in monolayer MoS2 by optical helicity", Nat. Nanotech. **7**, 494–498 (2012) (cit. on p. 122).

[221]H. Zeng, J. Dai, W. Yao, D. Xiao, and X. Cui, "Valley polarization in MoS2 monolayers by optical pumping", Nat. Nanotech. **7**, 490–493 (2012) (cit. on p. 122).

[222]T. Cao, G. Wang, W. Han, H. Ye, C. Zhu, J. Shi, Q. Niu, P. Tan, E. Wang, B. Liu, and J. Feng, "Valley-selective circular dichroism of monolayer molybdenum disulphide", Nat. Commun. **3**, 887 (2012) (cit. on p. 122).

[223]G. Moody, J. Schaibley, and X. Xu, "Exciton dynamics in monolayer transition metal dichalcogenides", J. Opt. Soc. Am. B **33**, C39–C49 (2016) (cit. on pp. 122, 146, 150).

[224]A. M. Jones, H. Yu, N. J. Ghimire, S. Wu, G. Aivazian, J. S. Ross, B. Zhao, J. Yan, D. G. Mandrus, D. Xiao, W. Yao, and X. Xu, "Optical generation of excitonic valley coherence in monolayer WSe2", Nat. Nanotech. **8**, 634–638 (2013) (cit. on p. 122).

[225]G. Wang, X. Marie, B. L. Liu, T. Amand, C. Robert, F. Cadiz, P. Renucci, and B. Urbaszek, "Control of exciton valley coherence in transition metal dichalcogenide monolayers", Phys. Rev. Lett. **117**, 187401 (2016) (cit. on p. 122).

[226]X. Liu, T. Galfsky, Z. Sun, F. Xia, E.-c. Lin, Y.-H. Lee, S. Kéna-Cohen, and V. M. Menon, "Strong light–matter coupling in two-dimensional atomic crystals", Nat. Photon. **9**, 30–34 (2015) (cit. on p. 122).

[227]S Dufferwiel, S Schwarz, F Withers, A. Trichet, F Li, M Sich, O Del Pozo-Zamudio, C Clark, A Nalitov, D. Solnyshkov, et al., "Exciton-polaritons in van der Waals heterostructures embedded in tunable microcavities", Nat. Commun. **6**, 8579 (2015) (cit. on p. 122).

[228]W. Liu, B. Lee, C. H. Naylor, H.-S. Ee, J. Park, A. T. C. Johnson, and R. Agarwal, "Strong exciton–plasmon coupling in MoS2 coupled with plasmonic lattice", Nano Lett. **16**, 1262–1269 (2016) (cit. on p. 122).

[229]Y. Li, A. Chernikov, X. Zhang, A. Rigosi, H. M. Hill, A. M. van der Zande, D. A. Chenet, E.-M. Shih, J. Hone, and T. F. Heinz, "Measurement of the optical dielectric function of monolayer transition-metal dichalcogenides: MoS_2, $MoSe_2$, WS_2, and WSe_2", Phys. Rev. B **90**, 205422 (2014) (cit. on p. 124).

[230]V. M. Agranovich, *Surface polaritons*, Vol. 1 (Elsevier, 2012) (cit. on p. 124).

[231]A. V. Zayats, I. I. Smolyaninov, and A. A. Maradudin, "Nano-optics of surface plasmon polaritons", Phys. Rep. **408**, 131–314 (2005) (cit. on pp. 124, 127).

[232]H. Raether, *Surface plasmons on smooth and rough surfaces and on gratings*, Vol. 111 (Springer, 2006) (cit. on p. 124).

[233]B. Stein, "Plasmonic devices for surface optics and refractive index sensing", Thèse de doctorat dirigée par Ebbesen, Thomas W. Physique Strasbourg 2012, PhD thesis (2012) (cit. on pp. 126, 133).

[234]S. R. K. Rodriguez, J. Feist, M. A. Verschuuren, F. J. Garcia Vidal, and J. Gómez Rivas, "Thermalization and cooling of plasmon-exciton polaritons: towards quantum condensation", Phys. Rev. Lett. **111**, 166802 (2013) (cit. on p. 129).

[235]P Törmä and W. L. Barnes, "Strong coupling between surface plasmon polaritons and emitters: a review", Rep. Prog. Phys. **78**, 013901 (2015) (cit. on p. 129).

[236]A. González-Tudela, P. A. Huidobro, L. Martín-Moreno, C. Tejedor, and F. J. García-Vidal, "Theory of strong coupling between quantum emitters and propagating surface plasmons", Phys. Rev. Lett. **110**, 126801 (2013) (cit. on pp. 129, 150).

[237]W. L. Barnes, "Fluorescence near interfaces: the role of photonic mode density", J. Mod. Opt. **45**, 661–699 (1998) (cit. on p. 129).

[238]M. L. Brongersma, N. J. Halas, and P. Nordlander, "Plasmon-induced hot carrier science and technology", Nat. Nanotech. **10**, 25–34 (2015) (cit. on p. 129).

[239]Z. Li, Y. Xiao, Y. Gong, Z. Wang, Y. Kang, S. Zu, P. M. Ajayan, P. Nordlander, and Z. Fang, "Active light control of the MoS2 monolayer exciton binding energy", ACS Nano **9**, 10158–10164 (2015) (cit. on p. 129).

[240]O. L. Muskens, V. Giannini, J. A. Sánchez-Gil, and J. Gómez Rivas, "Strong enhancement of the radiative decay rate of emitters by single plasmonic nanoantennas", Nano Lett. **7**, 2871–2875 (2007) (cit. on p. 129).

[241]T. Schwartz, J. A. Hutchison, C. Genet, and T. W. Ebbesen, "Reversible switching of ultrastrong light-molecule coupling", Phys. Rev. Lett. **106**, 196405 (2011) (cit. on p. 131).

[242]T. W. Ebbesen, C. Genet, and S. I. Bozhevolnyi, "Surface-plasmon circuitry", Phys. Today **61**, 44 (2008) (cit. on p. 133).

[243]D. O'Connor, P. Ginzburg, F. J. Rodríguez-Fortuño, G. A. Wurtz, and A. V. Zayats, "Spin-orbit coupling in surface plasmon scattering by nanostructures", Nat. Commun. **5**, 5327 (2014) (cit. on p. 134).

[244]Q. Jiang, A. Pham, M. Berthel, S. Huant, J. Bellessa, C. Genet, and A. Drezet, "Directional and singular surface plasmon generation in chiral and achiral nanostructures demonstrated by leakage radiation microscopy", ACS Photonics **3**, 1116–1124 (2016) (cit. on p. 134).

[245]K. Y. Bliokh, F. Rodríguez-Fortuño, F. Nori, and A. V. Zayats, "Spin-orbit interactions of light", Nat. Photon. **9**, 796–808 (2015) (cit. on p. 134).

[246]Z. Bomzon, G. Biener, V. Kleiner, and E. Hasman, "Space-variant Pancharatnam–Berry phase optical elements with computer-generated subwavelength gratings", Opt. Lett. **27**, 1141–1143 (2002) (cit. on p. 134).

[247]B. le Feber, N. Rotenberg, and L. Kuipers, "Nanophotonic control of circular dipole emission", Nat. Commun. **6**, 6695 (2015) (cit. on p. 134).

[248]J. Petersen, J. Volz, and A. Rauschenbeutel, "Chiral nanophotonic waveguide interface based on spin-orbit interaction of light", Science **346**, 67–71 (2014) (cit. on p. 134).

[249]M. Rafayelyan, G. Tkachenko, and E. Brasselet, "Reflective spin-orbit geometric phase from chiral anisotropic optical media", Phys. Rev. Lett. **116**, 253902 (2016) (cit. on p. 134).

[250]K. Y. Bliokh, Y. Gorodetski, V. Kleiner, and E. Hasman, "Coriolis effect in optics: unified geometric phase and spin-Hall effect", Phys. Rev. Lett. **101**, 030404 (2008) (cit. on p. 134).

[251]Y. Gorodetski, A. Drezet, C. Genet, and T. W. Ebbesen, "Generating far-field orbital angular momenta from near-field optical chirality", Phys. Rev. Lett. **110**, 203906 (2013) (cit. on p. 134).

[252]J. Lin, J. B. Mueller, Q. Wang, G. Yuan, N. Antoniou, X.-C. Yuan, and F. Capasso, "Polarization-controlled tunable directional coupling of surface plasmon polaritons", Science **340**, 331–334 (2013) (cit. on pp. 134, 137).

[253]F. J. Rodríguez-Fortuño, G. Marino, P. Ginzburg, D. O'Connor, A. Martínez, G. A. Wurtz, and A. V. Zayats, "Near-field interference for the unidirectional excitation of electromagnetic guided modes", Science **340**, 328–330 (2013) (cit. on p. 134).

[254]G. Spektor, A. David, B. Gjonaj, G. Bartal, and M. Orenstein, "Metafocusing by a metaspiral plasmonic lens", Nano Lett. **15**, 5739–5743 (2015) (cit. on p. 134).

[255]Q. Jiang, A. Pham, M. Berthel, S. Huant, J. Bellessa, C. Genet, and A. Drezet, "Directional and singular surface plasmon generation in chiral and achiral nanostructures demonstrated by leakage radiation microscopy", ACS Photonics **3**, 1116–1124 (2016) (cit. on pp. 134, 137).

[256]R. Mitsch, C. Sayrin, B. Albrecht, P. Schneeweiss, and A. Rauschenbeutel, "Quantum state-controlled directional spontaneous emission of photons into a nanophotonic waveguide", Nat. Commun. **5**, 5713 (2014) (cit. on p. 134).

[257]I. Söllner, S. Mahmoodian, S. L. Hansen, L. Midolo, A. Javadi, G. Kiršanskė, T. Pregnolato, H. El-Ella, E. H. Lee, J. D. Song, S. Stobbe, and P. Lodahl, "Deterministic photon-emitter coupling in chiral photonic circuits", Nat. Nanotech. **10**, 775–778 (2015) (cit. on p. 134).

[258]C. Gonzalez-Ballestro, A. Gonzalez-Tudela, F. J. Garcia-Vidal, and E. Moreno, "Chiral route to spontaneous entanglement generation", Phys. Rev. B **92**, 155304 (2015) (cit. on p. 134).

[259]C. Sayrin, C. Junge, R. Mitsch, B. Albrecht, D. O'Shea, P. Schneeweiss, J. Volz, and A. Rauschenbeutel, "Nanophotonic optical isolator controlled by the internal state of cold atoms", Phys. Rev. X **5**, 041036 (2015) (cit. on p. 134).

[260]A. B. Young, A. C. T. Thijssen, D. M. Beggs, P. Androvitsaneas, L. Kuipers, J. G. Rarity, S. Hughes, and R. Oulton, "Polarization engineering in photonic crystal waveguides for spin-photon entanglers", Phys. Rev. Lett. **115**, 153901 (2015) (cit. on p. 134).

[261]C. Gonzalez-Ballestro, E. Moreno, F. J. Garcia-Vidal, and A. Gonzalez-Tudela, "Nonreciprocal few-photons routing schemes based on chiral waveguide-emitter couplings", Phys. Rev. A **94**, 063817 (2016) (cit. on p. 134).

[262]R. J. Coles, D. M. Price, J. E. Dixon, B. Royall, E. Clarke, P. Kok, M. S. Skolnick, A. M. Fox, and M. N. Makhonin, "Chirality of nanophotonic waveguide with embedded quantum emitter for unidirectional spin transfer", Nat. Commun. **7**, 11183 (2016) (cit. on pp. 134, 155).

[263] P. Lodahl, S. Mahmoodian, S. Stobbe, P. Schneeweiss, J. Volz, A. Rauschenbeutel, H. Pichler, and P. Zoller, "Chiral quantum optics", Nature **541**, 473–480 (2017) (cit. on p. 134).

[264] A. M. Jones, H. Yu, N. J. Ghimire, S. Wu, G. Aivazian, J. S. Ross, B. Zhao, J. Yan, D. G. Mandrus, D. Xiao, W. Yao, and X. Xu, "Optical generation of excitonic valley coherence in monolayer WSe2", Nat. Nanotech. **8**, 634–638 (2013) (cit. on pp. 136, 149).

[265] G. Moody, J. Schaibley, and X. Xu, "Exciton dynamics in monolayer transition metal dichalcogenides", J. Opt. Soc. Am. B **33**, C39–C49 (2016) (cit. on p. 136).

[266] K. Hao, G. Moody, F. Wu, C. K. Dass, L. Xu, C.-H. Chen, L. Sun, M.-Y. Li, L.-J. Li, A. H. MacDonald, and X. Li, "Direct measurement of exciton valley coherence in monolayer WSe2", Nat. Phys. **Advance Online Publication** (2016) 10.1038/nphys3674 (cit. on pp. 136, 149).

[267] S. Dufferwiel, T. P. Lyons, D. D. Solnyshkov, A. A. P. Trichet, F. Withers, S. Schwarz, G. Malpuech, J. M. Smith, K. S. Novoselov, M. S. Skolnick, D. N. Krizhanovskii, and A. I. Tartakovskii, "Valley addressable exciton-polaritons in atomically thin semiconductors", (2016) arXiv:1612.05073[cond-mat.mes-hall] (cit. on pp. 136, 146, 147).

[268] Y.-J. Chen, J. D. Cain, T. K. Stanev, V. P. Dravid, and N. P. Stern, "Valley-polarized exciton-polaritons in a monolayer semiconductor", (2017) arXiv:1701.05579[cond-mat.mtrl-sci] (cit. on pp. 136, 147, 150).

[269] M.-E. Kleemann, R. Chikkaraddy, E. M. Alexeev, D. Kos, C. Carnegie, W. Deacon, A. de Casalis de Pury, C. Grosse, B. de Nijs, J. Mertens, A. I. Tartakovskii, and J. J. Baumberg, "Strong-coupling of WSe_2 in ultra-compact plasmonic nanocavities at room temperature", (2017) arXiv:1704.02756[physics.optics] (cit. on pp. 136, 147).

[270] K. Y. Bliokh, Y. Gorodetski, V. Kleiner, and E. Hasman, "Coriolis effect in optics: unified geometric phase and spin-

Hall effect", Phys. Rev. Lett. **101**, 030404 (2008) (cit. on p. 137).

[271] L. Huang, X. Chen, B. Bai, Q. Tan, G. Jin, T. Zentgraf, and S. Zhang, "Helicity dependent directional surface plasmon polariton excitation using a metasurface with interfacial phase discontinuity", Light Sci. Appl. **2** (2013) 10.1038/lsa.2013.26 (cit. on p. 137).

[272] F. Cadiz, E. Courtade, C. Robert, G. Wang, Y. Shen, H. Cai, T. Taniguchi, K. Watanabe, H. Carrere, D. Lagarde, M. Manca, T. Amand, P. Renucci, S. Tongay, X. Marie, and B. Urbaszek, "Excitonic linewidth approaching the homogeneous limit in MoS_2-based van der Waals heterostructures", Phys. Rev. X **7**, 021026 (2017) (cit. on p. 139).

[273] K. L. Seyler, J. R. Schaibley, P. Gong, P. Rivera, A. M. Jones, S. Wu, J. Yan, D. G. Mandrus, W. Yao, and X. Xu, "Electrical control of second-harmonic generation in a WSe2 monolayer transistor", Nat. Nanotech. **10**, 407–411 (2015) (cit. on p. 143).

[274] A. T. Hanbicki, K. M. McCreary, G. Kioseoglou, M. Currie, C. S. Hellberg, A. L. Friedman, and B. T. Jonker, "High room temperature optical polarization due to spin-valley coupling in monolayer ws2", AIP Advances **6**, 055804 (2016) (cit. on p. 146).

[275] R. J. Holmes and S. R. Forrest, "Strong exciton-photon coupling and exciton hybridization in a thermally evaporated polycrystalline film of an organic small molecule", Phys. Rev. Lett. **93**, 186404 (2004) (cit. on p. 146).

[276] A. M. Jones, H. Yu, J. R. Schaibley, J. Yan, D. G. Mandrus, T. Taniguchi, K. Watanabe, H. Dery, W. Yao, and X. Xu, "Excitonic luminescence upconversion in a two-dimensional semiconductor", Nat. Phys. **12**, 323–327 (2016) (cit. on p. 147).

[277] D. M. Whittaker, P. Kinsler, T. A. Fisher, M. S. Skolnick, A. Armitage, A. M. Afshar, M. D. Sturge, and J. S. Roberts, "Motional narrowing in semiconductor microcavities", Phys. Rev. Lett. **77**, 4792–4795 (1996) (cit. on p. 147).

[278]G. Wang, X. Marie, B. L. Liu, T. Amand, C. Robert, F. Cadiz, P. Renucci, and B. Urbaszek, "Control of exciton valley coherence in transition metal dichalcogenide monolayers", Phys. Rev. Lett. **117**, 187401 (2016) (cit. on p. 149).

[279]R Schmidt, A Arora, G Plechinger, P Nagler, A Granados del Aguila, M. V. Ballottin, P. C. M. Christianen, S Michaelis de Vasconcellos, C Schuller, T Korn, and R Bratschitsch, "Magnetic-field induced rotation of polarized emission from monolayer WS_2", Phys. Rev. Lett. **117**, 077402 (2016) (cit. on p. 149).

[280]Z. Ye, D. Sun, and T. F. Heinz, "Optical manipulation of valley pseudospin", Nat. Phys. **13**, 26–29 (2017) (cit. on p. 149).

[281]B. Zhu, H. Zeng, J. Dai, Z. Gong, and X. Cui, "Anomalously robust valley polarization and valley coherence in bilayer WS2", Proc. Natl. Acad. Sci. **111**, 11606–11611 (2014) (cit. on p. 149).

[282]S. Wüster, "Quantum Zeno suppression of intramolecular forces", Phys. Rev. Lett. **119**, 013001 (2017) (cit. on p. 152).

[283]T. Low, A. Chaves, J. D. Caldwell, A. Kumar, N. X. Fang, P. Avouris, T. F. Heinz, F. Guinea, L. Martin-Moreno, and F. Koppens, "Polaritons in layered two-dimensional materials", Nat. Mater. **16**, 182–194 (2017) (cit. on p. 155).

[284]K. Y. Bliokh, D. Smirnova, and F. Nori, "Quantum spin hall effect of light", Science **348**, 1448–1451 (2015) (cit. on p. 157).

[285]Y. Zhou, G. Scuri, D. S. Wild, A. A. High, A. Dibos, L. A. Jauregui, C. Shu, K. De Greve, K. Pistunova, A. Y. Joe, T. Taniguchi, K. Watanabe, P. Kim, M. D. Lukin, and H. Park, "Probing dark excitons in atomically thin semiconductors via near-field coupling to surface plasmon polaritons", Nat. Nanotech. **advance online publication** (2017) (cit. on p. 157).

[286]G Wang, C Robert, M. Glazov, F Cadiz, E Courtade, T Amand, D Lagarde, T Taniguchi, K Watanabe, B Urbaszek, and X Marie, "In-plane propagation of light in transition metal dichalcogenide monolayers: optical selection rules", arXiv preprint arXiv:1704.05341 (2017) (cit. on p. 157).

[287]X.-X. Zhang, T. Cao, Z. Lu, Y.-C. Lin, F. Zhang, Y. Wang, Z. Li, J. C. Hone, J. A. Robinson, D. Smirnov, S. G. Louie, and T. F. Heinz, "Magnetic brightening and control of dark excitons in monolayer WSe2", Nat. Nanotech. **advance online publication** (2017) (cit. on p. 157).

[288]K. P. Loh, "2D materials: brightening the dark excitons", Nat. Nanotech. **advance online publication** (2017) (cit. on p. 157).

Thibault CHERVY

Strong coupling regime of cavity quantum electrodynamics and its consequences on molecules and materials

Résumé

Cette thèse présente une étude exploratoire de plusieurs aspects du couplage fort lumière-matière dans des matériaux moléculaires. Différentes propriétés héritées d'un tel couplage sont démontrées, ouvrant de nombreuses possibilités d'applications, allant du transfert d'énergie à la génération de signaux optiques non-linéaires et à l'élaboration de réseaux polaritoniques chiraux. Au travers des thématiques abordées, l'idée d'un couplage lumière-matière entrant en compétition avec les différentes fréquences de dissipation des molécules se révèle être cruciale. Ainsi, la prédominance du couplage cohérent au champ électromagnétique apparaît comme un moyen de modifier les propriétés quantiques des états moléculaires, ouvrant la voie à une nouvelle chimie des matériaux en cavité.

Mots-clés : Couplage fort lumière-matière – Polariton de cavité – Chimie en cavité – Plasmonique

Résumé en anglais

This thesis presents an exploratory study of several aspects of strong light-matter coupling in molecular materials. Different properties inherited from such a coupling are demonstrated, opening the way to numerous applications, ranging from energy transfer to the generation of non-linear optical signals and to the development of chiral polaritonic networks. Through the topics covered, the idea of a light-matter coupling strength competing with the different frequencies of relaxation of the molecules proves to be crucial. Thus, the predominance of the coherent coupling to the electromagnetic field appears as a new mean of modifying the quantum properties of molecular systems, opening the way to a new chemistry of materials in optical cavities.

Key words: Light-matter strong coupling – Cavity polariton – Cavity chemistry – Plasmonics